



PACIFIC EARTHQUAKE ENGINEERING RESEARCH CENTER

Data Resources for NGA-Subduction Project

**NGA-Subduction Principal Investigator
Yousef Bozorgnia, Ph.D., PE**

**Department of Civil and Environmental Engineering
B. John Garrick Institute for Risk Sciences
University of California, Los Angeles**

**Report Editor
Jonathan P. Stewart, Ph.D., PE**

**Department of Civil and Environmental Engineering
B. John Garrick Institute for Risk Sciences
University of California, Los Angeles**

A report on research conducted with support from FM Global, the US Geological Survey, the California Department of Transportation, and the Pacific Gas & Electric Company.

PEER Report 2020/02
Pacific Earthquake Engineering Research Center
Headquarters, University of California at Berkeley

March 2020

Disclaimer

The opinions, findings, and conclusions or recommendations expressed in this publication are those of the author(s) and do not necessarily reflect the views of the study sponsor(s), the Pacific Earthquake Engineering Research Center, or the Regents of the University of California.

Data Resources for NGA-Subduction Project

**NGA-Subduction Principal Investigator
Yousef Bozorgnia, Ph.D., PE**

**Department of Civil and Environmental Engineering
B. John Garrick Institute for Risk Sciences
University of California, Los Angeles**

**Report Editor
Jonathan P. Stewart, Ph.D., PE**

**Department of Civil and Environmental Engineering
B. John Garrick Institute for Risk Sciences
University of California, Los Angeles**

A report on research conducted with support from FM Global, the
US Geological Survey, the California Department of
Transportation, and the Pacific Gas & Electric Company.

PEER Report 2020/02
Pacific Earthquake Engineering Research Center
Headquarters, University of California at Berkeley

March 2020

ABSTRACT

The NGA-Subduction (NGA-Sub) project is one in a series of Next Generation Attenuation (NGA) projects directed towards database and ground-motion model development for applications in seismic-demand characterization. Whereas prior projects had targeted shallow crustal earthquakes, active tectonic regions (NGA-West1 and NGA-West2), and stable continental regions (NGA-East), NGA-Sub is the first to address specifically subduction zones, which are a dominant source of seismic hazard in many regions globally, including the Pacific Northwest region of the United States and Canada.

This report describes the development of data resources for the NGA-Sub project. Agreements were formed with many owners and providers of ground-motion data and metadata worldwide to support data collection. Prior NGA projects organized the data collected into a series of spreadsheets. The enormous amount of the collected data for NGA-Sub required abandoning that strategy and ultimately the data was organized into a relational database consisting of 23 tables containing various data, metadata, and outputs of various codes required to compute desired quantities (e.g., intensity measures, distances, etc.). A schema was developed to relate fields in tables to each other through a series of primary and foreign keys. As with prior NGA projects, model developers and others largely interact with the data through flatfiles specific to certain types of intensity measures (e.g., pseudo-spectral accelerations at a certain oscillator damping level); such flatfiles are a time-stamped output of the database.

The NGA-Sub database contains 70,107 three-component records from 1880 earthquakes from seven global subduction zone regions: Alaska, Central America and Mexico, Cascadia, Japan, New Zealand, South America, and Taiwan. These data were processed on a component-specific basis to minimize noise effects in the data and remove baseline drifts. Component-specific usable period ranges are identified. Various ground-motion intensity measures (IMs) were computed including peak acceleration, peak velocity, pseudo-spectral accelerations for a range of oscillator periods and damping ratios, Fourier amplitudes, Arias intensity, significant durations, and cumulative absolute velocity-parameters.

Source parameters were assigned for earthquakes that produced recordings. Some of the 1880 earthquakes were screened out because of missing magnitudes or hypocenter locations, which decreased the number of potentially usable earthquakes to 1782. Further screening to remove events without an assigned event type (e.g., interface, intraslab, etc.) or distances reduced the number of events to 976. For those 976 events, source parameters of two general types are assigned: those related to the focus (including moment tensors) and those related to finite-fault representations of the source. A series of source-to-recording site distances and other parameters are provided using finite-fault representations of seismic sources. Finite-fault models of sources were developed from literature where available and from a simulation procedure otherwise. As part of the NGA-Sub project, the simulation procedure was revised and more fully documented. In addition, all events are reviewed to assign event types, event classes (mainshock, aftershock, etc.), and event locations relative to volcanic arcs.

Quality assurance (QA) of ground-motion data and source/path metadata was an important component of NGA-Sub. For ground motions, QA procedures included visual checks of records prior to processing, checks of records from each network that recorded each

earthquake to check for systematic outliers (perhaps indicative of gain problems), and checks of limiting distances beyond which data sampling for a given event is likely to be biased by data approaching noise thresholds. Source/path QA procedures largely involved checking that information in database fields accurately reflects source documents.

Site metadata was compiled into a site table containing time-averaged shear-wave velocities in the upper 30 m of sites (V_{S30}), basin depths, and related uncertainties. Major efforts were undertaken during the project to develop shear-wave velocity profile databases and to use those data to develop regional predictive models for site parameters when site-specific measurements are unavailable. Many of those predictive relations were published in journal or conference papers over the course of the NGA-Sub project (i.e., for Alaska, Cascadia, Chile, and Taiwan); those results are reviewed only briefly. Rather, emphasis in this report has been placed on procedures used for other regions. In addition to site parameters, all sites are also assigned a location relative to local volcanic arcs.

ACKNOWLEDGMENTS

Core support for the NGA-Sub research project was provided by FM Global, the US Geological Survey, the California Department of Transportation, and the Pacific Gas & Electric Company. Major support for the source/path component of the work was provided by the Chilean National Commission for Scientific and Technological Research (CONICYT) in the form of fellowship support for the first author of Chapter 4 (V. Contreras). Similarly, support for the site component of the work was provided by Bonneville Power Administration and the UCLA Civil & Environmental Engineering Department for the first author of Chapter 5 (S. K. Ahdi).

The support of these organizations is gratefully appreciated. The opinions, findings, conclusions, or recommendations expressed in this publication are those of the authors and do not necessarily reflect the views of the study sponsors, the Pacific Earthquake Engineering Research Center (PEER), or the Regents of the University of California.

CONTENTS

ABSTRACT	iii
ACKNOWLEDGMENTS	v
TABLE OF CONTENTS	vii
LIST OF TABLES	xi
LIST OF FIGURES	xiii
1 INTRODUCTION	1
1.1 NGA-Subduction Project Overview	1
1.2 Prior Subduction Databases	3
1.3 Organization of this Report	4
REFERENCES	5
2 RELATIONAL DATABASE	7
2.1 Introduction	7
2.2 Database Origins	9
2.3 Key Metadata	9
2.4 Source Metadata	9
2.5 Site and Station Metadata	11
2.6 Path Metadata	12
2.7 Ground-Motion Time Series and Intensity Measures	13
REFERENCES	16
3 GROUND MOTIONS AND INTENSITY MEASURES	17
3.1 Data Sources	17
3.2 Data Processing	19
3.2.1 Screening of Time Series.....	19
3.2.2 Time Windows for Data Processing.....	20
3.2.3 Fourier Spectra.....	22
(a) Mean removal and taper.....	22
(b) Computation of Fourier spectra.....	22

3.2.4	Filtering Methodology	25
	(a) <i>Acausal Butterworth filter</i>	25
	(b) <i>Causal Butterworth filter</i>	27
3.2.5	Baseline Correction.....	28
3.3	Computation of Ground-Motion Parameters	31
3.3.1	As-Recorded and RotDnn Pseudo-Spectral Accelerations	31
	(a) <i>As-recorded pseudo-spectral accelerations</i>	33
	(b) <i>RotDxx pseudo-spectral accelerations</i>	33
	(c) <i>Time series interpolation</i>	34
3.3.2	Other Ground-Motion Parameters	34
3.3.3	Ground-Motion Tables in Relational Database	35
3.4	Data-Quality Flags.....	36
	REFERENCES.....	39
4	SOURCE AND PATH METADATA.....	41
4.1	Overview and Organization.....	41
	4.1.1 Introduction.....	41
	4.1.2 Overview of Events.....	41
	4.1.3 Summary of NGA-Sub Events.....	52
4.2	General Earthquake Catalog.....	56
	4.2.1 Parameter Definitions	56
	4.2.2 Parameter Selection Procedures.....	57
	(a) <i>Magnitude</i>	58
	(b) <i>Hypocenter location</i>	63
	(c) <i>Fault type</i>	65
	(d) <i>Event type</i>	65
4.3	Source Parameters for Events with Finite-Fault Models.....	67
	4.3.1 Finite-Fault Models Collected	68
	4.3.2 Selection Criteria	76
	4.3.3 Trimming Criteria	80
	4.3.4 Multi-Segment Ruptures.....	81
4.4	Source Parameters for Events without Finite-Fault Models	84
	4.4.1 Subduction Earthquake Empirical Models for Fault Dimensions, Fault Orientations, and Hypocenter Location.....	84
	4.4.2 Finite-Fault Simulation Procedure.....	91
4.5	Site-to-Source Distance.....	92

4.5.1	Distance Computation.....	92
4.5.2	Calculation of R_{max}	93
	(a) <i>Data selection</i>	93
	(b) <i>Truncation levels</i>	94
	(c) <i>Regression</i>	94
	(d) <i>R_{max} calculations</i>	96
	(e) <i>R_{max} calculation for events not in regression dataset</i>	97
4.6	Quality-Assurance Procedures	97
4.7	Mainshock and Aftershock Classification	99
4.7.1	Methodology.....	100
4.7.2	Results.....	101
4.8	Volcanic-Arc Flags.....	102
	REFERENCES.....	105
5	SITE CONDITION PARAMETERS.....	113
5.1	Overview and Organization.....	113
5.1.1	Approach for <i>Site</i> Table Development	115
5.1.2	Sources of Station Data.....	116
5.2	Measured V_S data For V_{S30} Evaluation.....	118
5.2.1	Data Sources	118
5.2.2	V_{S30} Computation	120
5.3	Proxy-Based Estimation of V_{S30}.....	121
5.3.1	Methods used for Proxy-Based V_{S30} Prediction.....	122
5.3.2	Proposed V_{S30} Prediction Framework	122
	(a) <i>Approach I: Good quality V_S data and proxy maps</i>	123
	(b) <i>Approach II: Limited V_S data, good quality maps</i>	125
	(c) <i>Approach III: V_S data absent or of low quality, variable access to geologic maps</i>	125
5.3.3	Application of Existing Regional Proxy-Based V_{S30} Prediction Models.....	126
	(a) <i>Pacific Northwest</i>	126
	(b) <i>Alaska</i>	127
	(c) <i>Chile</i>	127
	(d) <i>New Zealand</i>	128
	(e) <i>Taiwan</i>	128
5.3.4	Previously Unpublished Proxy-Based V_{S30} Assignments	129
	(a) <i>Japan</i>	129
	(b) <i>Central and South America, excepting Chile</i>	133

	(c) <i>Western Canada and Alaska Panhandle</i>	133
5.4	V_{S30} Assignments	135
5.5	Basin-Depth Terms	135
5.5.1	Overview.....	135
5.5.2	Cascadia 3D Velocity Models	136
5.5.3	Taiwan 3D Velocity Model	139
5.5.4	Japan 3D Velocity Model	141
	REFERENCES	143

**ELECTRONIC SUPPLEMENT: NGA-SUBDUCTION PROJECT FLATFILE
(APRIL 2019 VERSION)**

LIST OF TABLES

Table 1.1	Summary of pre-NGA-Sub global subduction databases.	3
Table 2.1	Region identifier numbers used in assignment of earthquake and site keys.....	10
Table 2.2	Tables presenting source metadata in NGA-Sub relational database.	10
Table 2.3	Tables presenting site and station metadata in NGA-Sub relational database.	12
Table 2.4	Tables presenting path metadata in NGA-Sub relational database.....	13
Table 2.5	Tables related to ground-motion time series files in the NGA-Sub relational database.....	13
Table 2.6	Tables presenting ground-motion intensity measures and related metadata.	14
Table 3.1	Ground-motion catalogs contributing data to NGA-Sub database.	18
Table 3.2	Base duration used in the analysis.	21
Table 3.3	Cosine taper length applied to windowed accelerations.	22
Table 3.4	Minimum frequencies for Fourier spectra calculation.....	23
Table 3.5	Criteria for assignment of data-quality flags.	36
Table 4.1	Example events from NGA-Sub database (highlighted in maps in Figures 4.2–4.11), showing compiled source parameters.....	59
Table 4.2	Earthquake catalogs and published studies used to assign seismic moment.	60
Table 4.3	Earthquake catalogs and published studies used to assign hypocenter locations.	64
Table 4.4	Fault mechanism based on rake angle (after Ancheta et al. [2013]).....	65
Table 4.5	Flags in source database that indicate event-type classification.	66
Table 4.6	FFMs selected for use in NGA-Sub database.	69
Table 4.7	Computed distances (R_{rup}) using the seven FFMs for the 2010 Maule earthquake.	78
Table 4.8	Alternate FFMs for 2010 M8.81 Maule, Chile, earthquake.	79
Table 4.9	Summary of trimming applied for NGA-West and NGA-West 2 projects.	81
Table 4.10	Source review flags.....	99
Table 4.11	Description of volcanic-arc flags.....	103

Table 5.1	Number of sites in contributing strong motion station networks for NGA-Sub.	117
Table 5.2	Breakdown of measured- and proxy-based estimated V_{S30} data by NGA-Sub region.	119
Table 5.3	Literature summary for proxy-based methods for V_{S30} estimation.	124
Table 5.4	Computation of average epistemic uncertainty for similar V_{S30} geological age groups across multiple study regions.	126
Table 5.5	Moments for Iwahashi and Pike [2007] (IP07) terrain classes for application in Japan. Moments adopted from California are shown in parenthesis.....	130
Table 5.6	JEGM site categories, within-category moments from Matsuoka et al. [2006], (“Mea06”), and attributes of mapped V_{S30} within categories from Wakamatsu and Matsuoka [2013].	132
Table 5.7	Protocol used in NGA-Sub for assignment of preferred V_{S30} and related parameters.	135
Table 5.8	Summary of basin depth terms included in NGA-Sub <i>Site</i> table for various regions. “Estimated” depths are from 3D models, with exception of New Zealand.	136

LIST OF FIGURES

Figure 1.1	Locations of strong-motion recording stations with recordings in the NGA-Sub database.....	2
Figure 2.1	Components of NGA-Sub relational database.....	8
Figure 3.1	An example of a rejected time series.	19
Figure 3.2	Schematic drawing of different time windows.	21
Figure 3.3	Fourier amplitude spectra for time series in different windows.	24
Figure 3.4	Time domain response of acausally filtered impulse.....	26
Figure 3.5	Fourier amplitude spectra for acausally filtered impulse.....	26
Figure 3.6	Fourier phase spectra for acausally filtered impulse.....	26
Figure 3.7	Time domain response of causally filtered impulse.	27
Figure 3.8	Fourier amplitude spectra for causally filtered impulse.	27
Figure 3.9	Fourier phase spectra for causally filtered impulse.	28
Figure 3.10	Time series of acausally filtered pad-stripped record: (a) acceleration; (b) velocity; and (c) displacement time series by double integration of acceleration time series assuming the initial velocity and displacement are zero.	29
Figure 3.11	Acceleration (a) and velocity (b) time series of acausally filtered record with zero padding.....	29
Figure 3.12	Acausally filtered time series with baseline correction: (a) acceleration; (b) velocity; and (c) displacement.	30
Figure 3.13	Effect of baseline correction on PSA for acausally filtered time series.	30
Figure 3.14(a)	Distribution in magnitude-rupture distance space of recordings from 976 events that pass screening criteria (described in Chapter 4).	31
Figure 3.14(b)	Distribution in magnitude-rupture distance space of recordings from 360 interface events.	32
Figure 3.14(c)	Distribution in magnitude-rupture distance space of recordings from 383 intraslab events that pass screening criteria described in Chapter 4.	32
Figure 3.15	Fall-off of number of usable records from 976 screened events as oscillator period increases.....	33
Figure 3.16	Effect of time series interpolation on PSA.	34
Figure 3.17	Comparison of data to median +/- four standard deviations from Abrahamson et al. [2016] model, used for flag assignments.....	37

Figure 4.1	Locations of (a) epicenters and (b) strong-motion recording stations in the NGA-Sub database. Regions are indicated by color of the epicenters and stations, and labeled as ALK (Alaska), CAS (Cascadia), CAM (Central America and Mexico), JPN (Japan), NZL (New Zealand), SAM (South America), and TWN (Taiwan).....	42
Figure 4.2	Epicentral locations of earthquakes with recordings in Alaska.....	43
Figure 4.3	Epicentral locations of earthquakes with recordings in Cascadia.....	44
Figure 4.4	Epicentral locations of earthquakes with recordings in Central America and Mexico.....	45
Figure 4.5	Epicentral locations of earthquakes with recordings in Japan.....	46
Figure 4.6	Epicentral locations of earthquakes in northern Japan.....	47
Figure 4.7	Epicentral locations of earthquakes in southern Japan.....	47
Figure 4.8	Epicentral locations of earthquakes with recordings in New Zealand.....	48
Figure 4.9	Epicentral locations of earthquakes with recordings in South America.....	49
Figure 4.10	Epicentral locations of earthquakes with recordings in Taiwan. The central portion of Taiwan has many shallow crustal earthquakes that are not included in the NGA-Sub database.....	50
Figure 4.11	Event locations in CAM and SAM showing locations and magnitudes of classified and unclassified events.....	51
Figure 4.12	Regional distribution of earthquakes with event-type classifications.....	52
Figure 4.13	(a) Distribution of the events by type of earthquake; and (b) distribution of the recordings by type of earthquake.....	53
Figure 4.14	Magnitude distribution of the earthquakes.....	54
Figure 4.15	(a) Magnitude distribution of the events by type of earthquake; and (b) magnitude distribution of the recordings by type of earthquake.....	54
Figure 4.16	Cumulative number of events over time by type of earthquake using (a) linear and (b) logarithmic scales.....	55
Figure 4.17	Distributions of events with FFMs in the NGA-Sub database.....	55
Figure 4.18	Rake and dip angles for interface and intraslab events in the NGA-Sub database.....	56
Figure 4.19	Schematic representation of the fault-rupture plane [Ancheta et al. 2013]. Convention of fault strike, dip, and rake follows that described in Aki and Richards [1980].....	57
Figure 4.20	M_W - M_L relationships from Bastías and Montalva [2016]: (a) Equation (4.1) for shallow-focus earthquakes ($H \leq 50$ km); and (b) Equation (4.2) for deep-focus earthquakes ($H > 50$ km). We use a slightly modified form of the relation (shifted up 0.033 to reflect M).....	61

Figure 4.21	M_S - M_W and M_S - m_b relations from Leyton et al. [2009]: (a) Equation (4.3); and (b) original M_S - m_b relation reported by the authors. We use a slightly modified form of the M_S - m_b relation (shifted up 0.033 to reflect M).	62
Figure 4.22	Event-type classification scheme based on hypocenter location relative to the top of the surface of the subducting plate. Example event is NGAsubEQID 6000055, which is defined as interface.	67
Figure 4.23	Epicentral locations of the earthquakes in (a) Japan and (b) South America with available FFMs in the NGA-Sub database.	76
Figure 4.24	Finite-fault models for the 2010 M8.81 Maule earthquake using a trimming threshold of 50 cm of slip. Locations of the ground-motion stations included in Table 4.7 are shown using yellow triangles for the RENADIC network and red triangles for the C network. The focal plane solution is shown at the epicenter.	77
Figure 4.25	Multi-segment ruptures of interface events in the NGA-Sub database in (a) Japan and (b) South America regions.	82
Figure 4.26	Multi-segment ruptures of intraslab events in the NGA-Sub database: (a) 1987 M6.53 Off Eastern Chiba; (b) 2001 M6.83 Geiyo; (c) 2008 M6.82 Middle Iwate; and (d) 2012 M7.23 Miyagi-oki earthquakes.	83
Figure 4.27	Examples of multi-segment ruptures: (a) with continuity of the upper section of the segments; and (b) variable dip over the fault width, i.e., listric faults.	84
Figure 4.28	(a) Applied and (b) Complete geometric relations for rupture area for subduction interface earthquakes. JPN = Japan, SAM = South America, CAM = Central America and Mexico, ALK = Alaska, TWN = Taiwan, Sea16 = Skarlatoudis et al. [2016], MUR13 = Murotani et al. [2013].	86
Figure 4.29	(a) Applied and (b) Complete geometric relations for aspect ratio for subduction interface earthquakes. JPN = Japan, SAM = South America, CAM = Central America and Mexico, ALK = Alaska, TWN = Taiwan, Sea16 = Skarlatoudis et al. [2016].	86
Figure 4.30	Geometric relations for (a) rupture area and (b) aspect ratio for subduction intraslab earthquakes. JPN = Japan, CAS = Cascadia, ALK = Alaska, TWN = Taiwan, SAM = South America. Black asterisk represents an event in Japan that was initially considered as intraslab (for the regression analysis marked as “Applied”) and subsequently reclassified as outer-rise.	88
Figure 4.31	Parameterization of earthquake location on fault (view is normal to fault plane from hanging wall).	88
Figure 4.32	Locations of hypocenters on fault plane for interface events: (a) results for data analyzed to support project simulations (dated November 2017); and (b) results derived using the data in its current state (dated December 2019).	89

Figure 4.33	Locations of hypocenters on fault plane for intraslab events: (a) results for data analyzed to support project simulations (dated November 2017); and (b) results derived using the data in its current state (dated December 2019). The black asterisk represents an event in Japan originally considered as intraslab and later reclassified as outer-rise.	90
Figure 4.34	Regional coefficients ν , ϕ , and τ from regions to support development of R_{max}	96
Figure 4.35	R_{max} calculation for event 2000035. Records from different networks are plotted in different colors. The truncation level for each network is plotted as a horizontal line. The median prediction μ for the event is plotted as a black line, the dashed black line shows $\mu - 2.5\phi$. The calculated R_{max} values are shown as vertical lines.	97
Figure 4.36	Flowchart illustrating procedure used to resolve issues with prior version of the flatfile, ultimately resulting in an updated version of the database. Ovals represent start and finish points of the procedure, blue parallelograms represent data, yellow boxes represent data analyses, and white diamonds represent decision points.	99
Figure 4.37	Definition of the $R_{CLOSEST_P2H}$ and $R_{CLOSEST_P2P}$ distance metrics. The four-segment Class 1 rupture plane is defined as $C1_{a-d}$, and the four-segment potential Class 2 rupture plane is defined as $C2_{a-d}$. Each segment is divided into 1km^2 subfaults; the hypocenters are shown as red stars.	101
Figure 4.38	Number of Class 1 and Class 2 earthquakes resulting from a cutoff distance of 40 km, using the data screening described in the text.	101
Figure 4.39	Cascadia subduction-zone geometry displaying different earthquake sources. Interface earthquakes are labeled as “subduction zone earthquakes” and intraslab earthquakes are labeled as “deep earthquakes” (after Wells et al. [2000]).	102
Figure 4.40	Example of the extent of the volcanic flag region in Alaska/Aleutians subduction zone. The green line between zones 1 and 2 follows the average trend of volcanic peaks.	103
Figure 4.41	Extent of the volcanic flag region in Japan subduction zone. The green lines between zones 1, 2, and 3 follow the average trend of volcanic peaks.	104
Figure 5.1	Locations of strong-motion stations with recorded ground motions in NGA-Sub database.	114
Figure 5.2	Breakdown of number of sites in NGA-Sub database by region ($N = 6433$).	115
Figure 5.3	Distribution of all V_{S30} assigned to SMSs in the NGA-Sub database, with a histogram for the subset of sites with assignments from measured <i>in situ</i> V_S profiles.	119

Figure 5.4	Distribution of z_p for measured V_S profiles assigned to SMSs in the NGA-Sub <i>Site</i> table. “Inf” indicates infinity and is associated with the bottom layer given a half-space velocity.....	120
Figure 5.5	Comparison of V_{S30} means for Iwahashi and Pike [2007] terrain classes for Japan and California [Yong 2016]. Classes 2, 10, and 14 are poorly populated in the Japan dataset, and the values written in the figure from California are used for application in Japan.	129
Figure 5.6	Correlations of residuals from proxy-based V_{S30} estimates using data from Japan: (a) modest correlation using JEGM and terrain proxies; and (b) strong correlation using terrain- and slope-based proxies.	133
Figure 5.7	Map of stations in North America that have recorded Alaska events (purple icons) and Cascadia events (red icons), divided by the 55°N parallel (white line).	134
Figure 5.8	Bedrock geological map of terranes comprising the Canadian Cordillera in western Canada and Alaska. A thrust fault (thick black line) marks the “eastern limit of Cordilleran deformation”; the Canadian Shield lies east of this fault. Figure modified from Colpron and Nelson [2011].	134
Figure 5.9	Three-dimensional representation of Cascadia geology as used in velocity model of Stephenson [2007] and Stephenson et al. [2017] (source: Stephenson et al. [2017]).	137
Figure 5.10	Basin depths ($z_{2.5}$) from Stephenson et al. [2017] as a function of V_{S30} for various basin structures in the Cascadia region.	138
Figure 5.11	Basin edge outlines used in the definition of regional basin sediment-depth effects for the Pacific Northwest region of the U.S. Basin outlines modified from McPhee et al. [2014], Ramachandran et al. [2006], and Lowe et al. [2003]. Dashed line indicates Seattle basin outline subsequently adopted by the USGS and City of Seattle [Wirth et al. 2018].	139
Figure 5.12	Map showing Taipei basin, as identified from topography (source: Lin et al. [2014]).	140
Figure 5.13	Map showing Western Plain in Taiwan (source: Kuo et al. [2016]).	141
Figure 5.14	Spatial distributions of the $z_{1.0}$ and $z_{2.5}$ basin depth parameters in Japan based on NIED models (source: Ancheta et al. [2013]).	142

1 Introduction

Yousef Bozorgnia, Jonathan P. Stewart, Norman A. Abrahamson, Sean K. Ahdi, Timothy D. Ancheta, Ralph J. Archuleta, Gail M. Atkinson, David M. Boore, Rubén Boroscchek, Kenneth W. Campbell, Brian S.J. Chiou, Victor Contreras, Robert Darragh, Nick Gregor, Zeynep Gulerce, I.M. Idriss, Chen Ji, Ronnie Kamai, Tadahiro Kishida, Nicolas Kuehn, Dong Youp Kwak, Annie Kwok, Po-Shen Lin, Harold Magistrale, Silvia Mazzoni, Sifat Muin, Saburoh Midorikawa, Grace A. Parker, Hongjun Si, Walter J. Silva, Melanie Walling, Katie E. Wooddell, and Robert R. Youngs

1.1 NGA-SUBDUCTION PROJECT OVERVIEW

In 2003, the Pacific Earthquake Engineering Research Center (PEER) initiated a large research program to develop next generation ground-motion prediction equations (GMPEs)—formerly referred to as “attenuation relationships”—for shallow crustal earthquakes in active tectonic regions [Power et al. 2008]. This project, now referred to as NGA-West1, made a strong impact in the engineering and seismological community in three main respects:

1. It changed the research culture related to the database and GMPE development, bringing leading experts together to collaborate on database development who routinely shared thoughts and best practices during model development. This improved model thoroughness and quality.
2. The GMPEs were of high quality for the time, combining scaling from first principals (and informed by simulations) with data analyses to provide models that operated over the ranges required for many practical applications.
3. The database was shared by all GMPE developer teams and then publically disseminated via a PEER website, which ultimately supported many subsequent research projects and practical applications related to time-series selection.

The impact of the NGA-West1 project created demand for subsequent projects that were structured similarly. NGA-West2 [Bozorgnia et al. 2014] also applied to shallow crustal earthquakes in active tectonic regions and significantly expanded the database and certain GMPE attributes. NGA-East [Goulet et al. 2018] developed data resources and ground-motion models (GMMs) for stable continental regions, particularly central and eastern North America. NGA-East made more extensive use of simulations than other regions due to data paucity for the magnitudes and distances of typical engineering interest. NGA-Subduction applied the NGA framework to subduction zone regions.

The objectives of the NGA-Subduction project (NGA-Sub) were as follows: (1) develop a state-of-the-art database; (2) develop a series of GMPEs that operate over the parameter range

(magnitudes, event types, distances, and site conditions) required for typical hazard applications; and (3) provide guidance on application of the models, including epistemic uncertainties.

Regionalization of certain ground-motion attributes is an important feature of NGA-Sub. The last set of truly global GMPEs is that from NGA-West1. Regionalization in anelastic attenuation and site effects was introduced in NGA-West2 and was integral to NGA-East as well (mostly in relation to path effects). Figure 1.1 shows the major regions considered in NGA-Sub: Alaska (ALK), Central America and Mexico (CAM), Cascadia (CAS), Japan (JPN), New Zealand (NZL), South America (SAM), and Taiwan (TWN). Some NGA-Sub GMPEs are region-specific (e.g., Si et al. [2020] and Youngs et al. [2020] for Japan), while the remainder are global but include regional adjustments for various source, path, and site effects.

Many other regions, known to have subduction zone earthquakes, are not represented in this database (e.g., Indonesia, Greece, and Calabria/Italy). These omissions were not accidental as the significance of subduction earthquake hazards in those regions is well known. Data from these additional regions were not incorporated into the database because: (1) it was anticipated that the project team would not have ready access to sufficient data to benefit the project; or (2) the project team anticipated that the necessary data did not exist or was inaccessible.

As in other NGA projects, quality assurance (QA) of the database was a long-term effort that involved many people (essentially, all the authors of the chapters in this report). Two particularly notable aspects of our QA procedures relate to ground-motion data checking (described in Section 3.4) and an iterative data-checking process related to the assignment of source and path metadata (described in Section 4.6).

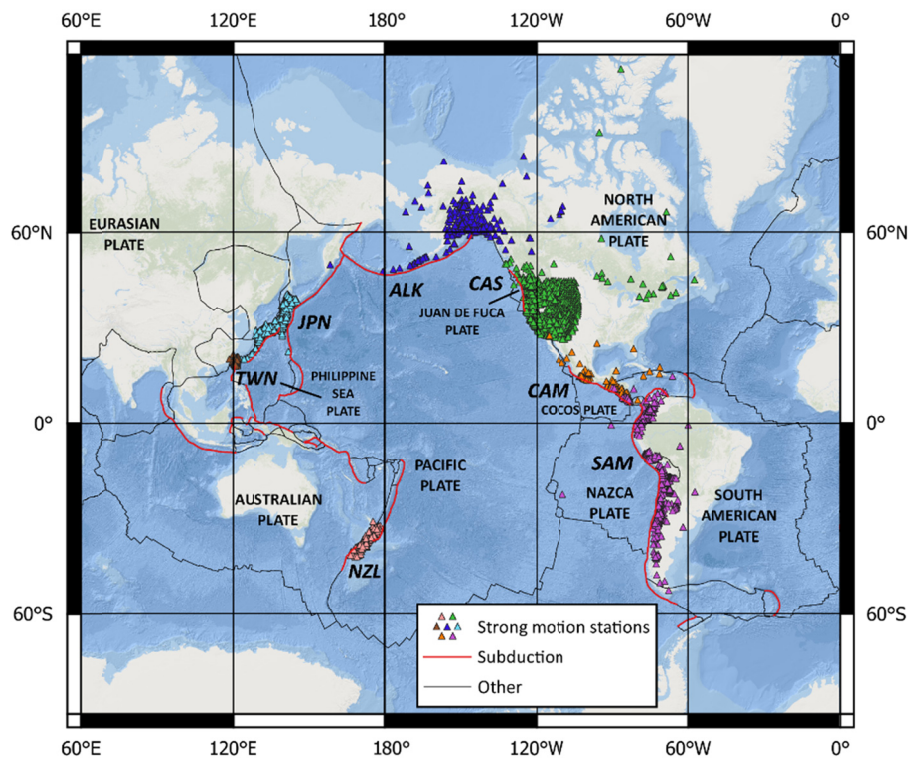


Figure 1.1 Locations of strong-motion recording stations with recordings in the NGA-Sub database.

Participants in NGA-Sub project fall into three main domains. Yousef Bozorgnia was the Principal Investigator, providing leadership pertaining to project funding and coordination. Four ground-motion modeling teams were active in the project, sharing experiences in applying the data that benefitted the database checking and development. Finally, the database development involved the full NGA-Sub team but certain individuals took lead roles in the ground motion, source/path, and site components of the database. Those individuals are recognized by leading positions in chapter authorship (Chapters 3–5). Finally, Silvia Mazzoni and several collaborators took a lead role in developing the database as a formal relational database as described in Chapter 2.

1.2 PRIOR SUBDUCTION DATABASES

The subduction ground-motion database presented in this report is the most comprehensive database developed for subduction zones worldwide. It is not the first. The project team wishes to acknowledge the data development efforts that preceded NGA-Sub.

Table 1.1 summarizes some key attributes of prior subduction databases. Most of the data in the Crouse et al. [1988] and Youngs et al. [1997] databases are from sparsely recorded events (often one recording). This gradually improved over time, with the Atkinson and Boore [2003] and Abrahamson et al. [2016] models having substantially more data, with some events being well recorded. Additional regional datasets have been prepared that are not shown in Table 1.1, e.g., Lin and Lee [2008] for Taiwan; Zhao et al. [2006] for Japan.

None of the prior global subduction databases listed in Table 1.1 includes the large-magnitude events from Tohoku Japan (2011) and Maule Chile (2010). These and many other events have dramatically expanded database size; see Chapters 3 and 4. Moreover, comparisons of large earthquakes to available models have not shown favorable results (e.g., Boroschek et al. [2012] and Stewart et al. [2013]). These issues illustrate the needs that the NGA-Sub project was formed to address.

Table 1.1 Summary of pre-NGA-Sub global subduction databases.

Reference	M range	R_{rup} or R_{hyp} range (km)	# events	# recs	Event types distinguished?
Crouse et al. [1988] ¹	5.1-8.2	28–470	84	129	No
Youngs et al. [1997]	5.0-8.2	8.5–550	160	474	Yes: interface, intraslab
Atkinson and Boore [2003]	5.5-8.3	10–400	77	1148	Yes: interface, intraslab
Abrahamson et al. [2016]	5.0-8.4	13–300	292	9946	Yes: interface, intraslab

¹ The database from Crouse et al. [1988] was subsequently updated for the development of a GMPE by Crouse [1991]; however, event details for the latter were not presented and hence are not shown in Table 1.1. The expanded Crouse [1991] database was used subsequently by Youngs et al. [1997].

1.3 ORGANIZATION OF THIS REPORT

Chapter 2 of this report describes the relational database whereby data are entered into organized tables and related to each other through a series of primary and foreign keys. The use of a formal relational database during model development is new to NGA-Sub.

Chapter 3 describes the processes used to identify, obtain, and process ground motions, as well as intensity measure (IM) computations. Procedures used for checking data for sampling bias at long distance are also explained.

Chapter 4 describes procedures used to assign source and path parameters. Source parameters are of two general types: those related to the focus (including moment tensors) and those related to finite-fault representations of the source (from literature or simulations). Procedures used for distance calculations are also provided, which are non-trivial in the case of simulated finite faults. Other issues addressed in this chapter are QA procedures, assignment of event types (interface, intraslab, etc.), assignment of event classes (mainshock, aftershocks, etc.), and assignment of event locations flags relative to volcanic arcs.

Chapter 5 describes the site tables used to assign time-averaged shear-wave velocity and basin depths to ground-motion recording sites. Major efforts were undertaken during the project to develop regional shear-wave velocity profile databases and to use those data to develop predictive models of site parameters when site-specific measurements are unavailable. The work described in the chapter produces mean estimates of site parameters and epistemic uncertainties.

Suggested Citation:

Bozorgnia Y., Stewart J.P., Abrahamson N.A., Ahdi S.K., Ancheta T.D., Archuleta R.J., Atkinson G.M., Boore D.M., Boroschek R., Campbell K.W., Chiou B.S.-J., Contreras V., Darragh R.B., Gregor N., Gulerce Z., Idriss I.M., Ji C., Kamai R., Kishida T., Kuehn N., Kwak D.Y., Kwok A.O., Lin P.S., Magistrale H., Mazzoni S., Muin S., Midorikawa S., Parker G.A., Si H., Silva W.J., Walling M., Wooddell K.E., Youngs R.R. (2020). Chapter 1: Introduction, in *Data Resources for NGA-Subduction Project, PEER Report No. 2020/02*, J.P. Stewart (editor), Pacific Earthquake Engineering Research Center, University of California, Berkeley, California (headquarters).

REFERENCES

- Abrahamson N.A., Gregor N., Addo K. (2016). BC Hydro Ground motion prediction equations for subduction earthquakes, *Earthq. Spectra*, 32: 23–44.
- Atkinson G.M., Boore D.M. (2003). Empirical ground-motion relationships for subduction-zone earthquakes and their application to Cascadia and other regions, *Bull. Seismol. Soc. Am.*, 93: 1703–1729.
- Boroschek R., Contreras V., Kwak D.Y., Stewart J.P. (2012). Strong ground motion attributes of the 2010 Mw 8.8 Maule Chile, Earthquake, *Earthq Spectra*, 28: S19–38.
- Bozorgnia, Y., Abrahamson N.A., Al Atik L., Ancheta T.D., Atkinson G.M., Baker J.W., Baltay A., Boore D.M., Campbell K.W., Chiou B.S.-J., Darragh R., Day S., Donahue J., Graves R.W., Gregor N., Hanks T., Idriss I.M., Kamai R., Kishida T., Kottke A., Mahin S.A., Rezaeian S., Rowshandel B., Seyhan E., Shahi S., Shantz T., Silva W.J., Spudich P., Stewart J.P., Watson-Lamprey J., Wooddell K., Youngs R.R. (2014). NGA-West 2 research project, *Earthq. Spectra*, 30: 973987.
- Crouse C.B. (1991). Ground-motion attenuation equation for earthquake on Cascadia subduction-zone earthquake, *Earthq. Spectra*, 7: 210–236.
- Crouse C.B., Yogesh K.V., Schell B.A. (1988). Ground motions from subduction zone earthquakes, *Bull. Seismol. Soc. Am.*, 78: 1–25.
- Goulet C.A., Borzorgnia Y., Abrahamson N.A., Kuehn N., Al Atik L., Youngs R.R., Graves R.W., Atkinson G.M. (2018). Central and Eastern North America Ground Motion Characterization: NGA-East Final Report, *PEER Report No. 2018/08*, Pacific Earthquake Engineering Research Center, University of California, Berkeley, CA.
- Lin P.-S., Lee C.-T. (2008). Ground-motion attenuation relationships for subduction-zone earthquakes in Northeastern Taiwan, *Bull. Seismol. Soc. Am.*, 98: 220–240.
- Power M., Chiou B.S.-J., Abrahamson N.A., Bozorgnia Y., Shantz T., Roblee C. (2008). An overview of the NGA Project, *Earthq. Spectra*, 24: 3–21.
- Si et al. (2020). Report in preparation.
- Stewart J.P., Midorikawa S., Graves R.W., Khodaverdi K., Miura H., Bozorgnia Y., Campbell K.W. (2013). Implications of Mw 9.0 Tohoku-oki Japan earthquake for ground motion scaling with source, path, and site parameters, *Earthq. Spectra*, 29: S1–21.
- Youngs R.R., Chiou B.S.-J., Silva W.J., Humphrey J. (1997). Strong ground motion attenuation relationships for subduction zone earthquakes, *Seismol. Res. Lett.*, 68: 58–73.
- Youngs et al. (2020). Report in preparation.
- Zhao J.X., Zhang J., Asano A., Ohno Y., Oouchi T., Takahashi T., Ogawa H., Irikura K., Thio H. K., Somerville P.G., Fukushima Y., Fukushima Y. (2006). Attenuation relations of strong ground motion in Japan using site classification based on predominant period, *Bull. Seismol. Soc. Am.*, 96: 898–913.

2 Relational Database

Silvia Mazzoni, Tadahiro Kishida, Sean K. Ahdi, Víctor Contreras, Robert B. Darragh, Brian S.-J. Chiou, Nico Kuehn, Yousef Bozorgnia, and Jonathan P. Stewart

2.1 INTRODUCTION

The database developed for the NGA-Subduction (NGA-Sub) project is a relational database, meaning that it has a well-defined data structure and can be queried using structured query language (SQL). Previous NGA projects have applied the term “database” to collections of spreadsheet files that were linked in an *ad hoc* manner using Excel macros [Chiou et al. 2008; Ancheta et al. 2014]. In contrast, a relational database is organized into a schema that describes the *tables*, *fields*, and relationships among tables. Tables are collections of information organized into fields (or columns). The contents of tables (i.e., each row) are identified using *keys*. Every entry in the database (i.e., a given row within a field) is assigned a *primary key* that uniquely identifies it. In some cases, a field from one table might appear in another table to relate the two tables. In such cases, the primary key from the host table appears as a *foreign key* in the other table to map the relationship. In other cases, the same primary key is used in multiple tables. This is applied for situations in which a series of tables could have been organized into a single table, but doing so would have made the table size inconveniently large and somewhat inefficient with respect to the information sources used to populate the table. For the present application, it was decided to use multiple tables that share primary keys in some cases.

We developed the NGA-Sub database schema as a working group, and benefitted from regular communication and feedback from the broader NGA-Sub project participants through regular in-person and web meetings. Databases are living products, and the version described here was “locked-in” April 22 2019 (in technical content) so that ground-motion model (GMM) development could proceed with a fixed dataset; however, population of the database is likely to continue into the future, including the incorporation of recent events from Alaska and Mexico; see Chapter 4. Additional ground-motion parameters and source, path, or site metadata may also be added in the future.

Outside of the relational database working group (the authors of this chapter), most NGA-Sub project participants interact with the data using a *flatfile*, which is a single file extracted from the database containing all fields of interest. The flatfile can be readily generated from the relational database using an SQL command; MS Access was used in this project, using

Visual Basic to write SQL commands. The April 22 2019 flatfile is included in this report as an electronic supplement.

The fields within the NGA-Sub database are composed of three types: instrument recordings, various metadata, and computed data. Digitized and processed instrument recordings are stored in individual ASCII files of acceleration, velocity, and displacement histories; the files have headers structured to convey information on the causative event, the station that produced the recording, and the time step. Record processing is described in Chapter 3.

Metadata defines the attributes of a record, such as earthquake location and magnitude, location and site conditions at the recording site, characteristics of the recording instrument, and attributes of the path between the earthquake source and the recording station. There are two types of metadata: (1) independent metadata, which are either measured or taken directly from literature or catalogs, and (2) dependent metadata, which are computed from the independent metadata fields. Source-to-site distance metrics and fault geometry are examples of dependent metadata.

Damped elastic response spectra, Fourier amplitude spectra (FAS), and duration metrics are examples of the third type of data within the NGA-Sub database (i.e., computed data) which are often referred to as Intensity Measures (IMs). These IMs are computed from the processed instrument recordings and are stored in individual tables within the database.

As shown in Figure 2.1, the NGA-Sub database broadly contains information on source, site, path, ground motions (which contain instrument/time-series metadata), and IMs. This information is contained in 23 tables. The contents of fields in these tables are mapped via database keys. There are three main keys in the database: (1) the Record Sequence Number (NGAsubRSN) applies to a given ground motion; (2) NGAsubEQID applies to an earthquake event; and (3) NGAsubSSN applies to a recording site.

Ground-motion time series are contained in files used in database development but are not part of the database tables; the file path as well as additional characteristics of these files are stored in the database. Following a discussion of the origins of the database, the remaining sections of this chapter describe the tables and keys employed for each of these groups. We do not describe all fields; instead we emphasize fields that carry unique information that was used in model development.

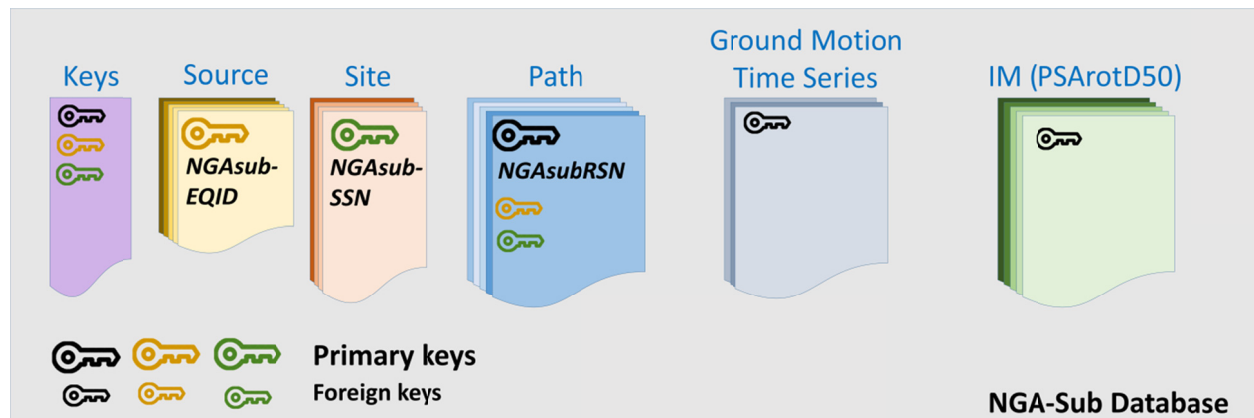


Figure 2.1 Components of NGA-Sub relational database.

2.2 DATABASE ORIGINS

The NGA-Sub database was not originally assembled as a relational database. Early stages of the project gathered data for various regions, which was organized into regional flatfiles. The regional flatfiles contained source, site, and ground-motion IMs for each of the following regions: Alaska (ALK), Cascadia (CAS), Central America and Mexico (CAM), Japan (JPN), New Zealand (NZL), South America (SAM), and Taiwan (TWN). The main emphasis of the work at that time was data collection from diverse sources, and relatively little effort was put forward to organizing the data in an optimal or consistent manner.

Once the decision was made to create a relational database, information from the regional flatfiles was transferred to database tables (Tables 2.1–2.6). In some cases, information in these tables was supplemented or modified to response to QA procedures; see Sections 3.4 and 4.6. Moreover, new data since about 2017 was added in the relational database tables.

2.3 KEY METADATA

The Key Metadata consists of a single table (*RecordMap* table) that contains primary and foreign keys of the NGA-Sub database as well as unique identifiers collected from the original regional flatfiles. The primary purpose of this table is to map the source (NGASubEQID) and site (NGASubSSN) keys to the primary record key (NGASubRSN). Additional data in this table provides a map to the original region-specific flatfiles. This map is made through the DatabaseRegion and OriginalFlatfile_RSN. The OriginalFlatfile_Station_Sequence_Number_SSNs are also stored in this table. These identifiers were included with rows for records in regional flatfiles, but in some cases are not unique (e.g., the same site may have multiple OriginalFlatfile_Station_Sequence_Number_SSNs in different regional flatfiles). Such non-unique flag assignments were corrected in the assignment of the final earthquake and site identification numbers.

2.4 SOURCE METADATA

The seismic source primary key is the Earthquake Identification Number (NGASubEQID), a unique value assigned to each event. The assignment of NGASubEQIDs is organized by region; see Table 2.1. Unique numbers were assigned as sequential integers of the pattern $N \times 10^6$ within each region, where N is an integer from one to seven accounting for each of the seven subduction zone regions; see Figure 1.1. Following the region identifier, additional digits were assigned sequentially. For example, NGASubEQID=3000197 corresponds to an event in Central America & Mexico. NGASubEQID is the primary key in the *EventHypo* table, with each of the other event-related tables listed in Table 2.2 representing different physical quantities. As described in Section 2.1, while the source data could have been stored in a single table, because different quantities are obtained from different sources, they are stored in different tables.

Table 2.2 lists relational database tables related to source parameters. The table name is provided along with an indication of whether the information contained in the tables consists of dependent or independent metadata. Because source attributes are contained in a series of tables

that interact according to a schema, in effect this collection of information comprises a source relational database.

The contents of the *EventHypo* and *EventType* table are largely drawn from global and local earthquake catalogs. As described in Section 4.2, critical issues in assembling these tables were selecting the preferred catalog when more than one is available, procedures for selecting a preferred rupture plane, and procedures for selecting event type (i.e., interface, intraslab, shallow crustal, outer rise, etc.) based on source location and focal mechanism.

Table 2.1 Region identifier numbers used in assignment of earthquake and site keys.

Region	Region Identifier
Alaska	1
Cascadia	2
Central America & Mexico	3
Japan	4
New Zealand	5
South America	6
Taiwan	7

Table 2.2 Tables presenting source metadata in NGA-Sub relational database.

Table Name	Contents	Information types
EventHypo	NGASubEQID*, region, geodetic coordinates (latitude, longitude), hypocentral depth, date, time, seismic moment (M_0), moment magnitude (mag), alternate magnitude scales (m_b , M_L , M_S), preferred moment tensor parameters (rake – prefrake, strike – prefstrike, dip – pref dip), nodal plane angles (strike – np1-s, np2-s; dip – np1-d, np2-d; rake – np1rake, np2rake), focal mechanism (focalmech)	Mostly independent Dependent = mag, focalmech
EventType	NGASubEQID*, flag (Table 4.5)	Dependent
FFmodel	NGASubEQID*, # rectangles (Norect), coordinates of upper left corner of fault as viewed from hanging wall, along-strike length (L), down-dip width (W), strike, dip, rake	Independent
FFmodelmultiseg	Applies for Norect > 1 only. NGASubEQID*, for $i=1:Norect$, each of the parameters listed in FFmodel	Independent
FFsim	NGASubEQID*, coordinates of upper left corner of fault as viewed from hanging wall, along-strike length (L), down-dip width (W), strike, dip	Dependent
Magbrk	NGASubEQID*, break magnitude	Independent
EventClass	NGASubEQID*, event class indicator (CL1 or CL2)	Dependent
EventVolArc	NGASubEQID*, flag (Table 4.11)	Dependent

* Assigned as primary key

The contents of the *FFmodel* and *FFmodelmultiseg* tables are drawn from published studies presenting finite-fault models inverted from various ground-motion and geodetic data. As described in Section 4.3, critical issues in assembling those tables included selecting a preferred model when more than one is available and trimming published models to identify portions of the fault that are mostly likely to produce strong ground motion. The parameters recorded in the tables are needed to establish the positions of the rectangles for distance calculations.

The contents of the *FFsim* table mirror those in *FFmodel*, except that the parameters in the *FFsim* table are the result of a simulation procedure (hence, they are dependent metadata). As described in Section 4.4, critical aspects of this process are statistical relations for fault dimensions given magnitude and event type, relations for hypocenter location on a rectangular fault, and details of the simulation procedure.

The contents of the *Magbrk*, *EventClass*, and *EventVolArc* tables provide region-specific information on magnitudes where breaks in ground-motion scaling slopes might be expected, assignment of events as mainshocks/foreshocks or aftershocks, and assignment of event positions relative to volcanic arcs, respectively. *EventClass* and *EventVolArc* contain fields with event attributes inferred from spatial analyses; see Sections 4.7–4.8. *Magbrk* fields are drawn from literature and are region specific; details can be found in Campbell [2020] for interface events and Ji and Archuleta [2018] for intraslab events.

2.5 SITE AND STATION METADATA

The site and station primary key is the Station Sequence Number (NGAsubSSN), a unique value of which is assigned to each site and each instrument at a given site that has produced a recording. The NGAsubSSN values were assigned in a manner similar to the NGAsubEQID, where the first digit represents the geographic region of the location of the station (Table 2.1), and the remainder of the number was assigned sequentially and randomly. NGAsubSSN is the primary key in the *Site* table and other tables defining site-related parameters and is a foreign key elsewhere.

Separate NGAsubSSNs were assigned for cases when the station network changed but the instrument ostensibly remained the same, or the instrument itself was changed at the same location. In the case of vertical arrays, with multiple sensors at the same latitude and longitude but different depths, multiple “sites” (with distinct NGAsubSSNs) are provided in the *Site* table, each having a different sensor depth. This is why the instrument depth is included in the *Site* Database instead of the record database.

Table 2.3 lists relational database tables related to site parameters. Most of the information is contained in the *Site* table. Additional information related to site position relative to volcanic arcs is contained in the *SiteVolArc* table. Additional information on instrument type is contained in the *Station* table. In Table 2.3, the table name is provided along with an indication of whether the information contained in the tables consists of dependent or independent metadata.

The contents of the *Site* table are drawn from diverse information sources including region-specific instrument catalogs, V_S -profile databases (many assembled as part of the NGA-Sub project), global digital elevation models, local or regional geologic maps, and models for the

structure of sedimentary basins. The fields in the *Site* table contain both independent variables taken directly from source materials and derived quantities. Chapter 5 describes procedures used during data collection and interpretation.

Table 2.3 Tables presenting site and station metadata in NGA-Sub relational database.

Table Name	Contents	Information types
Site	<ul style="list-style-type: none"> • NGASubSSN* • Site name and station ID (from data-providing networks) • Station location, including geodetic coordinates, elevation, depth, housing • Recommended V_{S30} in m/sec. Codes indicating how V_{S30} was assigned, associated NEHRP site category • Information on V_S profiles, as available, including profile depth (z_p) and time-average V_S to depth z_p (V_{Sz}) • Proxies used for V_{S30} prediction, as available, including surface geology, ground slope, geomorphic terrain class • Basin depth information, including depth to a particular V_S horizon (i.e., z_x = the depth to the x km/sec iso-surface; values of $x=1.0$ and 2.5 km/sec are used), source of depth information, basin name 	Mostly independent Dependent = V_{Sz} , V_{S30} (from profiles), V_{S30} (from proxy-based models), z_x ,
SiteVolArc	NGASubSSN*, region, flag	Dependent
Station	NGASubSSN*, instrument	Independent

* Assigned as primary key

2.6 PATH METADATA

A particular source-to-site path is associated with a unique record. The primary key for recordings (termed Record Sequence Numbers, NGASubRSNs) are assigned in the relational database tables related to path and also in tables related to ground motions and IMs. NGASubRSNs are not used as foreign keys. To minimize possible errors when using this table, the NGASubEQID and NGASubSSN are contained in this table as foreign keys even though they have been defined in the Keys table.

Table 2.4 lists the relational database tables related to path parameters. The *Path* table contains distance parameters and other fields derived from source, site, and ground-motion data (i.e., dependent metadata). The *PathVolArc* table contains dependent variables on relative percentages of path length in four zones on different sides of volcanic arcs (e.g., the forearc and backarc).

As described in Section 4.5.1, distance parameters were computed using a code (P4CF) that takes as input the finite geometry of the source (the position of one or more rectangles) and site locations. The code returns distance and directivity parameters. As described in Section 4.5.2, parameter R_{max} represents the distance beyond which data from a given event and recorded by a particular network may exhibit bias due to either lack of instrument triggering or motions near instrument noise levels (for weaker-than-average motions).

Table 2.4 Tables presenting path metadata in NGA-Sub relational database.

Table name	Contents	Information types
Path	NGAsubRSN*, various distance parameters (R_{rup} , R_{JB} , R_x , R_y , R_{y0} , R_{epi} , R_{hyp} , R_{rms}), location on fault surface from which the closest distance is measured (geodetic coordinates and depth), directivity parameters, maximum recommended distance R_{max}	Dependent
PathVolArc	NGAsubRSN*, Zone0%Dist, Zone1%Dist, Zone2%Dist, Zone3%Dist	Dependent

* Assigned as primary key

2.7 GROUND-MOTION TIME SERIES AND INTENSITY MEASURES

The primary key for a given ground-motion recording is the Record Sequence Number (NGAsubRSN), which is assigned in both the *Path* table (Table 2.4) and in the *RecordMeta* table and other tables containing ground-motion information.

The NGAsubRSN is connected to path parameters (Section 2.6) and various dependent fields derived from time series. Time series gathered and processed as part of the NGA-Sub project are described in Sections 3.1 and 3.2. Due to the large cumulative size of the ground-motion files, they are not incorporated into the NGA-Sub database, but they are called by codes that operate with the database.

Table 2.5 lists relational database tables related to ground-motion time series files and how the database interacts with them. Table 2.6 lists relational database tables related to IMs. Table names are provided along with an indication of whether the information contained in the tables consists of dependent or independent metadata.

Table 2.5 Tables related to ground-motion time series files in the NGA-Sub relational database.

Table name	Contents	Information types
RecordMeta	NGAsubRSN*, as-recorded horizontal azimuths, processing details (low-cut and high-cut corner frequencies)	Independent
RecordtoAT2	NGAsubRSN*, computer path to access time series data (.AT2 files)	Independent
HeaderData	NGAsubRSN*, time step, other information given in headers of .AT2 files (station name, event name, and date/time)	Independent

*Assigned as primary key

Table 2.6 Tables presenting ground-motion intensity measures and related metadata.

Table name	Contents	Information types
OscPeriods	List of oscillator periods for pseudo-spectral acceleration calculations (common to all motions, hence no NGAsubRSN)	Independent
OscDamp	List of oscillator damping values for pseudo-spectral acceleration calculations (common to all motions, hence no NGAsubRSN)	Independent
PSA _{ij}	NGAsubRSN*, period (one field per period), pseudo-spectral acceleration (provided in rows for each period) <i>i</i> = component (H1, H2, V, RotD0, RotD50, RotD100) <i>j</i> = damping ratio (decimal) A single file provides information for all records.	Dependent
DurationMetrics _i	NGAsubRSN*, Arias Intensity for components <i>i</i> =H1, H2, and V; times for <i>i</i> =H1, H2, and V (percentiles of Arias Intensity = 0.05 to 0.95, step of 0.05)	Dependent
FAS _i	NGAsubRSN*, frequencies (one field per frequency), Fourier amplitudes for components <i>i</i> =H1, H2, and smoothed EAS (provided in rows for each frequency)	Dependent
CAV _i	NGAsubRSN*, CAV for components <i>i</i> =H1, H2, and V, CAV ₅ for components <i>i</i> =H1, H2, and V	Dependent
RecordFlag	NGAsubRSN*, data quality assurance flag (Table 3.5)	Dependent

The *RecordMeta* and *HeaderData* tables contain independent metadata that are descriptive of individual ground-motion components. The information is from ground-motion catalogs and header files. As noted previously, ground-motion time series (.AT2 files) are not part of the database, but the database needs to interact with these files that are stored on a server. The *RecordMeta* table contains information obtained from regional flatfiles derived during record processing (e.g., unfiltered PGA, corner frequencies etc.) that connect with a particular version of the ground-motion file; in some cases, records were later re-processed, and the contents of this table may be out of date. The *RecordtoAt2* table provides links that allows individual ground-motion components to be found on the server and opened to compute ground-motion parameters.

The contents of the *OscPeriods* and *OscDamp* tables provide oscillator properties (periods and damping ratios) for which pseudo-spectral accelerations are computed. The results of the calculations appear in *PSA_{ij}* tables, with separate tables provided for each ground-motion component and damping ratio; see Table 2.5. Procedures used to calculate these parameters are given in Section 3.3.1.

Additional ground-motion parameters are provided in *DurationMetrics_i*, *FAS_i*, and *CAV_i* tables. Separate tables are provided for different components of *i*. Procedures used to calculate these parameters are given in Section 3.3.2.

The *RecordFlag* table assigns flags to individual records based on their being improbable for the event. Details on the flag assignments are given in Section 3.4, with the flags defined in Table 3.5.

Suggested Citation:

Mazzoni S., Kishida T., Ahdi S.K., Contreras V., Darragh R.B., Chiou B.S.-J., Kuehn N., Bozorgnia Y., Stewart J.P. (2020). Chapter 2: Relational Database, in *Data Resources for NGA-Subduction Project*, PEER Report No. 2020/02, J.P. Stewart (editor), Pacific Earthquake Engineering Research Center, University of California, Berkeley, California (headquarters).

REFERENCES

- Ancheta T.D., Darragh R.B., JP Stewart J.P., Seyhan E., Silva W.J., Chiou B.S.-J., Wooddell K.E., Graves R.W., Kottke A.R., Boore D.M., Kishida T., Donahue J.L. (2014). NGA-West2 database, *Earthq. Spectra*, 30: 989–1005.
- Campbell K.W. (2020). Proposed methodology for estimating the magnitude at which subduction megathrust ground motions and source dimensions exhibit a break in magnitude scaling: Example for 79 global subduction zones, *Earthq. Spectra*, 36, <https://doi.org/10.1177/8755293019899957>.
- Chiou B.S.-J., Darragh R.B., Gregor N., Silva W.J. (2008). NGA project strong-motion database, *Earthq. Spectra*, 24: 23–44.
- Ji C. Archuleta R.J. (2018). Scaling of PGA and PGV deduced from numerical simulations of intraslab earthquakes, Department of Earth Science, University of California, Santa Barbara, in press.

3 Ground Motions and Intensity Measures

Tadahiro Kishida, Robert B. Darragh, Brian S.J. Chiou, Yousef Bozorgnia, Silvia Mazzoni, Víctor Contreras, Rubén Boroschek, Fabián Rojas, and Jonathan P. Stewart

3.1 DATA SOURCES

An extensive effort was undertaken to coordinate the NGA-Subduction Project (NGA-Sub) with local agencies in areas affected by subduction earthquakes, with an emphasis on Alaska, Cascadia, Central America and Mexico, Japan, New Zealand, South America, and Taiwan. This included communications to identify relevant sources of ground-motion data and either (i) identifying public repositories of data that could be accessed by the project; or (ii) forming collaborative agreements to enable data sharing between the NGA-Sub project and individual network operators. We obtained digital but unprocessed versions of records from either accelerometers (accelerograms) or seismometers (velocity time series). This chapter describes the data processing and computation of the IMs.

Table 3.1 shows the agencies from each of the above regions from which we obtained uncorrected records. The Chilean Seismic Network (CSN) is operated by the Seismology Department at the University of Chile. As a result of the recent rapid growth of the Chilean seismic networks, uncorrected strong-motion recordings are distributed for earthquakes with magnitudes ≥ 4.0 for individual networks known as the C, CX, C1, and RNA networks. Both CSN and the individual networks will be referred to in various parts of this report.

In total, 70,107 recordings were obtained and processed for NGA-Sub from all sources. Section 3.2 describes steps in the data processing. Section 3.3 describes the computation of ground-motion parameters and the ground motion intensity measure (IM) tables incorporated into the relational database.

Table 3.1 Ground-motion catalogs contributing data to NGA-Sub database.

Region	Catalog	Number of processed motions
Alaska	CESMD	36
	IRIS	2,812
	GSC	178
Cascadia	CESMD	29
	COSMOS	100
	IRIS	1,432
	NSMP	112
	NCEDC	219
	GSC	217
Central America and Mexico	NORSAR	292
	COSMOS	349
	NOAA	727
	IRIS	908
	MARN	227
	Universidad de Costa Rica (Networks LIS, XY, OV)	145
Japan	NIED, K-NET	20,869
	NIED, KIK-NET	18,836
	JMA	444
	PARI	303
	NOAA	44
	HI-NET	72
	Electricity Companies (TEPCO, EPCO)	149
South America	CESMD	213
	NOAA	40
	IRIS	1,689
	GFZ	1,193
	RENADIC (U Chile, CEE Dept)	1,274
	CSN (U Chile, seismology), including C, CX, C1 and RNA networks	1,076
	CISMID	213
	RNAC (Columbia)	409
RENAC (Ecuador)	89	
Taiwan	CWB, TW	11,176
	IES	1,196
	K-NET	62
	JMA	69

3.2 DATA PROCESSING

Data processing starts with a digital time series (accelerograms or seismograms) with a sample rate (i.e., time step). Modern digital instruments produce a signal with a time stamp (a known reference time at the start of the record). The major steps in data processing are: (1) screening of time series to select the ground motions to process; (2) application of window functions that reduce the signal to zero outside of a time interval; (3) computation of FAS; (4) filtering of the record to remove noise-dominated features over selected frequency intervals; and (5) baseline correction. The procedures applied here are similar to those used in previous NGA projects, including NGA-West1 [Chiou et al. 2008], NGA-West2 [Ancheta et al. 2013], and NGA-East [Goulet et al. 2014]. Corrected time series are saved as .AT2 files for use in the computation of ground-motion parameters.

This procedure is applicable to accelerograms only. For seismograms, before Step (2), instrument corrections are applied to the time series and the signals are time-differentiated once to acceleration. The differentiated time series are then processed in an identical manner to accelerograms.

3.2.1 Screening of Time Series

To screen ground-motion data, we plot time series as-is (without filters or other modification) to visually evaluate record quality. Figure 3.1 shows an example of a recording that was rejected during this process. This signal is close to the resolution of the recording system, which resulted in the noisy recordings. Data processing is difficult for recordings of this type, and it is possible to identify a signal for only a limited frequency band.

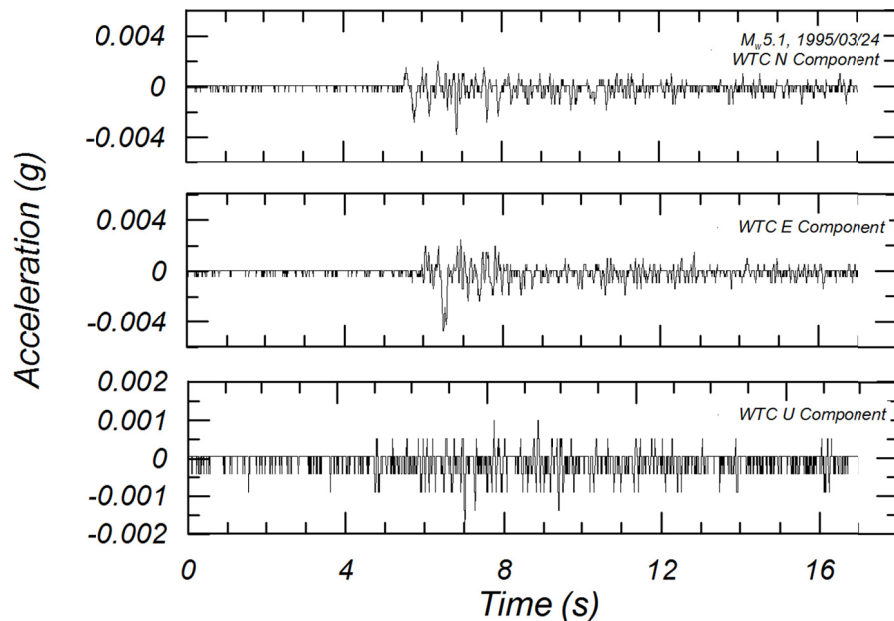


Figure 3.1 An example of a rejected time series.

3.2.2 Time Windows for Data Processing

Using a process introduced with the NGA-East project [Goulet et al. 2014], six time windows were selected for each time series; see Figure 3.2. The first time window includes the entire record (blue box in the figure). This window includes the pre-event noise (recorded before the P -wave onset), P -waves, S -waves, and coda waves. The second to fifth windows contain only the pre-event noise (magenta box), P -waves (yellow box), S -waves (green box), and coda waves (gray box), respectively. The sixth window contains both P - and S -waves. All time windows are selected during data processing in order to calculate the FAS from the different waves in these windows. Details on window selection are described by Ancheta et al. [2013], Goulet et al. [2014], and Ktenidou et al. [2014], and are briefly outlined below.

The start time of the P -wave window (t_p), which is also the end of the noise window, was first selected visually by inspecting the three components for the first, generally impulsive, large-amplitude wave arrival. Then, the end time of the P -wave window, which is the start time of S -wave window (t_s), was selected visually considering amplitude and frequency content of the three-component acceleration, velocity, and displacement time series. As a selection guide, the theoretical S arrival time (t'_s) is plotted with the time histories, based on the selected P arrival time and the hypocentral distance as follows:

$$t'_s = t_p + \Delta t_{s-p} \approx t_p + R_h/8 \quad (3.1)$$

where R_h is the hypocentral distance, and P - and S -wave velocities are assumed to be 6.0 and 3.5 km/sec for the crust, respectively.

The end time of the S -wave window was automatically selected using a computed S -wave duration, which is a function of magnitude and hypocentral distance and is expressed as follows:

$$D_S = T_{d-rup} + T_{d-prop} \quad (3.2)$$

where T_{d-rup} is a base duration, which is related to, but generally larger than, the rupture (source) duration, and T_{d-prop} is the additional duration introduced along the source-to-site path, including scattering effects. Table 3.2 shows the T_{d-rup} used in the data processing, where f_c in the table is calculated by the following formula [Aki 1967; Brune 1970; and Boore 1983]:

$$f_c = 4.9 \times 10^6 \beta \left(\frac{\Delta\sigma}{M_0} \right)^{\frac{1}{3}} \quad (3.3)$$

where M_0 is the seismic moment, given as Hanks and Kanamori [1979]

$$M_0 = 10^{1.5M+16.05} \quad (3.4)$$

β is the shear-wave velocity at the source (assumed as 3.2 km/sec); $\Delta\sigma$ is the stress drop (assumed as 6 MPa, an average value for large earthquakes in California [Atkinson and Silva 1997]; and M is the moment magnitude.

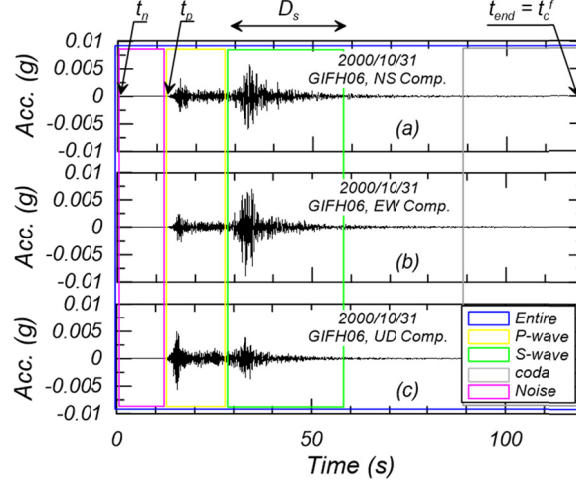


Figure 3.2 Schematic drawing of different time windows.

Table 3.2 Base duration used in the analysis.

Moment magnitude (M)	Base duration (sec)
$M < 4.5$	10
$4.5 \leq M < 6.9$	15
$6.9 \leq M < 7.6$	$1.4/f_c$
$7.6 \leq M \leq 9.1$	34

The hypocentral distance effect on the S -wave duration is approximated for active tectonic regions as:

$$T_{d-prop} = 0.1 \cdot R_h \quad (3.5)$$

The factor of 0.10 in this expression is consistent with the study by Kempton and Stewart [2006], in which the distance effects on significant durations of D_{a5-75} (5 to 75% duration) and D_{a5-95} (5 to 95% duration) were represented by similarly-defined factors of 0.07 and 0.15, respectively.

After computing S -wave duration D_s with Equation (3.2), the start time of the noise window (t_n) was obtained as follows, so that the noise duration equals the S window duration if possible:

$$t_n = \max(0, t_p - D_s) \quad (3.6)$$

The start time of the coda window (t_c) was selected by following the theoretical coda definition [Aki 1969; Philips and Aki 1986; and Kato et al. 1995], which gives the onset of the coda at a time equal to twice the S -wave travel time after the S -wave onset. However, to estimate this window for as many recordings as possible, we defined the end of coda window, t_c^f as:

$$t_c^f = \min(t_{end}, t_s + 3 \cdot D_s) \quad (3.7)$$

The start time of the coda window was then obtained by subtracting the S -window duration:

$$t_c = t_c^f - D_s \quad (3.8)$$

Finally, the entire time window was selected from t_n to t_c^f .

3.2.3 Fourier Spectra

(a) Mean removal and taper

Mean removal and tapers are applied to each windowed time series before calculating the Fourier spectra. Mean removal (also sometimes referred to as DC-removal) is defined by:

$$a' = a - \bar{a} \quad (3.9)$$

where a' denotes the acceleration time series after mean removal, and a and \bar{a} denote the windowed acceleration time series and the mean offset, respectively. After mean removal, cosine tapers are applied at the start and end of each window as (e.g., Kanasewich [1981]):

$$\text{Window start: } w_i = \frac{1}{2} \left[1 + \cos \left(\pi \frac{n_b + i - 1}{n_b} \right) \right], i = 1, \dots, n_b \quad (3.10)$$

$$\text{Window end: } w_i = \frac{1}{2} \left[1 + \cos \left(\pi \frac{i - 1}{n_e} \right) \right], i = 1, \dots, n_e \quad (3.11)$$

where n_b is the number of points within the beginning taper, and n_e is similarly defined for the end taper. For example, when the beginning taper is applied with a taper length of 0.5 sec to time series with $dt = 0.005$ sec, n_b is $0.5/0.005 = 100$. These functions produce a weight of zero at the first and last points in the time series, and gradually increase to 1.0 at the opposite ends of the tapers. Table 3.3 lists the durations of cosine tapers applied to the time series.

Table 3.3 Cosine taper length applied to windowed accelerations.

Windowed time histories	Cosine taper length	
	Start time	End time
Entire	1% of total length	1% of total length
Pre-Event Noise	0.5 sec	0.5 sec
<i>P</i> -Wave	0.5 sec	0.5 sec
<i>SL_g</i> -Waves	0.5 sec	0.5 sec
<i>Coda</i>	0.5 sec	0.5 sec

(b) Computation of Fourier spectra

Fourier spectra are calculated from the windowed time series after mean removal and tapering. Fourier amplitude spectra (FAS) and Fourier phase spectra (FPS) are saved as output files. Before calculating Fourier spectra, a series of zeroes are added at the end of recordings to increase the number of data points to a power of 2. The signal durations increase to approximately 40–50 minutes for signals to be used with acausal filters, depending on the

sampling frequency, as shown in Table 3.4. This window length was selected based on the longest-duration recording in the NGA-East dataset so that all the recordings become at least twice as long as the recorded duration, which avoids wrap-around effects in the time domain after applying acausal filters. The lengths of pre-event noise, *P*-wave, *S*-wave, and coda wave windows are all increased to 50 minutes with zeroes. This process provides a consistent frequency step (*df*) among the different windows and recordings; hence, these FAS are well-formatted for subsequent application without the need to perform frequency domain interpolation.

Consider an acceleration time series $a(t)$, which is sampled at N discrete points in time separated by step dt . Complex-valued Fourier coefficients are computed at $2N+1$ frequencies at step df :

$$C_k = \frac{1}{N} \sum_{j=1}^N a(j) \omega_N^{(j-1)(k-1)} \quad (3.12)$$

$$\omega_N = e^{(-2\pi i)/N} \quad (3.13)$$

where k is a frequency index, C_k is a Fourier coefficient, and $i = \sqrt{-1}$. The Fourier amplitude $|A(\omega)|$ is computed as:

$$|A| = dt \cdot N |C| \quad (3.14)$$

Equations (3.12) and (3.14) show that C_k decreases, but Fourier amplitudes are not changed by zero padding of the time series. Fourier phase spectra $\Phi(\omega)$ are calculated from the real and imaginary values of Fourier coefficients:

$$\Phi = \tan^{-1} [\text{Im}(C)/\text{Re}(C)] \quad (3.15)$$

where the phase ranges from $-\pi$ to π in the output file.

Table 3.4 Minimum frequencies for Fourier spectra calculation.

Sampling frequency (Hz)	dt (sec)	Duration (sec)	Power of 2	df (Hz)
10	0.1	3276.80	15	0.00030518
20	0.05	3276.80	16	0.00030518
40	0.025	3276.80	17	0.00030518
50	0.02	2621.44	17	0.00038147
100	0.01	2621.44	18	0.00038147
200	0.005	2621.44	19	0.00038147

Figure 3.3 shows the FAS for the UD-component recording in Figure 3.2. Blue, green, magenta, yellow, and gray lines show the FAS of the entire time window, S -, noise-, P -, and coda windows, respectively. The Fourier amplitudes in Figure 3.3 are smoothed to facilitate the selection of the low-pass corner frequency. Several smoothing methods were reviewed, in which smoothing is applied by averaging within frequency-domain windows. Windows considered include linear-scale rectangular, linear scale triangular, log-scale rectangular, and Konno-Ohmachi [Konno and Ohmachi, 1998]. The most appropriate choice of smoothing window depends on the purpose of the smoothing (e.g., see Konno and Ohmachi [1998] and Boore [2020]). We selected a log-scale rectangular window—which is computationally efficient—and provided satisfactory properties in the smoothed spectra. This window is expressed as:

$$W(f, f_o) = \begin{cases} 1, & 10^{-d/2} \leq f/f_o \leq 10^{d/2} \\ 0, & \text{otherwise} \end{cases} \quad (3.16)$$

where d is the window width in log scale, and f and f_o are frequency and the window central frequency, respectively. The default smoothing window size is $d = 0.05$ in log scale, which smooths within a range of $\pm 6\%$ around a given frequency. The smoothed Fourier amplitudes are calculated at the central frequency by giving equal weight to each amplitude within the window as follows:

$$\ln |A_0| = \sum_{i=1}^n w_i \ln |A_i| \quad (3.17)$$

where $|A_0|$ is the smoothed Fourier amplitude at the central frequency, n is the number of frequencies within the window, and weights w_i are:

$$w_i = 1/n \quad (3.18)$$

Since the rectangular window has a constant width in log scale, n increases with frequency. For example, if frequency step $df = 0.000763$, $n = 8$ for $f_o = 0.05$ Hz and 1510 for $f_o = 10$ Hz.

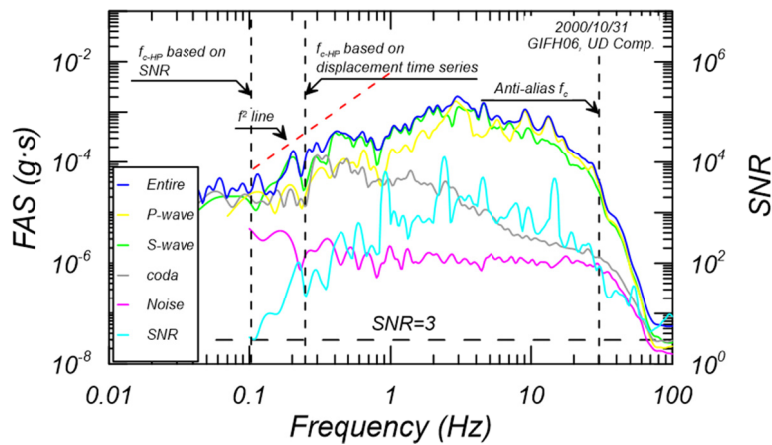


Figure 3.3 Fourier amplitude spectra for time series in different windows.

3.2.4 Filtering Methodology

High-pass (low-cut) and low-pass (high-cut) filters in the frequency domain are applied to the windowed record encompassing the entire signal; the other five time windows (the four shown in Figure 3.2 and the combined p- and s-windows) are not filtered. Causal and acausal Butterworth filters are applied in which 5 and 4 poles are used for high-pass and low-pass filters, respectively.

High-pass corner frequencies (f_{c-HP}) are selected based on the theoretical acceleration decay at low frequency according to the f^2 model [Brune 1970; Boore and Bommer 2005], which is shown on the FAS plots for guidance (Figure 3.3). Corner-frequency selection is also aided by comparison of the “entire signal” FAS to the “noise window” FAS; hence signal-to-noise ratio (SNR) is computed to guide these selections. At low/high frequencies, these will generally converge by approaching SNR = 1.0, and the high-pass/low-pass corner frequency is typically selected to be slightly higher/lower than the frequency of convergence. A SNR of 3.0 is typically referenced. Additionally, (f_{c-HP}) are iteratively selected by reviewing displacement amplitude in the noise window (e.g., Boore and Bommer [2005]). In consideration of both of the above factors (conformance with f^2 model and SNR, displacement amplitude in pre-event noise window), the (f_{c-HP}) selected for the example recording is 0.1 Hz. A low-pass corner frequency (f_{c-LP}) is selected at 30 Hz due to anti-alias filter of the recording instrument; this is a commonly encountered situation for ground motions recorded by modern digital instruments. The methodology described and illustrated here was applied to all NGA-Sub records that passed screening criteria; see Section 3.2.1. This resulted in selected values of (f_{c-HP}) and (f_{c-LP}) for all three as-recorded components for each ground motion. The usable frequency is calculated with a multiplicative factor of 1.25 inward as is standard practice in NGA projects (e.g., Ancheta et al. [2014]).

Filtered versions of each record are provided using acausal Butterworth filters. Boore and Akkar [2003] and Bazzurro et al. [2005] reviewed attributes of acausal vs. causal filters and determined that the phase shift introduced in the application of causal filters that is absent in acausal filters is the most important distinction. Both filters have the same amplitude of the transfer function. The following sections describe both filters in greater detail.

(a) Acausal Butterworth filter

The acausal Butterworth filter (high-pass) is applied by modifying both real and complex components of signal Fourier coefficients as:

$$Y = \frac{(f/f_c)^{2n_p}}{\sqrt{1 + (f/f_c)^{2n_p}}} \quad (3.19)$$

where n_p is the number of poles, and f_c is the corner frequency. Acausally filtered time series were used for computation of RotDxx IMs [Boore 2010]; see Section 3.3. Figure 3.4 shows the time domain response of Equation (3.19) for different corner frequencies. The input time series is an impulse at $t = 20$ sec with an amplitude of $1/dt$. The figure shows that the filter produces time-domain responses prior to impulse arrival (also referred to as pre-event motions; see Bazzurro et al. [2005]). Figures 3.5 and 3.6 show the Fourier amplitude and phase spectra for acausal filters

with different corner frequencies. Figure 3.5 shows that amplitudes rapidly decrease for frequencies lower than (f_{c-HP}). Figure 3.6 shows that phase is not modified by filtering. Because phase is not modified, pseudo-spectral accelerations are not affected by the selected values of (f_{c-HP}) within the pass-band [Boore and Akkar 2003]. As a result, acausal filters are preferred for computing IMs.

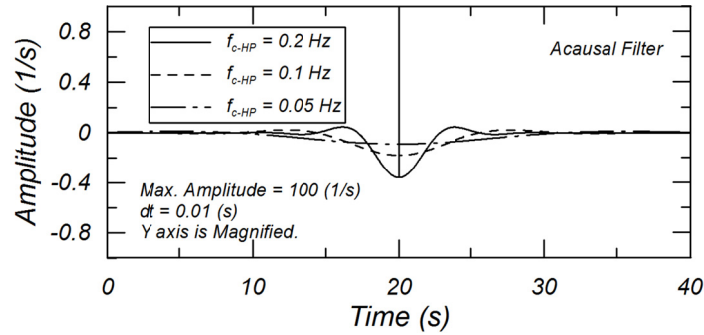


Figure 3.4 Time domain response of acausally filtered impulse.

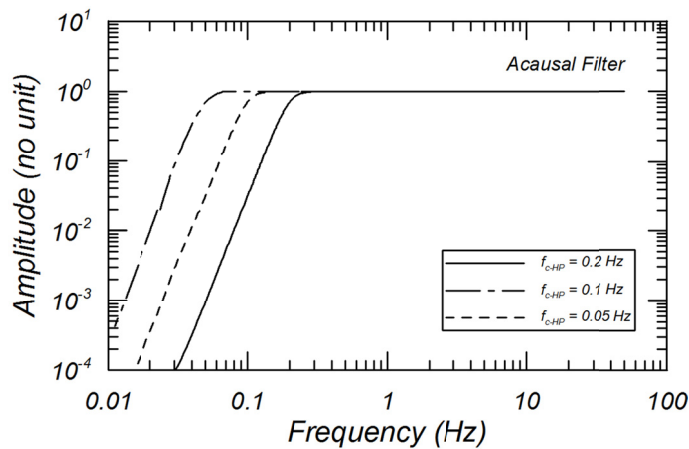


Figure 3.5 Fourier amplitude spectra for acausally filtered impulse.

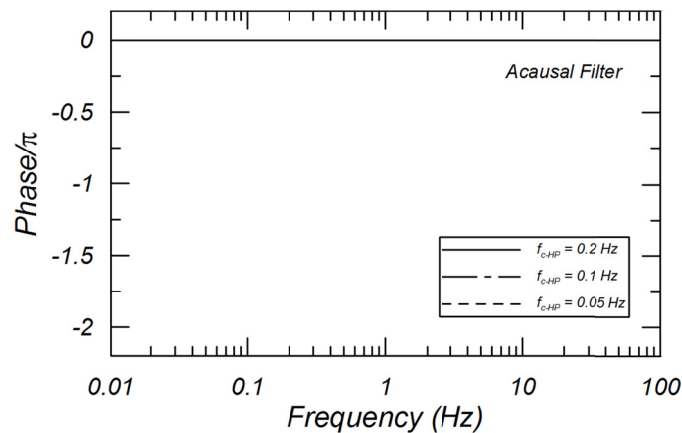


Figure 3.6 Fourier phase spectra for acausally filtered impulse.

(b) Causal Butterworth filter

Although Causal Butterworth filters were not used in correction of time series for the NGA-Sub project, such filters were referenced during data processing to differentiate the filter responses to noise in pre-event displacement time series (e.g., Kishida et al. [2017]). The causal Butterworth filter (high-pass) is applied by modifying both real and complex components of Fourier coefficients as:

$$Y = \frac{1}{\prod_{j=1}^n \left\{ i(f_c/f) - \exp\left[\frac{i\pi}{2n} (2j-1+n) \right] \right\}} \quad (3.20)$$

Figure 3.7 shows the time domain response of the causal filter [Equation (3.20)] for different corner frequencies when applied to an impulse at $t = 20$ sec with amplitude $1/dt$. The filter does not create a time-domain response prior to signal arrival, thus preserving the correct arrival time for each frequency component. Figures 3.8 and 3.9 show Fourier amplitudes and phases for the different corner frequencies in Figure 3.7. Figure 3.8 shows that amplitudes rapidly decrease at frequencies lower than (f_{c-HP}) , similar to Figure 3.5 for the acausal filter. Figure 3.9 shows that the causal filter distorts phase near corner frequencies. As a result, pseudo-spectral accelerations of filtered signals are affected by filtering even for oscillator frequencies higher than (f_{c-HP}) [Boore and Akkar 2003].

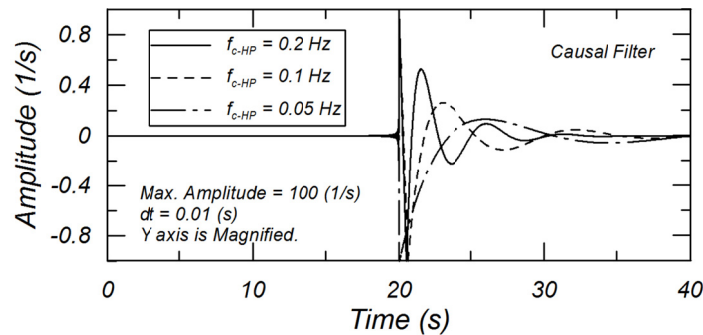


Figure 3.7 Time domain response of causally filtered impulse.

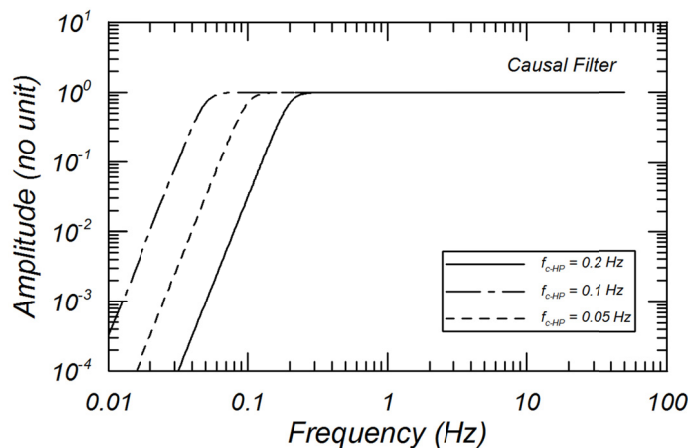


Figure 3.8 Fourier amplitude spectra for causally filtered impulse.

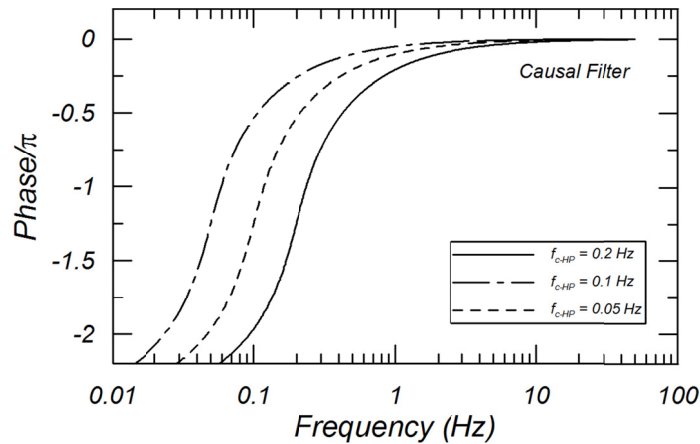


Figure 3.9 Fourier phase spectra for causally filtered impulse.

3.2.5 Baseline Correction

After the filtering procedures described in the previous section are applied, the zero pads are removed to provide pad-stripped time series; see Figure 3.10(a) as an example of an acausally filtered record. This acceleration time series is then integrated to velocity and then displacement, with the initial velocity and displacement assumed to be zero; see Figures 3.10(b) and (c). The integration occurs in the time domain using the linear acceleration method [Nigam and Jennings 1969].

A problem that is sometimes encountered with the integrated time series is the appearance of baseline drift in displacements. For example, Figure 3.10(c) shows a linear baseline drift, suggesting that the velocity time series has a constant offset. Such drifts are caused by an initial velocity in pad-stripped recordings after applying the acausal filter (as expected based on the impulse response shown in Figure 3.4); the error occurs because the actual non-zero value is mis-represented by the assumption of zero in the integration process.

A baseline correction procedure from Boore et al. [2012] could be applied to correct the errors shown in Figure 3.10. Figure 3.11 shows the zero-padded acausally filtered time series (i.e., zero-pads were kept at the beginning of recording after applying acausal filter). The slope of the velocity time series during the zero-padded interval indicates that there is a non-zero acceleration before the start time of the original record; therefore, the velocity time series has a positive bias if the initial velocity is assumed to be zero for a pad-stripped time series. This positive bias in velocity appears as a ramp in the displacement time series; see Figure 3.10(c). Boore et al. [2012] demonstrated that this drift does not occur if the correct initial velocity and displacement are used in integrating acceleration time series. This does not occur if zero-padded filtered time series are provided, which is an approach that has been applied in other databases [Akkar et al. 2010]. If either of these approaches is used, baseline correction is not a required step in data processing.

The NGA-Sub project did not adopt the remedies suggested by Boore et al. [2012] because we aimed to provide pad-stripped acceleration time series that can be integrated to displacement without baseline drift when initial velocity and displacement are taken as zero. Baseline correction was required to achieve this aim. The baseline correction has three steps:

1. A cosine taper is applied at the onset of the pad-stripped record per Equation (3.10);
2. A 6th order polynomial is fit to the displacement time series; and
3. The polynomial fit is subtracted from the filtered displacement time series, which can be differentiated to velocity and acceleration.

Figure 3.12 shows the record from Figure 3.10 following application of the baseline procedure, which shows that the baseline drift has been removed. The process of baseline correction also ensures compatibility of processed acceleration, velocity, and displacement time histories as described in Chiou et al. [2008], and discussed in Boore et al. [2012]. Figure 3.13 compares 5%-damped pseudo-spectral accelerations before and after application of the baseline correction procedure, showing a negligible impact.

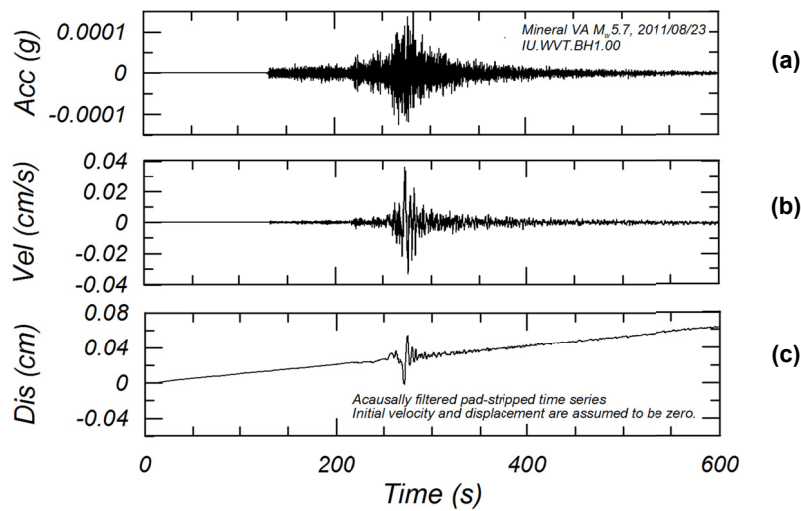


Figure 3.10 Time series of acausally filtered pad-stripped record: (a) acceleration; (b) velocity; and (c) displacement time series by double integration of acceleration time series assuming the initial velocity and displacement are zero.

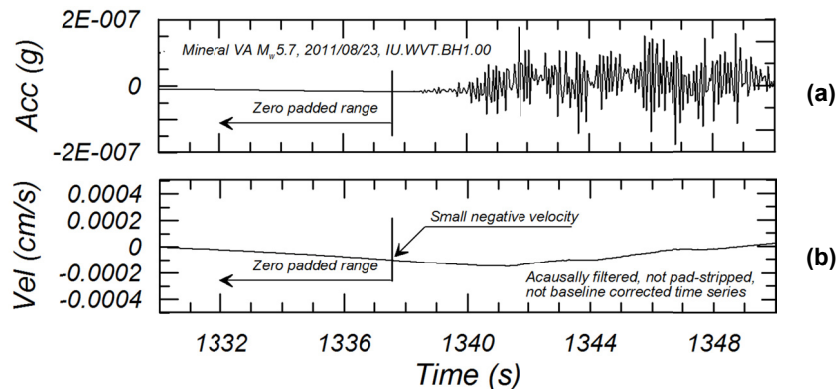


Figure 3.11 Acceleration (a) and velocity (b) time series of acausally filtered record with zero padding.

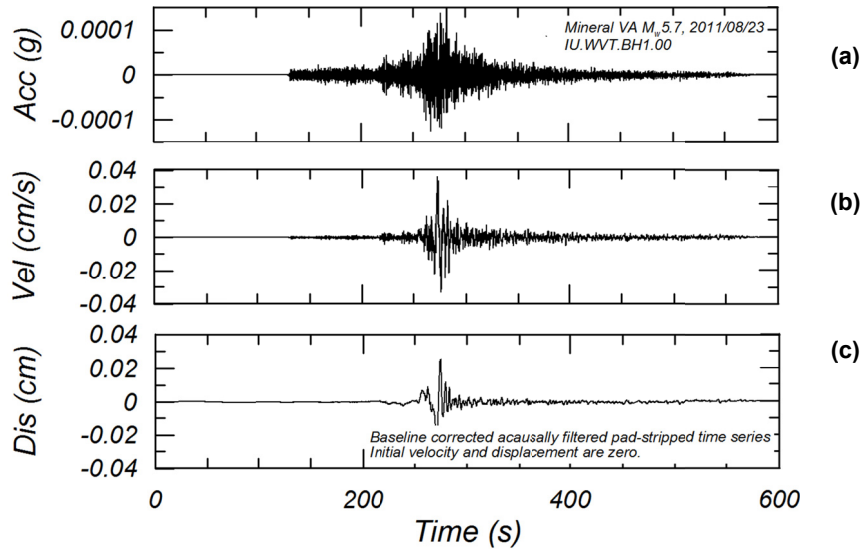


Figure 3.12 Acausally filtered time series with baseline correction: (a) acceleration; (b) velocity; and (c) displacement.

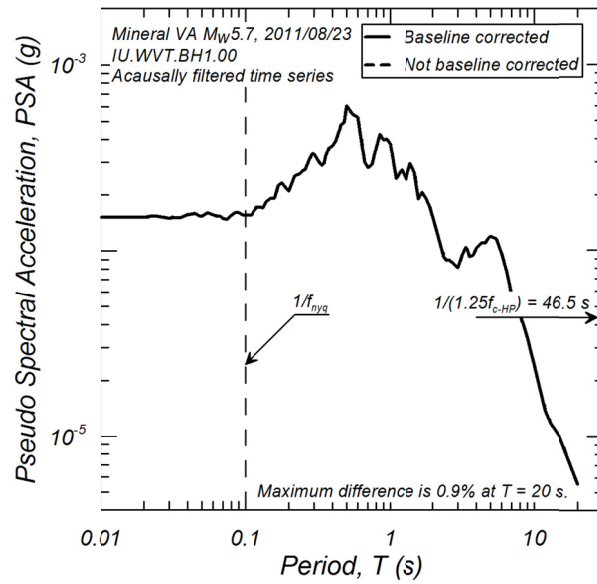


Figure 3.13 Effect of baseline correction on PSA for acausally filtered time series.

3.3 COMPUTATION OF GROUND-MOTION PARAMETERS

3.3.1 As-Recorded and RotDnn Pseudo-Spectral Accelerations

Acceleration time series processed using the procedures described in Section 3.2 were used to compute two types of pseudo spectral accelerations (PSA). One is “as-recorded spectral acceleration,” which computes the PSA for three components independently. The other PSA is “RotDnn,” which is an orientation-independent combination of the two horizontal components [Boore 2010]. The following sections describe each type of PSA computation as well as time series interpolation that was applied in the calculations.

As described in Chapter 4, there are 70,107 three-component records from 1880 events. Following screening to remove events without magnitudes, hypocenter locations, assigned event types, or distances, the database is reduced to 65,276 recordings from 976 events. Figure 3.14(a) shows the data distribution for these 976 events in magnitude-distance space for peak acceleration. Figures 3.14(b) and (c) show peak ground acceleration (PGA) distributions for 360 events classified as interface (23,552 recordings) and 383 intraslab events (27,547 recordings), respectively. Figure 3.15 shows the number of records as a function of oscillator period. There is fall-off in the amount of data as period increases as some records become outside of their usable range based on the selected low-cut frequency. Figure 3.15 shows this fall-off begins at 1 sec, and two-thirds of the data is lost at 20-sec period.

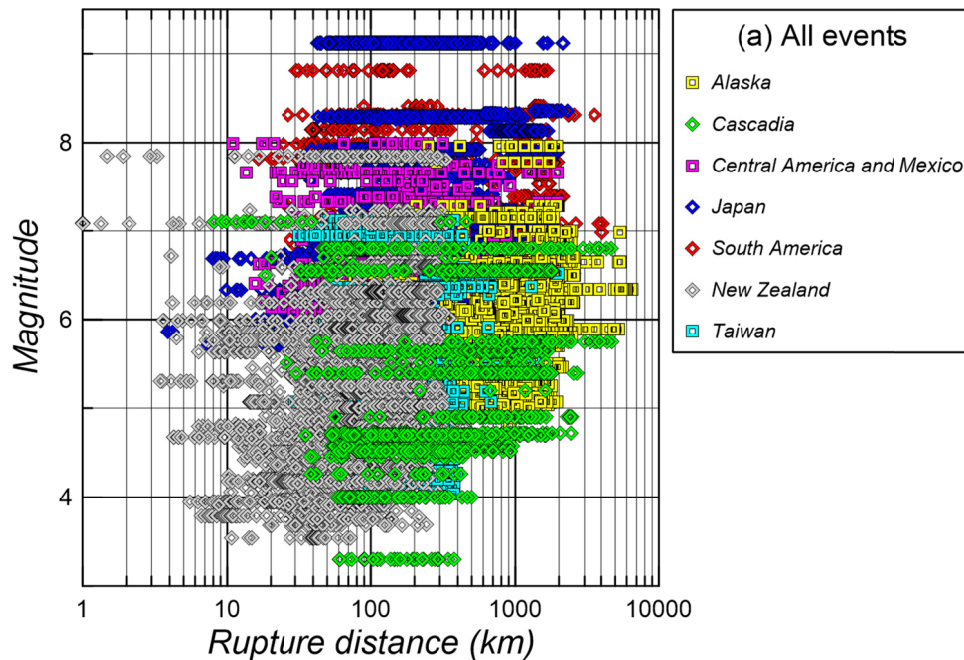


Figure 3.14(a) Distribution in magnitude-rupture distance space of recordings from 976 events that pass screening criteria (described in Chapter 4).

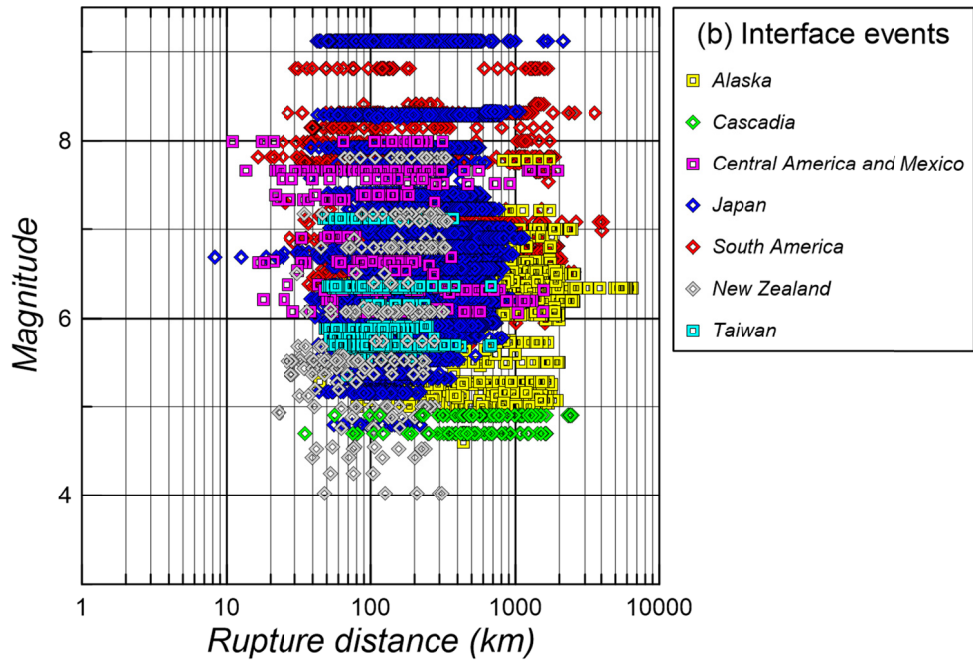


Figure 3.14(b) Distribution in magnitude-rupture distance space of recordings from 360 interface events.

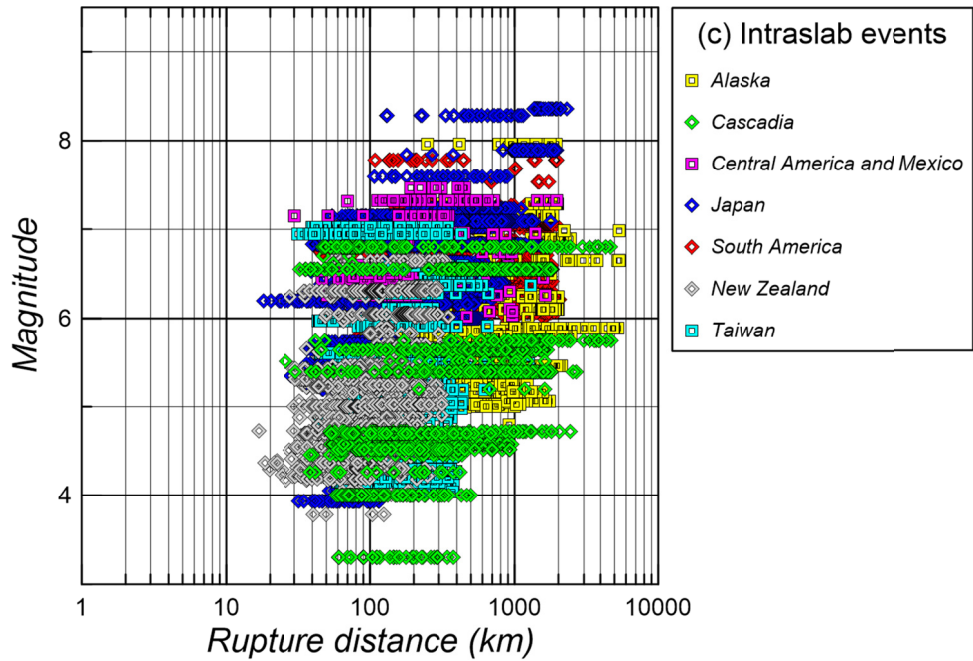


Figure 3.14(c) Distribution in magnitude-rupture distance space of recordings from 383 intraslab events that pass screening criteria described in Chapter 4.

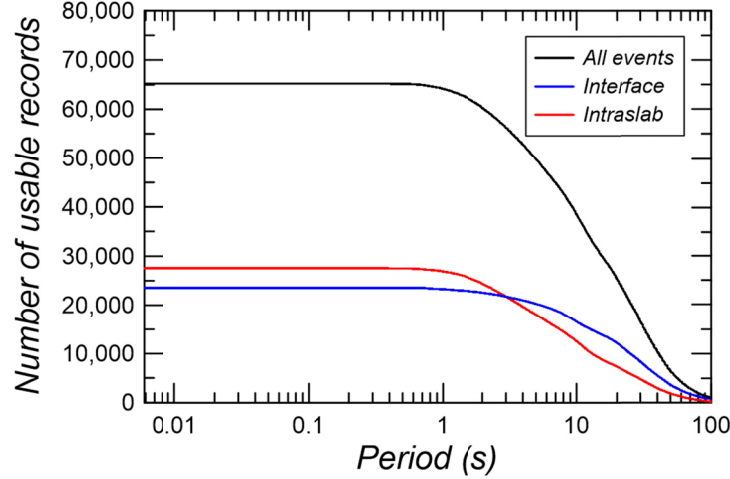


Figure 3.15 Fall-off of number of usable records from 976 screened events as oscillator period increases.

(a) As-recorded pseudo-spectral accelerations

Pseudo-spectral accelerations are computed from spectral displacement (SD), which is the maximum relative displacement of the single-degree-of-freedom (SDOF) elastic oscillator with a specific period and damping. A damping ratio of 5% was used. Spectral displacement is converted to PSA as follows:

$$PSA = SD \cdot \left(\frac{2\pi}{T}\right)^2 \quad (3.21)$$

where T is the structural period. Pseudo-spectral accelerations are computed using the acausal-filtered acceleration histories for the reasons given in Section 3.2.4. Pseudo-spectral accelerations for as-recorded components are listed in the PSA_{ij} table in the relational database as H1, H2, and V. Orientations for the horizontal components are provided in $RecordMeta$ table in the relational database.

(b) RotDxx pseudo-spectral accelerations

As described in Boore [2010], the RotDnn spectra represent the range of oscillator responses to a given pair of horizontal input motions. The responses are computed across all non-redundant rotation angles, and “nn” represents the fractile of the spectra sorted by amplitude. The “D” indicates that rotation angle will be specific to the period of the oscillator.

RotDnn spectra for a given azimuth can be computed from the horizontal ground motion for that same azimuth. The ground motion for a particular azimuth (rotated an amount θ from the azimuths of the original recordings) can be computed from the orthogonal horizontal-component time series, $a_1(t)$ and $a_2(t)$, as follows:

$$a_{ROT}(t, \theta) = a_1(t) \cos \theta + a_2(t) \sin \theta \quad (3.22)$$

where a_{ROT} the rotated time series, and θ is the rotation angle from the a_1 axis. Using the RCTC code from Wang et al. [2017] (or an equivalent Fortran code from Dave Boore [2020]), response spectra for the rotated time series are calculated for non-redundant rotation angles between zero

and 180°. Three fractiles are saved: the minimum (RotD00), median (RotD50), and the maximum (RotD100).

(c) Time series interpolation

Figure 3.16 shows PSA for an example recording (record sequence number, RSN 1002911). The black line shows the PSA computed from a time series for which accelerations between data points are interpolated linearly [Nigam and Jennings 1969]. The blue line shows the PSA for which time series are interpolated in frequency domain using *sinc* interpolation [Shannon 1998], which increases sample rate by powers of 2 (i.e., 2, 4, 8, etc.). *Sinc* interpolation involves padding the time series with zeros, computing the Fourier transform, and then performing an inverse Fourier transform to obtain the revised signal. Boore and Goulet [2014] recommend *sinc* interpolation to avoid the underestimation of PSA near the anti-aliasing corner frequency and introduction of spurious energy at high frequencies from linear interpolation, e.g., as shown in Figure 3.16 at 0.04 sec (25 Hz) by the small bump in PSA. We applied *sinc* interpolation, as coded in RCTC, for the computation of PSA for NGA-Sub.

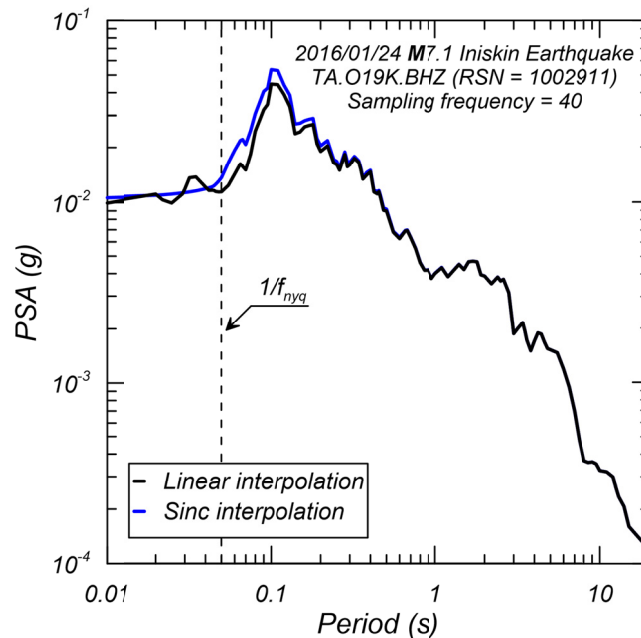


Figure 3.16 Effect of time series interpolation on PSA.

3.3.2 Other Ground-Motion Parameters

Ground-motion parameters beyond PSA that were considered in the NGA-Sub project are:

- Arias intensity (AI);
- Times to different percentiles of AI (5% to 95% in steps of 5%), which can be used to compute significant durations;
- Cumulative absolute velocity (CAV) parameters, including CAV and CAV integrated beyond a lower limit of 5 cm/sec² (CAV₅); and
- Fourier amplitudes.

Arias Intensity is computed per Arias 1970]:

$$AI = \frac{\pi}{2g} \int a(t)^2 dt \quad (3.23)$$

Arias intensity is provided in units of cm/sec. Times to various percentiles of AI are provided as measured from the start of the pad-stripped acceleration time series that is produced by the processing procedures described in Section 3.2. Cumulative absolute velocity is computed as:

$$CAV = \int |a(t)| dt \quad (3.24)$$

Cumulative absolute velocity is also computed excluding portions of the absolute accelerogram with amplitudes less than 5 cm/sec², which is referred to as CAV_5 . This definition of CAV has been used, for example, to predict pore pressure generation in sands [Kramer and Mitchell 2006].

Smoothed FAS are provided for vertical as-recorded components as well as for a smoothed effective amplitude spectrum (EAS) defined per Goulet et al. [2018] as:

$$EAS(f) = \sqrt{\frac{1}{2} \left[|A_{H1}(f)|^2 + |A_{H2}(f)|^2 \right]} \quad (3.25)$$

where $|A_{H1}(f)|$ and $|A_{H2}(f)|$ are Fourier amplitudes of the two as-recorded horizontal motions. Smoothing and desampling were performed after computing EAS following the approach by Goulet et al. [2018]. The values stored in the relational database are for the entire window. The calculations provide Fourier amplitude for all windows, but these additional data are not incorporated into the relational database. Fourier phases were not retained following smoothing and desampling.

3.3.3 Ground-Motion Tables in Relational Database

Chapter 2 of this report describes the database schema and introduces the various tables that comprise the database. Tables in the database that relate to ground-motion parameters and related information described in this chapter include the following (RSN = record sequence number, which is a unique identifying index for each ground motion):

RecordMeta: RSNs, as-recorded azimuths, high-pass corner frequencies;

RecordtoAT2: maps RSNs to the corrected time series (.AT2 files);

HeaderData: contains time step and other information from headers of AT2 files;

OscPeriods: list of oscillator periods used to compute PSA;

OscDamp: list of oscillator damping values used to compute PSA;

PSA_ij: RSN, periods, PSAs (periods are columns, RSN are rows);

- i = component (H1, H2, V, RotD0, RotD50, RotD100)
- j = damping ratio

DurationMetrics_k: RSN; *AI* for components $k = H1, H2,$ and V ; times for $k = H1, H2,$ and V (i.e., percentiles of $AI = 0.05$ to 0.95 in steps of 0.05);

FAS_k: RSN; frequencies; Fourier amplitudes for components $k = H1$ amp, $H2$ amp, EAS ; Frequency in columns, FAS in rows; and

CAV_k: RSN; CAV for components $k = H1, H2,$ and V ; CAV_5 for $k = H1, H2,$ and V .

3.4 DATA-QUALITY FLAGS

Individual recordings may have amplitudes that are so low or high that they are likely in error, and as such, may not be suitable for use in ground motion model (GMM) development. Sources of such errors might include incorrect gain, calibration problems, or incorrect units. Similarly, the population of recordings for individual earthquake events might be unreasonably high or low, which could indicate source location errors.

We sought to identify recordings potentially subject to such errors through the assignment of data-quality flags. The assignment of flags occurred mid-way through the NGA-Sub project and prior to GMM development. Our approach was to evaluate data for individual events relative to a global GMM available at that time (i.e., the “BC Hydro” model of Abrahamson et al. [2016]). Using ground-motion IMs and metadata from a regional flatfiles (Section 2.2), residuals were computed relative to the Abrahamson et al. [2016] model. An IM from a recording is considered potentially problematic if its residual falls outside the range of $\pm 4\sigma$, where σ is the total standard deviation. Figure 3.17 shows IMs vs. distance for a sample event in Japan, from which several records falling below the range can be seen.

Residuals were computed for the four IMs for which data are illustrated in Figure 3.17: PGA and 5%-damped pseudo-spectral accelerations at oscillator periods of 0.1, 0.3, and 1.0 sec. Flags were then assigned as indicated in Table 3.5. The -999 flag is assigned for recordings from non-interface or intraslab events (the Abrahamson et al. [2016] GMM does not apply in such cases), records with missing IMs, or missing metadata (most often distance). Data-quality flags are provided in the *RecordFlag* table for incorporation into the NGA-Sub relational database.

Table 3.5 Criteria for assignment of data-quality flags.

Flag	Description
0	All residuals within $\pm 4\sigma$
1	Residuals for one intensity measure beyond $\pm 4\sigma$
2	All four residuals beyond $\pm 4\sigma$
-999	Residuals not calculated due to missing data or metadata and for event types other than intraslab or interface

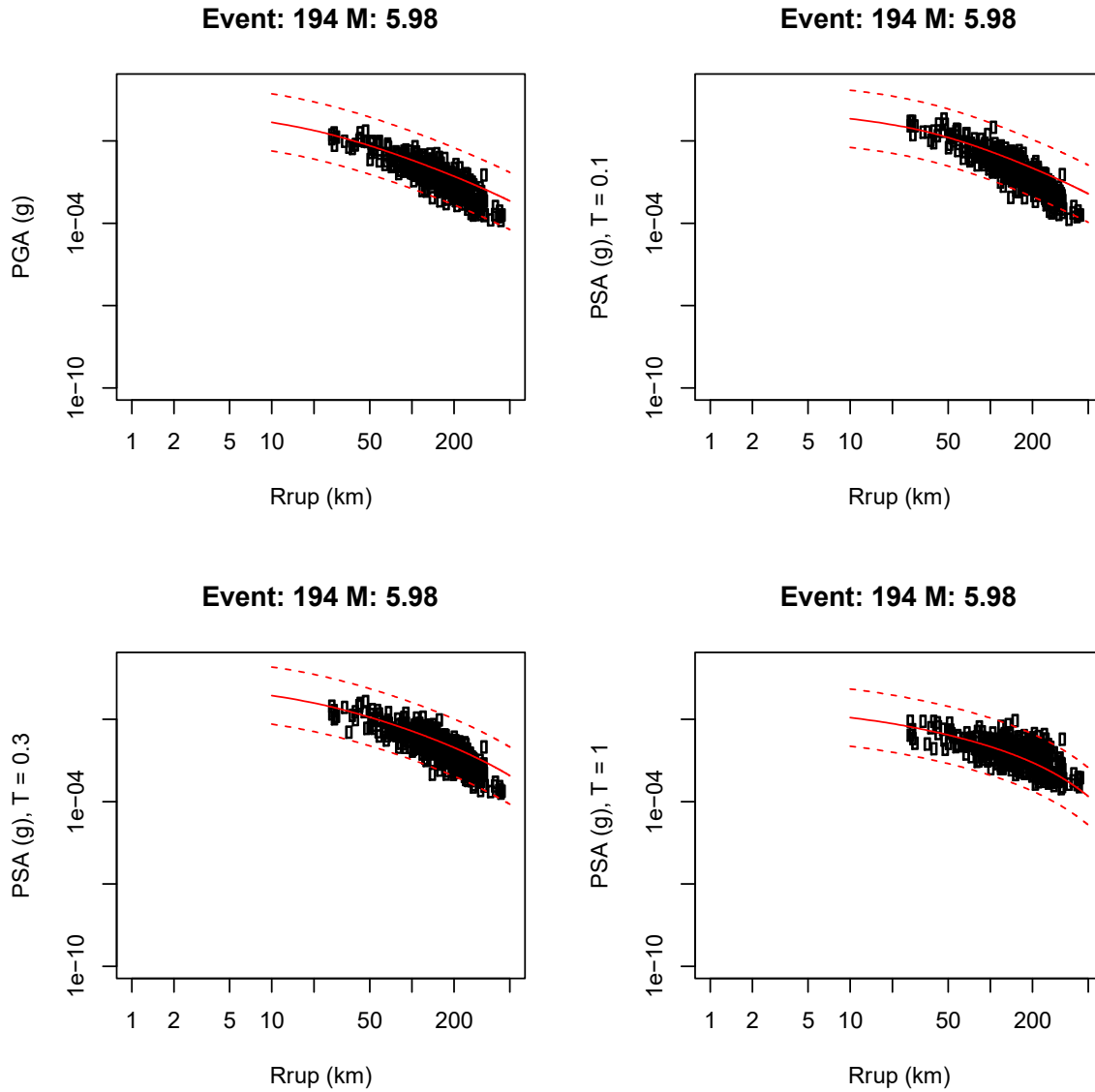


Figure 3.17 Comparison of data to median +/- four standard deviations from Abrahamson et al. [2016] model, used for flag assignments.

Suggested Citation:

Kishida T., Darragh R.B., Chiou B.S.-J., Bozorgnia Y., Mazzoni S., Contreras V., Boroscsek R., Rojas F., Stewart J.P. (2020). Chapter 3: Ground Motions and Intensity Measures, in *Data Resources for NGA-Subduction Project*, *PEER Report 2020/02*, J.P. Stewart (editor), Pacific Earthquake Engineering Research Center, University of California, Berkeley, California (headquarters).

REFERENCES

- Abrahamson N.A., Gregor N., Addo K. (2016). BC Hydro ground motion prediction equations for subduction earthquakes, *Earthq. Spectra*, 32: 23–44.
- Aki K. (1967). Scaling law of seismic spectrum, *J. Geophys. Res.*, 72: 1217–1231.
- Aki K. (1969). Analysis of the seismic coda of local earthquakes as scattered waves, *J. Geophys. Res.*, 74: 615–631.
- Akkar S., Çağnan Z., Yenier E., Erdoğan Ö., Sandıkkaya M.A., Gülkan P. (2010). The recently compiled Turkish strong motion database: Preliminary investigation for seismological parameters, *J. Seismol.*, 14: 457–479.
- Ancheta T.D., Darragh R.B., Stewart J.P., Seyhan E., Silva W.J., Chiou B.S.-J., Woodell K.E., Graves R.W., Kottke A.R., Boore D.M., Kishida T., Donahue J.L. (2013). PEER NGA-West 2 database, *PEER Report No. 2013/03*, Pacific Earthquake Engineering Research Center, University of California, Berkeley, CA.
- Arias A. (1970). A measure of earthquake intensity, in *Seismic Design for Nuclear Power Plants*, R.J. Hansen, ed., MIT Press, Cambridge, MA, pp. 438–483.
- Atkinson G.M., Silva W.J. (1997). An empirical study of earthquake source spectra for California earthquakes, *Bull. Seismol. Soc. Am.*, 87: 97–113.
- Bazzurro P., Sjöberg B., Luco N., Silva W.J., Darragh R.B. (2005). Effects of strong motion processing procedures on time histories, elastic and inelastic spectra, *Report CP-2005/02*, Consortium of Organizations for Strong-Motion Observation Systems and U.S. Geological Survey, Richmond, CA.
- Boore D.M. (1983). Stochastic simulation of high-frequency ground motions based on seismological models of the radiated spectra, *Bull. Seism. Soc. Am.*, 73: 1865–1894.
- Boore D.M. (2010). Orientation-independent, non-geometric-mean measures of seismic intensity from two horizontal components of motion, *Bull. Seismol. Soc. Am.*, 100: 1830–1835.
- Boore D.M. (2020). TSPP—A Collection of FORTRAN Programs for Processing and Manipulating Time Series, *USGS Open-File Report 2008-1111* (Revised 10 January 2020), U.S. Geological Survey, Menlo Park, CA.
- Boore D.M., Akkar S. (2003). Effect of causal and acausal filters on elastic and inelastic response spectra, *Earthq. Eng. Struct. Dyn.*, 32: 1729–1748.
- Boore D.M., Bommer J.J. (2005). Processing of strong-motion accelerograms: needs, options and consequences, *Soil Dyn. Earthq. Eng.*, 25: 93–115.
- Boore D.M., Goulet C.A. (2008). The effect of sampling rate and anti-aliasing filters on high-frequency response spectra, *Bull. Earthq. Eng.*, 12: 203–216.
- Boore D.M., Azari Sisi A., Akkar S. (2012). Using pad-stripped acausally filtered strong-motion data, *Bull. Seismol. Soc. Am.* 102: 751–760.
- Brune J.N. (1970). Tectonic stress and the spectra of seismic shear waves from earthquakes, *J. Geophys. Res.* 75: 4997–5009.
- Chiou B.S.-J., Darragh R.B., Gregor N., Silva W.J. (2008). NGA project strong-motion database, *Earthq. Spectra*, 24: 23–44.
- Goulet C.A., Kishida T., Cramer C.H., Darragh R.B., Silva W.J., Hashash Y.M.A., Harmon J., Stewart J.P., Woodell K., Youngs R.R. (2014). PEER NGA-East database, *PEER Report No. 2014/17*, Pacific Earthquake Engineering Research Center, University of California, Berkeley, CA.
- Goulet C. A., Kottke A., Boore D.M., Bozorgnia Y., Hollenback J., Kishida T., Der Kiureghian A., Ktenidou O.J., Kuehn N.M., Rathje E.M., et al. (2018). Effective amplitude spectrum (EAS) as a metric for ground motion modeling using Fourier amplitudes, *Proceedings, 2018 Seismology of the Americas Meeting*, Miami, Florida.
- Hanks T.C., Kanamori H. (1979). A moment magnitude scale, *J. Geophys. Res.*, 84: 2348–2350.
- Kanasewich E.R. (1981). *Time Sequence Analysis in Geophysics*, University of Alberta Press, Canada.

- Kato K., Aki K., Takemura M. (1995). Site amplification from Coda waves: Validation and application to S-wave site response, *Bull. Seismol. Soc. Am.*, 85: 467–477.
- Kempton J.J., Stewart J.P. (2006). Prediction equations for significant duration of earthquake ground motions considering site and near-source effects, *Earthq. Spectra*, 22: 985–1013.
- Kishida T., Giacinto D., Iaccarino G. (2017). Comparison of manual and automated ground motion processing for small- to-moderate-magnitude earthquakes in Japan, *Earthq. Spectra*, 33: 875–894.
- Konno K., Ohmachi T. (1998). Ground-motion characteristics estimated from spectral ratio between horizontal and vertical components of microtremor, *Bull. Seismol. Soc. Am.*, 88: 228–241.
- Kramer S.L., Mitchell R.A. (2006). Ground motion intensity measures for liquefaction hazard evaluation, *Earthq. Spectra*, 22: 413–438.
- Ktenidou O.-J., Cotton F., Abrahamson N.A., Anderson J.G. (2014). Taxonomy of κ : A review of definitions and estimation approaches targeted to applications, *Seismol. Res. Lett.*, 85: 135–146.
- Nigam N.C., Jennings P.C. (1969). Calculation of response spectra from strong-motion earthquake records, *Bull. Seismol. Soc. Am.*, 59: 909–922.
- Philips W.S., Aki K. (1986). Site amplification of coda waves from local earthquakes in central California, *Bull. Seismol. Soc. Am.*, 76: 627–648.
- Shannon C.E. (1998). Communication in the presence of noise (a reprint of the classic 1949 paper), *Proceedings, IEEE*, 86(2): 447–457.
- Wang, P., Stewart J.P., Bozorgnia Y., Boore D.M., Kishida T. (2017). “R” package for computation of earthquake ground-motion response spectra, *PEER Report No. 2017/09*, Pacific Earthquake Engineering Research Center, University of California, Berkeley, CA.

4 Source and Path Metadata

Víctor Contreras, Jonathan P. Stewart, Tadahiro Kishida, Robert B. Darragh, Brian S.J. Chiou, Silvia Mazzoni, Nico Kuehn, Sean K. Ahdi, Katie Wooddell, Robert R. Youngs, Yousef Bozorgnia, Rubén Boroschek, Fabián Rojas, and Jennifer Órdenes

4.1 OVERVIEW AND ORGANIZATION

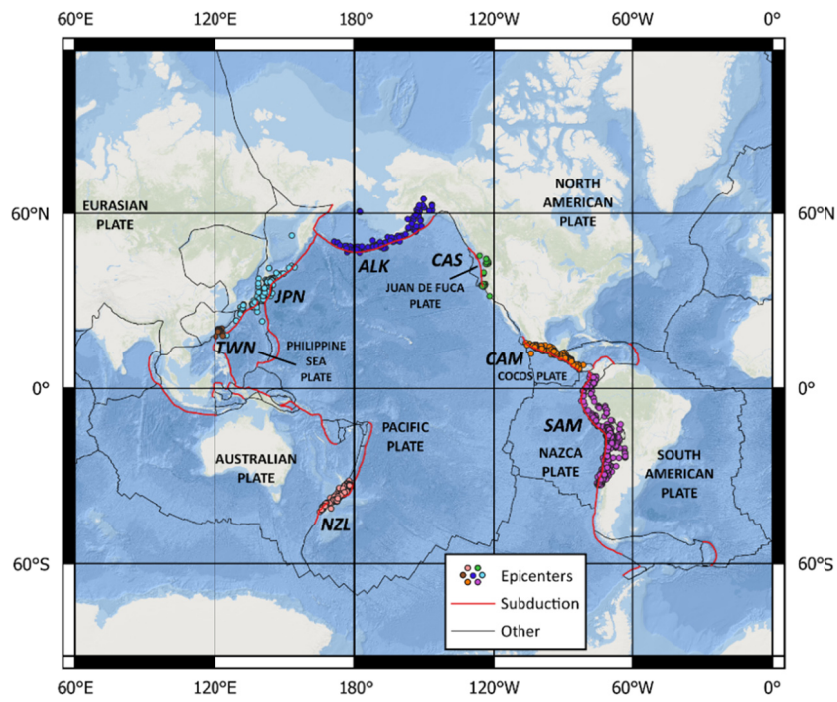
4.1.1 Introduction

For the earthquakes considered in the NGA-Subduction (NGA-Sub) project, a series of descriptive source parameters are needed to support the development of ground-motion models (GMMs). For a given ground-motion recording site, source parameters also allow path parameters to be defined, so the issues of source and path are strongly linked in the NGA-Sub database development. This chapter describes the manner by which those parameters were compiled and assembled in a source and path database file, which has been developed for events with ground-motion recordings obtained in different regions affected by subduction-zone earthquakes around the world.

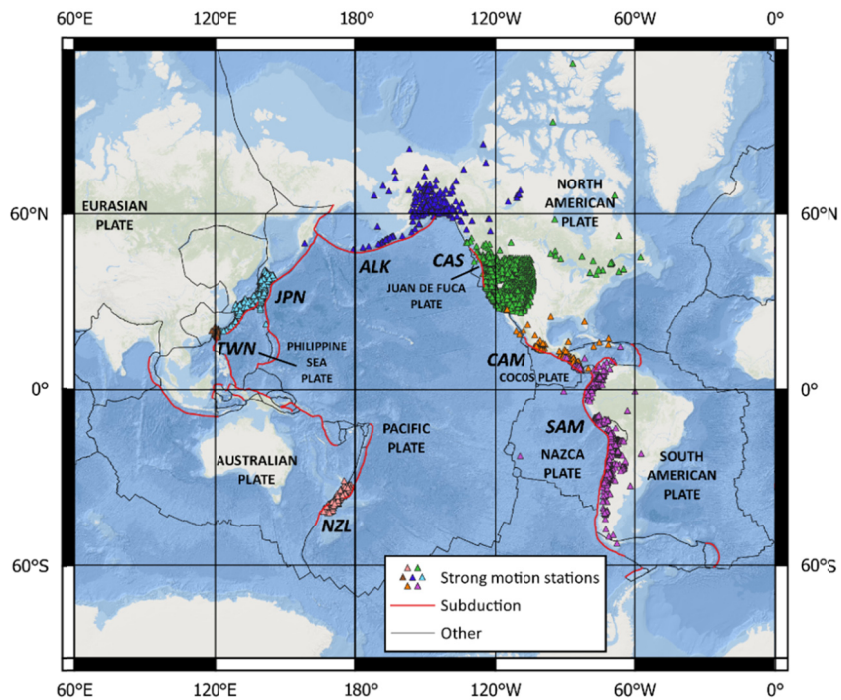
Chapter 2 describes the overall schema for the NGA-Sub database. This chapter concerns the source and path database and its contributing tables, which is a component of the broader database. The individual fields that comprise the source and path database are listed in Chapter 2. Certain obvious parameters listed in Chapter 2 are not explained here (e.g., region flags). This chapter describes what many of those parameters are in more detail and explains how they were developed.

4.1.2 Overview of Events

Figure 4.1 shows global maps with locations of the epicenters and the strong-motion recording stations in the NGA-Sub database. As presented in this figure, the source and path database has been organized into seven major regions: Alaska (ALK), Cascadia (CAS), Central America and Mexico (CAM), Japan (JPN), New Zealand (NZL), South America (SAM), and Taiwan (TWN). Also shown in Figure 4.1 are the main tectonic plates and plate boundaries as defined in a digital model assembled by Bird [2003]; the boundaries shown in red are mostly classical oceanic-beneath-continental subduction boundaries whereas other plate boundaries are shown in black.



(a)



(b)

Figure 4.1 Locations of (a) epicenters and (b) strong-motion recording stations in the NGA-Sub database. Regions are indicated by color of the epicenters and stations, and labeled as ALK (Alaska), CAS (Cascadia), CAM (Central America and Mexico), JPN (Japan), NZL (New Zealand), SAM (South America), and TWN (Taiwan).

The NGA-Sub source and path database contains source information on event date, origin time, seismic moment, moment magnitude, hypocenter location, nodal planes, and finite-fault geometric parameters. These and other parameters are listed and defined in Chapter 2. A key aspect is classification of each earthquake into one of four types: interface, intraslab, shallow crustal, or outer-rise. While the NGA-Sub project focuses on subduction-zone events (i.e., interface and intraslab), there is an important number of shallow crustal events and a small number of outer-rise events. The presence of these events in the database is a byproduct of the manner in which the database was developed; ground-motion recordings were collected in the seven study regions in Figure 4.1 without establishing *a priori* earthquake type. Once the data had been collected and processed, instead of discarding data from non-subduction sources, it was retained and flagged based on the event-type.

Figure 4.2 presents the locations of earthquakes included in the NGA-Sub database in the Alaska region, with differentiation by magnitude and type of earthquake. Subduction earthquakes are generated in Alaska by subduction of the north-west dipping Pacific Plate beneath the North American Plate. As shown in Figure 4.2, the plate boundary is immediately south of the Aleutian Island chain and about 330 km south of mainland Alaska in the vicinity of Anchorage. Along the Aleutian island chain, although a mixture of event types occur, most events are interface; further to the east the available events are predominantly intraslab. The largest interface event is the 2003 **M7.78** Rat Islands earthquake, and the largest intraslab event in the eastern region is the 2016 **M7.15** Iniskin earthquake. The 2018 **M7.1** Anchorage earthquake is not included in the NGA-Sub database because the earthquake occurred after data collection for the project terminated; however, it is also in the eastern part of the subduction zone.

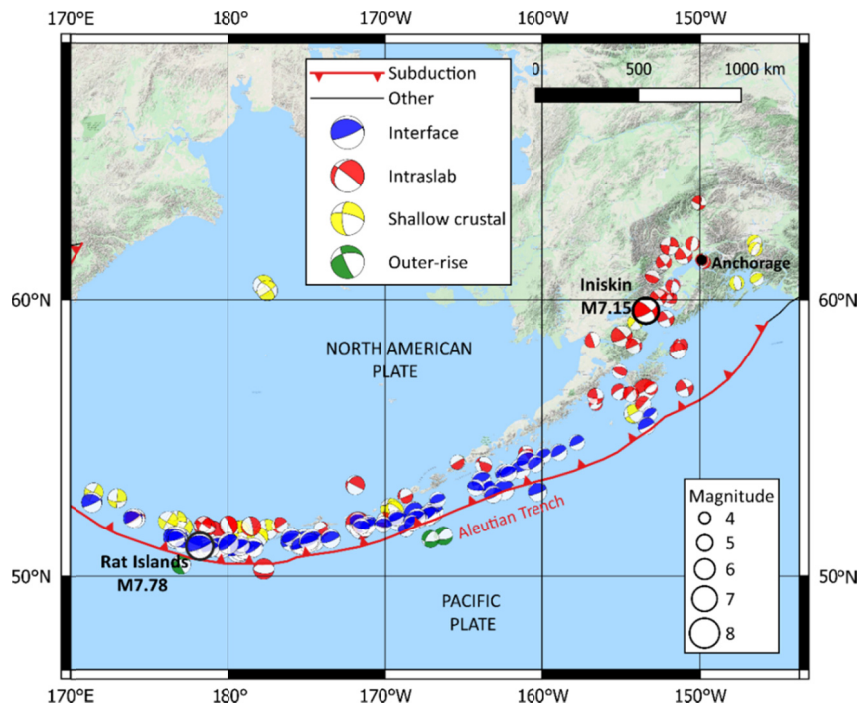


Figure 4.2 Epicentral locations of earthquakes with recordings in Alaska.

Figure 4.3 presents the locations of earthquakes included in the NGA-Sub database in the Cascadia region, with differentiation by magnitude and type of earthquake. Subduction earthquakes are generated in Cascadia by subduction of the east-dipping Juan de Fuca Plate beneath the North American Plate. As shown in Figure 4.3, the plate boundary is approximately 60–140 km west of the coastline in Oregon and Washington. There are three clusters of events. Starting from the south near Eureka, California, a series of shallow crustal and intraslab earthquakes have occurred, with a magnitude range of 4.26–7.22. North of this region, but south of the cluster of events in the Seattle and Vancouver areas, there is a paucity of events; however, two interface events occurred in this region east of Eugene, Oregon, with magnitudes of 4.7 and 4.9. Events in the Seattle–Vancouver regions are intraslab, with magnitudes ranging from 3.3–6.8. The largest event in the NGA-Sub database for Cascadia is the 2001 **M6.8** Nisqually (Washington) earthquake.

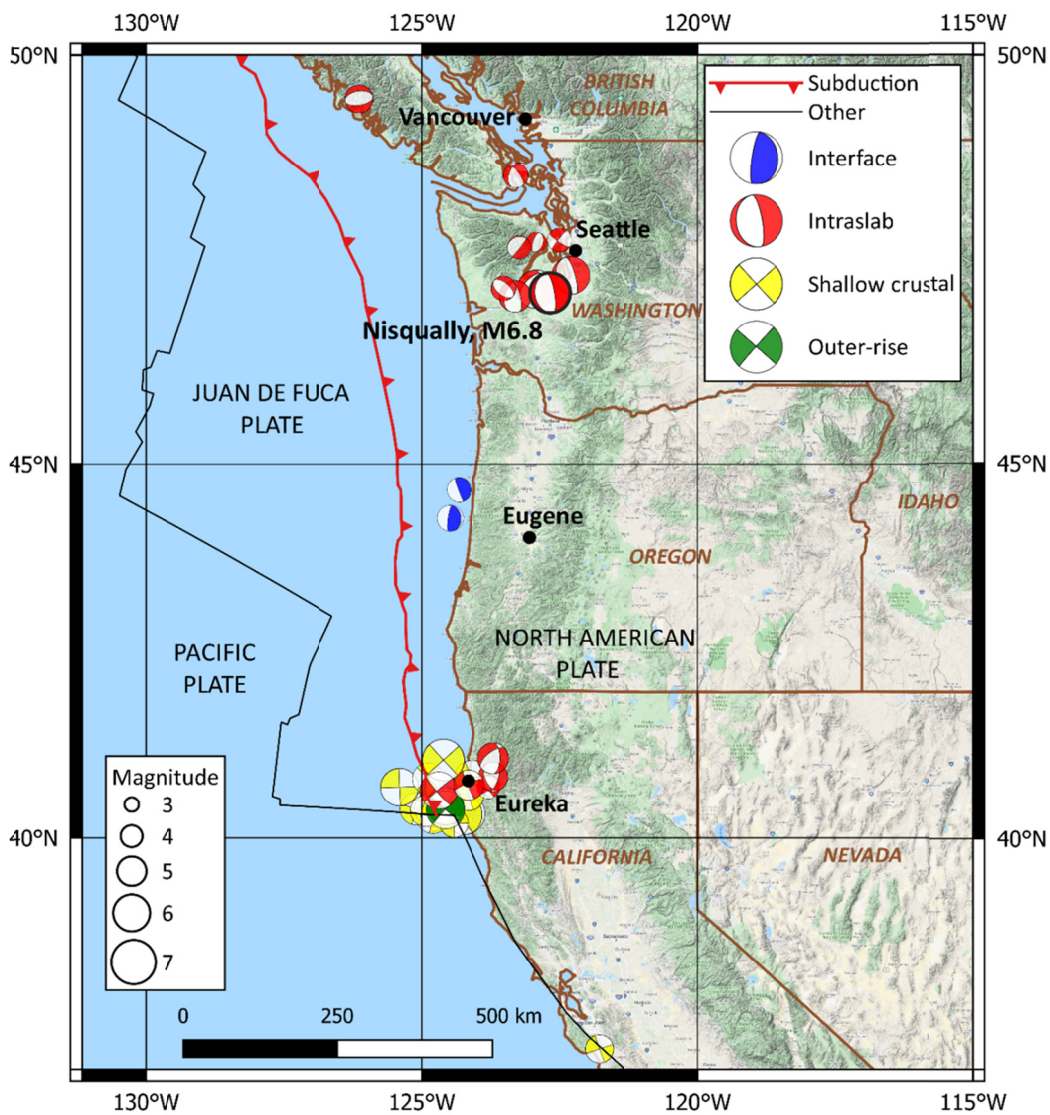


Figure 4.3 Epicentral locations of earthquakes with recordings in Cascadia.

Figure 4.4 presents the locations of earthquakes included in the NGA-Sub database in the Central America and Mexico region, with differentiation by magnitude and type of earthquake. Subduction earthquakes are generated in Central America and Mexico by subduction of the north-east-dipping Cocos Plate beneath the North American Plate, the Caribbean Plate, and the Panama Plate. The small Rivera Plate, north of Cocos, also subducts beneath the North American Plate. As shown in Figure 4.4, the plate boundary is approximately 30–170 km southwest of the coastline. Significant numbers of interface and intraslab events occur throughout this region. The largest interface events are clustered in the northwest sector, including the 1985 **M7.99** Michoacan (Mexico) earthquake. The largest intraslab event included in the NGA-Sub database is the 1999 **M7.46** Oaxaca (Mexico) earthquake. Two relatively recent large events occurred in Mexico in September 2017: the September 8, 2017, **M8.2** offshore Chiapas earthquake and the September 19, 2017, **M7.1** Puebla earthquake. The former is an interface event, whereas the latter is an intraslab event. These earthquakes are not currently part of the NGA-Sub database. Each produced substantial numbers of recordings and will be included in future updates.

Figure 4.5 presents the locations of earthquakes included in the NGA-Sub database in the Japan region, with differentiation by magnitude and type of earthquake. Because of the large number of earthquakes in Japan and the complexity of the tectonics, Figures 4.6 and 4.7 show more detailed views of the northern and southern sectors, respectively. In the north, the northwest-dipping Pacific Plate subducts beneath the Okhotsk Plate (an extension of the North American Plate) at the Japan Trench. To the west, in the Sea of Japan, a convergent plate boundary occurs between the Okhotsk Plate to the east and the Amur plate to the west. Near the middle of the main island (Honshu), the Pacific Plate’s western boundary bends south and east, and the Philippine Sea Plate subducts beneath Japan at the Nankai Trough.

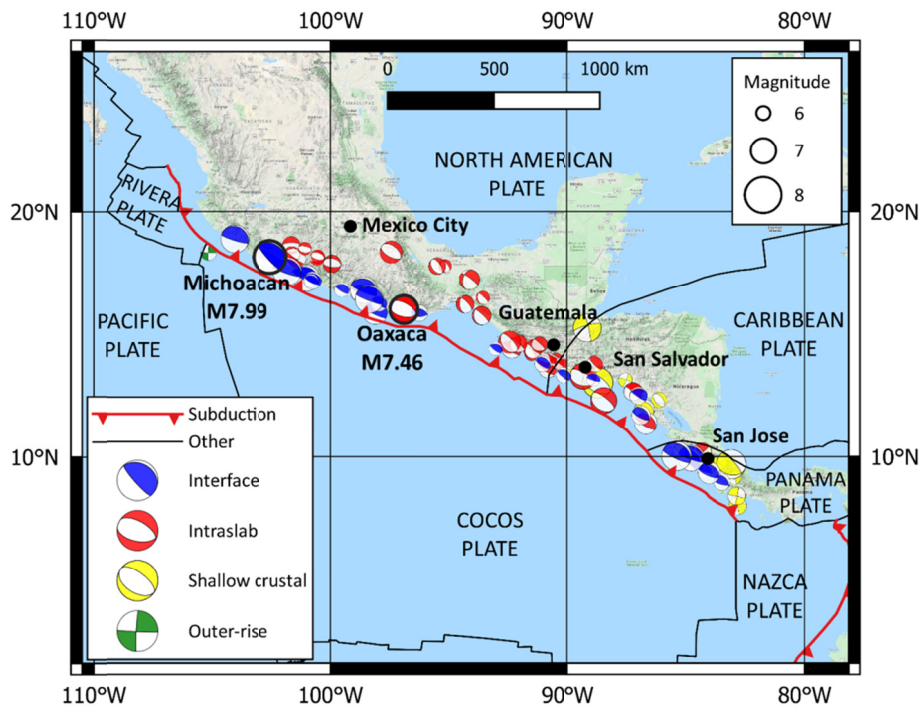


Figure 4.4 Epicentral locations of earthquakes with recordings in Central America and Mexico.

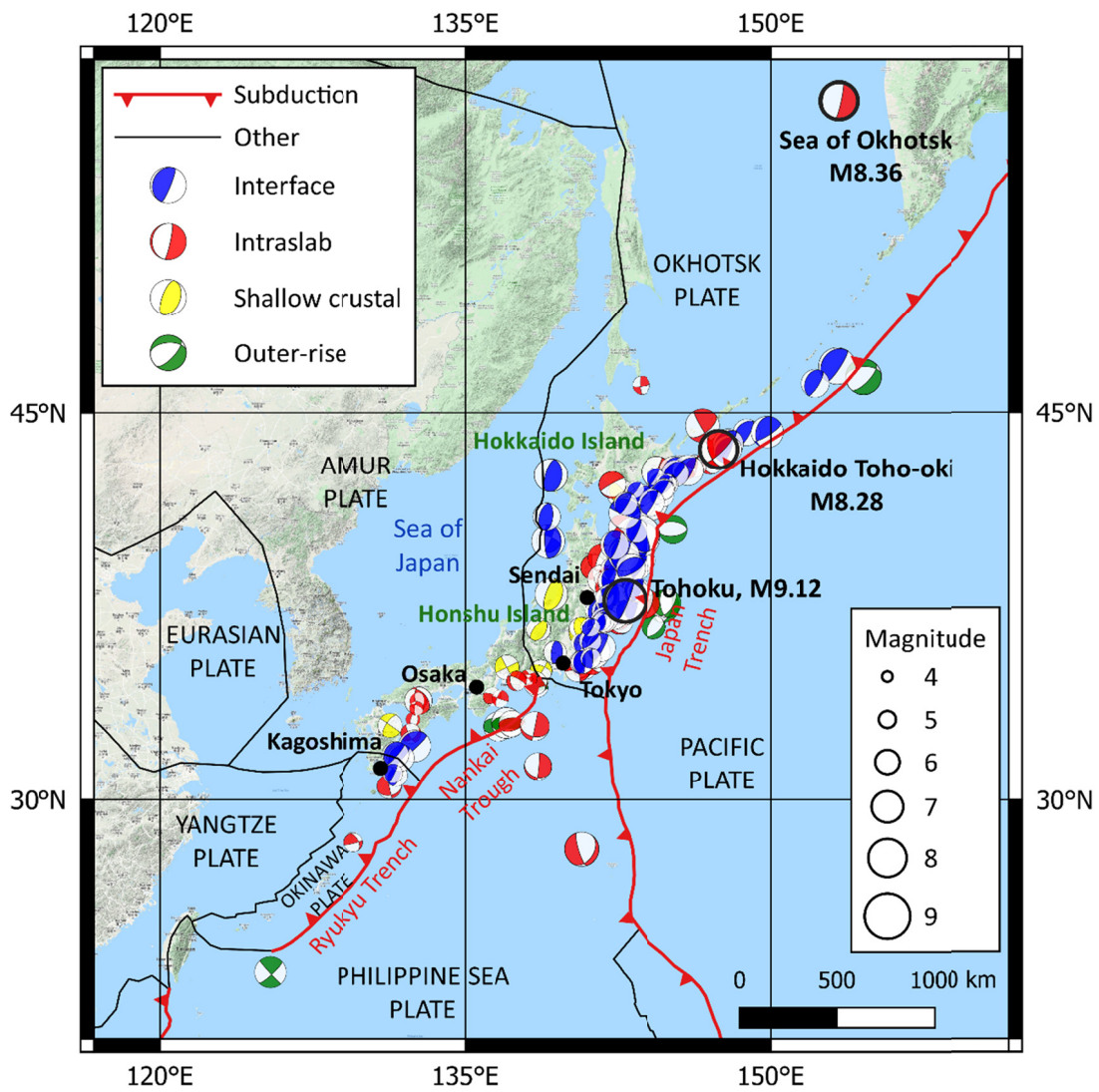


Figure 4.5 Epicentral locations of earthquakes with recordings in Japan.

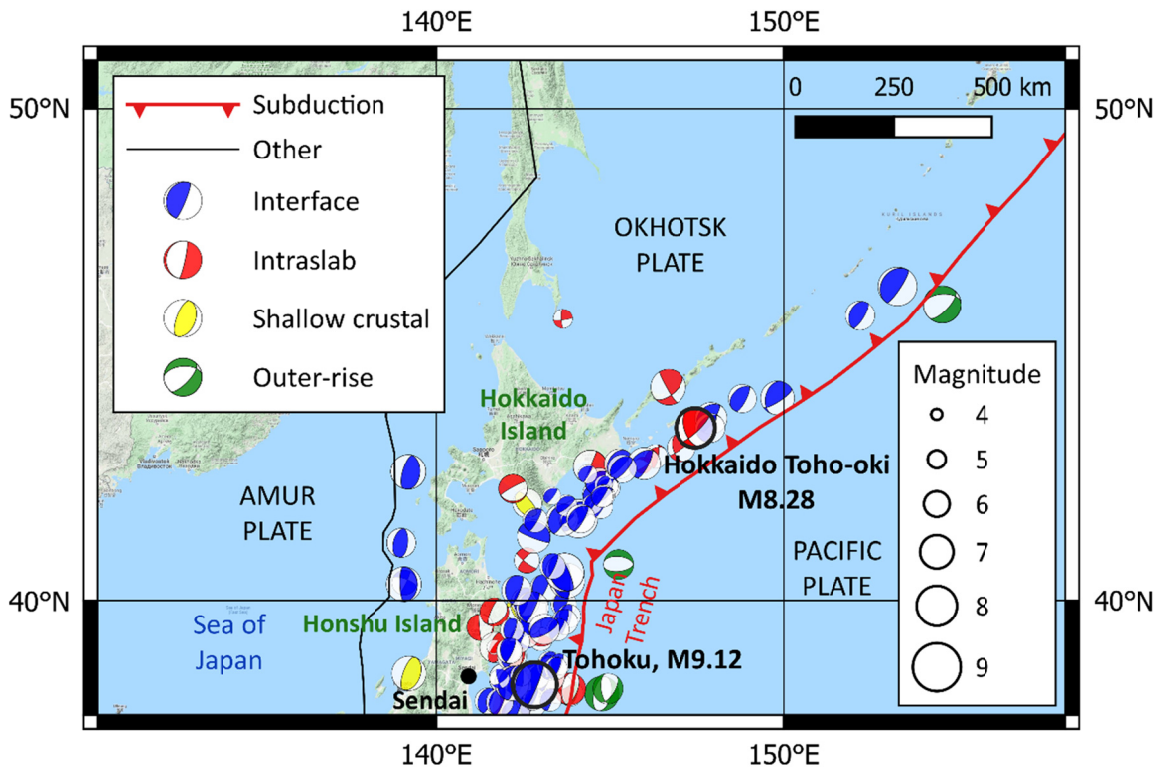


Figure 4.6 Epicentral locations of earthquakes in northern Japan.

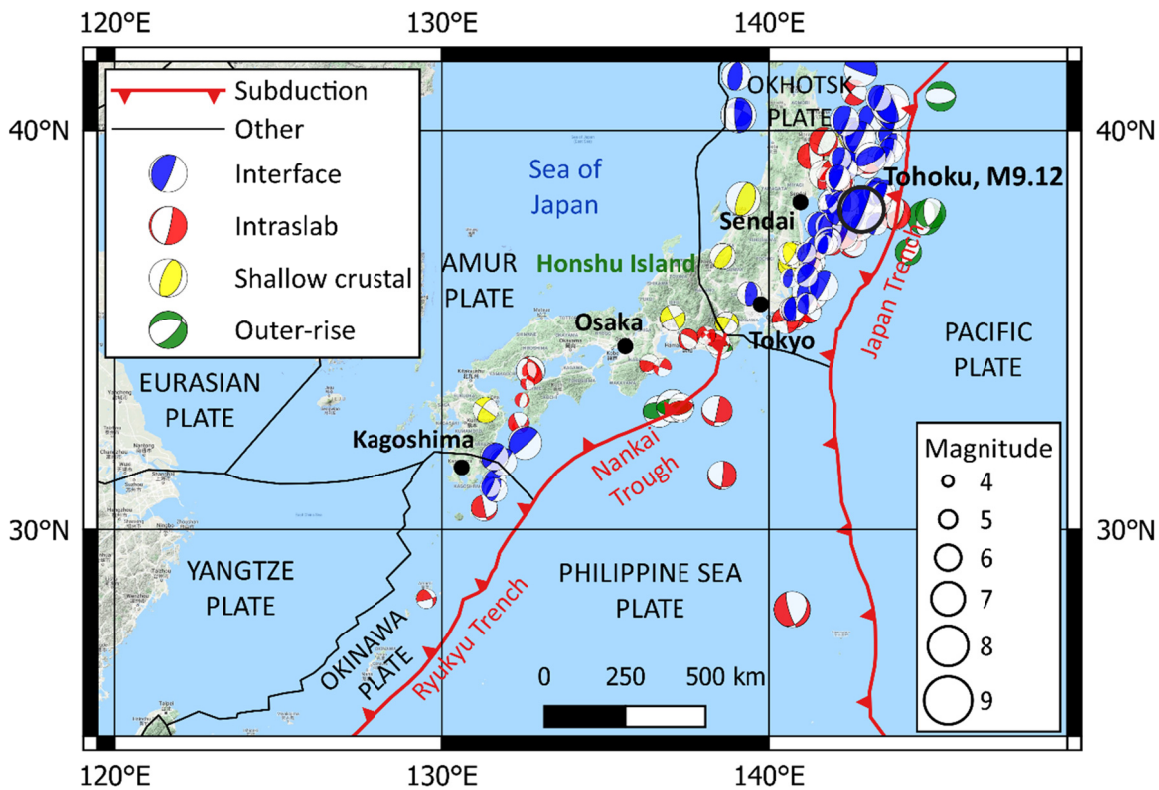


Figure 4.7 Epicentral locations of earthquakes in southern Japan.

Figure 4.8 presents the locations of earthquakes included in the NGA-Sub database in the New Zealand region, with differentiation by magnitude and type of earthquake. The occurrence of subduction earthquakes in New Zealand is associated with its position across the boundary between the Pacific Plate to the southeast and the Australian Plate to the northwest, with the transform Alpine fault passing across the South Island. To the east of the North Island is the Kermadec Trench. The subducting Pacific Plate has produced many intraslab earthquakes in this northern sector. To the west of the southwest end of the South Island is the Puysegur Trench, where the Australian Plate subducts beneath the Pacific Plate. This Fiordland region has primarily produced a series of interface events. The largest interface and intraslab events are the 2009 **M7.81** Fiordland earthquake and the 1988 **M6.69** Te Anau earthquake, respectively; both are located in the South Island of New Zealand.

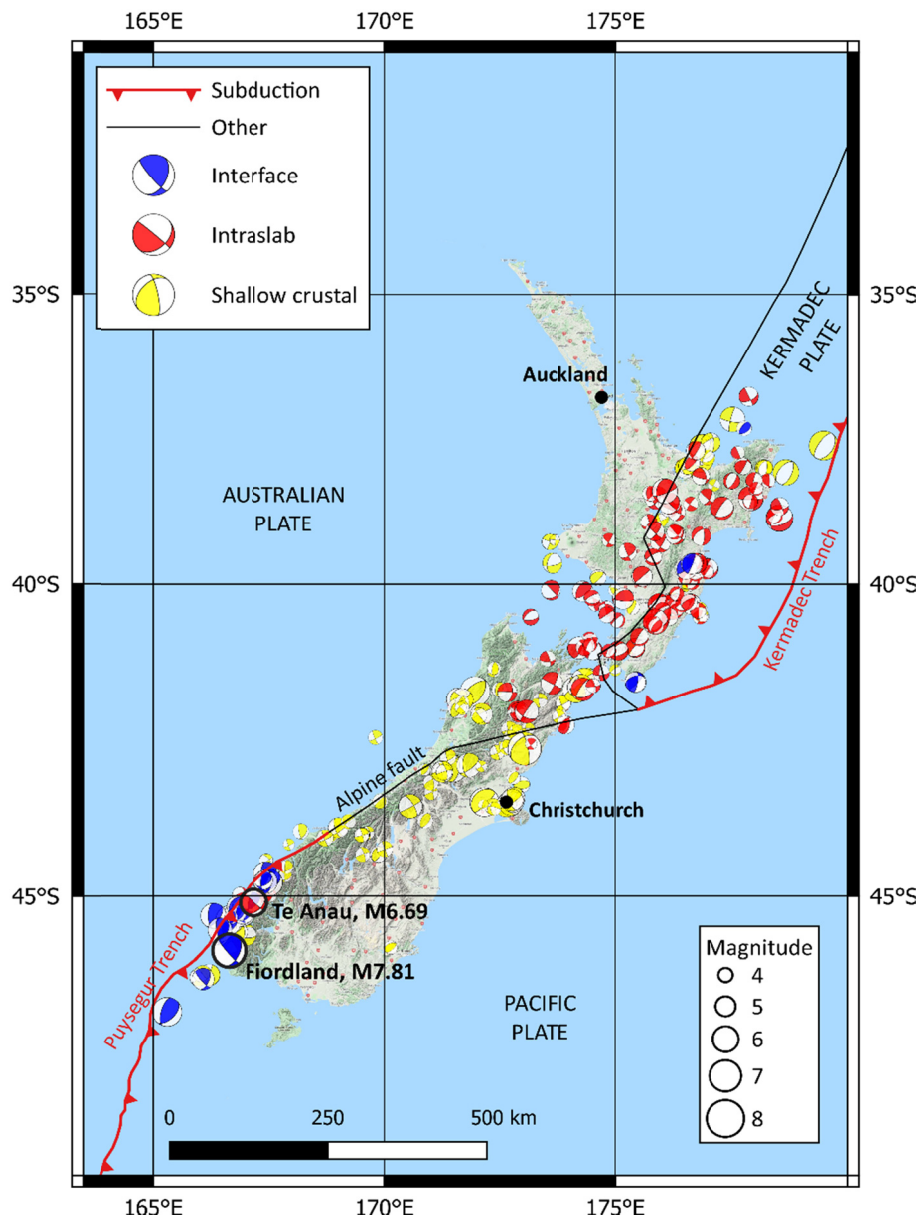


Figure 4.8 Epicentral locations of earthquakes with recordings in New Zealand.

Figure 4.9 presents the locations of earthquakes included in the NGA-Sub database in the South America region, with differentiation by magnitude and type of earthquake. Subduction earthquakes are generated in South America by subduction of the east-dipping Nazca Plate beneath the South American Plate at the Peru-Chile Trench (also called Atacama Trench). As shown in Figure 4.9, the plate boundary is approximately 80–200 km west of the coastline. The database contains many interface events located near the trench, as well as intraslab events located further east beneath the South American Plate. The interface events are most concentrated off the coast of Chile, and include the 1985 **M7.98** Valparaiso and 2010 **M8.81** Maule (Chile) earthquakes. There is a particular concentration of intraslab earthquakes in the north of Chile near Antofagasta, including the 2005 **M7.78** Tarapaca earthquake. Event concentrations are relatively sparse further north in Peru, Ecuador, and Colombia.

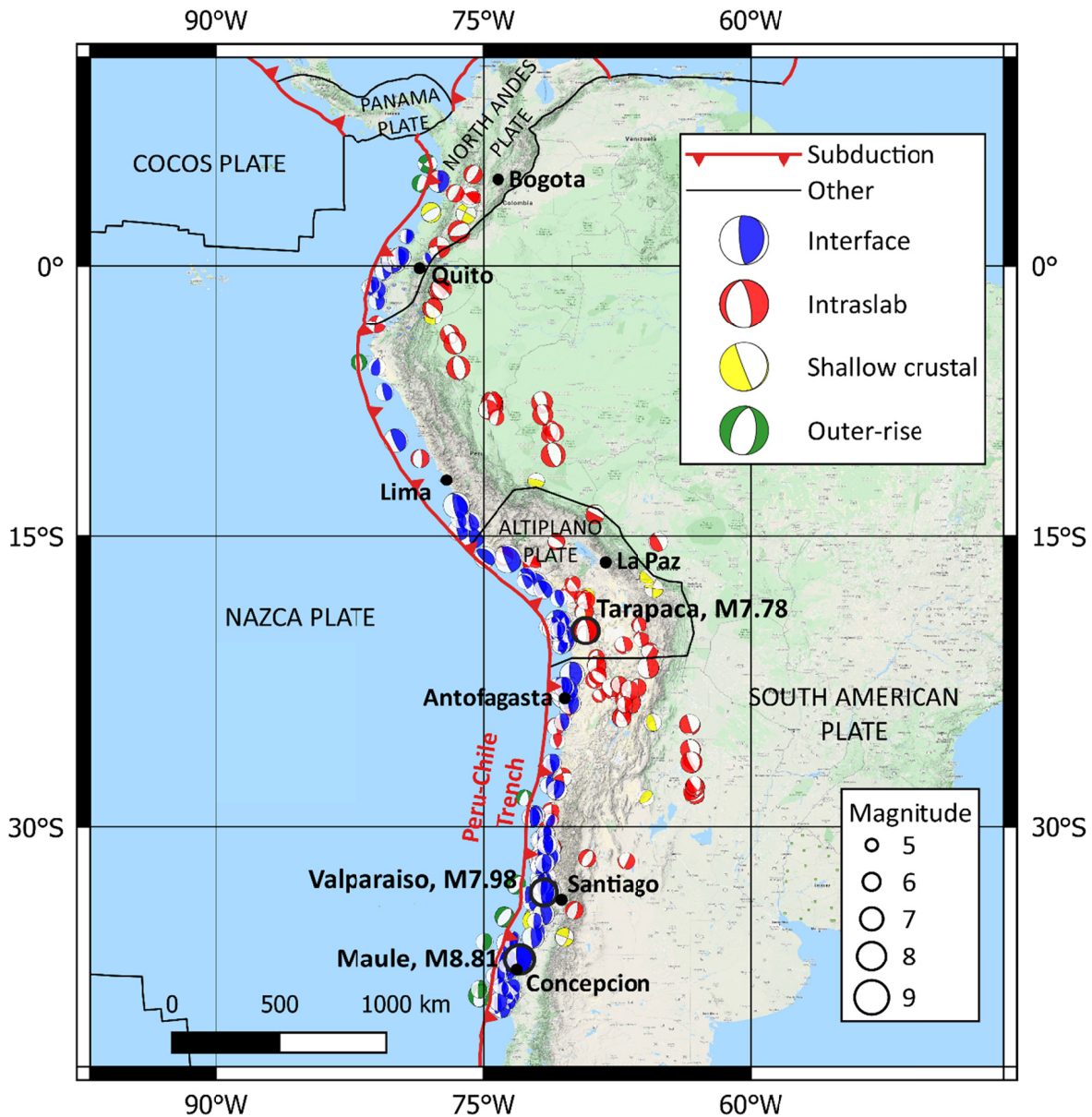


Figure 4.9 Epicentral locations of earthquakes with recordings in South America.

Figure 4.10 presents the locations of earthquakes included in the NGA-Sub database in the Taiwan region, with differentiation by magnitude and type of earthquake. Taiwan occupies a position amidst a complex series of plate boundaries, which give rise to a couple of atypical subduction zones. Because of this complexity, region-specific studies were used to define some of the boundaries shown in Figure 4.10, which do not match the digital global model assembled by Bird [2003]. The predominant boundary is convergent between the northwest-displacing Philippine Sea Plate to the southeast and the Yangtze Plate to the northwest; however, this boundary has not produced earthquakes in the NGA-Sub database (shallow crustal earthquakes have occurred in this region that are in the NGA-West2 database). Rather, the events are clustered near other plate boundaries northeast and south of the island.

Well northeast of Taiwan, the Philippine Sea Plate subducts beneath the Okinawa Plate at the Ryukyu Trench. As that boundary approaches Taiwan from the east, it transitions to a convergent boundary, and the subduction persists. This subduction terminates near the northeastern portion of Taiwan [Wu et al. 2009]. As shown in Figure 4.10, interface subduction events occur immediately north of the convergent boundary, and intraslab events occur beneath much of the southwestern portion of the Okinawa Plate. The largest interface event in Taiwan, the 2002 $M7.12$ Offshore Hualien (Taiwan) earthquake, occurred in this region. The largest intraslab event in this region is the 2004 $M6.59$ earthquake with event ID 7000045.

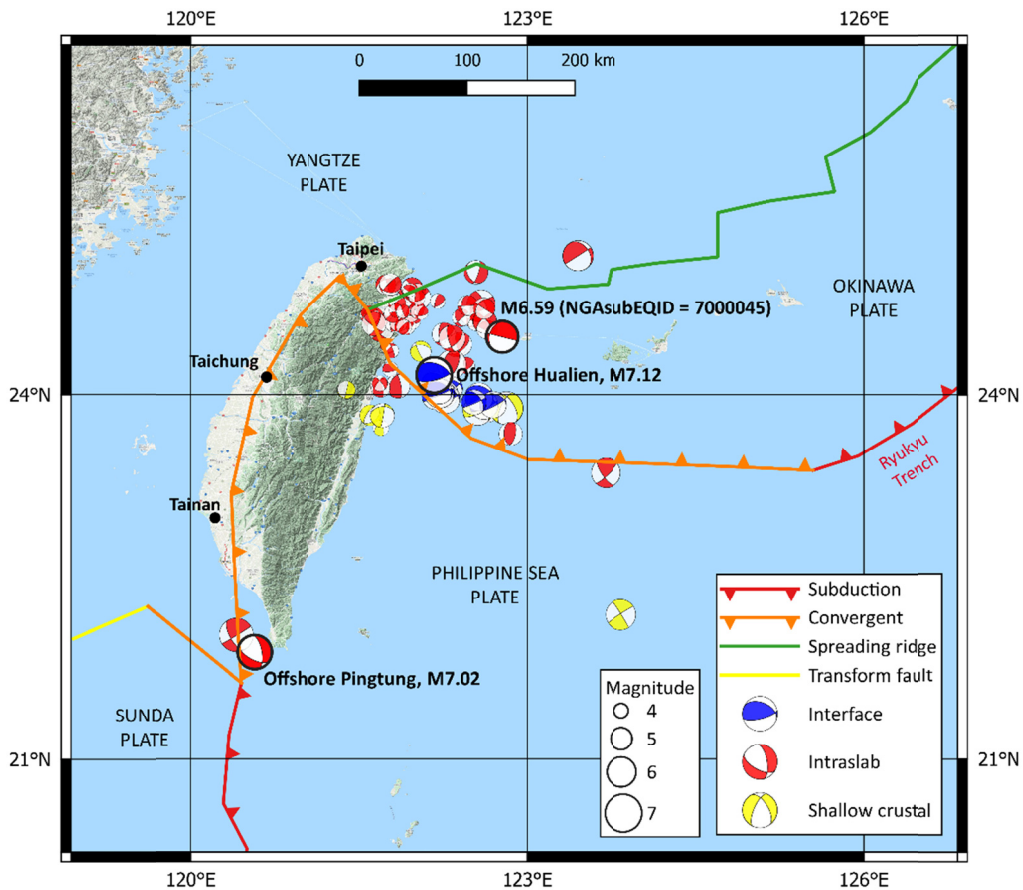


Figure 4.10 Epicentral locations of earthquakes with recordings in Taiwan. The central portion of Taiwan has many shallow crustal earthquakes that are not included in the NGA-Sub database.

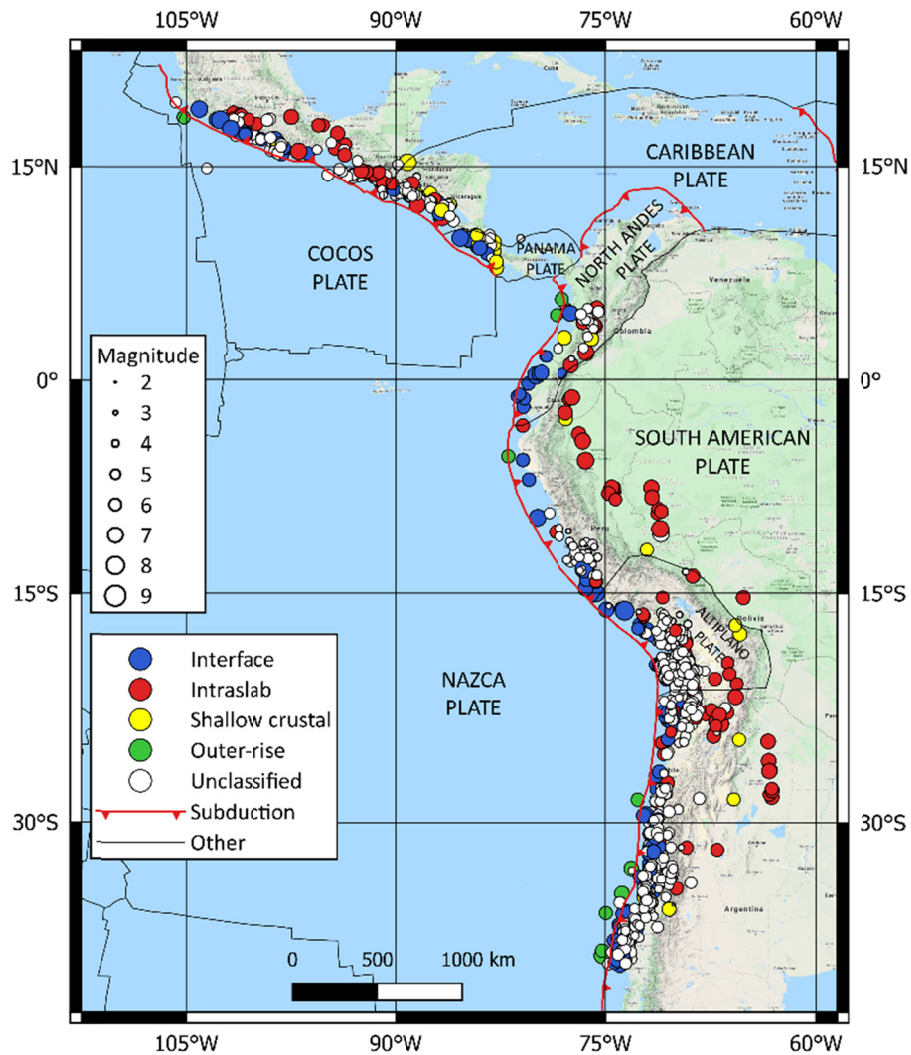


Figure 4.11 Event locations in CAM and SAM showing locations and magnitudes of classified and unclassified events.

In the south, the east-dipping Sunda Plate subducts beneath the Philippine Sea Plate. That boundary evolves into a convergent boundary from south to north, but the subduction continues in the transition between southern Taiwan and north of the Sunda Plate [Malavielle et al. 2002]. The database does not contain interface events in this region, but does include two intraslab events east of the boundary, including the 2006 $M7.02$ Offshore Pingtung (Taiwan) earthquake.

There are a significant number of earthquakes included in the NGA-Sub database for which classification according to event type (interface, intraslab, shallow crustal, or outer-rise) was not performed as part of the NGA-Sub project. As a result of these missing classifications, these events did not go through the quality assurance (QA) procedures described in Section 4.2.1; therefore their source parameters may be less reliable and certain information may be missing. Figure 4.11 shows the regions of South and Central America and Mexico, with locations of both classified and unclassified events (most of the unclassified events are in these regions). As shown in Figure 4.11, the unclassified events have small magnitudes ($M < 6$) and are

in the same general locations as larger events that are included in the NGA-Sub database. The unclassified earthquakes by region consist of:

- 594 events with magnitudes $M < 6$ in South America; most of these earthquakes (61%) have only one or two recordings;
- 181 events with magnitudes $M < 6$ in Central America and Mexico; 41% of these earthquakes have only one or two recordings; and
- Three events with magnitudes $M < 5.2$ in New Zealand.

The lack of event classification and application of QA procedures for these events resulted from allocating limited resources elsewhere during the data compilation and refinement phases of the NGA-Sub project.

4.1.3 Summary of NGA-Sub Events

The total number of events in the source database with an assigned earthquake identification number (NGAsubEQID) is 1880. As discussed in Section 4.2.1, QA procedures eliminated some events, mostly because of missing magnitudes or hypocenter locations, which decreased the number of potentially usable earthquakes to 1782. Further screening to remove events without an assigned event type reduced the number of events to 991.

Figure 4.12 shows the distribution of these 991 events by region. The South America region contributes the largest number of subduction earthquakes, followed by Japan and New Zealand. The events tallied in Figure 4.12 are those in the NGA-Sub database with event-type classifications. For most regions, subduction-type events (interface or intraslab) are dominant; New Zealand is an exception, with 135 shallow crustal and 139 subduction earthquakes.

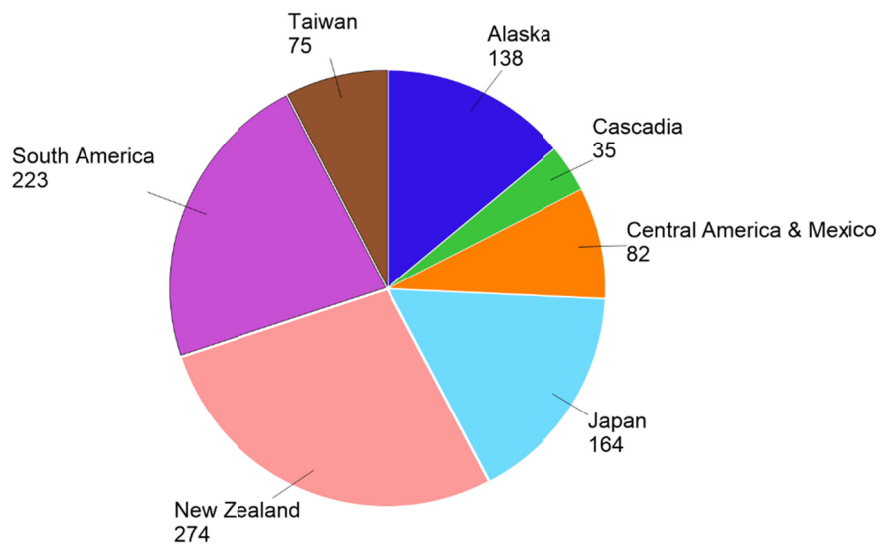


Figure 4.12 Regional distribution of earthquakes with event-type classifications.

Figure 4.13(a) shows the event-type distribution. The dataset is dominated by interface and intraslab earthquakes, which are nearly evenly distributed. There are 221 shallow crustal earthquakes in the database, mostly from New Zealand. While not directly useful for NGA-Sub modeling, these data were retained in the database. The contribution of outer-rise earthquakes is small. Figure 4.13(b) shows the distribution of recordings by event type, which generally mirrors the event distribution. If unclassified events were included in Figure 4.13, they would comprise more than 40% of the events but only 5% of the recordings.

Figure 4.14 presents the magnitude distribution of all earthquakes included in the NGA-Sub database, including those without event-type classifications. Approximately 73% of the events have magnitudes $M \geq 5.0$; the dataset is dominated by mid-size earthquakes with magnitudes between approximately 4.5 and 7.0. There are 13 large events with magnitudes $M \geq 8$; six of these occurred in South America while seven occurred in Japan. Ten of the $M \geq 8$ events are interface and three are intraslab. The majority of the earthquakes with magnitudes $M < 5$ are from South America (~40%) and New Zealand (~30%).

Figure 4.15(a) shows the magnitude distribution of earthquakes differentiated by event type; similarly, Figure 4.15(b) shows the magnitude distribution of recordings. Unclassified events are a significant fraction of the database for $M < 6$, intraslab, and interface events contribute roughly equally for magnitudes between 4.5 and 7; interface events dominate at larger magnitudes.

The time period covered by the source database extends from the late 1930s to 2016. Figure 4.16 presents the cumulative number of earthquakes over time with differentiation by type of earthquake in linear and logarithmic scales. More than 80% of the events in the database occurred after 2000, including the 2010 $M8.81$ Maule (Chile) earthquake and the 2011 $M9.12$ Tohoku (Japan) earthquake. Relatively recent large earthquakes include the 2015 $M7.89$ Chichishima (Japan) earthquake, the 2015 $M8.31$ Illapel (Chile) earthquake, the 2016 $M7.82$ Ecuador earthquake, and the 2016 $M7.85$ Kaikoura (New Zealand) earthquake.

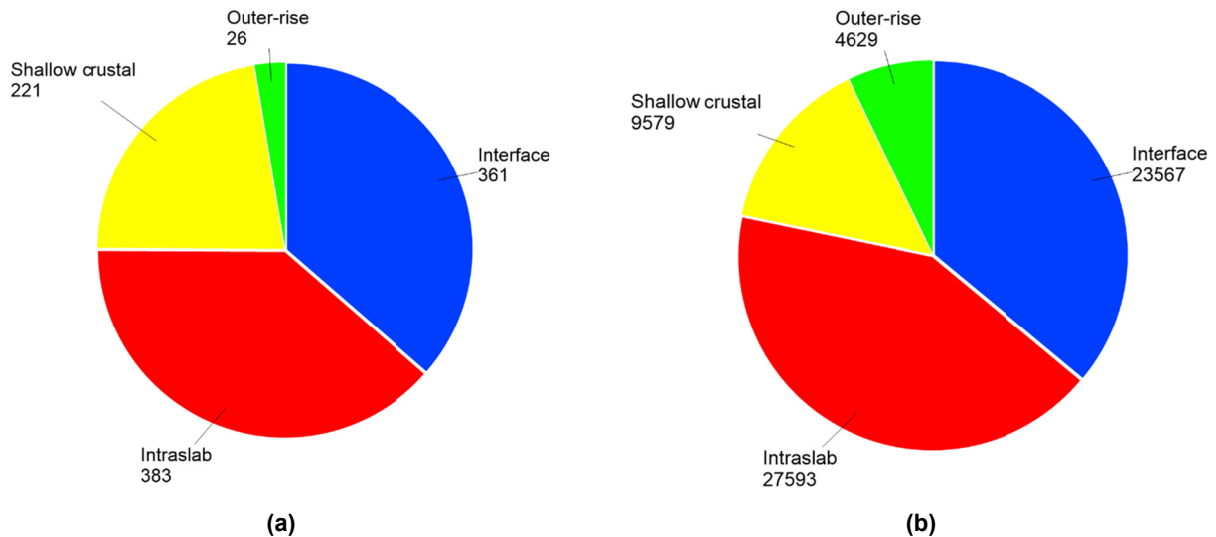


Figure 4.13 (a) Distribution of the events by type of earthquake; and (b) distribution of the recordings by type of earthquake.

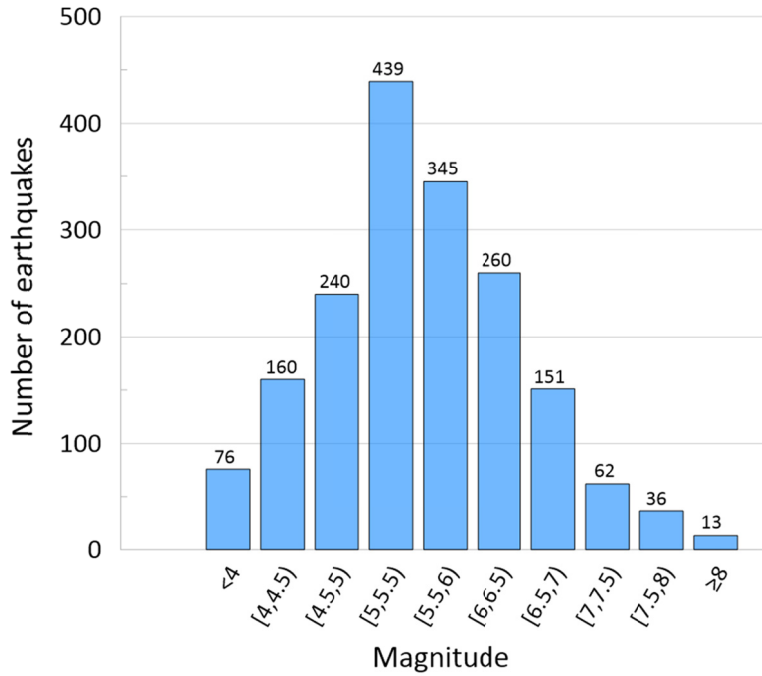


Figure 4.14 Magnitude distribution of the earthquakes.

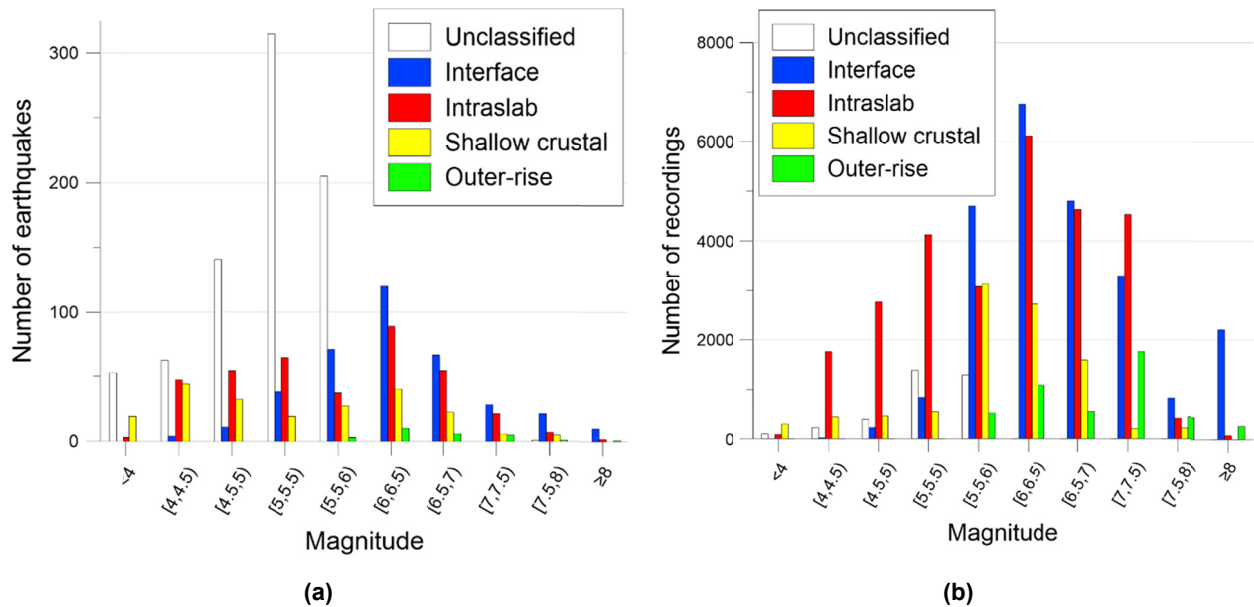


Figure 4.15 (a) Magnitude distribution of the events by type of earthquake; and (b) magnitude distribution of the recordings by type of earthquake.

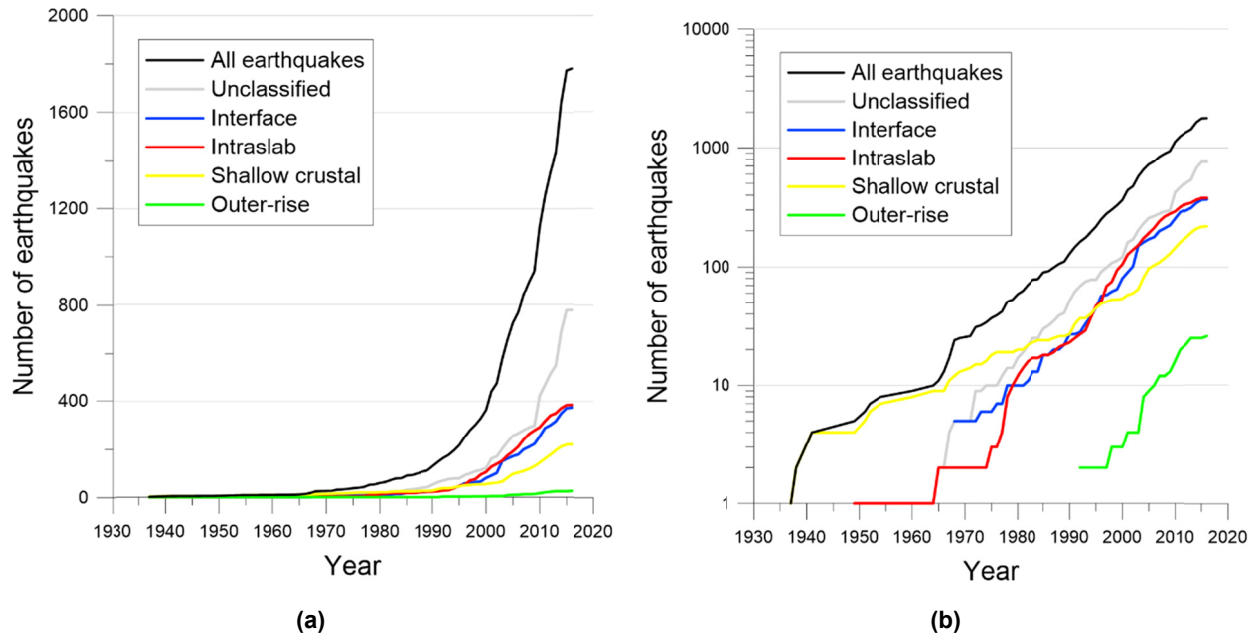


Figure 4.16 Cumulative number of events over time by type of earthquake using (a) linear and (b) logarithmic scales.

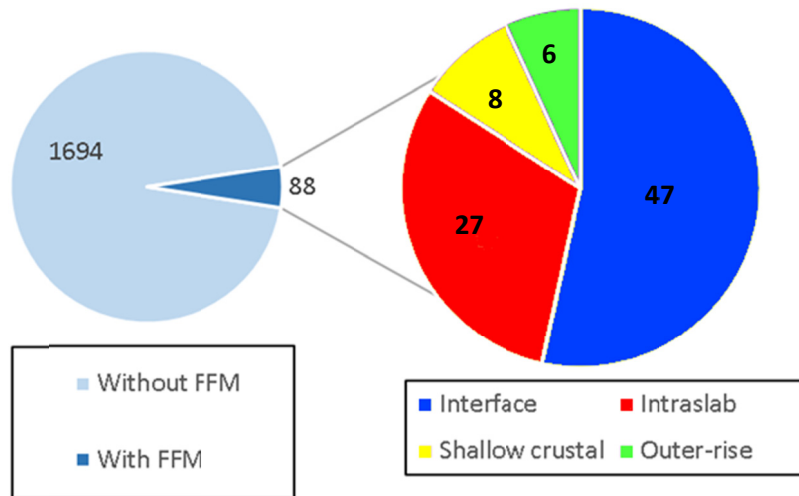


Figure 4.17 Distributions of events with FFMs in the NGA-Sub database.

Finite-fault models (FFMs) based on seismological inversions reported in literature have been compiled as part of the NGA-Sub project. More than 80 events have published FFMs that have been incorporated into the database. While only 8% of the total number of events, these events comprise 35% of the ground-motion recordings. Figure 4.17 summarizes the distribution of FFMs by event type. Section 4.3 describes the methods applied to select and interpret FFMs.

Parameters descriptive of style-of-faulting (or fault type) are compiled independently of event type. For example, intraslab earthquakes can commonly have normal or strike-slip fault types. In NGA-Sub, fault type is defined based on rake angle, as described in Section 4.2. Figure 4.18 shows the distribution of NGA-Sub events with respect to rake and dip angles. Interface events (blue squares) are mostly associated with reverse faulting ($60^\circ < \text{rake} < 120^\circ$) and with reverse-oblique faulting ($30^\circ < \text{rake} < 60^\circ$ and $120^\circ < \text{rake} < 150^\circ$), whereas intraslab events (red circles) have different faulting styles. Furthermore, most of the interface events have dip angles lower than 30° , which is consistent with the geometry of the subducting plates; intraslab events dip in different directions. There are two apparently misclassified events that have been assigned as “low confidence” events (Section 4.2.2d), one with dip of 79° and rake -152° (Event 4000017), the other with dip of 33° and rake of 5° (Event 4000013).

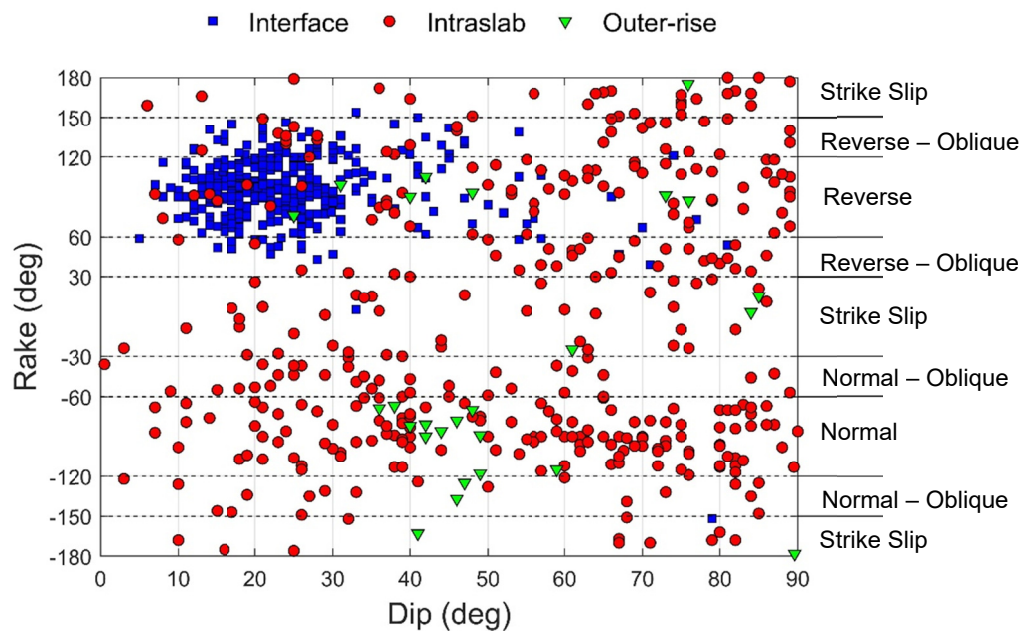


Figure 4.18 Rake and dip angles for interface and intraslab events in the NGA-Sub database.

4.2 GENERAL EARTHQUAKE CATALOG

4.2.1 Parameter Definitions

The source-related parameters that were collected from different sources or derived for the NGA-Sub database are date, origin time, moment magnitude (M), hypocenter location (latitude, longitude, and focal depth), and the following features regarding source geometry and type of earthquake, as illustrated in Figure 4.19:

- Location of the fault-rupture plane (upper left corner when viewed from hanging wall) and number of segments;
- Fault-rupture plane dimensions: length (L), width (W), and area (A);

- Strike (ϕ), dip (δ), and rake (λ) angles;
- Depth to top of the fault-rupture plane (Z_{TOR});
- Fault type as either strike-slip, normal, reverse, reverse-oblique, or normal-oblique, as inferred from rake angle; and
- Earthquake type as either interface, intraslab, shallow-crustal, or outer-rise.

The geometric parameters in the first two bullets define a single rectangular fault surface, which is sufficient to define the geometry of the ruptured fault in most cases. The FFMs for some large earthquakes are described by multiple, connected rectangles (e.g., Maule, Chile).

Whenever possible, the geometric and slip-direction parameters listed above are taken from published FFMs, as described in Section 4.3. When FFMs are not available, which is the case for most events, simulation procedures described in Section 4.4 are used to approximate finite-fault geometric parameters and associated computations of closest distance for ground-motion stations.

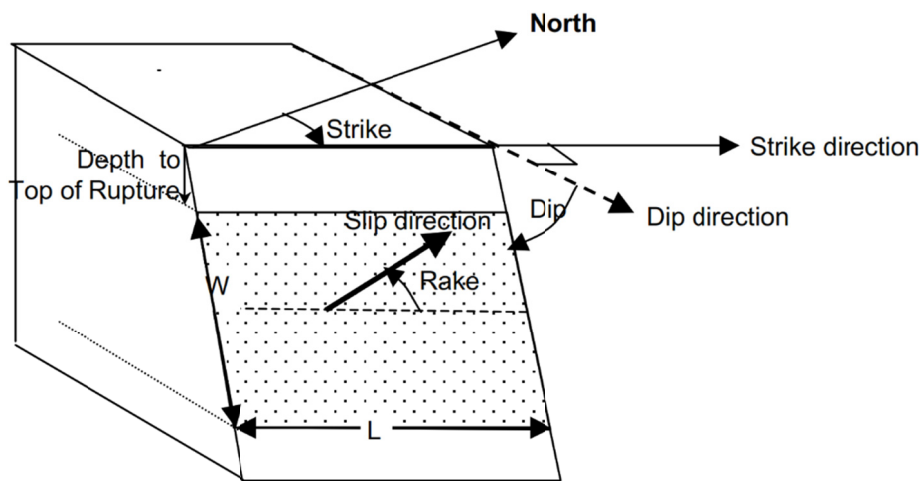


Figure 4.19 Schematic representation of the fault-rupture plane [Ancheta et al. 2013]. Convention of fault strike, dip, and rake follows that described in Aki and Richards [1980].

4.2.2 Parameter Selection Procedures

To the extent possible, we applied uniform procedures to define the source parameters listed in Section 4.2.1. Those procedures are described here for the case of magnitude, hypocenter location, fault type, and event type. The development of finite-fault parameters—and the associated computation of distances to ground-motion stations—is addressed in Sections 4.3–4.4. Table 4.1 lists source parameters for the 18 events highlighted in the regional maps discussed in Section 4.1.2. Source parameters for all events are provided in the EventHypo table in the NGA-Sub database.

(a) Magnitude

Moment magnitude is the magnitude scale used in NGA projects, including NGA-Sub. Whenever possible, moment magnitude is computed from seismic moment, M_0 [Hanks and Kanamori 1977] as:

$$\mathbf{M} = \frac{2}{3} \log M_0 - 10.7 \quad (4.1)$$

Seismic moment (M_0) and/or hypocenter location was collected from the following agencies:

- The Global Centroid Moment Tensor (CMT, Ekström et al. [2012])
- The National Earthquake Information Center (NEIC) at the United States Geological Survey (USGS)
- The Lamont-Doherty Cooperative Seismographic Network (LD) at Columbia University
- The International Seismological Centre [ISC 2019]; a “groomed” version of the ISC catalogue was produced by Engdahl et al. [1998], and is referred to as the EHB catalogue
- The Duputel et al. W phase catalog (DUPUTEL) [Duputel et al. 2012] at the University of Strasbourg
- In Alaska, the Alaska Earthquake Center (AEC), housed at the University of Alaska Fairbanks
- In Cascadia, the Pacific Northwest Seismic Network (PNSN), housed at the University of Washington, and Natural Resources Canada (NRCAN)
- In northern California, the Northern California Earthquake Data Center (NCEDC), housed at UC Berkeley
- In Chile, the Chilean National Seismological Center (CSN), also referred as GUC (Department of Geophysics at the University of Chile)
- In Taiwan, the National Center for Research on Earthquake Engineering (NCREE) and the Broadband Array in Taiwan for Seismology (BATS)
- In Japan, the National Research Institute for Earth Science and Disaster Resilience (NIED) and the Japan Meteorological Agency (JMA)

Seismic moments from the CMT catalog were preferred when available, which was the case for most events. Other catalogs were used when CMT estimates of M_0 were not available; Table 4.2 lists the catalogs considered by region in order of preference for the selected M_0 . For eight earthquakes in Japan with FFMs and ten earthquakes in Cascadia, the seismic moment was taken from specific studies published in the literature; see Section 4.3 for details.

Table 4.1 Example events from NGA-Sub database (highlighted in maps in Figures 4.2–4.11), showing compiled source parameters.

Region	NGA-sub EQID	Earthquake name, Country/State	Date	M	Hypocenter location			Event-Type flag ¹	FFM flag ²	No. of segments	L (km)	W (km)	Z _{tor} (km)	Strike (deg)	Dip (deg)	Rake (deg)	Source-review flag ³	# recs.
					Latitude (deg)	Longitude (deg)	Depth (km)											
ALK	1000002	Rat Islands, Alaska	2003/11/17	7.78	51.1965	178.1844	29.7262	0	1	1	120	140.4	5.61	280.4	18.8	121.9	0	6
	1000142	Iniskin, Alaska	2016/1/24	7.15	59.6531	-153.4457	129.4159	1	1	1	30	28	108.62	60	66	33	0	191
CAS	2000004	Nisqually, Washington	2001/2/28	6.8	47.1574	-122.6801	53.1749	1	1	1	24	21	46.13	350	70	-91	0	147
	2000009	1815881, Oregon	2004/7/12	4.9	44.2977	-124.4869	12.82	0	0	1	3.6	3.6	12.279	353	16	75	0	92
	2000011	1852721, Oregon	2004/8/19	4.7	44.6677	-124.3201	18.09	0	0	1	2.7	2.8	17.908	349	7	99	0	76
CAM	3000271	Michoacan, Mexico	1985/9/19	7.99	18.1814	-102.5691	16.2637	0	1	1	150	139	6	300	14	72	0	26
	3000201	Oaxaca, Mexico	1999/9/30	7.46	16.054	-96.907	40	1	0	1	69.9	32.3	32.582	300	49	-78	0	8
JPN	4000001	Tohoku, Japan	2011/3/11	9.12	38.1165	142.823	17.4965	0	1	3	482	186	8.65	200	12	88	0	1293
	4000219	Sea of Okhotsk, Russia	2013/5/24	8.36	54.8172	153.3558	608.1717	1	1	1	195	70	601	184	10	-98	0	48
	4000093	Hokkaido Tohu-oki, Japan	1994/10/4	8.28	43.711	147.457	27.459	1	1	1	60	70	18.1	160	40	30	0	30
NZL	5000179	Fiordland, New Zealand	2009/7/15	7.81	-45.8339	166.6363	20.9	0	1	1	100.23	100.23	8.76	27	33	154	-999	27
	5000013	Te Anau, New Zealand	1988/6/3	6.69	-45.1	167.17	60	1	0	1	25	55	32.57	310	86	118	-999	3
SAM	6000149	Maule, Chile	2010/2/27	8.81	-36.2089	-72.9587	30.4055	0	1	1	480	160	0.74	15	18	109.3	2	49
	6000323	Valparaiso, Chile	1985/3/3	7.98	-33.125	-71.61	40	0	1	2	222	135	6.4	5	20.4	97.2	0	27
	6000061	Tarapaca, Chile	2005/6/13	7.78	-20.03	-69.28	110	1	1	1	47.5	45	101.21	187	23	-73	0	30
TWN	7000044	Offshore Hualien, Taiwan	2002/3/31	7.12	24.1602	122.172	33	0	1	1	33	32	21.34	292	32	121	0	426
	7000048	Offshore Pingtung, Taiwan	2006/12/26	7.02	21.88703	120.56844	44.1	1	1	1	89.9	35	24.13	349	53	-54	0	458
	7000045	7418598, Taiwan	2004/10/15	6.59	24.470833	122.777833	88.02	1	0	1	18.7	23.5	84.756	200	17	6	0	439

¹ Intra/Inter flag' is defined in section 4.2.2d and refers to the event-type (interface, intraslab, shallow crustal, outer-rise).

² 'FFM flag' indicates if the event has an available FFM in the database as described in Section 4.3 (0 = event without FFM, 1 = event with FFM).

³ Source review flag' is defined in Section 4.6 and refers to the QA procedure applied to review the source parameters of each event.

The seismic moment is not available for some events. This is most frequently the case for older events (pre-1976 when the CMT catalog began) and events of small magnitude. In the NGA-Sub source database, 96% of $M > 6$ events and 79% of $M < 6$ events are based on seismic moment (considering only earthquakes with an event-type classification). For those events without a reported M_0 value, linear relationships between different magnitude scales were utilized to estimate M . Alternate magnitude scales used in these relationships include local magnitude (M_L), surface-wave magnitudes (M_S), and body-wave magnitude (m_b).

Table 4.2 Earthquake catalogs and published studies used to assign seismic moment.

Region	Catalog	No. of events
Alaska	CMT	128
	ISC	7
	NEIC	2
	IDC	1
Cascadia	Adopted from NGA-West2	13
	NEIC	6
	CMT	3
	Ichinose et al. [2006b]	3
	Oppenheimer et al. [1993]	3
	NRCAN	2
	Williams et al. [2011]	2
	PNSN	1
	Ichinose et al. [2004]	1
Ichinose et al. [2006*]	1	
Central America and Mexico	CMT	79
	NEIC	1
Japan	CMT	142
	NIED	10
	LD	1
	Abe [1975]	1
	Hatanaka & Takeo [1989]	1
	Kanamori [1971]	1
	Kikuchi & Fukao [1987]	1
	Shiba & Uetake [2011]	1
	Takeo & Mikami [1990]	1
	Yagi et al. [1998]	1
	Yoshioka & Abe [1976]	1
	South America	CMT
Taiwan	CMT	34
	NIED/BATS	15
	BATS	8
	DUPUTEL	4
	NEIC	3
	LD	1

For Chilean earthquakes, alternate magnitude scales were obtained from the CSN. We applied an adjusted version of the relations developed by Bastías and Montalva [2016] for M_L and by Leyton et al. [2009] for M_S and m_b . These relations, shown in the following equations and presented in Figures 4.20 and 4.21, were developed using only information from Chilean earthquakes. These correlations were developed for M_W whereas we use \mathbf{M} ; accordingly, we increase intercept terms by 0.033.

$$Z_{hyp} < 50 \text{ km} : \mathbf{M} = 0.915M_L + 0.524 \quad (\sigma = 0.26) \quad (4.2)^*$$

$$Z_{hyp} > 50 \text{ km} : \mathbf{M} = 0.847M_L + 0.727 \quad (\sigma = 0.25) \quad (4.3)^*$$

$$\mathbf{M} = 0.887M_S + 1.095 \quad (4.4)^{**}$$

$$\mathbf{M} = 1.173m_b - 0.634 \quad (4.5)^{**}$$

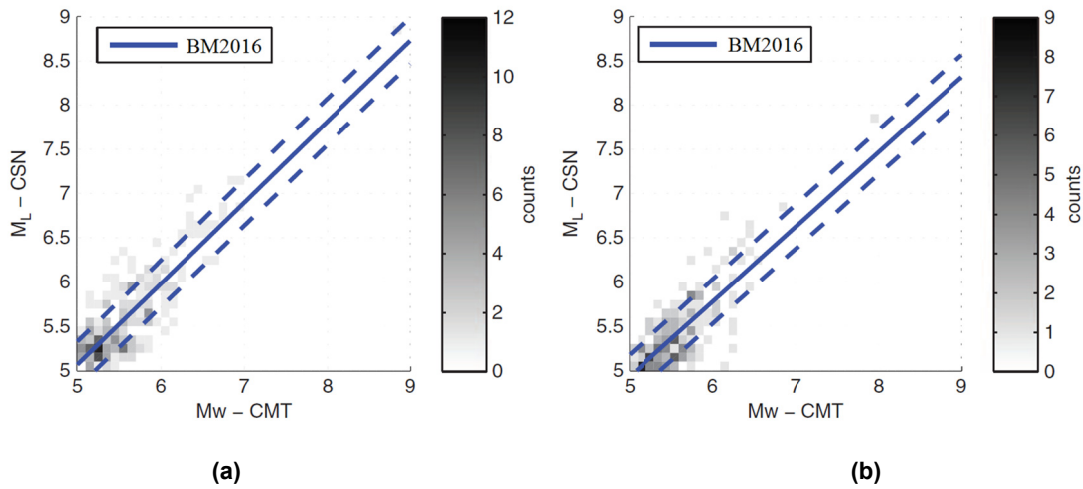


Figure 4.20 M_W - M_L relationships from Bastías and Montalva [2016]: (a) Equation (4.1) for shallow-focus earthquakes ($H \leq 50$ km); and (b) Equation (4.2) for deep-focus earthquakes ($H > 50$ km). We use a slightly modified form of the relation (shifted up 0.033 to reflect \mathbf{M}).

* Modified from Bastías and Montalva [2016].

** Modified from Leyton et al. [2009].

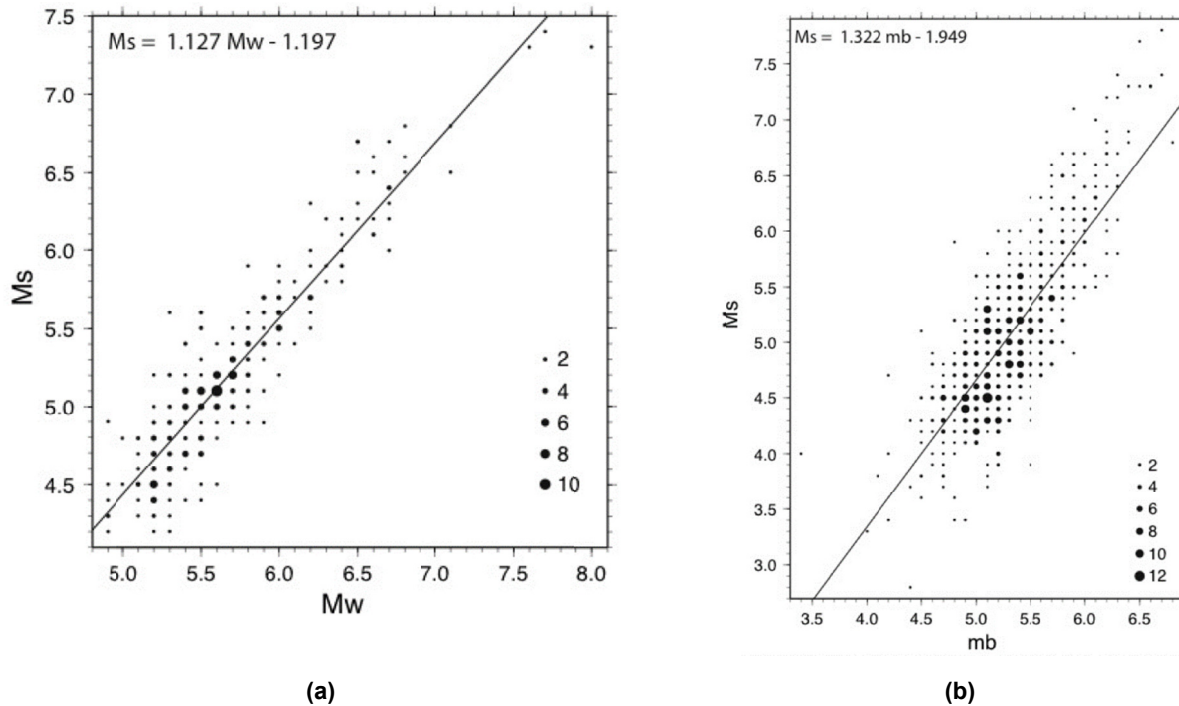


Figure 4.21 M_S - M_W and M_S - m_b relations from Leyton et al. [2009]: (a) Equation (4.3); and (b) original M_S - m_b relation reported by the authors. We use a slightly modified form of the M_S - m_b relation (shifted up 0.033 to reflect M).

For New Zealand events, we adopted source tables from Van Houtte et al. [2017]. These tables include seismic moment; therefore, conversions from other magnitude scales are not required. For other regions, the following procedures were applied to estimate moment magnitudes:

1. **M** is derived from other magnitude types either by taking the magnitude estimate as-is or by using relationships between **M** and other magnitude scales. In order of preference, the selection criterion uses M_S , then M_L , then m_b ; these preferences are intended to minimize the potential for saturation bias (i.e., to use the scale that tracks **M** over the widest possible range). M_S has the least saturation because it is derived from 20-sec period surface waves. M_L is derived from the peak of horizontal displacements from broadband sensors (which are controlled by lower periods). m_b is based on 1-sec P -waves and generally is measured from the vertical component;
2. **Alaska**: Eight events that occurred in 2001, 2002, 2003, and 2014 lack seismic moments. These events collectively have only 14 recordings. For these events, **M** is taken as M_S , m_b , and M_L for 6, 1, and 1 event, respectively;
3. **Cascadia**: No events lack seismic moment;
4. **Central America and Mexico**: Two events lack seismic moment. **M** is taken as M_w from NEIC for one event, and **M** is taken as M_S for the other event;
5. **Japan**: A set of 25 earthquakes prior to 1974 lack seismic moment. Due to various problems with the recordings from these events, the source database does not include

information for these events. In addition, two aftershocks of the 2003 Tokachi-oki earthquake (events 4000199 and 4000200) lack seismic moment because they occurred just after the large magnitude event; for event 4000199 we take \mathbf{M} as M_L and for event 4000200 we take \mathbf{M} as M_S ;

6. **South America:** Ten events lack seismic moment. \mathbf{M} is taken as M_w from CSN for four events, \mathbf{M} – M_L relations [Equations (4.2) and (4.3)] are applied to four events, and the \mathbf{M} – M_S relation [Equation (4.4)] is applied to two events; and
7. **Taiwan:** 10 events prior to 2000 lack seismic moments, mostly because in this period the Broadband Array in Taiwan for Seismology (BATS) did not routinely compute M_0 for events with magnitudes < 6.2 . These events have produced 928 records. For these events, \mathbf{M} is taken as m_b , and M_L for 8 and 2 events, respectively.

(b) Hypocenter location

Hypocenter locations incorporated into selected FFM were used when available; in most cases the hypocenter is on the ruptured fault plane. In some cases, the hypocenter documented in the FFM paper is not on the fault plane. In those cases, the hypocenter was projected on to the fault-rupture plane (the projection was made in the direction orthogonal to the plane).

When FFMs were not available, which is the case for most events, hypocenter locations were obtained from the different catalogues listed in Section 4.2.2(a). The preferred catalogues for location assignments differed from those used for magnitudes. Table 4.3 lists catalogues in the order of preference for each region. For New Zealand, this information is provided in Van Houtte et al. [2017] and is not shown in Table 4.3.

Table 4.3 Earthquake catalogs and published studies used to assign hypocenter locations.

Region											
Alaska		Cascadia		Central America and Mexico		Japan		South America		Taiwan	
Catalogue	No. of events	Catalogue	No. of events	Catalogue	No. of events	Catalogue	No. of events	Catalogue	No. of events	Catalogue	No. of events
CMT	117	Adopted from NGA-West2	13	EHB	56	JMA	115	CSN	107	NCREE	75
ISC	10	ISC	12	ISC	23	JMA / Bai et al. [2014]*	16	EHB	69		
NEIC	8	Oppenheimer et al. [1993]	3	CMT	1	NEIC	5	ISC	31		
IDC	2	Williams et al. [2011]	2	Mendoza and Hartzell [1989]	1	ISC	2	NEIC	3		
AEC	1	NRCAN	2	Mendoza [1993]	1	CMT	2	Delouis et al. [2010]	1		
		PNSN	1			SEVO [1996]	2	Lay et al. [2010]	1		
		Ichinose et al. [2004]	1			NIED	1	Melgar et al. [2016]	1		
		Ichinose et al. [2006(a)]	1			JMA / EIC [2003]	1	Lay et al. [2014]	1		
						JMA / Ref. 135.1	1	Shao and Ji (n.d.)	1		
						Yagi [2004]	2	Sladen [2007]	1		
						Shiba and Uetake [2011]	1	Mendoza et al. [1994]	1		
						Yagi et al. [1998]	1	Hayes [2016]	1		
						Nagai et al. [2001]	1	Kuge et al. [2010]	1		
						Abe [1975]	1	Lay et al. [2014]	1		
						Takeo and Mikami [1990]	1	Schurr et al. [2012]	1		
						Namegaya and Tsuji [2005]	1	Salichon et al. [2003]	1		
						Yamanaka and Kikuchi [2004]	1				
						Tsuchida et al. [1983]	1				
						Takiguchi et al. [2011]	1				
						Fukuyama and Irikura [1986]	1				
						Tanioka et al. [1995]	1				
						Nakayama and Takeo [1997]	1				
						Koketsu et al. [2004]	1				
						Atkinson and Macias [2009]	1				
						Yamanaka [2005]	1				
						JMA [2012(b)]	1				
						JMA [2012(c)]	1				

* for aftershocks of the 2011 Tohoku earthquake.

(c) Fault type

The style of faulting was defined based on the rake angle as shown in Table 4.4. The rake angle was compiled for all events with moment tensor solutions from earthquake catalogs; see Tables 4.2 and 4.3. When a rake angle is provided with a FFM (Section 4.3), it is preferred to values from catalogs.

Table 4.4 Fault mechanism based on rake angle (after Ancheta et al. [2013]).

Fault mechanism	Flag	Range of rake angle (°)
Strike-slip	0	$-180 < \lambda < -150$ $-30 < \lambda < 30$ $150 < \lambda < 180$
Normal	1	$-120 < \lambda < -60$
Reverse	2	$60 < \lambda < 120$
Reverse-oblique	3	$30 < \lambda < 60$ $120 < \lambda < 150$
Normal-oblique	4	$-150 < \lambda < -120$ $-60 < \lambda < -30$
Unknown	-999	Unknown

(d) Event type

When event type (interface, intraslab, shallow crustal, and outer-rise) is defined in literature (typically the same documents that have FFMs), we adopted the event-type classification from those prior studies. For events without a prior event-type classification, we applied an automated process to identify earthquake type. This process considers the location of the hypocenter relative to the depth of the surface of the subducting (typically oceanic) plate as defined by Hayes et al. [2012]. Also considered is the event focal mechanism. Exceptions to the use of these automated procedures are Taiwan and New Zealand; in Taiwan we used event-type classifications from NCREE, and for New Zealand we used event-type classifications from Van Houtte et al. [2017].

Figure 4.22 shows an example for Event 6000055 in Chile that illustrates the procedure. The blue solid line is the geometry of the top surface of the subducting Nazca plate and the dashed lines represent the estimated error of the Hayes et al. [2012] model (± 10 km). Three regions are defined:

- Region A: depth to top of subducting plate, using the mean representation, is < 10 km;
- Region B: $10 \text{ km} \leq \text{depth to top of subducting plate} \leq Z_{BC}$; and
- Region C: depth to top of subducting plate $> Z_{BC}$.

Depth Z_{BC} is the mean depth to the top of subducting slab at the maximum depth of interface earthquakes and is region-dependent (50 km in ALK and CAM, 55 km in JPN and SAM; Hayes

et al. [2012]; Tichelaar and Ruff [1993]). Depth Z_{BC} defines the boundary between Zones B and C.

These three regions and the plate boundary are used to define several zones as follows:

- Shallow depths, above the shallowest interpretation of the subducting plate depth (mean – standard deviation depth), or 20 km in region B, or 30 km in region C, whichever is shallower. Marked in green and taken as *shallow crustal*;
- Region B, below the shallowest interpretation of the subducting plate depth or 20 km, whichever is shallower, and above 60 km. Marked in light blue and taken as *interface*;
- Region C, below the shallowest interpretation of the subducting plate depth, as well as depths > 60 km in Regions A-B. Marked in gray and taken as *intraslab*;
- Region A, depths < 60 km. Marked in yellow and taken as *outer rise*; and
- Region C, below 30 km and above 60 km. It taken as *undetermined*.

For Event 6000055 in Figure 4.22, the location is in Zone 2 and the event type is classified as *interface*.

Following these assignments, event types are checked using moment tensor solutions. Interface earthquakes should have a reverse mechanism. If an event near the interface is not reverse, we assign a shallow crustal designation. Intraslab earthquakes are typically normal or strike slip. Event type is reported in the source database using flags as defined in Table 4.5. Low-confidence flags are assigned when (1) nodal planes are not available to check event-type assignments; (2) event locations are near the boundaries between regions; and (3) moment tensors are incompatible with the region (e.g., normal faulting in an interface region). Procedures similar to these have been described previously by Poblete [2008] and Contreras [2009].

Table 4.5 Flags in source database that indicate event-type classification.

Event-type classification	Flag
Interface	0
Intraslab	1
Shallow crustal / overriding intraplate	2
Outer-rise	4
Intraslab, specially lower double seismic zone	5
Outer-rise event with lower confidence	-444
Shallow crustal / overriding events with lower confidence	-666
Intraslab events with lower confidence	-777
Interface events with lower confidence	-888
Unknown	-999

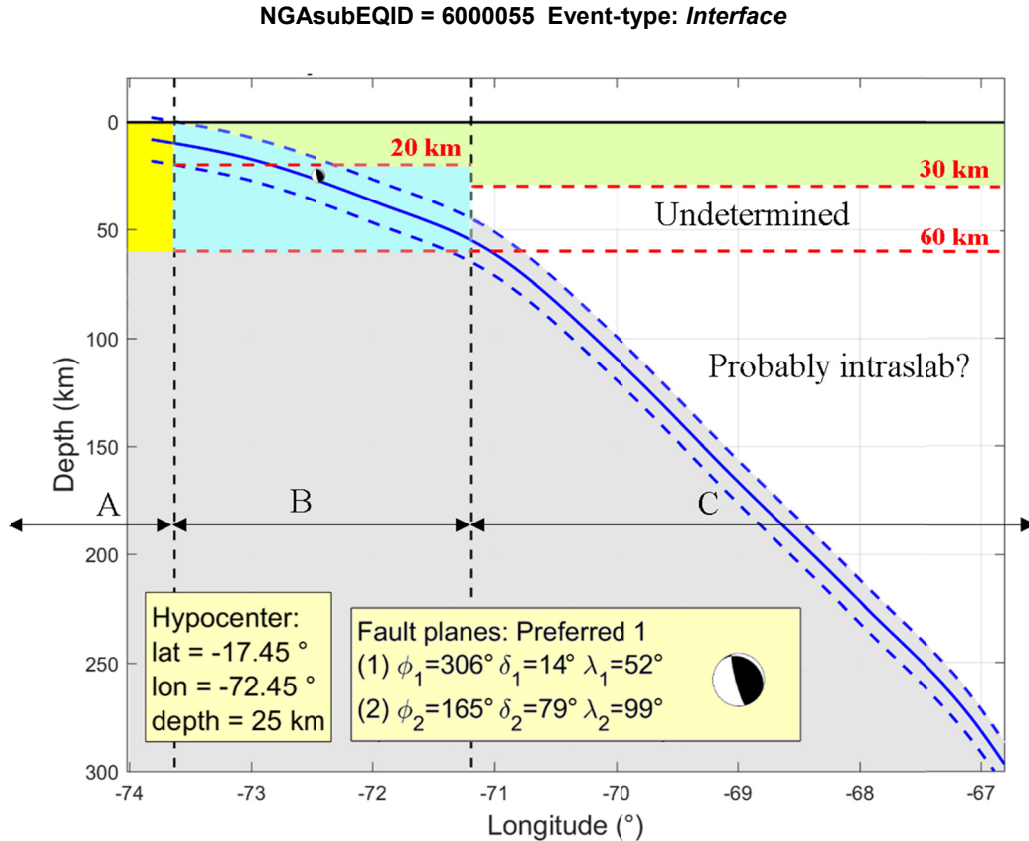


Figure 4.22 Event-type classification scheme based on hypocenter location relative to the top of the surface of the subducting plate. Example event is NGASubEQID 6000055, which is defined as interface.

4.3 SOURCE PARAMETERS FOR EVENTS WITH FINITE-FAULT MODELS

Some of the parameters compiled for the NGA-Sub source database describe attributes of one or more rectangles, which represent the approximate surface over which fault slip occurred in a given event. The principle need for these parameters is for the calculation of distances measured from a recording site to a fault surface, including rupture distance R_{rup} (the closest distance to the fault surface) and Joyner-Boore distance R_{JB} (the closest distance to the surface projection of a fault). While not used in NGA-Sub GMMs, other applications include defining parameters used to derive hanging wall effects and rupture directivity effects for dipping faults.

The parameters listed in Section 4.2.1 that are derived from FFMs include location of the plane's upper left corner as viewed from the hanging wall (geodetic coordinates and depth), plane dimensions, and rake angle. This section describes how FFMs from the literature were identified and (in most cases) modified for application in NGA-Sub. Section 4.4 describes how these parameters were derived for earthquakes without FFMs.

Information derived from FFMs is contained in the *FFmodel* table in the NGA-Sub database. In the case of events for which the FFM includes more than one segment, information on specific planes within the model are contained in the *FFmodelmultiseg* table. For those

events, the finite fault parameters in the *FFmodel* table are for a single planar representation of the full model (needed for when single values of L and W are required for modeling purposes, e.g., for studies of directivity).

4.3.1 Finite-Fault Models Collected

We identified FFMs mainly by reviewing compilations of past studies in the literature presented at the following websites:

- SRCMOD website [Mai and Thingbaijam 2014], available at <http://equake-rc.info/SRCMOD/> (last accessed November 2019);
- Source Models of Large Earthquakes, Caltech Tectonic Observatory, available at http://www.tectonics.caltech.edu/slip_history/index.html (last accessed November 2019); and
- Rupture processes of global large earthquakes ($M > 7$), UC Santa Barbara, available at http://www.geol.ucsb.edu/faculty/ji/big_earthquakes/home.html (last accessed November 2019).

We also performed independent literature searches for the largest magnitude events (2010 $M8.81$ Maule, Chile, and 2011 $M9.12$ Tohoku, Japan) and other recent, large events, some of which occurred contemporaneously with the data compilation for NGA-Sub (e.g., the 2001 $M8.41$ Arequipa earthquake in Southern Peru and the 2007 $M7.75$ Tocopilla, 2014 $M8.15$ Iquique, and 2015 $M8.31$ Illapel earthquakes in Chile).

Table 4.6 lists the FFMs used in NGA-Sub for 88 earthquakes. For some earthquakes, more than one FFM is available in the literature; Section 4.3.2 describes how a preferred model was selected in these cases. In many cases, the fault dimensions in the literature were trimmed to develop the values shown in Table 4.6; Section 4.3.3 presents the procedures used to perform this trimming. Section 4.3.4 discusses special considerations related to multi-segment models.

Table 4.6 FFM s selected for use in NGA-Sub database.

NGA Sub EQID	Date	Earthquake name, Country/State	M	FFM reference	Hypocenter location ¹			Nodal plane ²			Slip ³ (cm)		Rupture dimensions		Upper-left corner			Event Class. Flag ⁴			
					Lat. (°)	Lon. (°)	Depth (km)	ϕ (°)	δ (°)	λ (°)	M	T	L (km)	W (km)	Lat. (°)	Lon. (°)	Z _{TOR} (km)				
Japan (JPN) – 63 events																					
4000001	3/11/2011	Tohoku, Japan	9.12	Yokota et al. [2011]	38.1165	142.823	17.4965	200	5	88	3500	NO	482	63	39.5163	144.4071	8.65	0			
								12								482	62		39.7144	143.7911	13.9
								20								482	61		39.9103	143.1683	26.4
4000219	5/24/2013	Okhotsk, Russia	8.36	Ye et al. [2013]	54.8172	153.3558	608.1717	184	10	-98	990	220	195	70	55.4265	154.0676	601	1			
4000222	11/15/2006	Kuril Doublet1	8.33	Ammon et al. [2008]	46.592	153.266	11	215	15	92	700	NO	310	130	48.1243	155.5177	0	0			
4000068	9/25/2003	Tokachi-oki	8.29	Koketsu et al. [2004]	41.7796	144.0786	25.0101	230	20	90	706	NO	120	100	42.1796	144.8114	23.3	0			
4000093	10/4/1994	Hokkaido Toho-oki	8.28	Tanioka et al. [1995]	43.711	147.457	27.459	160	40	30	1680	NO	60	70	43.8256	147.5468	18.1	1			
4000095	5/16/1968	Tokachi-oki	8.26	Nagai et al. [2001]	40.6184	143.6866	7.851	156	20	90	929	NO	200	80	41.6671	143.1441	5.58	0			
4000223	1/13/2007	Kuril Doublet2	8.13	Ammon et al. [2008]	46.229	154.5457	20.6325	43	59	-115	1400	200	235	55	45.6304	153.5358	0	4			
4000010	3/11/2011	IbarakiOff	7.92	JMA [2011]	36.1037	141.2473	32.3653	200	29	90	488	NO	90	90	36.2174	141.8235	7.8	0			
4000220	5/30/2015	Chichi-shima	7.89	JMA [2015]	27.8713	140.7021	627.5655	32	25	-44	656	98	36	40	27.8226	140.3958	617	1			
4000094	12/28/1994	Sanriku-ho	7.76	Nakayama & Takeo [1997]	40.4365	143.7558	10.6174	180	6	90	495	74	100	80	40.9315	144.05	8	0			
								16								90	10		40.9315	143.1	16.36
								30								90	80		40.9315	142.9734	19.45
4000091	7/12/1993	Hokkaido_sw	7.74	Mendoza & Fukuyama [1996]	42.7814	139.2002	20.015	20	29.8	100	436	NO	110	70	42.355	138.6511	5	0			
							340										80		70	41.4618	138.9642
4000097	5/26/1983	Middle.Japan.Sea	7.74	Fukuyama & Irikura [1986]	40.3583	139.0708	8.0782	15	20	90	758	NO	30	30	40.2998	138.9469	5	0			
							350										60		30	40.5607	139.0387
4000096	6/12/1978	Miyagi-oki	7.65	Yamanaka & Kikuchi [2004]	38.1496	142.1672	36.9798	200	20	95	211	NO	80	70	38.6003	142.4336	35.28	0			
4000173	6/16/1964	Niigata	7.65	Shiba & Uetake [2011]	38.3672	139.2182	24.7595	200	60	90	880	NO	84	24	38.6882	139.5023	5.7	2			
4000092	1/15/1993	Kushiro-oki	7.59	Ide & Takeo [1996] Nozu [2007]	42.8903	144.4208	107.1658	256	0.5	-36	800	NO	60	40	42.748	144.6072	107	1			
4000108	4/1/1968	Hyuganada	7.57	Yagi et al. [1998]	32.2798	132.5302	14.9961	227	12	90	403	60	63	63	32.2729	132.8647	10.32	0			
4000074	9/5/2004	Ki_se	7.41	Yagi [2004]	33.235	137.0304	12.6998	85	40	90	390	110	108	21.3	33.242	136.3208	7.1	-444			
4000009	3/11/2011	Iwate_off	7.40	JMA [2011]	39.8339	142.6992	32.0373	187	10	74	346	NO	45	50	40.0155	142.9985	28	0			
4000132	6/17/1973	Nemuro-oki	7.40	Nomegaya & Tsuji [2005]	42.9571	145.9611	33.4149	230	27	111	120	NO	90	100	42.8375	146.9804	1	0			
4000069	9/25/2003	Tokachiokiaft	7.37	Atkinson & Macias [2009]	41.7534	143.6114	44.8185	208	18	86	N/A	N/A	60	24	41.9021	143.7943	43	0			
4000002	3/9/2011	Tohoku foreshock	7.36	JMA [2011]	38.301	143.221	18.0334	187	11	75	222	78	70	70	38.7201	143.5146	14.2	0			
4000102	10/9/1994	Hokkaido.Eastoff.as	7.28	Ye et al. [2016]	43.9124	147.9175	33.2881	227	19	104.6	270	50	50	50	43.936	148.3136	26.5	0			
4000054	12/7/2012	Miyagi-oki	7.23	JMA [2012]	38.0216	143.8381	21.0373	174	61	82	908	136	24	24	37.9492	144.1553	41	-777			
								188	44	-100					75	40	38.2722		144.0363	8.2	
4000073	9/5/2004	Ki_se	7.23	Yagi [2004]	33.0904	136.619	18.4711	280	42	105	510	150	54	30	32.9064	136.9093	4.6	-444			
4000078	8/16/2005	Miyagi-Eq	7.22	Yamanaka [2005]	38.1438	142.2324	39.5357	198	25	76	90	30	25	20	38.2335	142.3349	37	0			
4000035	4/7/2011	Miyagi_Pre.Off	7.15	JMA [2011]	38.253	141.9645	66.4296	24	37	87	250	51	45	35	38.1898	141.6554	50	1			
4000111	6/12/1968	Iwate-oki	7.11	Yoshioka & Abe [1976]	39.3549	143.0977	29.0773	241	30	90	N/A	N/A	80	30	39.4374	143.8059	16.7	0			
4000167	8/9/2009	TokaidoSouth	7.09	ERI [2009]	33.1017	138.4143	334.2059	105	25	-176	140	40	50	30	33.2104	138.0448	332.9	1			
4000042	7/10/2011	Sanrikuoki	7.03	JMA [2011]	38.0338	143.51	34.3521	67	74	7	117	NO	100	30	37.9547	143.1135	14.8	-777			

¹ Hypocenter location is not necessarily exactly the same as in the FFM. Many times it was adjusted to make it consistent with the trimmed FFM, ² ϕ = strike, δ = dip, λ = rake, ³ M = maximum, T = trimmed. N/A = Slip values are not reported (only relative distribution). The model is already trimmed using approx. 15-20% of maximum slip as limit. NO = no trimming was applied, and ⁴ Event classification defined in Table 4.5.

Table 4.6 FFM's selected for use in NGA-Sub database.

NGA Sub EQID	Date	Earthquake name, Country/State	M	FFM reference	Hypocenter location ¹			Nodal plane ²			Slip ³ (cm)		Rupture dimensions		Upper-left corner			Event Class. Flag ⁴
					Lat. (°)	Lon. (°)	Depth (km)	ϕ (°)	δ (°)	λ (°)	M	T	L (km)	W (km)	Lat. (°)	Lon. (°)	Z _{TOR} (km)	
4000067	5/26/2003	SouthSanriku	7.03	Okada & Hasegawa [2003]	38.9471	141.6793	65.2354	198	60	92	300	60	24	20	38.9436	141.7217	59	1
4000146	7/23/1982	Ibaraki-oki	7.03	Takiguchi et al. [2011]	36.2699	141.65	29.9684	203	14	86	660	NO	11.4	11.4	36.2958	141.7642	27.9	0
4000077	11/28/2004	Kushirooki	7.01	HERP [2006]	42.9533	145.2529	51.0142	211	24	81	400	150	25	25	42.9775	145.4365	45.93	0
4000162	11/14/2005	Sanriku	7.01	JMA [2005]	38.0255	144.927	8.0399	173	49	-118	140	NO	56	22	38.3626	144.9447	1	4
4000072	10/31/2003	Fukushima-oki	7.00	EIC [2003]	37.7175	142.7453	30.8572	204	14	92	60	20	80	76	38.0882	143.4563	20.8	0
4000050	3/14/2012	Sanrikuoki	6.98	JMA [2012]	40.7922	145.2319	15.2067	276	42	-81	367	NO	31	24.5	40.7016	145.2839	6.6	4
4000145	3/21/1982	S.Urakawa	6.91	Tsuchida [1983]	42.1079	142.6131	12.5433	320	65	90	60	NO	30	40	42.0466	142.5898	0	-666
4000059	1/28/2000	NemuroSE	6.83	Takahashi & Hirata [2003]	43.2973	147.0443	67.4	160	35	15	N/A	N/A	30	15	43.4429	147.0521	63.1	1
4000063	3/24/2001	Geiyo	6.83	Kakehi [2004]	34.1298	132.7025	45.8808	170	60	110	240	NO	15	18	34.1744	132.7258	40	1
								177	63				3	18	34.0375	132.7511	40	
								183	67				3	18	34.0075	132.7489	40	
								190	70				9	18	33.9779	132.7385	40	
								5	84				-73	103	NO	31	25	
4000049	1/1/2012	Torishima	6.82	JMA [2012]	31.4268	138.5691	364.9843	179	71	-93	240	50	14	35	39.6856	141.7613	94.2	5
4000224	7/23/2008	Middle Iwate	6.82	Suzuki et al. [2009]	39.739	141.6665	114.8789	223	65	-107	16	35	39.872	141.7623	93.3	0	0	
4000225	9/11/2008	Toakchi-oki	6.80	JMA [2008]	41.7792	144.1493	30.6548	228	21	108	160	NO	36	31	41.8064	144.4086	26	0
4000161	12/6/2004	KushiroAs	6.77	HERP [2006]	42.8463	145.3371	45.9837	222	26	90	200	50	20	20	42.859	145.5011	41.6	0
4000041	6/22/2011	Iwateoff	6.76	JMA [2011]	39.9678	142.5565	36.7789	185	17	74	86	17	18.25	12	40.0639	142.5974	36	0
4000165	10/19/1996	Hyuganada	6.74	Yagi et al. [1999]	31.7808	131.8515	3.3449	210	12	80	290	NO	32.12	29.2	31.9065	132.0591	1.22	0
4000048	9/16/2011	Iwate-oki	6.70	JMA [2011]	40.2604	143.0867	24.8842	172	17	57	94	NO	36	37	40.4121	143.3957	16.23	0
4000036	4/11/2011	Hamadori	6.69	Anderson et al. [2013]	36.9597	140.726	4.2147	342	66	-75	172	NO	23	20	36.9492	140.7081	0	2
4000166	12/2/1996	Hyuganada2	6.69	Yagi et al. [1999]	31.9197	131.5977	5.1662	210					12	80	140	NO	29.2	
4000100	12/17/1987	ChibaEastoff	6.53	Fukuyama [1991]	35.4012	140.5014	50.4243	349	85	180	N/A	NO	16	24	35.3556	140.4907	28.5	1
4000070	9/29/2003	Tokachias	6.47	Atkinson & Macias [2009]	42.3041	144.579	35.5	79	90	0	N/A	NO	6.4	8	35.3483	140.4069	45	
4000119	9/9/1969	Gifu	6.43	Takeo & Mikami [1990]	35.47	137.05	2	244	17	114	N/A	N/A	19	10	42.3029	144.7082	34	0
4000045	7/30/2011	Fukushimaaoki	6.40	JMA [2011]	36.852	141.3085	56.9556	333	89.9	180	170	NO	20	11.2	35.3899	137.1001	0.6	2
4000043	7/23/2011	Miyagi-oki	6.37	JMA [2011]	38.8743	142.0966	39.9204	21	39	93	205	31	14	18	36.8429	141.1918	49.4	1
4000044	7/24/2011	Fukushimaaoki	6.34	JMA [2011]	37.7479	141.4771	51.2429	173	26	62	53	8	15	15	38.9722	142.1837	35.62	0
4000014	3/11/2011	NorthNagano	6.33	Nagumo [2012]	36.9883	138.5921	9.3111	200	22	88	51	8	24	24	37.7474	141.6788	44.5	0
4000047	8/19/2011	Fukushima-oki	6.32	JMA [2011]	37.6415	141.7811	50.96	26	32	80	100	NO	12	10	37.0028	138.5025	4.4	2
4000038	4/11/2011	ChibaEastoff	6.25	HERP [2011]	35.4786	140.8657	26.4153	190	53	92	117	NO	14	15	37.7	141.8146	48.6	1
4000082	8/10/2009	Suruga-bay	6.20	GSI [2009]	34.8406	138.4434	19.2	299	75	162	78	N/A	20	10	35.3986	141.0067	20.5	1
4000218	11/24/2011	UrakawaOff	6.19	JMA [2011]	41.7457	142.8422	43.0034	309	38	122	77	N/A	16.7	5.6	34.7779	138.4993	17.5	1
4000112	7/1/1968	Saitama	6.10	Abe [1975]	36.072	139.3972	52	223	16	103	132	17	16	14	41.7644	142.9922	40.8	0
4000022	3/15/2011	ShizuokaEast	6.00	JMA [2011]	35.3354	138.7148	14.1	6	30	90	N/A	N/A	6	10	36.0534	139.2979	47	0
4000046	8/1/2011	Surugawan	5.98	JMA [2011]	34.7054	138.5393	21.3002	31	80	42	110	NO	12	7	35.2915	138.6758	11.1	2
4000037	4/12/2011	Nakadori	5.97	JMA [2011]	37.0497	140.6217	18.3625	284	31	99	150	33	10	8	34.6431	138.6105	18.21	-444
4000024	3/19/2011	NorthIbaraki	5.86	JMA [2011]	36.7729	140.6166	3.5106	170	40	58	248	NO	12	6	37.0904	140.6522	15.47	2
								150	45	-81	28	7	14	8.4	36.8353	140.5938	1.8	2

¹ Hypocenter location is not necessarily exactly the same as in the FFM. Many times it was adjusted to make it consistent with the trimmed FFM, ² ϕ = strike, δ = dip, λ = rake, ³ M = maximum, T = trimmed. N/A = Slip values are not reported (only relative distribution). The model is already trimmed using approx. 15-20% of maximum slip as limit. NO = no trimming was applied, and ⁴ Event classification defined in Table 4.5.

Table 4.6 FFM s selected for use in NGA-Sub database.

NGA Sub EQID	Date	Earthquake name, Country/State	M	FFM reference	Hypocenter location ¹			Nodal plane ²			Slip ³ (cm)		Rupture dimensions		Upper-left corner			Event Class. Flag ⁴
					Lat. (°)	Lon. (°)	Depth (km)	ϕ (°)	δ (°)	λ (°)	M	T	L (km)	W (km)	Lat. (°)	Lon. (°)	Z _{TOR} (km)	
South America (SAM) – 13 events																		
6000149	2/27/2010	Maule, Chile	8.81	Delouis et al. [2010]	-36.2089	-72.9587	30.4055	15	18	109.3	2129	319	480	160	-37.8975	-74.5879	0.74	0
6000057	6/23/2001	Arequipa, Peru	8.41	Lay et al. [2010]	-16.2081	-73.6217	28.7746	310	18	62	N/A	N/A	264	145	-18.1423	-72.4881	0.24	0
6000338	9/16/2015	Illapel, Chile	8.31	Melgar et al. [2016]	-31.5571	-71.6617	29.81	3.7	10.5	109	1070	161	240	50	-32.1337	-72.6568	7.4	0
													140	38	-31.6236	-72.0986	16.51	
													130	55	-31.9598	-71.7436	27.62	
6000079	4/1/2014	Iquique, Chile	8.15	Lay et al. [2014]	-19.6420	-70.8173	20.1125	357	18	106	670	101	157.5	105	-20.3526	-71.0105	12.20	0
6000081	7/30/1995	Antofagasta, Chile	8.02	Shao and Ji (n.d.)	-23.4317	-70.4542	36.86	4	18	97	387	58	180	91	-24.9529	-71.4113	9.10	0
													150	52	-24.3340	-70.5128	37.21	
6000272	8/15/2007	Pisco, Peru	8.00	Sladen [2007]	-13.3247	-76.5154	38.55	318	6	59.5	986	148	144	20	-14.5955	-76.5687	5.53	0
									20				144	70	-14.4809	-76.4289	7.25	
									30				144	90	-14.0844	-75.9724	31.05	
6000323	3/3/1985	Valparaiso, Chile	7.98	Mendoza et al. [1994]	-33.125	-71.610	40.0	5	15	90	329	49	255	75	-34.6044	-72.8109	6.4	0
									30	110			180	60	-34.1236	-71.9781	25.81	
6000339	4/16/2016	Coastal Ecuador, Ecuador	7.82	Hayes [2016]	0.2988	-79.9979	19.0058	29	15	114	397	60	168	155	-0.0722	-80.9329	0.00	0
6000061	6/13/2005	Tarapaca, Chile	7.78	Kuge et al. [2010]	-20.03	-69.28	110.0	187	23	-73	>1000	200	47.5	45	-19.8048	-69.0515	101.21	1
6000080	4/3/2014	Iquique afs., Chile	7.76	Lay et al. [2014]	-20.5165	-70.4689	25.6509	357	18	113.6	279	42	90	90	-20.9471	-70.8842	10.8	0
6000095	11/14/2007	Tocopilla, Chile	7.75	Schurr et al. [2012]	-22.3421	-70.0235	49.844	3	20	98	258	39	180	60	-23.2348	-70.5310	32.78	0
6000050	11/12/1996	Nazca, Peru	7.74	Salichon et al. [2003]	-15.0056	-75.6422	31.7612	307	30	47	437	66	180	120	-16.1123	-74.7536	8.00	0
6000055	7/7/2001	Arequipa afs., Peru	7.64	Kikuchi & Yamada [2001]	-17.543	-72.077	20.0	315	16	64	450	68	80	80	-18.0399	-72.0691	9.00	0
Cascadia (CAS) – 4 events																		
2000004	2/18/2001	Nisqually, Washington	6.80	Ichinose et al. [2004]	47.1574	-122.6801	53.1749	350	70	-91	200	30	24	21	47.0337	-122.6825	46.13	1
2000001	4/13/1949	Olympia, Washington	6.70	Ichinose et al. [2006(a)]	47.2028	-122.9315	57.1527	0	66	-111	166	25	34	28	47.0371	-122.9907	47.1	1
2000002	4/29/1965	Olympia, Washington	6.62	Ichinose et al. [2004]	47.3714	-122.3060	59.9797	344	70	-90	200	30	20	18	47.2876	-122.3037	53.4	1
2000014	1/10/2010	Ferndale, California	6.55	Pitarka et al. [2013]	40.6548	-124.6933	21.6881	230	86	11	120	N/A	25	14	40.7259	-124.5766	18	1
Alaska (ALK) – 3 events																		
1000001	6/23/2014	Aleutian_Is-Alaska	7.96	USGS [2014]	51.6928	178.8871	103.7969	206	25	-13	789	NO	80	130	51.8207	179.8826	77.92	1
1000002	11/17/2003	Rat_Islands-Alaska	7.78	USGS [2003]	51.1965	178.1844	29.7262	280.4	18.8	121.9	184	28	120	140.4	50.4649	178.8753	5.61	0
1000142	1/24/2016	Iniskin	7.15	USGS [2016]	59.6531	-153.4457	129.4159	60	66	33	302	45	30	28	59.6912	-153.644	108.62	1
Taiwan (TWN) – 3 events																		
7000044	3/31/2002	2944860	7.12	Lee [2019]	24.16020	122.17200	33.0	292	32	121	462.4	<100	33	32	23.9104	122.3585	21.34	0
7000048	12/26/2006	Pingtung_Doublet1	7.02	Lee et al. [2008]	21.88703	120.56844	44.1	349	53	-54	319	48	89.9	35	21.376	120.527	24.13	1
7000049	12/26/2006	Pingtung_Doublet2	6.94	Lee et al. [2008]	22.02975	120.40508	33.8	151	55	4	260	39	84.9	35	22.29	120.313	25.61	1
Central America and Mexico (CAM) – 2 events																		
3000271	9/19/1985	Michoacan, Mexico	7.99	Mendoza & Hartzell [1989]	18.1814	-102.5691	16.2637	300	14	72	749	112.4	150	139	17.2996	-101.7377	6.0	0
3000272	9/21/1985	Zihuatanejo, Mexico	7.56	Mendoza [1993]	17.5977	-101.8192	20.1586	300	14	100	209	31.4	67.5	67.5	17.1640	-101.6485	12.0	0

¹ Hypocenter location is not necessarily exactly the same as in the FFM. Many times it was adjusted to make it consistent with the trimmed FFM, ² ϕ = strike, δ = dip, λ = rake, ³ M = maximum, T = trimmed. N/A = Slip values are not reported (only relative distribution). The model is already trimmed using approx. 15-20% of maximum slip as limit. NO = no trimming was applied, and ⁴ Event classification defined in Table 4.5.

Most of the earthquakes with FFMs are off the coast of Japan (63) and South America (13). Figure 4.23 shows the locations of the earthquakes with FFMs in these regions. The magnitude range of events with FFM is 5.86 to 9.12. Interface events comprise 53% of the events with FFMs, 31% are intraslab, and the balance (16%) are shallow crustal and outer-rise earthquakes.

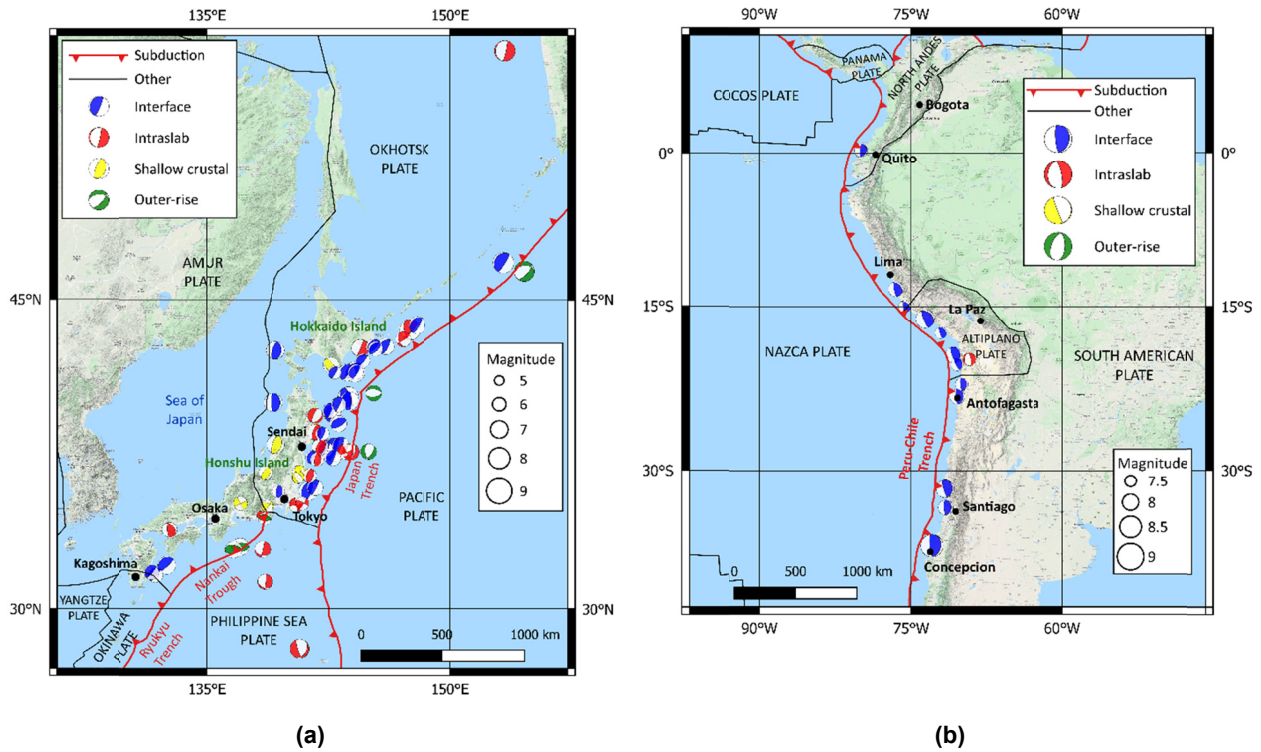


Figure 4.23 Epicentral locations of the earthquakes in (a) Japan and (b) South America with available FFMs in the NGA-Sub database.

4.3.2 Selection Criteria

A detailed review of the collected FFMs has been conducted to select the most appropriate model for each earthquake. The 2010 $M_{8.81}$ Maule, Chile, earthquake is utilized as an example to illustrate the approach. For this event, seven different FFMs were considered. Following some trimming (for details see Section 4.3.3), the outlines of these seven models are shown in Figure 4.24, along with the locations of strong-motion stations in the near-fault region.

The selection of a model among the seven candidates in Figure 4.24 is a topic of practical importance because they produce different source-to-site distances. Table 4.7 presents rupture distances (R_{rup}) for the 29 stations in the NGA-Sub database that recorded this event with rupture distances (from any of the alternate models) less than 500 km. Rupture distances are shown for all of the FFMs. The results show considerable differences in some cases; the sites with the largest ranges of distances are highlighted.

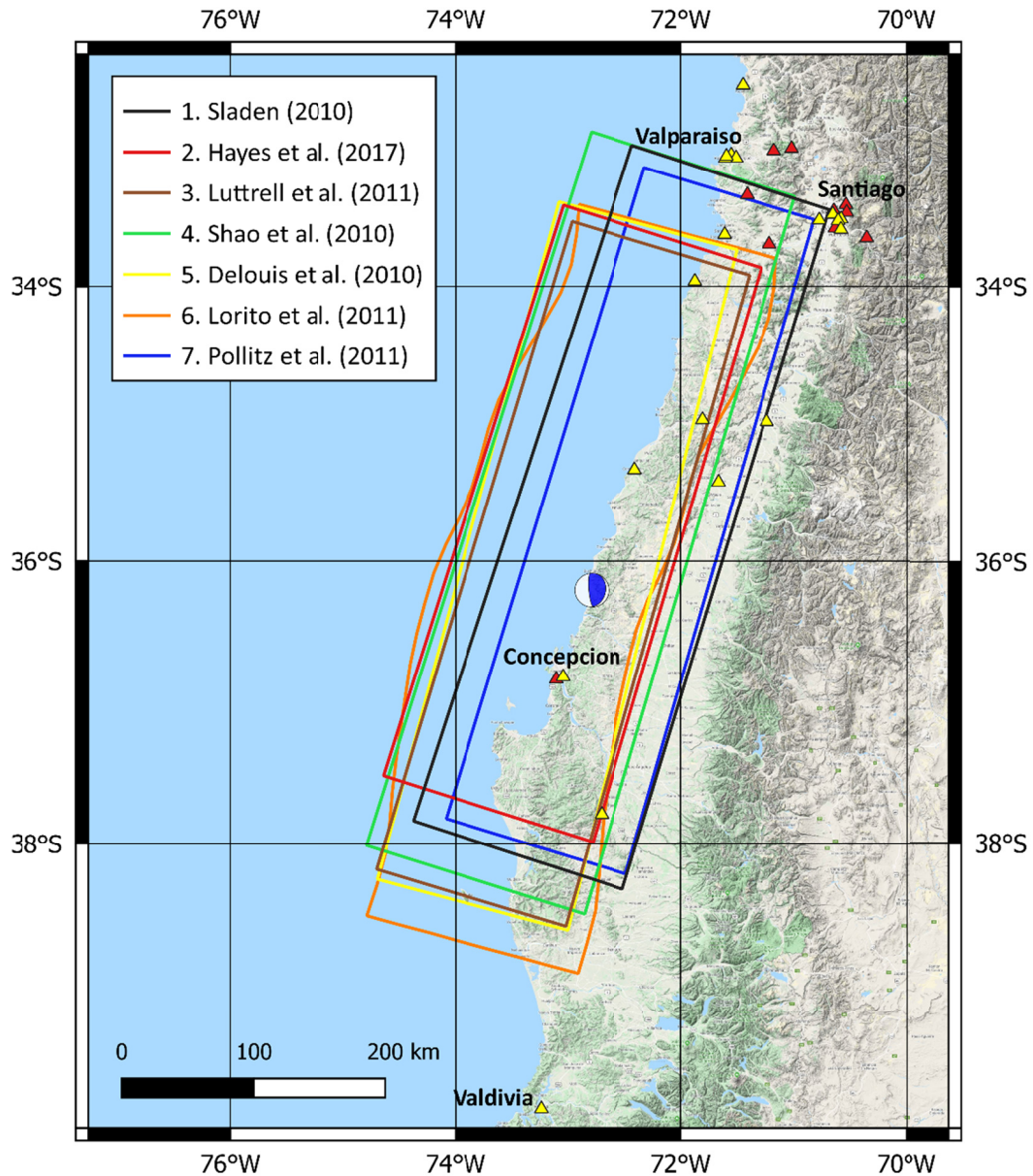


Figure 4.24 Finite-fault models for the 2010 M8.81 Maule earthquake using a trimming threshold of 50 cm of slip. Locations of the ground-motion stations included in Table 4.7 are shown using yellow triangles for the RENADIC network and red triangles for the C network. The focal plane solution is shown at the epicenter.

Table 4.7 Computed distances (R_{rup}) using the seven FFM s for the 2010 Maule earthquake.

Recorded strong motion			Closest distance to the fault-rupture plane, R_{rup} (km)								
No	NGA-sub RSN	Network	FFM 1	FFM 2	FFM 3	FFM 4	FFM 5	FFM 6	FFM 7	Range (min-max)	
1	6001819	RENADIC	82	142	150	82	137	135	86	82	150
2	6001829	RENADIC	39	88	94	41	83	80	36	36	94
3	6001810	RENADIC	39	88	93	42	83	80	36	36	93
4	6001827	RENADIC	36	84	90	38	80	76	32	32	90
5	6001828	RENADIC	37	86	92	39	81	78	33	33	92
6	6001817	RENADIC	39	43	40	42	43	41	30	30	43
7	6001824	RENADIC	63	88	91	66	93	83	54	54	93
8	6001821	RENADIC	60	80	81	63	83	75	51	51	83
9	6001822	RENADIC	65	91	94	70	97	86	56	56	97
10	6001811	RENADIC	65	89	91	69	95	84	56	56	95
11	6001823	RENADIC	66	87	90	71	95	83	57	57	95
12	6001818	RENADIC	36	36	28	38	38	34	26	26	38
13	6001815	RENADIC	64	66	60	66	74	68	54	54	74
14	6001816	RENADIC	48	49	38	51	49	51	38	38	51
15	6001825	RENADIC	57	57	46	59	58	63	47	46	63
16	6001813	RENADIC	36	36	27	38	36	40	26	26	40
17	6001809	RENADIC	35	35	25	37	32	38	24	24	38
18	6001812	RENADIC	54	54	41	56	50	53	43	41	56
19	6001826	RENADIC	189	215	146	163	146	120	197	120	215
20	6001799	C	34	33	24	35	30	36	22	22	36
21	6001807	C	50	55	50	53	54	52	41	41	55
22	6001805	C	66	99	103	70	104	93	58	58	104
23	6001802	C	73	101	105	84	113	96	66	66	113
24	6001803	C	63	90	93	66	95	85	54	54	95
25	6001804	C	65	84	86	68	92	80	55	55	92
26	6001800	C	66	96	100	71	103	91	57	57	103
27	6001801	C	61	112	116	63	106	104	59	59	116
28	6001806	C	41	68	71	44	64	61	32	32	71
29	6001808	C	54	105	109	56	99	97	52	52	109

The three major considerations in evaluation of FFM s are: (1) the model is generated using default (automated) procedures vs. an inversion process managed and interpreted by experts; (2) the data sources considered in the inversion; and (3) peer-review, or lack thereof, of the model and the process by which it was derived. The data sources used in FFM development can include:

- Permanent crustal displacement caused by the earthquake, typically measured from GPS sensors, InSAR, or measurements of on-land elevation change (typically in coastal areas);
- Teleseismic waveforms from global network;
- Broadband ground-motion sensors in reasonably close proximity to the source;
- Tsunami-related data (run up heights and wave heights as measured by ocean buoys); and
- Spatial distribution of aftershocks, typically within 24 to 60 hours of the mainshock event.

We prefer FFM s that have been reviewed/developed by experts (not preliminary or automatic solutions), have been developed using multiple data sources (inclusive of ground-motion data, preferably from proximate stations), and have appeared in peer-reviewed documents.

In the case of the Maule, Chile, earthquake, the seven considered models have the attributes shown in Table 4.8. Three are automatically generated models. Five consider only a single data source (teleseismic or ground displacement only). The model by Delouis et al. [2010] was ultimately identified as the preferred model because it considered multiple data sources, is not from an automated procedure, and appears in a peer-reviewed journal. Lorito et al. [2011] has similar attributes, but the considered data sources do not include ground motions, which is why we prefer Delouis et al. [2010]. The hypocenter of the Maule, Chile, earthquake from the preferred FFM is shown in Figure 4.24. This hypocenter is located essentially on the fault plane (no projection required).

Table 4.8 Alternate FFM s for 2010 M8.81 Maule, Chile, earthquake.

Model	Automated (Y/N)	Data sources	Peer-review document (Y/N)
Sladen [2010]	Y	Teleseismic	N
Hayes [2010; 2017]	Y [2010]; N [2017a]	Teleseismic	N
Luttrell et al. [2011]	N	Crustal displacement	Y
Shao et al. [2010]	Y	Teleseismic	N
Delouis et al. [2010]	N	Teleseismic; crustal displacement	Y
Lorito et al. [2011]	N	Crustal displacement; tsunami	Y
Pollitz et al. [2011]	N	Crustal displacement	Y

4.3.3 Trimming Criteria

Once a published FFM model is selected, it is typically necessary to apply some trimming of the rupture dimensions. This is important because faults are often set as large geometric objects at the outset of the inversion so as to avoid “missing” areas of potential rupture. As a result, the inverted fault may contain broad regions with relatively little slip in addition to concentrated areas of high slip. This need for trimming is not unique to NGA-Sub; it was addressed earlier in the NGA-West1 project [Power et al. 2008]. At that time, on average, a threshold of 50 cm of slip was generally applied, i.e., portions of the fault having slip below this value were trimmed (excluded) in the development of representative fault geometries used for distance calculations. Similar procedures were subsequently used in NGA-West2.

Because the amounts of slip on subduction sources can be very large relative to the crustal sources considered in NGA-West1 and NGA-West2, we were concerned that the 50 cm threshold may not provide a reliable basis for fault trimming in all cases. Accordingly, we re-examined this issue, starting with a fresh look at the source models used to develop the 50 cm threshold in previous NGA projects. The trimmed models were of seven crustal events in California, Idaho, and northern Mexico summarized in Table 4.9 (three of the ten models in this analysis were trimmed by the FFM authors), which shows the calculation of the average threshold that was utilized in the trimming of the source models. These events had maximum slips in the approximate range of 45 to 790 cm, so that, on average, the 50 cm threshold corresponded to approximately 15% of the maximum. For NGA-Sub, we consider this percentage of the maximum slip, in lieu of the 50-cm threshold directly, given the large rupture dimensions and slip values involved in subduction-zone earthquakes when compared to the M6-7 shallow crustal events upon which the original criteria had been based. When the 15% criteria was applied to large subduction events with FFMs, the results were judged to be reasonable by the source working group. Accordingly, we trim the FFMs by applying a threshold of 15% of the maximum slip and then draw one or more rectangles around the high-slip areas. Dimensions derived using this process appear in Table 4.6 and in the *FFmodel* tables in the source database.

Table 4.9 Summary of trimming applied for NGA-West and NGA-West 2 projects.

EQ ID	Earthquake name	Magnitude, M	Maximum slip in the FFM (cm)	Maximum slip in the trimmed row or column of the FFM (cm)	Percentage of the maximum trimmed value relative to the maximum slip
48	Coyote Lake	5.9	120	0	0%
87	Borah Peak	6.8	128	9	7%
101	North Palm Springs	6.2	45	9-11	22%
113*	Whittier Narrows	5.9	90	No trim (< 58 cm)	No trim (<64)
125	Landers	7.3	790	60	8%
127*	Northridge	6.7	319	No trim (< 140 cm)	No trim (<46)
118*	Loma Prieta	6.9	513	0 (< 105 cm)	0 (< 20 cm)
280	El Mayor-Cucupah	7.2	700	180	26%
177	San Simeon	6.5	300	70	23%
179	2004 Parkfield	6.0	52	18	35%
		Average**	305 cm	50 cm	~15%

* Events 113 (Whittier Narrows), 127 (Northridge), and 118 (Loma Prieta) applied models as published, because trimming appears to have been done by the FFM authors.

**Average is computed without the pre-trimmed events.

4.3.4 Multi-Segment Ruptures

Some FFMs involve multiple segments. Figure 4.25 presents all eight interface events in the NGA-Sub database having a multiple-segment rupture. Four of them are located in Japan, including the 2011 **M9.12** Tohoku earthquake [Figure 4.25(a)], and four in South America, including the 2016 **M8.31** Illapel, Chile, earthquake [Figure 4.25(b)]. Both the Tohoku and Illapel earthquakes are modeled with three segments. Figure 4.26 presents four intraslab events having multiple-segment ruptures. All of them are located in Japan, including the 2001 **M6.83** Geiyo earthquake [Figure 4.26(b)], which is the event with the most number of segments (four) in the NGA-Sub database.

Multiple-segment ruptures introduce issues related to distance calculation and representation of the fault with a single rectangle, as required for the *FFmodel* table. To describe the manner in which multi-segment faults are managed for distance calculation, the required configuration of fault geometry for the distance computation code (P4CF; Section 4.5) should be understood. While most earthquakes are represented by a single rectangle, this code can take as input a series of rectangles provided they share a continuous line at the top (shallowest portion) of the fault [e.g., Figure 4.27(a), which shows continuous (at the top) rupture segments for the 1983 Middle Japan Sea earthquake]. In this case, the various rectangles are provided to the code, closest distance parameters are computed for each internally within the code, and the segment producing the smallest values is used. For multi-segment ruptures that are discontinuous at the top [e.g., Figures 4.26(a) and 4.26(d)], or that are listric [dip varies across fault width, see Figure

4.27(b)], each segment must be entered separately for distance calculation, and the smallest value selected by the analyst. Listric-fault events included in the NGA-Sub database are the 1994 **M7.76** Sanriku-ho and the 2011 **M9.12** Tohoku earthquakes in Japan [Figure 4.25(a)], the 2007 **M8** Pisco (Peru), the 1985 **M7.98** Valparaiso (Chile), and the 2016 **M8.31** Illapel (Chile) earthquakes in South America [Figure 4.25(b)].

As a separate exercise from distance calculation, multi-segment faults were represented as a single rectangle for inclusion on the *FFmodel* table. This was done to support potential future work related to rupture directivity. In the case of multiple segments having the same strike but different widths and dips [e.g., Figure 4.27(b) showing the trimmed area of the 1985 **M7.98** Valparaiso, Chile, earthquake], the width of the rectangle is taken as the sum of the segment widths, and a weighted average length and dip are computed. The weights are proportional to the widths of each segment. In the case of multiple segments having different strikes, widths, and dips, a width is computed as the ratio of total fault-rupture area divided by the sum of segment lengths. The length in this case is taken as the cumulative lengths of the multiple segments. The strike and dip are taken as a weighted average by area. In some cases involving discontinuous segments and significantly different segment areas [e.g., intraslab events in Figures 4.26(a) and 4.26(d)], only the segment with the largest area is considered whereas the smaller segment is ignored.

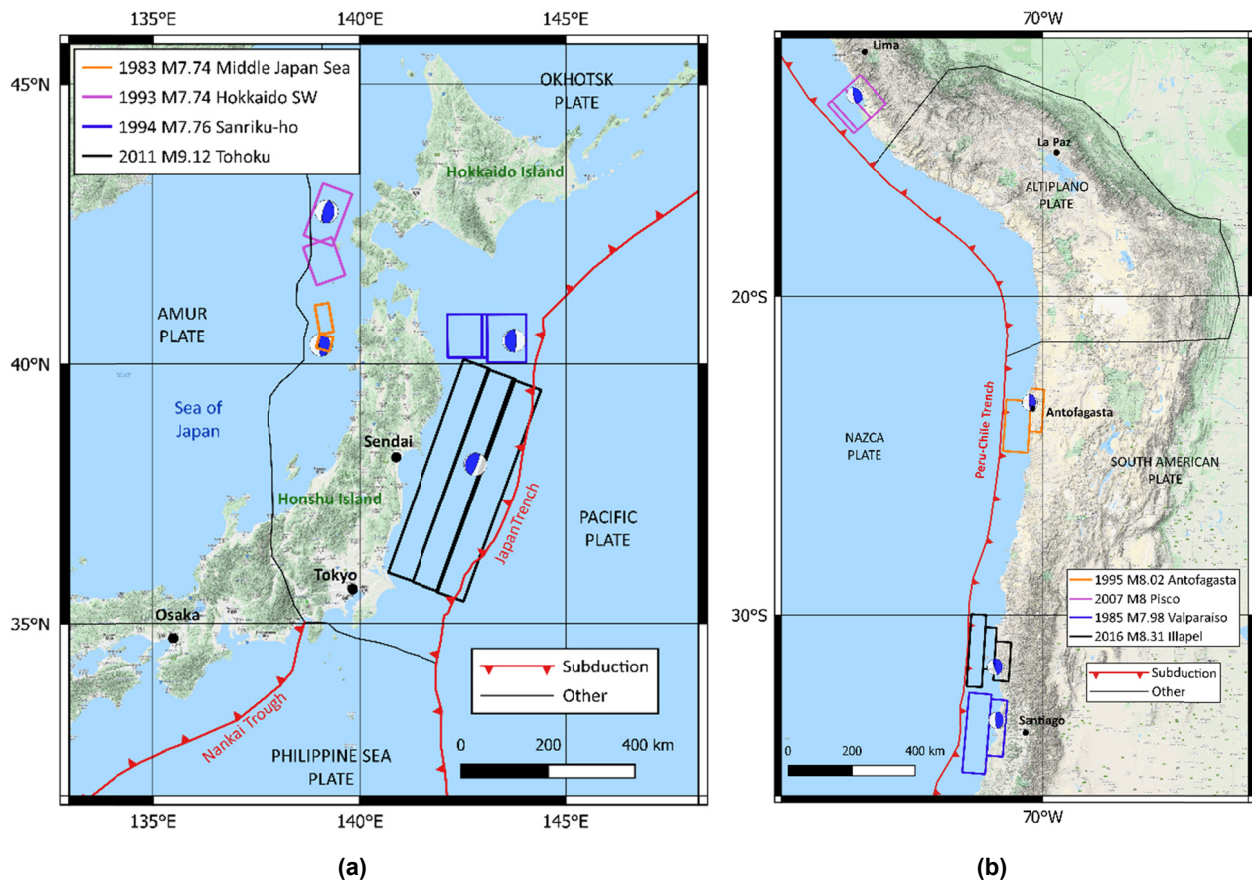


Figure 4.25 Multi-segment ruptures of interface events in the NGA-Sub database in (a) Japan and (b) South America regions.

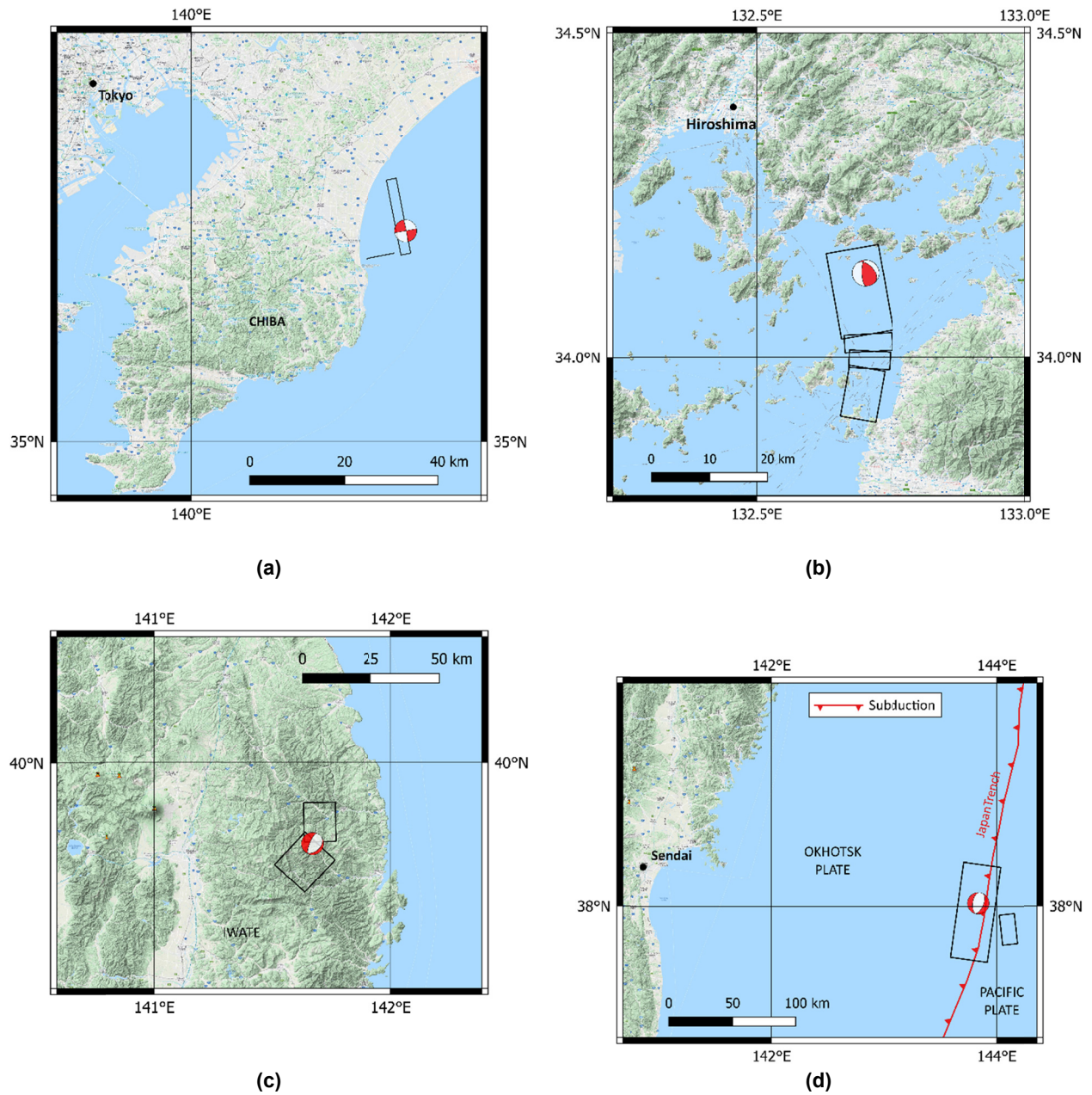


Figure 4.26 Multi-segment ruptures of intraslab events in the NGA-Sub database: (a) 1987 M6.53 Off Eastern Chiba; (b) 2001 M6.83 Geiyo; (c) 2008 M6.82 Middle Iwate; and (d) 2012 M7.23 Miyagi-oki earthquakes.

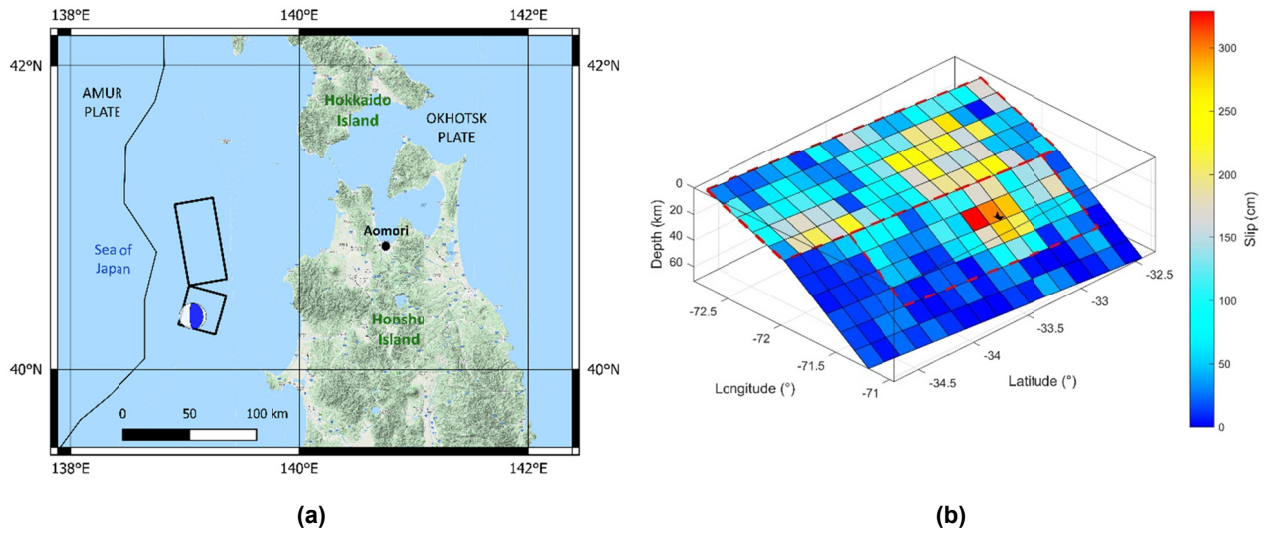


Figure 4.27 Examples of multi-segment ruptures: (a) with continuity of the upper section of the segments; and (b) variable dip over the fault width, i.e., listric faults.

4.4 SOURCE PARAMETERS FOR EVENTS WITHOUT FINITE-FAULT MODELS

Most earthquakes with event types in the NGA-Sub database do not have FFMs in literature (903 out of 991). Because there is a need for a finite-fault representation of each earthquake source, we applied a simulation procedure for events without published models. This section describes empirical models for fault dimensions of subduction earthquakes, which are needed in the simulation procedure (Section 4.4.1), and the simulation procedure that is applied (Section 4.4.2).

4.4.1 Subduction Earthquake Empirical Models for Fault Dimensions, Fault Orientations, and Hypocenter Location

The simulation procedure requires models for the rectangular dimensions of finite faults (along-strike length L and width W), the orientation of the rectangles (strike ϕ and dip δ), and hypocenter location within the rectangle. Models for fault area (A) and aspect ratio (L/W) are provided for interface subduction events by Murotani et al. [2013] and Skarlatoudis et al. [2016]. A model for hypocenter location is provided by Mai et al. [2005].

Figure 4.28 shows fault-rupture areas and Figure 4.29 shows aspect ratios for the 47 interface events with FFMs (dimensions are available from Table 4.6) in the NGA-Sub database. Also shown are source dimension data from Skarlatoudis et al. [2016] and regression fits. For the rupture-area data shown in Figure 4.28, linear regression fits are shown from Murotani et al. [2013], Skarlatoudis et al. [2016], and the present study using the following linear expression:

$$\ln A = a_1 + a_2 \mathbf{M} + \varepsilon_{n1} \sigma_A \quad (4.6)$$

where A is rupture area in km^2 , a_1 and a_2 are regression coefficients, ε_{n1} is the standard normal variate (zero mean, standard deviation of 1), and σ_A is the standard deviation. Regressions were performed at two stages in the NGA-Sub project. The first regression was performed using data from 29 earthquakes (a subset of data from Table 4.6) available at that time (approximately November 2017) along with data from Skarlatoudis et al. [2016]; the 29 events used at that time are depicted in Figure 4.28(a), and the resulting coefficients are indicated in the figure (marked as “Applied”). The next regression was performed near the end of the project (December 2019) using all 47 events and Skarlatoudis et al. [2016] data for non-redundant events, with the results shown in Figure 4.28b (marked as “Complete”).

Note that self-similarity is assumed, which is typical in models of this sort, i.e., a_2 is unity for the \log_{10} of area [equivalent to $a_2 = \ln(10)$]. The regression coefficients and standard deviations from the two models in literature and the present model are provided in Figure 4.28. There is no appreciable difference between the “Applied” and “Complete” versions of the mean model although dispersion increases in the update. The fits derived in the present study are similar to those derived by Murotani et al. [2013]. The fit provided by Skarlatoudis et al. [2016] was on A directly, not its logarithm. The present results are lower because Equation (4.6) fits the mean of the log of the data.

For the aspect-ratio relation the following expression was used:

$$\ln(L/W) = \begin{cases} \mathbf{M} \geq 7.25 : a_3 (\mathbf{M} - \mathbf{M}_1) + \varepsilon_{n2} \sigma_{L/W} \\ \mathbf{M} < \mathbf{M}_1 : \varepsilon_{n2} \sigma_{L/W} \end{cases} \quad (4.7)$$

where L/W is the aspect ratio, and a_3 and \mathbf{M}_1 are model coefficients. Results are shown in Figure 4.29 for the first regression [“Applied”; see Figure 4.29(a)] and the subsequent regression [“Complete”; Figure 4.29(b)], with similar results. The mean aspect ratio does not extend below unity. Figure 4.29 shows data both from literature [Skarlatoudis et al. 2016] and the present study. No prior fits are available from literature; therefore, only the fit from Equation (4.7) is shown.

Figure 4.30 shows fault-rupture areas and aspect ratios for the 27 intraslab events with FFMs; dimensions were taken from Table 4.6. A model from Strasser et al. [2010] for the rupture area, with the same form as Equation (4.6), is shown in Figure 4.30(a). That model was considered to provide an adequate fit to the data and was applied in the present study. We did not find a model for L/W in literature for intraslab events. The November 2017 dataset was fit using Equation (4.7) with the result shown in Figure 4.30(b) and marked as “applied.” That dataset included 16 earthquakes in Table 4.6 and one event in Japan (marked with a black asterisk) that was initially considered as intraslab and subsequently reclassified as outer-rise; those events are depicted in Figure 4.30(b) using filled symbols. The open symbols represent ten events in Japan and one event in Cascadia that were not used in the regression analysis but are now part of the NGA-Sub database. The addition of the new data suggests that the dependency of the aspect ratio on magnitude for intraslab events is not as strong as initially considered. The mean of all the data (excluding the outer-rise event) is also shown in Figure 4.30(b) for reference.

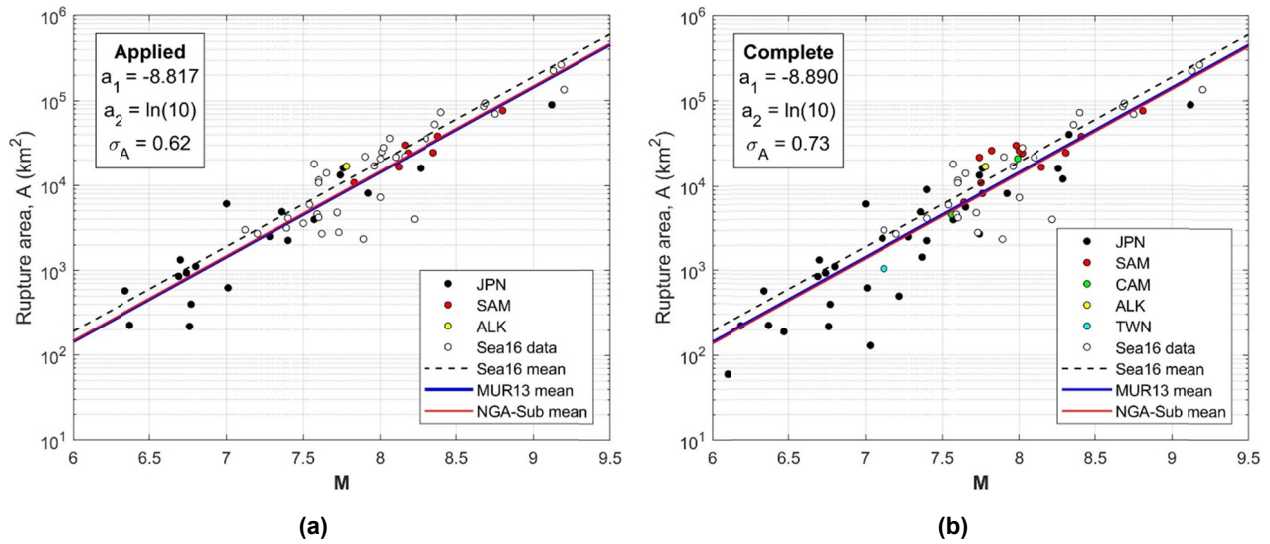


Figure 4.28 (a) Applied and (b) Complete geometric relations for rupture area for subduction interface earthquakes. JPN = Japan, SAM = South America, CAM = Central America and Mexico, ALK = Alaska, TWN = Taiwan, Sea16 = Skarlatoudis et al. [2016], MUR13 = Murotani et al. [2013].

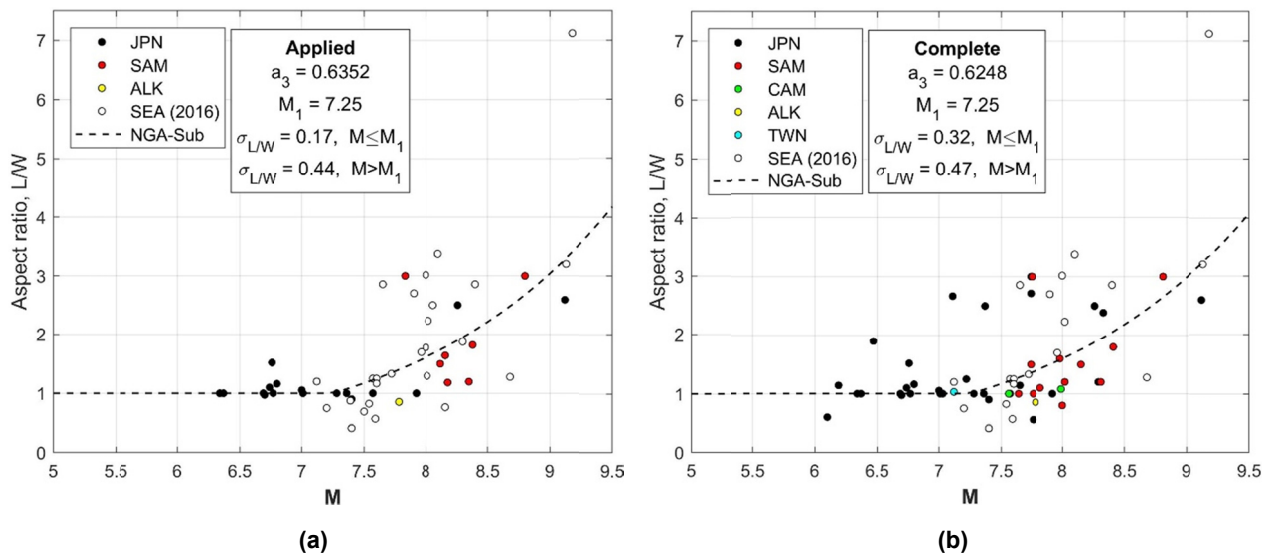


Figure 4.29 (a) Applied and (b) Complete geometric relations for aspect ratio for subduction interface earthquakes. JPN = Japan, SAM = South America, CAM = Central America and Mexico, ALK = Alaska, TWN = Taiwan, Sea16 = Skarlatoudis et al. [2016].

Figure 4.30 shows fault-rupture areas and aspect ratios for the 27 intraslab events with FFMs; dimensions were taken from Table 4.6. A model from Strasser et al. [2010] for the rupture area, with the same form as Equation (4.6), is shown in Figure 4.30(a). That model was considered to provide an adequate fit to the data and was applied in the present study. We did not find a model for L/W in literature for intraslab events. The November 2017 dataset was fit using Equation (4.7) with the result shown in Figure 4.30(b) and marked as “applied.” That dataset included 16 earthquakes in Table 4.6 and one event in Japan (marked with a black asterisk) that was initially considered as intraslab and subsequently reclassified as outer-rise; those events are depicted in Figure 4.30(b) using filled symbols. The open symbols represent ten events in Japan and one event in Cascadia that were not used in the regression analysis but are now part of the NGA-Sub database. The addition of the new data suggests that the dependency of the aspect ratio on magnitude for intraslab events is not as strong as initially considered. The mean of all the data (excluding the outer-rise event) is also shown in Figure 4.30(b) for reference.

The orientation of the fault rectangle is represented by strike angle ϕ and dip angle δ ; see Figure 4.19. Among earthquakes without FFMs, most have moment tensor solutions that provide two estimates of these angles. One is often preferred based on physical considerations (i.e., alignment of dip angle with slab orientation) and is used in the simulations “as-is.” Where a particular nodal plane is not preferred, both are considered; see Section 4.4.2. For events without a moment tensor, the mean strike ($\bar{\phi}$) is estimated as parallel to the nearest portion of the subducting plate (for all event types). Mean dip ($\bar{\delta}$) is similarly taken from the dip of the subducting plate for interface events. For intraslab events, mean dip is taken as an average of nearby events with available moment tensor solutions. A specific set of angles used in simulations is given as:

$$\phi = \bar{\phi} + \varepsilon_{\phi} \quad (4.8)$$

$$\delta = \bar{\delta} + \varepsilon_{\delta} \quad (4.9)$$

where ε_{ϕ} and ε_{δ} are uniform distributions centered on the means with ranges of $\pm 30^\circ$ and 10° , respectively.

Figure 4.31 shows the parameterization of hypocenter location on the fault plane, with θ_L and θ_W representing normalized location relative to the upper left corner (as viewed from the hanging wall). A model for these locations was presented by Mai et al. [2005]. The mean location along strike is at the midpoint ($\bar{\theta}_L = 0.5$) and slightly deeper than the mid-point in the down-dip direction ($\bar{\theta}_W = 0.57$) [Mai et al. 2005].

Figure 4.32 shows hypocenter locations using the data from Table 4.6 for interface events. An earlier analysis (November 2017) used to derive parameters applied in simulations was based on a subset of 27 events, mainly from Japan and South America; see Figure 4.32(a). The results confirm an along-strike mean close to the mid-point ($\bar{\theta}_L = 0.535$) whereas the down-dip mean varies by region ($\bar{\theta}_W = 0.451$ for events in Japan and $\bar{\theta}_W = 0.624$ for events in South America). Figure 4.32(b) presents updated results derived using data in its current state, which include 18 additional interface events. Results are congruent with previous observations, though

the difference observed in the down-dip direction by region is less evident in the light of the new data.

Similarly, Figure 4.33 shows hypocenter locations using the data from Table 4.6 for intraslab events. A subset of 15 events was used to perform the analysis shown in Figure 4.33(a). The results indicate that both along-strike and down-dip means are close to the mid-point ($\bar{\theta}_L = 0.424$) and ($\bar{\theta}_W = 0.511$) independent of region. Updated results derived after adding nine events since November 2017 are presented in Figure 4.33(b). These new observations do not differ significantly from the previous results.

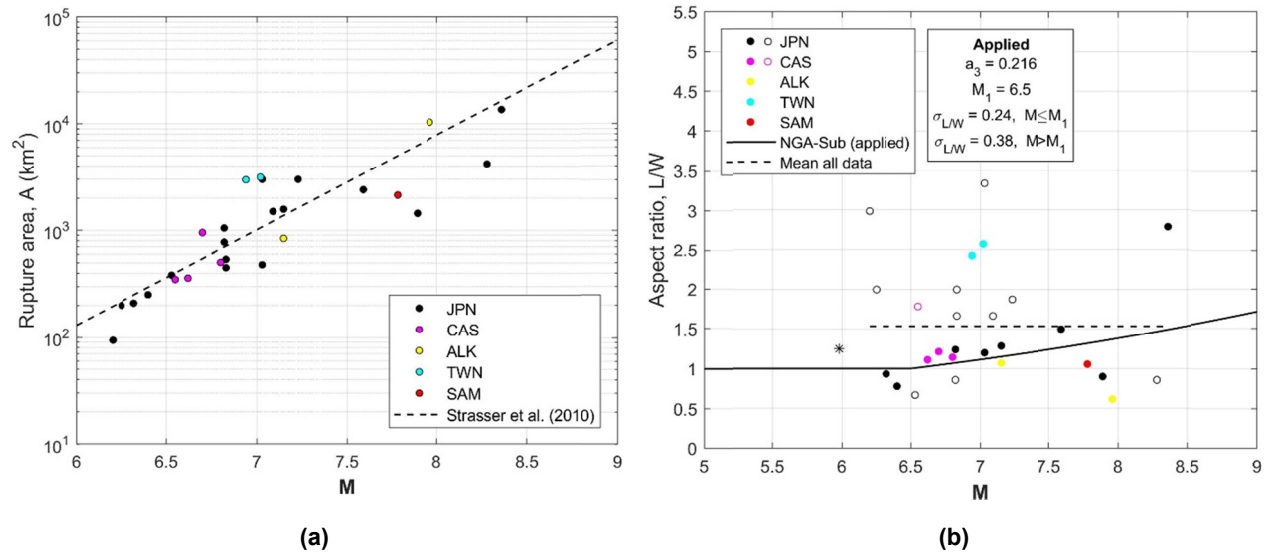


Figure 4.30 Geometric relations for (a) rupture area and (b) aspect ratio for subduction intraslab earthquakes. JPN = Japan, CAS = Cascadia, ALK = Alaska, TWN = Taiwan, SAM = South America. Black asterisk represents an event in Japan that was initially considered as intraslab (for the regression analysis marked as “Applied”) and subsequently reclassified as outer-rise.

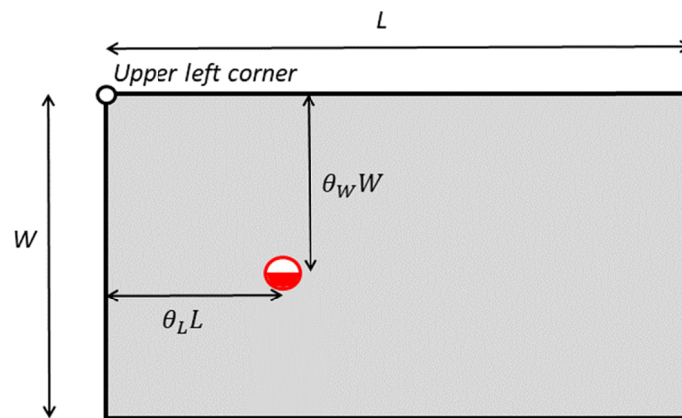
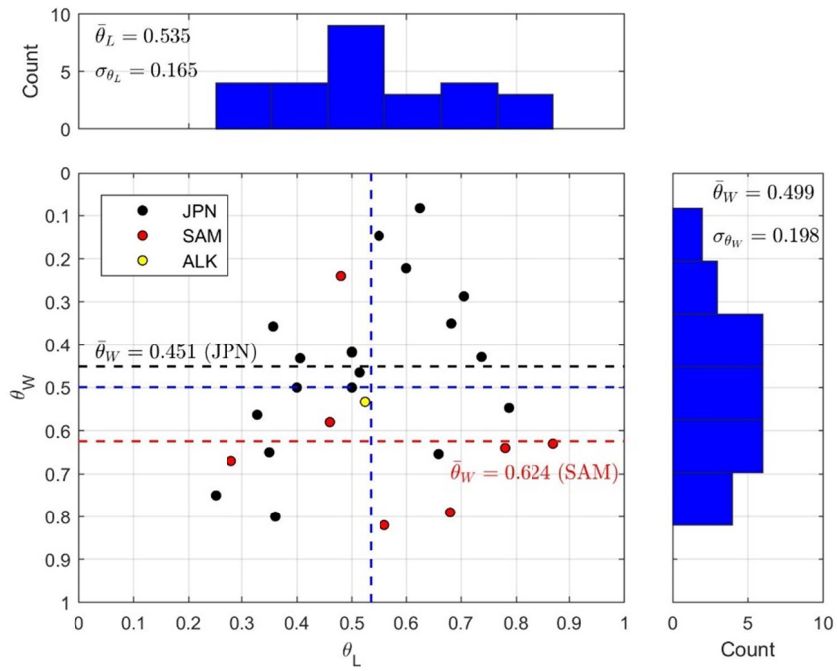
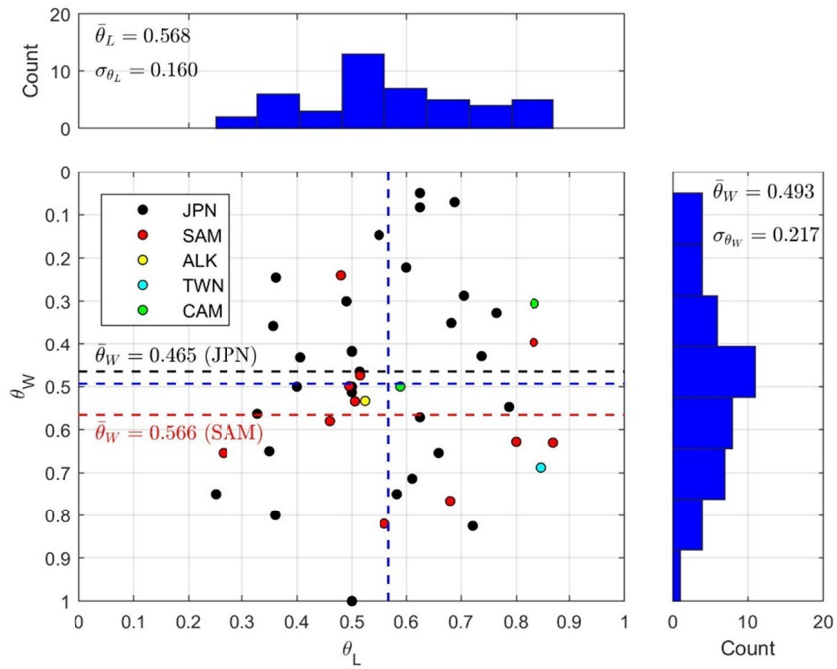


Figure 4.31 Parameterization of earthquake location on fault (view is normal to fault plane from hanging wall).

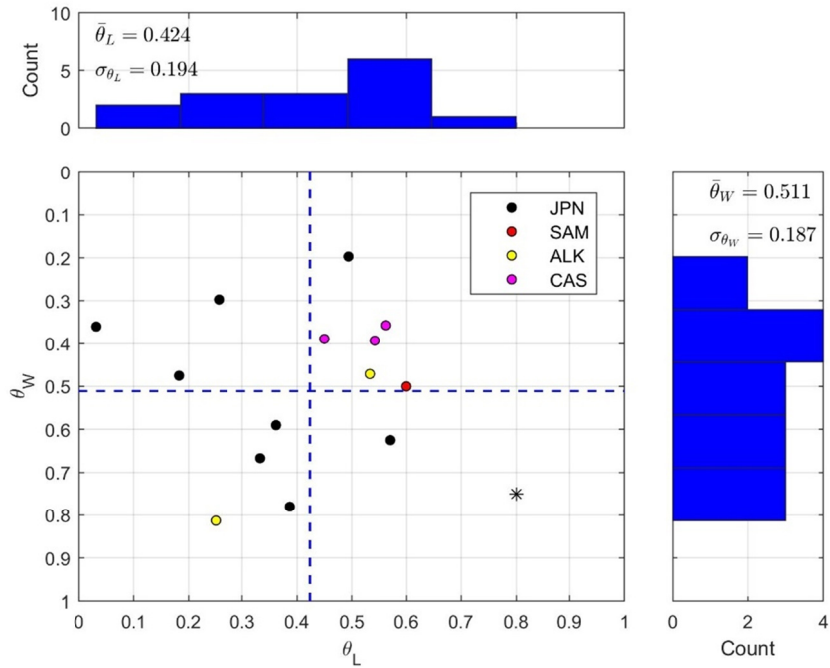


(a)

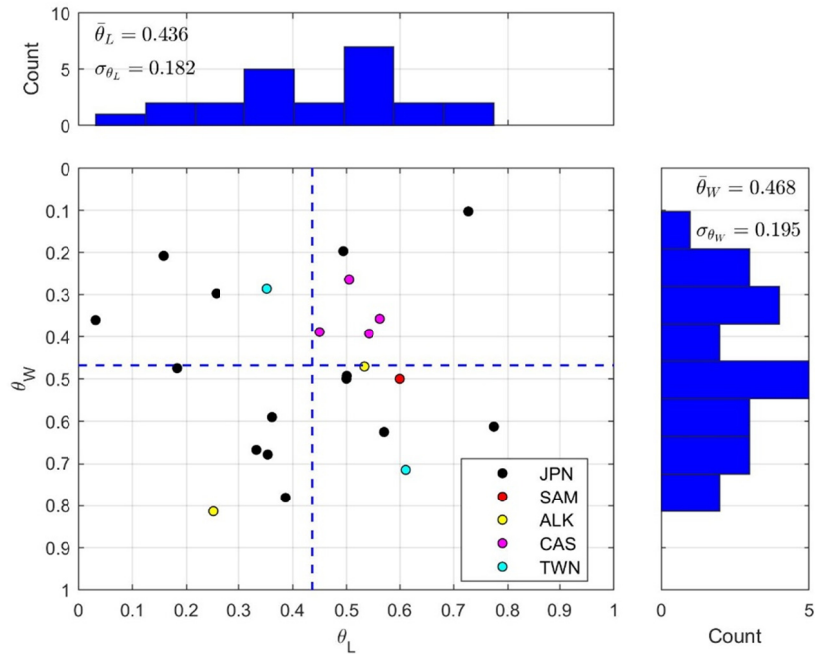


(b)

Figure 4.32 Locations of hypocenters on fault plane for interface events: (a) results for data analyzed to support project simulations (dated November 2017); and (b) results derived using the data in its current state (dated December 2019).



(a)



(b)

Figure 4.33 Locations of hypocenters on fault plane for intraslab events: (a) results for data analyzed to support project simulations (dated November 2017); and (b) results derived using the data in its current state (dated December 2019). The black asterisk represents an event in Japan originally considered as intraslab and later reclassified as outer-rise.

For modeling purposes, a specific hypocenter location is expressed as:

$$\theta_L = \bar{\theta}_L + \varepsilon_{n3} \sigma_{\theta_L} \quad (4.10)$$

$$\theta_W = \bar{\theta}_W + \varepsilon_{n4} \sigma_{\theta_W} \quad (4.11)$$

where ε_{n3} and ε_{n4} are standard normal variates. The distributions are truncated at the limits of the rectangle (i.e., both θ_L and θ_W have a range of 0 to 1.0). Based on the results of earlier analyses performed to support project simulations (dated November 2017) and shown in Figures 4.32(a) and 4.33(a), the along-strike mean was taken at the mid-point ($\bar{\theta}_L = 0.5$) for both interface and intraslab earthquakes. Down-dip means were taken using the regionally variable values in Figure 4.32(a) for interface events and at mid-depth ($\bar{\theta}_W = 0.5$) regardless of region for intraslab. The utilized standard deviation values as derived from data are shown in Figure 4.32(a) for interface events and in Figure 4.33(a) for intraslab events.

4.4.2 Finite-Fault Simulation Procedure

A simulation procedure is used to generate approximate fault dimensions conditional on the magnitude of the earthquake (M), the earthquake type, the hypocenter location (latitude, longitude, and focal depth), and orientation of one or two nodal planes (strike and dip). As part of the NGA-Sub project, we modified a procedure presented by Chiou and Youngs [2008]. The modified procedure operates as follows:

1. Identify source-specific information that comprises the input to the simulation procedure—hypocenter location, M , nodal plane strikes, and dips (if available). The procedure allows for one preferred nodal plane from a moment tensor, two equally likely nodal planes from a moment tensor, or variable plane strike/dip angles when no moment tensor is available [per Equations (4.8–4.9)].
2. Compute mean values of along-strike length as $\overline{\ln L} = 0.5(\overline{\ln A} + \overline{\ln L/W})$ and down-dip width as $\overline{\ln W} = 0.5(\overline{\ln A} - \overline{\ln L/W})$, with mean area and aspect ratio taken from Equations (4.6–4.7), respectively (with “applied” coefficients and ε_n terms set to zero).
3. Using independent random number generators, select a realization of variates ε_{n1} to ε_{n4} .
4. Define the fault dimensions L and W for the realization in (3) as:

$$\overline{\ln L} = 0.5(\overline{\ln A} + \varepsilon_{n1} \sigma_A + \overline{\ln L/W} + \varepsilon_{n2} \sigma_{L/W}) \quad (4.12)$$

$$\overline{\ln W} = 0.5(\overline{\ln A} + \varepsilon_{n3} \sigma_A - \overline{\ln L/W} + \varepsilon_{n4} \sigma_{L/W}) \quad (4.13)$$

6. Define the specific fault location aligned with the strike and dip of the nodal plane using Equations (4.8–4.9). Note that the absolute location of the hypocenter in space is fixed and does not change.
7. Sample across random variables as follows:
 - a. If a preferred moment tensor nodal plane is defined for the event, use $N = 101$ realizations across variates ε_{n1} to ε_{n4} .
 - b. If two alternative nodal planes are to be considered, repeat the process in (4a) for both nodal planes. For this case we use $N = 101$ realizations across both variates ε_{n1} to ε_{n4} and across both nodal planes (approximately 50 realizations of the variates for each plane).
 - c. For events without a moment tensor in which strike and dip are estimated, $N = 101$ realizations are applied for variates ε_{n1} to ε_{n4} and ε_{ϕ} to ε_{δ} .
8. For all 101 realizations of fault rectangles from (3)–(6), compute distances to a grid of points on the ground surface. The grid is defined as an array in polar coordinates (ρ, θ) . The radius (ρ) extends to 300 km from the epicenter, with variable spacing between grid points ranging from 2 km near the epicenter ($\rho \leq 20$ km) to 25 km in the outermost region ($125 \text{ km} \leq \rho \leq 300 \text{ km}$). The angular coordinate (θ) varies from 0 to 345° in 15° increments.
9. For each grid point, compute the median distance among realizations. Identify the single fault plane among the 101 realizations that minimizes the misfit (sum of square of residuals) to the set of medians for all grid points.

This procedure is coded in Fortran (CCLD5).

4.5 SITE-TO-SOURCE DISTANCE

4.5.1 Distance Computation

Final site-to-source distance computations were performed using a code (P4CF) that takes as input the locations of ground-motion stations that recorded the event (geodetic coordinates) and the three-dimensional representation of the ruptured fault. The fault is represented by one or more rectangles, each of which is located by geodetic coordinates and depth of the upper left corner (when viewed from hanging wall), strike, dip, along-strike length, and down-dip width. As described in Sections 4.3 and 4.4, attributes of the fault surface rectangles are established from FFMs in literature with some trimming, as discussed in Section 4.3.3, and from a simulation procedure otherwise. Where more than one rectangle is used to represent a rupture surface, distances are computed to each and the closest distances are used.

The output of P4CF for a given site is rupture distance (closest distance from site to any point on the fault surface), Joyner-Boore distance (closest distance from site to any point on the surface projection of the fault surface), R_x (distance measured perpendicular to the fault strike from the surface projection of the up-dip edge of the fault plane), R_y (distance measured parallel to the fault strike from the midpoint of the surface projection of the fault plane), R_{y0} (distance

measured parallel to the fault strike from the end of the surface projection of the fault plane), R_{hyp} (hypocentral distance), R_{epi} (epicentral distance), R_{rms} (root-mean-square distance), the location on the fault surface from which the closest distance was measured (geodetic coordinates and depth), and a series of parameters related to rupture directivity modeling that were not used in NGA-Sub. These outputs are saved to the *Path* table. Another path-related table, derived using procedures described in Section 4.8, lists percentages of the path through zones with different volcanic-arc flags (*EventVolArc* table).

4.5.2 Calculation of R_{max}

Earthquake ground motions can be subject to sampling errors for conditions that tend to produce low-amplitude shaking near the trigger threshold for triggered instruments or the noise threshold for instruments that record continuously. This is typically the case at large distances; it is more pronounced for small magnitude events than large magnitude.

The problem is not that no records are obtained for such conditions, but that the recorded ground motions may be unusually strong. Weaker motions that do not exceed trigger thresholds are not recorded and those near noise levels are not useful, which tend to bias the dataset. One way of managing this problem in the development of ground-motion models is to not consider data beyond a limiting distance, which is referred to as R_{max} . The selection of R_{max} should take into account event magnitude and the sensitivity of the recording instruments.

As part of the NGA-Sub project, R_{max} values were calculated for different events, networks, and instrument types. The R_{max} values were calculated by fitting a truncated robust regression to the data from each source region, and then calculating the intersection of the median prediction for each event minus a scale factor times the estimated within-event standard deviation with the truncation levels. Values of R_{max} are saved to the *Path* tables.

(a) Data selection

The analysis was carried out using the version of the NGA-sub flatfile dated 11/17/2017. An initial data screening was performed with the following exclusion criteria:

- $M > 4$;
- $R_{rup} > 0$;
- $V_{S30} > 0$;
- $Z_{HYP} > 0$;
- dip angle larger than zero;
- rake angle not equal to -999 or -888;
- multiple event flag not equal to 1;
- Inter Intra Flag equal to 0,1,5 ;
- sensor depth < 2 m;
- exclude Geomatrix 1st letter equal to F [Chiou et al. 2008];
- visual quality flag not equal to 2 or 9 (late S-trigger and “do not use”); and
- exclude records with absolute value of peak acceleration < 0 .

(b) Truncation levels

The calculation of R_{max} values depends on the truncation level for each network: the truncation level affects the fit of the truncated regression as well as the calculation of the intersection with the fit. For some networks, the truncation level is known, but not all networks in the database have an associated trigger level. In addition, even for a known trigger threshold, it is possible to observe ground motions that are lower than the trigger threshold [e.g., if one of the horizontal components has a peak ground acceleration (PGA) value that is larger than the trigger threshold but the other has a smaller PGA value, then it is possible that RotD50 is lower than the nominal truncation level]. For the truncated regression, it is required that the target variable is larger than the truncation level, so the truncation levels are set dependent on the observed data for each network.

By plotting histograms of the PGA values from each network, as well as plots of PGA vs. distance, it is possible to visually identify truncation levels; however, these truncation levels are subjective, and the analysis does not work for networks with a limited amount of data.

The truncation levels were set in an automated way. Different truncation levels were used for instrument types “A” (accelerometers) and “V” (broadband instruments). For instrument type “V”, the truncation level is set to $10^{-7}g$ for all networks, which is assumed to correspond to the noise level.

For instrument type “A”, first, a list of possible truncation levels was generated. The possible truncation levels are $0.0001gal$, $0.0002gal$, $0.0003gal...$, $0.001gal$, $0.002gal...$, $1gal$, $2gal...$. Then, the following methodology to estimate truncation levels for the different networks was carried out:

1. For each network, select all records of instrument type “A”;
2. Discard 10% of the selected records that have the lowest PGA values; and
3. Find the largest truncation level from the list of possible values that is lower than the lowest PGA value of the remaining records.

Records with instrument type –999 (unknown) were treated as accelerometers.

(c) Regression

For each source region, a truncated robust multilevel regression was performed. The following functional form was used:

$$\begin{aligned} \mu_{in} = & \beta_1 + (\beta_2 + \beta_{2a}F_S + \beta_3M) \ln \{ R_{rup} + c_4 \exp[\theta_9(M-6)] \} a \\ & + lh(\mathbf{M}, \beta_4, \beta_5, m_b, \delta) + \beta_6R + \beta_8F_S \\ & + F_S lh(Z_H, \beta_9, \beta_{10}, z_b, \delta) + \eta_E \end{aligned} \quad (4.14)$$

where μ_{in} is the median prediction (including the event term η_E), and the event term is sampled from a normal distribution with mean zero and standard deviation τ . The ground-motion likelihood is modeled as a truncated Student-t distribution with degree-of-freedom parameter ν and standard deviation ϕ . F_S denotes the interface/intraslab flag, and $lh(\cdot)$ is a logistic hinge function defined as follows:

$$\ln(\mathbf{M}, \beta_4, \beta_5, m_b, \delta) = \beta_4(\mathbf{M} - m_b) + (\beta_5 - \beta_4) \delta \ln \left[1 + \exp\left(\frac{\mathbf{M} - m_b}{\delta}\right) \right] \quad (4.15)$$

The following coefficients were fixed using values in the “BC Hydro” model [Abrahamson et al. 2016]:

$$c_4 = 10$$

$$\theta_9 = 0.4$$

$$\beta_{10} = 0$$

$$\beta_3 = 0.1$$

$$\beta_{2a} = -0.23$$

$$\delta = 0.1$$

$$z_b = 120 \text{ km}$$

Coefficients evaluated by region include $\beta_1, \beta_2, \beta_4, \beta_5, \beta_6, \beta_8, \beta_9$, as well as the standard deviations τ and ϕ together with the parameter ν and the event terms η_E . The other coefficients are set to values estimated by a global regression. The magnitude break point is $m_b = 8$ for interface events and $m_b = 7.5$ for intraslab events.

The Student-t distribution has heavier tails than the normal distribution and is thus less sensitive to outliers. For large values of ν , the Student-t distribution approximates a normal distribution.

All parameters of the model were estimated via Bayesian inference, with weakly informative priors. Only events with at least five recordings were used for the regression.

The estimated standard deviations and parameters ν for the different regions are shown in Figure 4.34. Large values of τ are probably due to the fact that several coefficients are fixed, making the model less flexible. Low values of ν might indicate that there are a lot of outliers for that particular region.

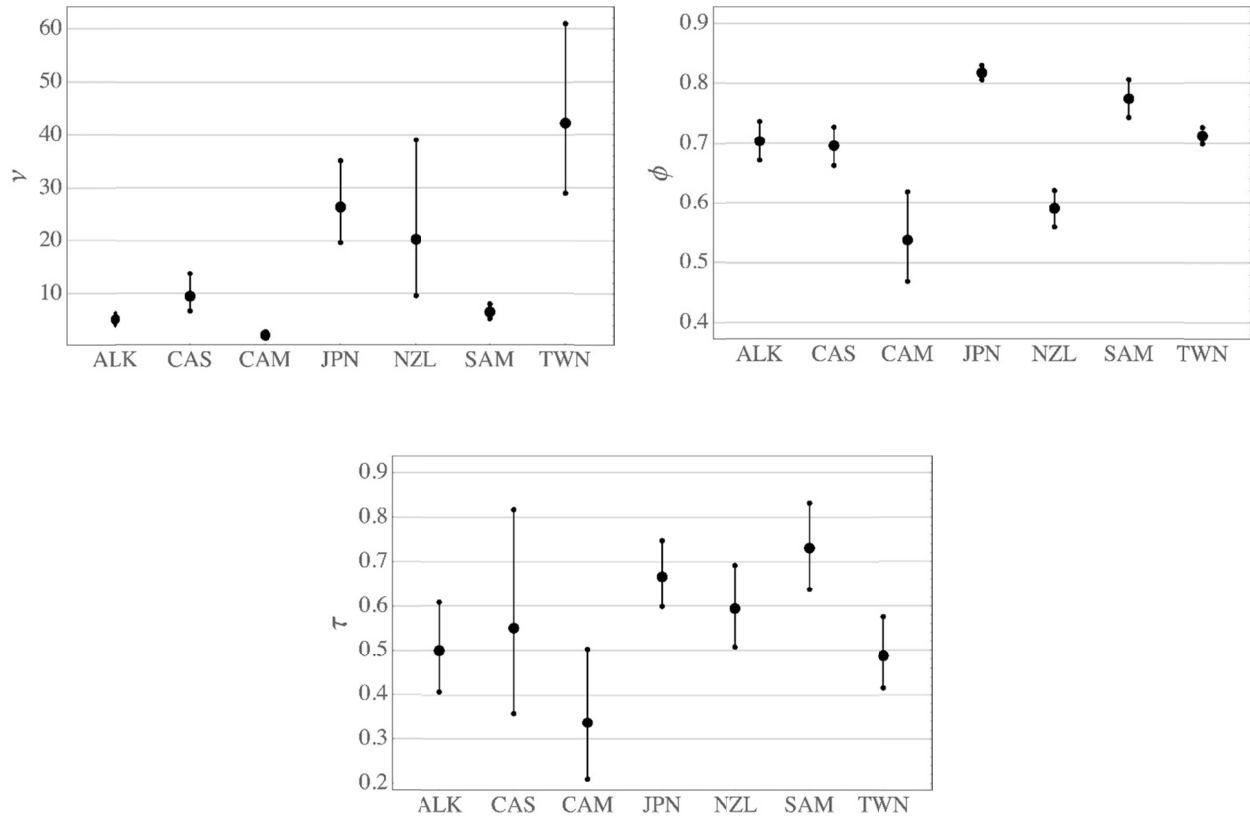


Figure 4.34 Regional coefficients ν , ϕ , and τ from regions to support development of R_{max} .

(d) R_{max} calculations

Different R_{max} values are calculated for different events, networks, and instrument types. The R_{max} values for event i are calculated as the distance where the median prediction for event i [including the event term, see Equation (4.14)], minus 2.5 times the within-event standard deviation ϕ intersects with the truncation levels. Hence, a function $f_i = (R_{RUP}) = \mu_i$ is defined, where μ_i is calculated according to Equation (4.14), with the appropriate values of magnitude, hypocentral depth and interface/intraslab flag, as well as the coefficients for the correct source region. Then, the intersection of $f_i(R_{RUP}) - 2.5\phi$, with the truncation levels for the networks that recorded event i is found. An example is shown in Figure 4.35 for one event.

EQID 2000035

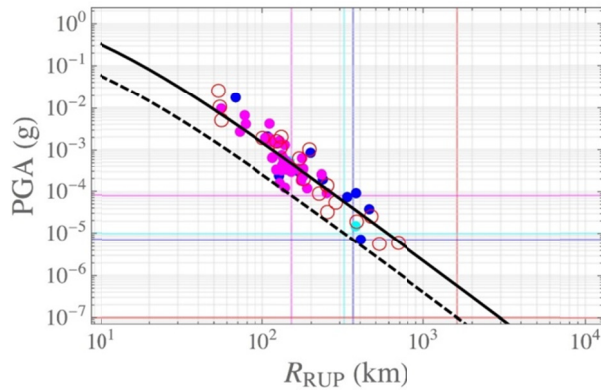


Figure 4.35 R_{max} calculation for event 2000035. Records from different networks are plotted in different colors. The truncation level for each network is plotted as a horizontal line. The median prediction μ for the event is plotted as a black line, the dashed black line shows $\mu - 2.5\phi$. The calculated R_{max} values are shown as vertical lines.

(e) R_{max} calculation for events not in regression dataset

To obtain good estimates of event terms, only events with a minimum of five records were used for the truncated regression. To calculate R_{max} values for the remaining events, a simple regression of the previously computed R_{max} vs. magnitude was performed. Based on the estimated model, R_{max} values for the events not used in the truncated regression were calculated. The model has the following functional form:

$$R_{max} = a_1 + a_2 \mathbf{M} \quad (4.16)$$

Different a_1 and a_2 values are estimated for each network.

4.6 QUALITY-ASSURANCE PROCEDURES

The process of assembling the NGA-Sub database included iterative procedures for checking information for accuracy and consistency. These QA procedures operate on a “current” version of the database for which some issues are to be checked. Those issues often involve seismic-source details as described in this chapter (e.g., missing source parameters, protocol errors in parameter assignments, duplicate events, and inconsistencies in hypocentral locations, event-type classifications, or distance metrics). This is depicted with the white oval on the left side of Figure 4.36 (*NGA-Sub flatfile (ver i) issues*). Figure 4.36 refers to a “flatfile,” which is a large table extracted from the full relational database; see Chapter 2. Most NGA-Sub project team members interact with the database through various versions of the flatfile. Changes to the database are made at the relational database level through edits to component tables. Once the database is updated, a new flatfile is generated and internally disseminated to NGA-Sub researchers.

The QA procedure in Figure 4.36 begins by comparing entries in the “current” flatfile with information from regional flatfiles, which preceded the relational database. These regional flatfiles consist of source, site, and ground-motion tables developed in early stages of the NGA-Sub project, when the main emphasis was data collection from diverse sources. Regional flatfiles

were assembled for Alaska, Cascadia, Central America and Mexico, Japan, New Zealand, South America, and Taiwan. The *Data Comparison* depicted in Figure 4.36 is to check for consistency between the content of the relational database and the regional flatfiles. Differences could occur due to logistical errors in copying material from one set of tables to another, or from technical updates made following completion of the regional flatfiles.

If an inconsistency is found (in Figure 4.36, *Consistent?* → *No*), we next check regional source information (i.e., the information used to assemble the regional flatfiles). This occurs in the *Analyze Issues* box in Figure 4.36. This might include, for example, re-examining the regional earthquake catalogs used to assign seismic moments and hypocenter locations (e.g., Tables 4.2–4.3). These comparisons check for data entry errors or protocol errors (e.g., not using the preferred earthquake catalog for a given region). Various iterations of these checks have impacted event locations (and therefore site-to-source distances), magnitudes, event types (interface, intraslab, shallow crustal, outer-rise), and fault types (focal mechanisms). On the basis of this review, a source review flag is assigned, as shown in Table 4.10. In many cases, events with negative source review flags are not considered in model development. Other aspects of the data that might be evaluated in the *Analyze Issues* box include data derived from recordings (see Chapter 3) and site data (see Chapter 5).

Moving to the right within Figure 4.36, if issues cannot be resolved through the checks of source documents (*Resolved?* diamond), the data in question is marked with a flag; see Table 4.10 for the case of issues with source parameters and Table 3.5 for ground motions. If the issues are resolved, the data enter the protocol for distance metrics calculation. This phase is also reached when the consistency check between regional databases and the current flatfile does not identify problems.

Moving forward in Figure 4.36, in order to compute distance metrics, different paths are followed depending on the availability of a FFM (*Available FFM?* diamond). For events with a FFM, the fault plane is used in P4CF to compute distances (*Distance calculation (P4CF)*). In the absence of a FFM, source geometry simulations are performed using CCLD5 (*Fault plane simulation (CCLD5)*), which produce a fault plane that is then used in P4CF. Distance revisions, along with any updates to source and other parameters, including the source review flag, are then applied to component tables in the relational database (*Update Relational Database*). A new flatfile is then generated, which completes an iteration of the review-and-update process.

Table 4.10 Source review flags.

Source review flag	Description
-999	Earthquake review is pending. Avoid using the recordings from these events.
-888	NGA-West 2 event. Source parameters were not reviewed in NGA-Sub project.
-2	Earthquake was not reviewed because of limited information or missing moment tensor solution
-1	Earthquake was reviewed but there are important inconsistencies
0	Earthquake was reviewed based on the existing information. All the required parameters were available or estimated
1	Rake angle is defined based on the inter_intra_flag (not from FFM or MT solution)
2	Hypocentral coordinates were slightly modified to be consistent with the FFM.
3	Moment Magnitude M is estimated from other magnitude scales (M_S , M_L , or m_b)
4	Strike, dip, and rake angles are based on the inter_intra_flag and/or simulations (not from FFM or MT solution)

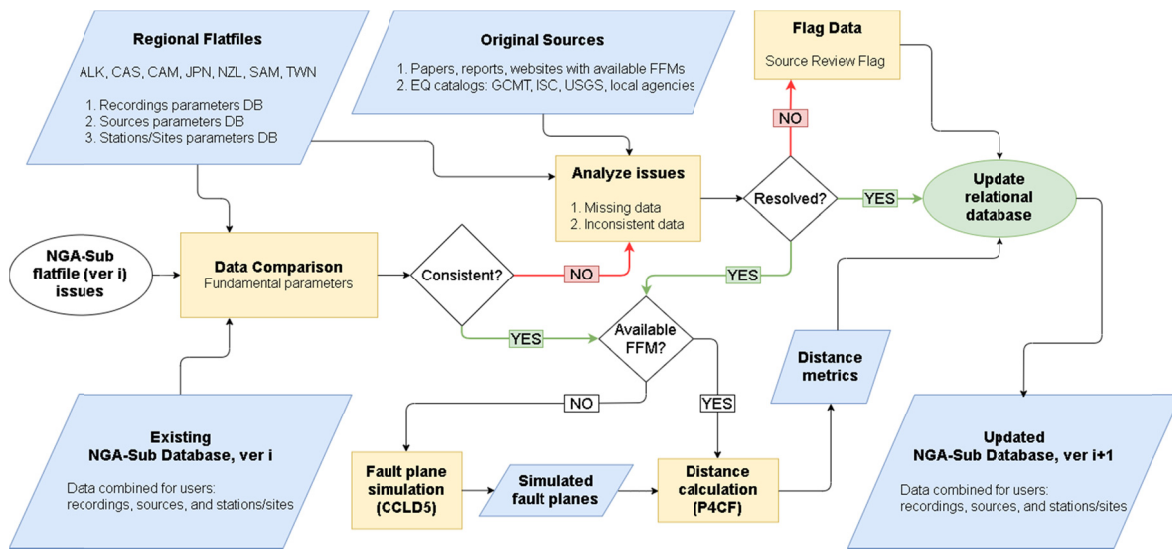


Figure 4.36 Flowchart illustrating procedure used to resolve issues with prior version of the flatfile, ultimately resulting in an updated version of the database. Ovals represent start and finish points of the procedure, blue parallelograms represent data, yellow boxes represent data analyses, and white diamonds represent decision points.

4.7 MAINSHOCK AND AFTERSHOCK CLASSIFICATION

Our hypothesis for the NGA-Sub project is aftershocks that re-rupture the mainshock rupture plane and surrounding damaged zones will have lower stress drops, and therefore lower short-period ground motions than the aftershocks that occur in more competent material further from the mainshock rupture plane. Thus, the goal of aftershock classification for NGA-subduction was

not to identify all aftershocks but to identify the subset of aftershocks that allow for testing of the hypothesis. To avoid confusion with definitions used in seismology, the NGA-Sub project classifies earthquake mainshocks as Class 1 (C1) events, and the subset of aftershocks that occur sufficiently close to the Class 1 rupture plane in both space and time are classified as Class 2 (C2) events. The main content of this section was previously presented by Wooddell [2018].

4.7.1 Methodology

Similar to NGA-West 2 [Wooddell and Abrahamson 2014], the NGA-Sub earthquake classification algorithm is based on the windowing approach of Gardner and Knopoff [1974]. The Gardner–Knopoff time window was adopted without modification. The distance window was modified and two new distance metrics were developed, resulting in two new algorithms for classifying earthquakes. The first approach is based on the closest distance from the Class 1 rupture plane to the potential Class 2 hypocenter ($R_{\text{CLOSEST_P2H}}$). In this approach, if a potential Class 2 event is within the Gardner–Knopoff time window and has a hypocenter within a predetermined cutoff distance, it is a Class 2 event. The second approach is based on the closest distance from the Class 1 rupture plane to the potential Class 2 rupture plane ($R_{\text{CLOSEST_P2P}}$). In this approach, if a potential Class 2 event is within the Gardner–Knopoff time window and has a $R_{\text{CLOSEST_P2P}}$ distance within a predetermined cutoff distance, it is a Class 2 event. For this method, the percentage of the Class 2 rupture plane within the predetermined cutoff distance is also computed. Development of two alternative distance metrics was motivated by different ideas about what part of the rupture process has the greatest effect on the resulting ground motion. The metric $R_{\text{CLOSEST_P2H}}$ suggests that closeness of the Class 1 rupture plane to the center of the moment release in the Class 2 event will have a greater effect on the resulting ground motion, whereas the $R_{\text{CLOSEST_P2P}}$ metric assumes that the more important parameter is the distance between the two rupture planes and the percentage of the Class 2 rupture plane within the defined distance window from the Class 1 rupture plane.

Figure 4.37 illustrates the difference between the different distance metrics for two faults with four segments (each represented by a plane). The Class 1 rupture plane is defined as $C1_{a-d}$, and the potential Class 2 rupture plane is defined as $C2_{a-d}$. Each rupture plane is divided into subfaults of dimension 1km^2 and a red star indicates the location of the hypocenter. In this case, $R_{\text{CLOSEST_P2H}}$ results in a greater distance than the $R_{\text{CLOSEST_P2P}}$ metric because the potential Class 2 hypocenter is far from the Class 1 rupture plane. Therefore, for this pair of faults, the potential Class 2 earthquake would be less likely to be classified as a Class 2 event if the $R_{\text{CLOSEST_P2H}}$ metric is used and more likely to be classified as a Class 2 event if the $R_{\text{CLOSEST_P2P}}$ metric is used.

For each distance metric, classifications were made using earthquake datasets from the following regions: Alaska, Cascadia, Central America and Mexico, Japan, South America, and Taiwan. Classifications were not made for New Zealand. Classifications were made for cutoff distances of 10, 20, 40, and 80 km, and the results are included in the *EventClass* table of the relational database. For the $R_{\text{CLOSEST_P2P}}$ metric, an additional column is also included showing the percentage of the Class 2 rupture plane within the prescribed cutoff distance from the Class 1 rupture plane.

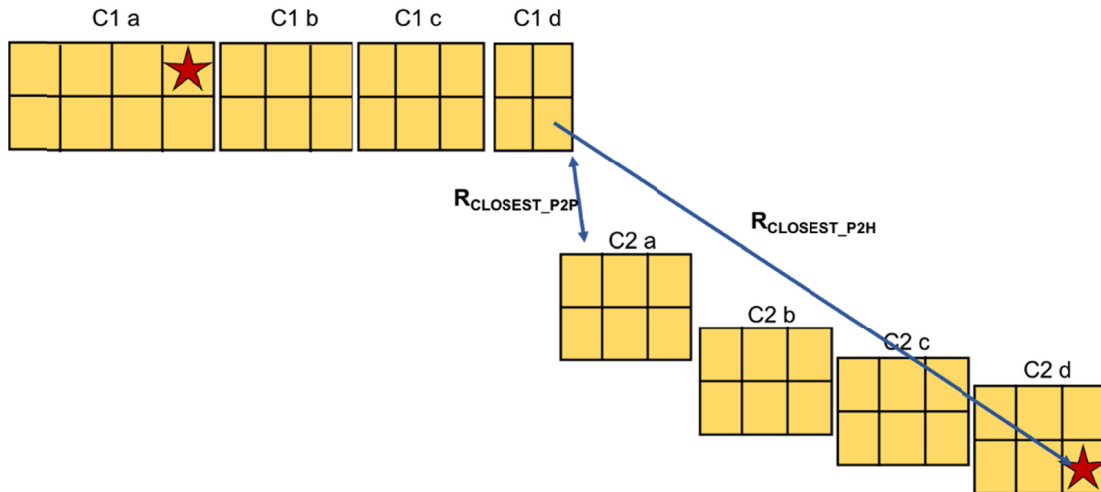


Figure 4.37 Definition of the $R_{\text{CLOSEST_P2H}}$ and $R_{\text{CLOSEST_P2P}}$ distance metrics. The four-segment Class 1 rupture plane is defined as $C1_{a-d}$, and the four-segment potential Class 2 rupture plane is defined as $C2_{a-d}$. Each segment is divided into 1km^2 subfaults; the hypocenters are shown as red stars.

4.7.2 Results

The results of this classification algorithm are evaluated for each distance metric using a subset of the better recorded data (at least five records) with recordings spanning a distance range of a factor of 3.5 for distances up to 400 km. Figure 4.38 shows the total number of earthquakes over a range of spectral periods for this subset of data, and how many of these earthquakes are Class 1 and Class 2 if a distance cutoff of 40 km is used.

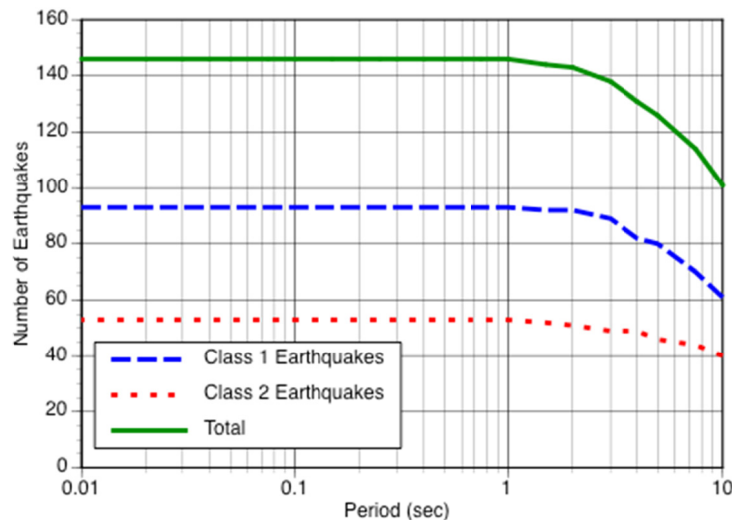


Figure 4.38 Number of Class 1 and Class 2 earthquakes resulting from a cutoff distance of 40 km, using the data screening described in the text.

4.8 VOLCANIC-ARC FLAGS

Subduction zone plate boundaries produce geologic structures in the crust and upper mantle that affect seismic-wave propagation. Many subduction zones are associated with a volcanic arc, where the down-going oceanic slab begins to melt, and plumes of magma rise to form volcanoes on the surface of the overriding slabs. For NGA-Sub, volcanic-arc locations were used to categorize the forearc (trench-side) and backarc of each subduction-zone region.

The delineation of the volcanic arc allows both epicentral locations and strong-motion sites to be classified as forearc or backarc. Most subduction-zone events occur either at the interface or within the subducting slab. Interface events are generally in the forearc. Intraslab events are also mostly in the forearc, but some can occur in the backarc when located in the slab at great depth (e.g., see Figure 4.39).

Volcanic arcs were determined for each of the seven regions in the NGA-Sub database by drawing a line (by eye) through the average trend of volcanic peaks. The locations of volcanic peaks, based on volcanoes with eruptions during the Holocene period (approximately the last 10,000 years), were obtained from the Smithsonian Institute's Global Volcanism Program [2013]. Judgment was used to draw a smooth line for the volcanic arc rather than representing the arc as a jagged piecewise line connecting individual volcanic peaks. Figure 4.40 shows for the example of Alaska volcano locations (orange symbols) and the volcanic arc passing through them (green line between zones 1 and 2). This task was repeated for all of the NGA-Sub regions except Taiwan. All Taiwan sites received a forearc flag assignment of 2, as the island largely consists of forearc accretionary sediments [Ho 1986; Chemenda et al. 1997; and Lundberg et al. 1997].

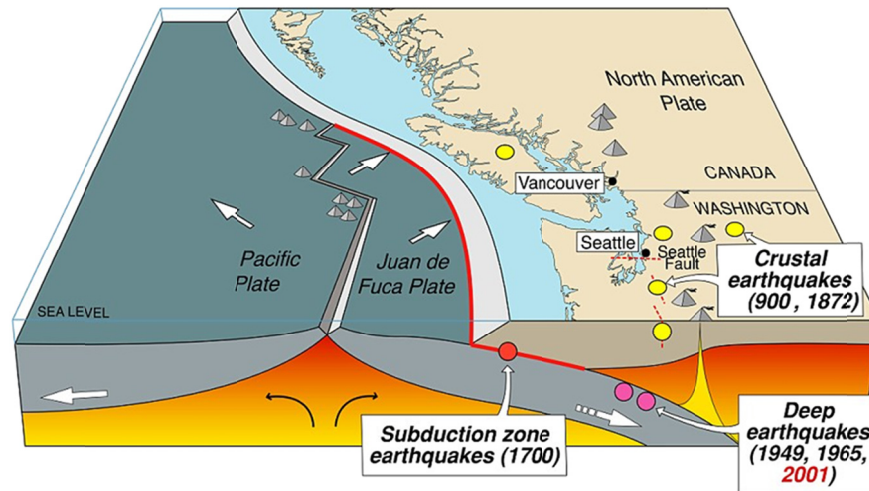


Figure 4.39 Cascadia subduction-zone geometry displaying different earthquake sources. Interface earthquakes are labeled as “subduction zone earthquakes” and intraslab earthquakes are labeled as “deep earthquakes” (after Wells et al. [2000]).

All events and ground-motion recording sites were assigned one of the volcanic-arc flags listed in Table 4.11. Volcanic-arc flags are provided for each event in the *EventVolArc* table within the source database and for each site in the *SiteVolArc* table. Most back-arcs correspond to Flag 1 and most forearcs to Flag 2. Japan’s complex tectonic geometry required it to be separated into multiple forearc and backarc regions. There are two forearcs relating to subduction of both the Pacific and Philippine Sea plates under Japan; see Figure 4.41. The Philippine Sea plate subducts beneath the southern portion of Japan at the Nankai Trough; the associated forearc is designated Flag 3.

The lateral limits of the volcanic arc correspond to the limits of the subducting slab. In general, the edges of the subducting slab were defined by the limits of slab-depth contours as defined by the USGS’s Slab1.0 model [Hayes et al. 2012]. Figure 4.40 shows how the edges of the slab, as well as the edges of the forearc and backarc zones, were defined for the example of the Alaska subduction zone. Areas deemed to be outside of the subduction zone (east of the edge in Figure 4.40) are assigned Flag 0. Similarly, Figure 4.41 shows how the boundaries for the forearc and backarc zones were defined for the Japan subduction zone.

Table 4.11 Description of volcanic-arc flags.

Flag	Event Count	Site Count	Description
0	168	561	Outside of volcanic-arc zone
1	175	1927	Backarc
2	1408	3169	Forearc
3	31	708	Forearc, Ryukyu Trench

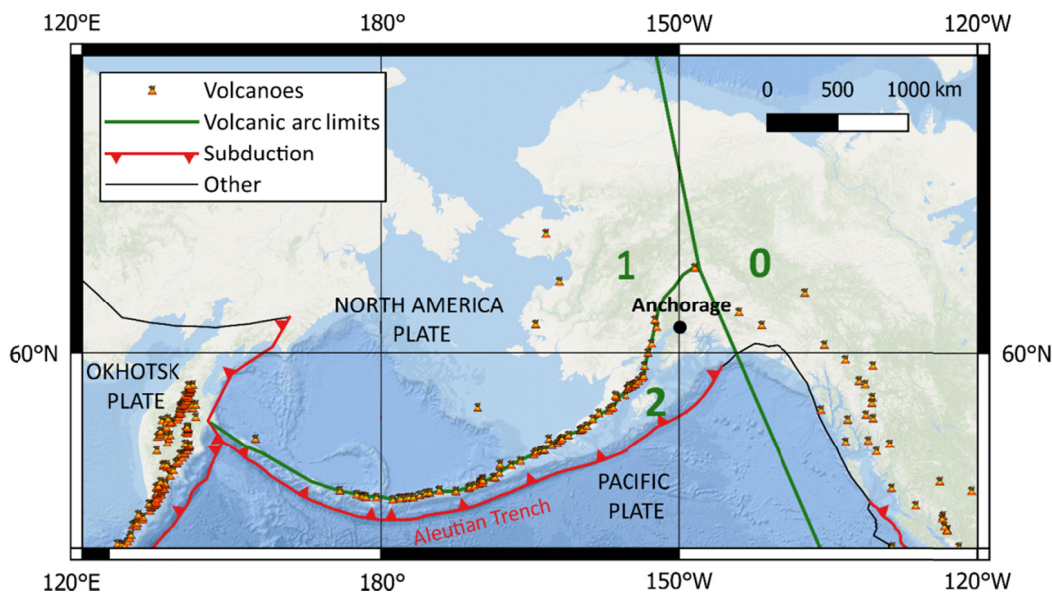


Figure 4.40 Example of the extent of the volcanic flag region in Alaska/Aleutians subduction zone. The green line between zones 1 and 2 follows the average trend of volcanic peaks.

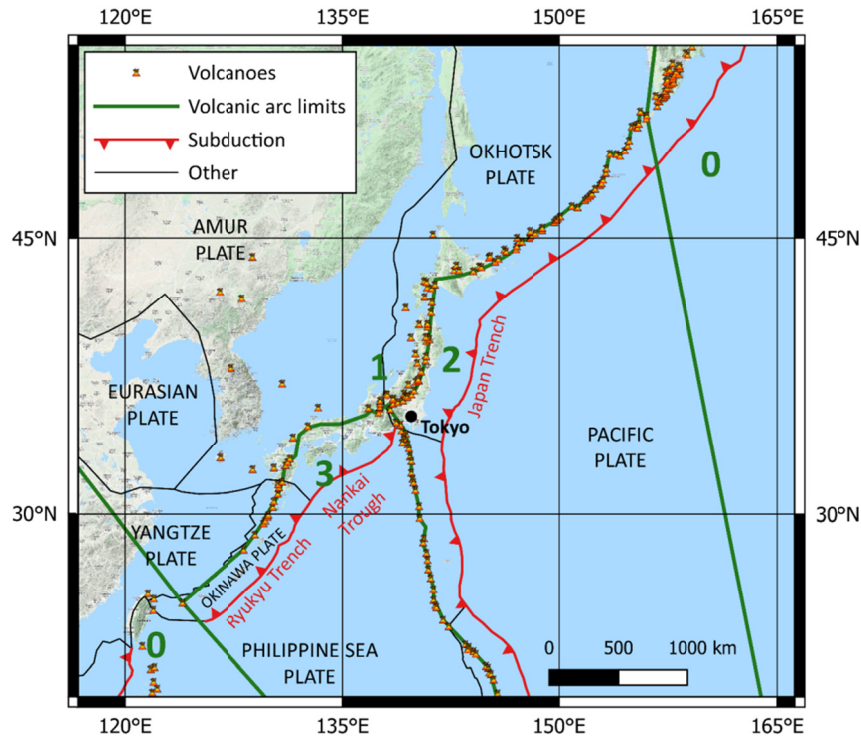


Figure 4.41 Extent of the volcanic flag region in Japan subduction zone. The green lines between zones 1, 2, and 3 follow the average trend of volcanic peaks.

The volcanic-arc regions described in this section were used to compute portions of path lengths within each zone for use in GMM development. Path length is computed from the point on the fault from which the closest distance is measured (an output of the P4CF code; Section 4.5) to the site, and the fractions are evaluated based on the portion of the path in zones with different flags, as applicable. Zone percentages for a given path are listed in the *PathVolArc* table.

Suggested Citation:

Contreras V., Stewart J.P., Kishida T., Darragh R.B., Chiou B.S.J., Mazzoni S., Kuehn N., Ahdi S.K., Wooddell K., Youngs R.R., Bozorgnia Y., Boroschek R., Rojas F., Órdenes J. (2020). Chapter 4: Source and Path Metadata, in *Data Resources for NGA-Subduction Project, PEER Report 2020/02*, J.P. Stewart (editor), Pacific Earthquake Engineering Research Center, University of California, Berkeley, CA (headquarters).

REFERENCES

- Abe K. (1975). Static and dynamic fault parameters of the Saitama earthquake of July 1, 1968, *Tectonophys.*, 27: 223–238.
- Abrahamson N.A., Gregor N., Addo K. (2016). BC Hydro Ground motion prediction equations for subduction earthquakes, *Earthq. Spectra*, 32: 23–44.
- Aki K., Richards P.G. (1980). *Quantitative Seismology*, 2nd Ed., W.H. Freeman, San Francisco, CA.
- Ammon C.J., Kanamori H., Lay T. (2008). A great earthquake doublet and seismic stress transfer cycle in the central Kuril islands, *Nature*, 451(31): 561–565.
- Ancheta T.D., Darragh R.B., Stewart J.P., Seyhan E., Silva W.J., Chiou B.S.J., Woodell K.E., Graves R.W., Kottke A.R., Boore D.M., Kishida T., Donahue J.L. (2013). PEER NGA-West 2 database, *PEER Report No. 2013/03*, Pacific Earthquake Engineering Research Center, Berkeley, CA.
- Anderson J.G., Kawase H., Biasi G.P., Brune J.N., Aoi S. (2013). Ground motions in the Fukushima Hamadori, Japan, normal-faulting earthquake, *Bull. Seismol. Soc. Am.*, 103(3): 1935–1951.
- Atkinson G.M., Macias M. (2009). Predicted ground motions for great interface earthquakes in the Cascadia subduction zone, *Bull. Seismol. Soc. Am.*, 99(3): 1552–1578.
- Bai L., Luna L.M., Hetland E.A., Ritsema J. (2014). Focal depths and mechanisms of Tohoku-Oki aftershocks from teleseismic P wave modeling, *Earthq. Sci.*, 27: 1–13.
- Bastías N., Montalva G.A. (2016). Chile strong ground motion flatfile, *Earthq. Spectra*, 32(4): 2549–2566.
- Bird P. (2003). An updated digital model of plate boundaries, *Geochem., Geophys., Geosys.*, 4(3): 1–52.
- Chemenda A.I., Yang R.K., Hsieh C.-H., Groholsky A.L. (1997). Evolutionary model for the Taiwan collision based on physical modeling, *Tectonophys.*, 274: 253–274.
- Chiou B.S.-J. Youngs R.R. (2008). NGA model for average horizontal component of peak ground motion and response spectra, *PEER Report No. 2008/09*, Pacific Earthquake Engineering Research Center, Berkeley, CA.
- Chiou B.S.-J., Darragh R.B., Gregor N., Silva W.J. (2008). NGA project strong motion database, *Earthq. Spectra*, 24(1): 23–44.
- Contreras V. (2009). *Curvas de Atenuación para Sismos Chilenos*, Thesis, Department of Civil Engineering, University of Chile, Santiago, Chile. (In Spanish).
- Delouis B., Nocquet J.-M., Vallée M. (2010). Slip distribution of the February 27, 2010 Mw = 8.8 Maule Earthquake, central Chile, from static and high-rate GPS, InSAR, and broadband teleseismic data, *Geophys. Res. Lett.*, 37: L17305.
- Duputel Z., Rivera L., Kanamori H., Hayes G. (2012). W phase source inversion for moderate to large earthquakes (1990–2010), *Geophys. J. Int.*, 189(2): 1125–1147, <https://doi.org/10.1111/j.1365-246X.2012.05419.x>.
- EIC (2003). 2003/10/31 Fukushima-oki (Mj6.8) Inversion analysis by farfield waveforms (preliminary) *EIC Seismology Note No.141*, Nov. 02, 03, http://www.eri.u-tokyo.ac.jp/sanchu/Seismo_Note/EIC_News/031031.html.
- Ekström G., Nettles M., Dziewonski A.M. (2012). The global CMT project 2004–2010: Centroid-moment tensors for 13,017 earthquakes, *Phys. Earth Planet. Inter.*, 200–201: 1–9.
- Engdahl E.R., van der Hilst R., Buland R. (1998). Global teleseismic earthquake relocation with improved travel times and procedures for depth determination, *Bull. Seism. Soc. Am.*, 88: 722–743.
- ERI (2009). 2009/08/09 Tokaido South-oki Earthquake: inversion process, Earthquake Research Institute, University of Tokyo, http://www.eri.u-tokyo.ac.jp/topics/200908_Tokaido/#SourceInversion.
- Fukuyama E., Irikura K. (1986). Rupture process of the 1983 Japan sea (Akita-Oki) earthquake using a waveform inversion method, *Bull. Seism. Soc. Am.*, 76: 1623–1640.

- Fukuyama E. (1991). Inversion for the rupture details of the 1987 East Chiba earthquake, Japan, using a fault model based on the distribution of relocated aftershocks, *J. Geophys. Res.*, 96(B5): 8205–8217.
- Gardner J., Knopoff L. (1974). Is the sequence of earthquakes in Southern California, with aftershocks removed, Poissonian?, *Bull. Seism. Soc. Am.*, 64(5): 1363–1367.
- Geospatial Information Authority of Japan (2009). 2009/08/11 05:07:00 Surugawan Earthquake: Source model and crustal displacement (preliminary).
- Hanks T.C., Kanamori H. (1977). A moment magnitude scale, *J. Geophys. Res.*, 84(B5): 2348–2350.
- Hatanaka Y., Takeo M. (1989). Detailed rupture process of the 1975 Central Oita, Japan, earthquake inferred from near-field data, *J. Phys. Earth*, 37: 251–264.
- Hayes G.P. (2010). Updated result of the Feb 27, 2010 Mw 8.8 Maule, Chile, earthquake, NEIC, available at http://earthquake.usgs.gov/earthquakes/cqinthenews/2010/us2010tfan/finite_fault.php (last accessed August 19, 2013).
- Hayes G.P., Wald DJ., Johnson R.L. (2012). Slab1.0: A three-dimensional model of global subduction zone geometries, *J. Geophys. Res.*, 117:B01302.
- Hayes G.P. (2016). Preliminary Finite Fault Results for the Apr 16, 2016 Mw 7.8 28 km SSE of Muisne, Ecuador earthquake (Version 1), <http://earthquake.usgs.gov/earthquakes/eventpage/us20005j32#finite-fault>
- Hayes G. (2017). Preliminary Finite Fault Results for the Feb 27, 2010 Mw 8.9 -36.2200, -73.1740 earthquake (Version 1), NEIC, available at https://earthquake.usgs.gov/earthquakes/eventpage/official20100227063411530_30#finite-fault (last accessed May 2017).
- HERP (2006). Evaluation of seismic activity in November 2004, Headquarters for Earthquake Research Promotion, http://www.static.jishin.go.jp/resource/monthly/2004/2004_11.pdf, in Japanese.
- HERP (2011). Source model of 2011/04/12 Chiba East-oki earthquake (M6.4) (preliminary), Headquarters for Earthquake Research Promotion, <http://www.jishin.go.jp/main/chousa/11may/p26.htm>, in Japanese.
- Ho C.S. (1986). A synthesis of the geologic evolution of Taiwan, *Tectonophysics*, 125: 1–16.
- Ichinose G.A., Thio H.K., Somerville P.G. (2004). Rupture process and near-source shaking of the 1965 Seattle-Tacoma and 2001 Nisqually, intraslab earthquakes, *Geophys. Res. Lett.*, 31: L10604, <https://doi.org/10.1029/2004GL019668>.
- Ichinose G.A., Thio H.K., Somerville P.G. (2006a). Ground motion studies of modern and historical Cascadia intraslab earthquakes using one and three-dimensional waveform modeling methods to generate ground shaking maps, *USGS Technical Report Award Number 04HQGR0050*, United States Geological Survey, Washington, D.C.
- Ichinose G.A., Thio H.K., Somerville P.G. (2006b). Moment tensor and rupture model for the 1949 Olympia, Washington, earthquake and scaling relations for Cascadia and global intraslab earthquakes, *Bull. Seismol. Soc. Am.*, 96(3): 1029–1037.
- Ide S., Takeo M. (1996). The dynamic rupture process of the 1993 Kushiro-oki earthquake, *J. Geophys. Res.*, 101(B3): 5661–5675.
- International Seismological Centre (2019). On-line Bulletin, <https://doi.org/10.31905/D808B830>. ISC, Thatcham, United Kingdom (last accessed Dec. 2019).
- JMA (2005). The earthquake that occurred off Sanriku on November 15, 2005, http://cais.gsi.go.jp/KAIHOU/report/kaihou75/03_15.pdf
- JMA (2008). Earthquake Prediction Information Division, Earthquake and Tsunami Observation Division, JMA, The M7.1 Earthquake off Tokachi district on September 11, 2008, http://cais.gsi.go.jp/KAIHOU/report/kaihou81/02_02.pdf
- JMA (2011a). 2011/03/11 Ibaraki-oki Earthquake - Inversion analysis by nearfield waveforms (preliminary)
- JMA (2011b). 2011/03/11 Iwate-oki Earthquake - Inversion analysis by nearfield waveforms (preliminary)
- JMA (2011c). 2011/03/09 Sanriku-oki Earthquake - Inversion analysis by nearfield waveforms (preliminary)

- JMA (2011d). 2011/04/07 Miyagi-oki Earthquake - Inversion analysis by farfield waveforms (preliminary)
- JMA (2011e). 2011/07/10 Sanriku-oki Earthquake - Inversion analysis by farfield waveforms (preliminary)
- JMA (2011f). 2011/06/23 Iwate-oki Earthquake - Inversion analysis by nearfield waveforms (preliminary)
- JMA (2011g). 2011/09/17 Iwate-oki Earthquake - Inversion analysis by farfield nearforms (preliminary)
- JMA (2011h). 2011/07/31 Fukushima Earthquake - Inversion analysis by nearfield waveforms (preliminary)
- JMA (2011i). 2011/07/23 Miyagi-oki Earthquake - Inversion analysis by nearfield waveforms (preliminary)
- JMA (2011j). 2011/07/25 Fukushima-oki Earthquake - Inversion analysis by nearfield waveforms (preliminary)
- JMA (2011k). 2011/08/19 Fukushima-oki Earthquake - Inversion analysis by nearfield nearforms (preliminary)
- JMA (2011l). 2011/11/24 Urakawa-off earthquakes- inversion analysis by nearfield waveforms
- JMA (2011m). 2011/03/15 East Shizuoka Earthquake - Inversion analysis by nearfield waveforms (preliminary)
- JMA (2011n). 2011/08/01 Surugawan Earthquake - Inversion analysis by nearfield waveforms (preliminary)
- JMA (2011o). 2011/04/12 Fukushima Nakadori Earthquake - Inversion analysis by nearfield waveforms (preliminary)
- JMA (2011p). 2011/03/19 North Ibaraki Earthquake - Inversion analysis by nearfield waveforms (preliminary)
- JMA (2012a). 2012/12/07 Miyagi-oki Earthquake - Inversion analysis by farfield waveforms (preliminary)
- JMA (2012b). 2012/03/14 Sanriku-oki Earthquake - Inversion analysis by farfield waveforms (preliminary)
- JMA (2012c). 2012/01/01 Torishima Near Sea Earthquake - Inversion analysis by farfield waveforms (preliminary)
- JMA (2015). 2015/05/30 Ogawawara west-off earthquakes- inversion analysis by farfield waveforms.
- Kakehi, Y. (2004). Analysis of the 2001 Geiyo, Japan, earthquake using high-density strong ground motion data: Detailed rupture process of a slab earthquake in a medium with a large velocity contrast. *J. Geophys. Res.*, 109:(B8), B08306, <https://doi:10.1029/2004JB002980>.
- Kanamori H. (1971). Great earthquakes at island arcs and the lithosphere, *Tectonophysics*, 12(3): 187–198.
- Kikuchi M., Fukao Y. (1987). Inversion of long-period P-waves from great earthquakes along subduction zones, *Tectonophysics*, 144(1-3): 231–247.
- Kikuchi M., Yamanaka Y. (2001) Near Coast of Peru earthquake (Mw 8.2) on June 23, 2001 (Revised), *EIC Seismological Note: N°105*, University of Tokyo Earthquake Information Center, http://www.eic.eri.utokyo.ac.jp/EIC/EIC_News/105E.html.
- Koketsu K., Hikima K., Miyazaki S., Ide S. (2004). Joint inversion of strong motion and geodetic data for the source process of the 2003 Tokachi-oki, Hokkaido, earthquake, *Earth Planets Space*, 56: 329–334.
- Kuge K., Kase Y., Urata Y., Campos J., Perez A. (2010). Rupture characteristics of the 2005 Tarapaca, northern Chile, intermediate-depth earthquake: Evidence for heterogeneous fluid distribution across the subducting oceanic plate?, *J. Geophys. Res.*, 115: B09305.
- Lay T., Ammon C.J., Hutko A.R., Kanamori H. (2010). Effects of kinematic constraints on teleseismic finite-source rupture inversions: Great Peruvian earthquakes of 23 June 2001 and 15 August 2007, *Bull. Seismol. Soc. Am.*, 100: 969–994.
- Lay T., Yue H., Brodsky E.E., An C. (2014). The 1 April 2014 Iquique, Chile, Mw 8.1 earthquake rupture sequence, *Geophys. Res. Lett.*, 41: 3818–3825.
- Lee S.J., Liang W.T., Huang B.S. (2008). Source mechanisms and rupture processes of the 26 December 2006 Pingtung earthquake doublet as determined from the regional seismic records. *Terr. Atmos. Ocean. Sci.*, 19: 555-565, [https://doi:10.3319/TAO.2008.19.6.555\(PT\)](https://doi:10.3319/TAO.2008.19.6.555(PT)).
- Lee S.J. (2019). *Inversion of finite fault model for Taiwan earthquakes*, Appendix B in *Development of the Hazard Input Document for Taiwan Using SSHAC Level 3 Methodology*" National Center for Research on Earthquake Engineering, Taiwan.
- Leyton F., Ruiz S., Sepúlveda S.A. (2009). Preliminary re-evaluation of probabilistic seismic hazard assessment in Chile: from Arica to Taitao Peninsula, *Adv. Geosci.*, 22: 147–153.

- Lorito S., Romano F., Atzori S., Tong X., Avallone A., McCloskey J., Cocco M., Boschi E., Piatanesi A. (2011). Limited overlap between the seismic gap and coseismic slip of the great 2010 Chile earthquake, *Nature Geosci.*, 4: 173–177.
- Lundberg N., Reed D., Liu C.-S., Lieske J. (1997). Forearc-basin closure and arc accretion in the submarine suture zone south of Taiwan, *Tectonophys.*, 274 5–23.
- Luttrell K.M., Tong X., Sandwell D.T., Brooks B.A., Bevis M.G. (2011). Estimates of stress drop and crustal tectonic stress from the 27 February 2010 Maule, Chile, earthquake: Implications for fault strength, *J. Geophys. Res.: Solid Earth*, 116(B11).
- Mai P.M., Spudich P., Boatwright J. (2005). Hypocenter locations in finite-source rupture models, *Bull. Seismol. Soc. Am.*, 95: 965–980.
- Mai P.M., Thingbaijam K.K.S. (2014). SRCMOD: An online database of finite-fault rupture models. *Seismol. Res. Lett.*, 85(6): 1348–1357.
- Malavieille J., Lallemand S.E., Dominguez S., Deschamps A., Lu C.-Y., Liu C.-S., Schnürle P. (2002). Arc-continent collision in Taiwan : New marine observations and tectonic evolution, in *Geology and Geophysics of an Arc-Continent collision*, T.B. Byrne and C.-S. Liu, (eds.), Taiwan, Republic of China: Boulder, Colorado, Geological Society of America Special Paper 358, pp. 189–213.
- Melgar D., Fan W., Riquelme S., Geng J., Liang C., Fuentes M., Vargas G., Allen R.M., Shearer P. M., Fielding E.J. (2016). Slip segmentation and slow rupture to the trench during the 2015, Mw8.3 Illapel, Chile earthquake, *Geophys. Res. Lett.*, 43: 961–966.
- Mendoza C., Fukuyama E. (1996). The July 12, 1993, Hokkaido-Nansei-Oki, Japan, earthquake' Coseismic slip pattern from strong-motion and teleseismic recordings, *J. Geophys. Res.*, 101: 791–801.
- Mendoza C. (1993). Coseismic Slip of 2 Large Mexican Earthquakes from Teleseismic Body Wave-Forms - Implications for Asperity Interaction in the Michoacan plate boundary segment, *J. Geophys. Res: Solid Earth*, 98(B5): 8197–8210.
- Mendoza C., Hartzell S.H. (1989). Slip distribution of the 19 September 1985 Michoacan, Mexico, earthquake - nearsource and teleseismic constraints. *Bull. Seismol. Soc. Am.*, 79(3): 655–669.
- Mendoza C., Hartzell S., Monfret T. (1994). Wide-band analysis of the 3 March 1985 central Chile earthquake - Overall source process and rupture history, *Bull. Seismol. Soc. Am.*, 84(2): 269–283.
- Murotani S., Satake K., Fujii Y. (2013). Scaling relations of seismic moment, rupture area, average slip, and asperity size for M~ 9 subduction-zone earthquakes, *Geophys. Res. Lett.*, 40: 1–5.
- Nagai R., Kikuchi M., Yamanaka Y. (2001). Comparative study on the source processes of recurrent large earthquakes in Sanriku-oki region: the 1968 Tokachi-oki earthquake and the 1994 Sanriku-oki earthquake, *Jishin*, 54: 267–280
- Nagumo H. (2012), Rupture process of northern Nagano Prefecture earthquake on March 12th, 2011 (Mj6.7), Annual Meeting of Japan Association for Earthquake Engineering, Japan Association for Earthquake Engineering, Tokyo, Japan.
- Nakayama W., Takeo M. (1997). Slip history of the 1994 Sanriku-Haruka-Oki, Japan, earthquake deduced from strong-motion data, *Bull. Seismol. Soc. Am.*, 87(4): 918–931.
- Namegaya Y., Tsuji Y. (2005). Delayed peaks of tsunami waveforms at Miyako from earthquakes east of Hokkaido, Earthquake Research Institute, University of Tokyo, Tokyo, Japan.
- Nozu (2007) 1993 Kushiro-Oki earthquake finite fault model (2nd ver.) – with digital supplement, http://www.pari.go.jp/bsh/jbn-kzo/jbn-bsi/taisin/research_jpn/research_jpn_2007/japanese_research_24.html.
- Okada T., Hasegawa A. (2003). The M7.1 May 26, 2003 off-shore Miyagi Prefecture earthquake in northeast Japan: Source process and aftershock distribution of an intra-slab event, *Earth Planets Space*, 55: 731–739.

- Oppenheimer D., Eaton J., Jayko A., Lisowski M., Marshall G., Murray M., Simpson R., Stein R., Beroza G., Magee M., Carver G., Dengler L., McPherson R., Gee L., Romanowicz B., Gonzalez F., Li W. H., Satake K., Somerville P., Valentine D. (1993). The Cape Mendocino, California, earthquakes of April 1992: Subduction at the triple junction, *Science*, 261(5120): 433–438.
- Pitarka A., Thio H. K., Somerville P.G., Bonilla L.F. (2013), Broadband ground-motion simulation of an intraslab earthquake and nonlinear site response: 2010 Ferndale, California, earthquake case study, *Seismol. Res. Lett.*, 84(5): 785–795.
- Poblete J.D. (2008). *Determinación Experimental de la Intensidad de Mercalli Modificada para Chile*, Thesis, Department of Civil Engineering, University of Chile, Santiago, Chile (in Spanish).
- Pollitz F.F., Brooks B., Tong X., Bevis M.G., Foster J.H., Bürgmann R., Smalley R., Vigny C., Socquet A., Ruegg J.C., Campos J. (2011). Coseismic slip distribution of the February 27, 2010 Mw 8.8 Maule, Chile earthquake, *Geophys. Res. Lett.*, 38: L09309.
- Power M., Chiou B.S.-J., Abrahamson N., Bozorgnia Y., Shantz T., Roblee C. (2008). An overview of the NGA project, *Earthq. Spectra*, 24(1): 3–21.
- Salichon J., Delouis B., Lundgren P., Giardini D., Costantini M., Rosen P. (2003). Joint inversion of broadband teleseismic and interferometric synthetic aperture radar (InSAR) data for the slip history of the Mw = 7.7, Nazca ridge (Peru) earthquake of 12 November 1996, *J. Geophys. Res.*, 108(B2), <https://doi:10.1029/2001JB000913>.
- Schurr B., Asch G., Rosenau M., Wang R., Oncken O., Barrientos S., Salazar P., Vilotte J.-P. (2012). The 2007 M7.7 Tocopilla northern Chile earthquake sequence: Implications for along-strike and downdip rupture segmentation and megathrust frictional behavior, *J. Geophys. Res.*, 117: B05305.
- SEVO (1996). Institute of Seismology and Vulcanology, Faculty of Science, Kyushu University.
- Shao G., Ji C. (n.d.). Preliminary result of the Jul 30, 1995 Mw 8.14 Antofagasta Earthquake, UCSB, available at http://www.geol.ucsb.edu/faculty/ji/big_earthquakes/1995/07/chile.html (last accessed May 2017).
- Shao G., Li X., Liu Q., Zhao X., Yano T., Ji C. (2010). Preliminary slip model of the Feb 27, 2010 Mw 8.9 Maule, Chile Earthquake, UCSB, http://ji.faculty.geol.ucsb.edu/big_earthquakes/2010/02/27/chile_2_27.html.
- Shiba Y., Uetake T. (2011) Rupture process of the 1964 MJMA 7.5 Niigata earthquake estimated from regional strong-motion records, *Bull. Seismol. Soc. Am.*, 101: 1871–1884.
- Skarlatoudis A.A., Somerville P.G., Thio H.K. (2016). Source-scaling relations of interface subduction earthquakes for strong ground motion and tsunami simulation, *Bull. Seismol. Soc. Am.*, 106: 1652–1662.
- Sladen A. (2007). Preliminary Result 11/14/2007 (Mw 7.7), Tocopilla Earthquake, Chile, Source Models of Large Earthquakes, Caltech, available at http://www.tectonics.caltech.edu/slip_history/2007_tocopilla/tocopilla.html (last accessed July 1, 2013).
- Sladen A. (2010). Preliminary Result, 02/27/2010 (Mw 8.8), Chile, Source Models of Large Earthquakes, Caltech, available at http://www.tectonics.caltech.edu/slip_history/2010_chile/index.html (last accessed May 2017).
- Smithsonian Institute’s Global Volcanism Program (2013). <https://volcano.si.edu/>.
- Strasser F.O., Arango M.C., Bommer J.J. (2010). Scaling of the source dimensions of interface and intraslab subduction-zone earthquakes with moment magnitude, *Seismol. Res. Lett.*, 81: 941–950.
- Suzuki W., Aoi S. Sekiguchi H. (2009). Rupture process of the 2008 Northern Iwate intraslab earthquake derived from strong-motion records, *Bull. Seismol. Soc. Am.*, 99: 2825–2835.
- Takahashi H., Hirata K. (2003). The 2000 Nemuro-Hanto-Oki earthquake, off eastern Hokkaido, Japan, and the high intraslab seismic activity in the southwestern Kuril Trench, *J. Geophys. Res.*, 108:(B4): 2-1–2-9.
- Takeo M., Mikami N. (1990). Fault heterogeneity of inland earthquakes in Japan, *Bull. Earthq. Res. Inst.*, University of Tokyo, 65(2): 541–569.

- Takiguchi M., Asano K., Iwata T. (2011). The comparison of source models of repeating subduction-zone earthquake estimated using broadband strong motion records - 1982 and 2008 Ibaraki-ken-oki M7 earthquakes, *J. Seism. Soc. Japan*, 63: 223–242.
- Tanioka Y., Ruff L., Satake K. (1995). The great Kurile earthquake of October 4, 1994 tore the slab, *Geophys. Res. Lett.*, 22: 1661–1664.
- Tichelaar B.W, Ruff L.J. (1993). Depth of seismic coupling along subduction zones, *J. Geophys. Res.: Solid Earth*, 98:(B2), 2017–2037.
- Tsuchida H., Inatomi T., Ueda H. (1983). The damage to port facilities by the 1982 Urakawa-oki earthquake, *Technical Note No.472*, Port and Harbour Research Institute Ministry of Transport, Japan.
- USGS (2003). M7.8 Rat Islands, Alaska earthquake of 17 November 2003, <ftp://hazards.cr.usgs.gov/maps/sigeqs/20031117/20031117.pdf>.
- USGS (2014). Preliminary finite fault results for the Jun 23, 2014 Mw 7.9 51.7968, 178.7591 earthquake (Version 1), <http://earthquake.usgs.gov/earthquakes/eventpage/usc000rki5#finite-fault>.
- USGS (2016). Preliminary finite fault results for the Jan 24, 2016 Mw 7.1 83 km E of Old Iliamna, Alaska earthquake (Version 1), <http://earthquake.usgs.gov/earthquakes/eventpage/us10004gqp#finite-fault>.
- Van Houtte C., Bannister S., Holden C., Bourguignon S., McVerry G. (2017). The New Zealand strong motion database, *Bull. N.Z. Soc. Earthq. Eng.*, 50(1): 1–20, <https://doi.org/10.5459/bnzsee.50.1.1-20>.
- Wells R.E., Blakely R.J., Simpson R.W., Weaver C.S., Haugerud R., Wheeler K. (2000). Tectonic plate motions, crustal blocks, and shallow earthquakes in Cascadia, *Great Cascadia Earthquake Tricentennial Open House, 26 January 2000*, Burke Museum, University of Washington, Seattle, WA (poster).
- Williams M.C., Tréhu A.M., Braunmiller J. (2011). Seismicity at the Cascadia plate boundary beneath the Oregon continental shelf, *Bull. Seismol. Soc. Am.*, 101: 940–950.
- Wooddell K. (2018). New earthquake classification for the NGA-subduction project, *Proceedings, 11th National Conference on Earthquake Engineering*, Los Angeles, CA, Paper 1275.
- Wooddell K., Abrahamson N.A. (2014). Classification of mainshocks and aftershocks in the NGA-West2 database, *Earthq. Spectra*, 30: 1257–1267.
- Wu F.T., Liang W.-T., Lee J.-C., Benz H., Villasenor A. (2009). A model for the termination of the Ryukyu subduction zone against Taiwan: A junction of collision, subduction/separation, and subduction boundaries, *J. Geophys. Res.*, 114: B07404, <https://doi:10.1029/2008JB005950>.
- Yagi Y. (2004). 2004/09/05 Kii Peninsula southeast offshore earthquake, http://iisee.kenken.go.jp/staff/yagi/eq/Japan20040905/Japan20040905_1j.html
- Yagi Y., Kikuchi M., Yoshida S., Yamanaka Y. (1998). Source Process of the Hyuga-nada Earthquake of April 1, 1968 (Mjma 7.5), and its relationship to the subsequent seismicity, *J. Seismol. Soc. Japan*, 51: 139–148.
- Yagi Y., Kikuchi M., Yoshida S., Sagiya T. (1999). Comparison of the coseismic rupture with the aftershock distribution in the Hyuga-nada earthquakes of 1996, *Geophys. Res. Lett.*, 26(20): 3161–3164.
- Yamanaka Y., Kikuchi M. (2004). Asperity map along the subduction zone in northeastern Japan inferred from regional seismic data, *J. Geophys. Res.*, 109: (B7), B07307, <https://doi:10.1029/2003JB002683>.
- Yamanaka Y. (2005). EIC Semiology Note No.168, http://www.eic.eri.u-tokyo.ac.jp/sanchu/Seismo_Note/2005/EIC168a.html (last access 01/17/2017).
- Ye L., Lay T., Kanamori H., Koper K.D. (2013). Energy release of the 2013 Mw 8.3 Sea of Okhotsk earthquake and deep slab stress heterogeneity, *Science*, 341: 1380–1384.
- Ye L., Lay T., Kanamori H., Rivera L. (2016). Rupture characteristics of large ($M_w \geq 7$) megathrust earthquakes from 1990-2015: I. Moment-scaling relationships, *J. Geophys. Res.*, 121: 826–844.
- Yokota Y., Koketsu K., Fujii Y., Satake K., Sakai S., Shinohara M., Kanazawa T. (2011). Joint inversion of strong motion, teleseismic, geodetic, and tsunami data sets for the rupture process of the 2011 Tohoku earthquake, *Geophys. Res. Lett.*, 38: L00G21, <https://doi:10.1029/2011GL050098>.

Yoshioka N., Abe K. (1976). Focal mechanism of the Iwate-oki earthquake of June 12, 1968, *J. Phys. Earth*, 24: 251–262.

5 Site Condition Parameters

Sean K. Ahdi, Timothy D. Ancheta, Víctor Contreras, Tadahiro Kishida, Dong Youp Kwak, Annie O.L. Kwok, Grace A. Parker, Francisco Ruz, and Jonathan P. Stewart

5.1 OVERVIEW AND ORGANIZATION

The site component of the NGA-Sub relational database comprises a list of metadata for stations that have recorded the contributing events from Chapter 4. The principle regions from which data has been collected are: Alaska (ALK), the Cascadia region of North America (CAS), Central America and Mexico (CAM), Japan (JPN), New Zealand (NZL), South America (SAM), and Taiwan (TWN). A global map of stations with recorded ground motions that are included in the NGA-Sub project database is presented in Figure 5.1.

The words “site” and “station” are used somewhat interchangeably, with “station” generally referring to the actual strong-motion instrument, and “site” referring to a more general description of the location of interest (which for this project coincides with the strong-motion stations). The site component of the NGA-Sub database contains 6433 sites. For each site the following data is provided:

- Site name and station ID, often adopted from the original strong motion network’s station code/name;
- A unique station sequence number (SSN) that acts as the identifier for every site in the database;
- Information about station location, such as latitude, longitude, depth below ground surface, elevation, and in some cases, information on sensor housing;
- Recommended V_{S30} values and uncertainties linked to codes that describe V_{S30} assignment protocols, along with associated NEHRP site classes [Dobry et al. 2000];
- Details related to measured V_S profiles when available, such as the maximum depth of the profile (z_p) and time averaged V_S to z_p (V_{SZ});
- Site information used to predict V_{S30} from proxy-based models when measured V_{S30} values are absent;

- Basin depth information such as the depth to a particular V_S horizon (i.e., z_x = the depth to the x km/sec iso-surface) where available from measurements or regional 3D velocity models; and
- Indicators of whether a station is located in the forearc or backarc of the particular subduction zone region for which it recorded data.

The above information on site conditions is contained in the *Site* table within the relational database; the only exception is the forearc and backarc indicators, which are contained in the *SiteVolArc* table.

A breakdown of the number of sites by region is presented in Figure 5.2, which is based principally on the region that produced the earthquake, not necessarily the site location. In most cases, these coincide. For example, Japan contributes the most sites (35%), and those sites have collectively produced 57% of the NGA-Sub ground motions, virtually all of which are from earthquakes in Japan. Conversely, the Cascadia group in Figure 5.2, which comprises 18% of the sites (second highest after Japan), includes sites in the Pacific Northwest region (British Columbia, Washington, Oregon, and the region of northern California north of Cape Mendocino), as well as other, more distant regions including other parts of California, intermountain west states, and central and eastern North America (generally east of the Rocky Mountains). Despite the large number of sites, the number of ground-motion records from Cascadia events is relatively small (only 3% of the ground-motion inventory).

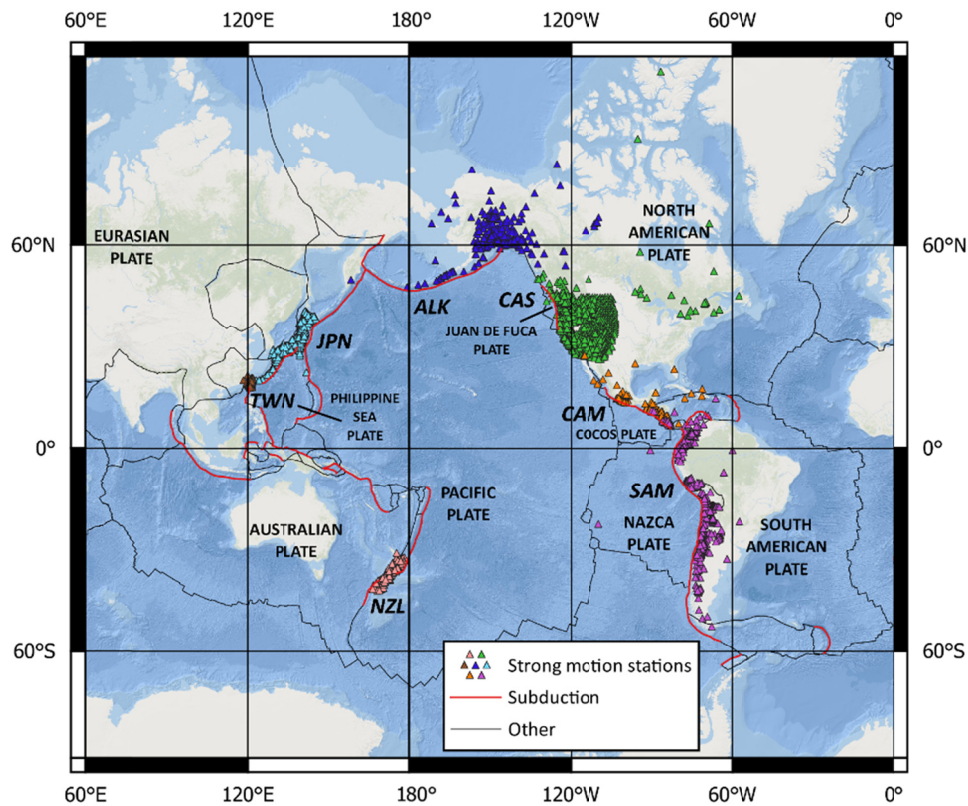


Figure 5.1 Locations of strong-motion stations with recorded ground motions in NGA-Sub database.

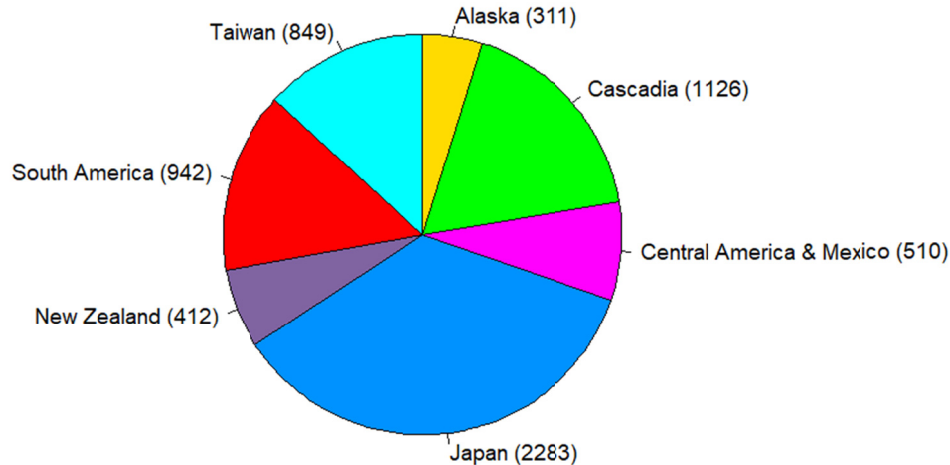


Figure 5.2 Breakdown of number of sites in NGA-Sub database by region ($N = 6433$).

Some strong-motion stations included in the NGA-Sub database, particularly in California, Alaska, Taiwan and Japan, have also recorded shallow crustal events. As such, the sites are included in the NGA-West2 and NGA-East project databases. Where overlap exists, station metadata and any assigned V_{S30} and basin depth values that existed in those databases were adopted for assignment in the NGA-Sub *Site* table, except for sites in California that recorded Cascadia events, for which V_{S30} was updated using more recent methods; see Section 5.3.3(a). This updating was not performed systematically because of complexities related to inconsistent station-naming conventions, station numbering, and other problems.

5.1.1 Approach for *Site* Table Development

In past NGA projects, the “database” took the form of spreadsheets (i.e., Microsoft Excel spreadsheets [XLS] or comma-separated values [CSV] files). In NGA-Sub, the project team has organized the data into a relational database, where interrelated tables of data and metadata communicate using various unique keys, called primary keys, to ensure consistency between and across tables. A more in-depth description of the relational database is provided in Chapter 2. Within the NGA-Sub relational database, there is a *Site* table. The contents of this table can be exported to spreadsheet format (.XLS or .CSV).

The *Site* table is organized by region, with the unique SSNs assigned as sequential integers of the pattern $N \times 10^6$ within each region, where N is an integer from one to seven that accounts for each of the seven subduction-zone regions shown in Figure 5.2; they are listed in alphabetical order (i.e., Alaska stations are numbered 1000001, 1000002, ..., and Taiwan stations are numbered 7000001, 7000002, ...). This methodology was adopted to: (1) facilitate using the SSN as a primary key for the *Site* table within the NGA-Sub relational database; and (2) allow the *Site* table to grow in the future when new stations are inevitably added or when *Site* tables from NGA-West2 and NGA-East are merged with this one, ensuring that each region will not feasibly run out of integer values for SSNs. The extensibility of the relational database prevents the need for maintaining sequential site spreadsheet files (up to 32 versions of which were used in NGA-West and NGA-West2 [Seyhan et al. 2014]).

To avoid redundant listings of sites, a hierarchy for removal of duplicate sites was applied, whereby sites were combined when they had identical latitude and longitude coordinates (within 0.0001-decimal degree precision), reasonably consistent station names, and/or identification numbers from the station network. Separate SSNs were assigned for cases when the station network changed, but the instrument ostensibly remained the same, or the instrument itself was changed at the same location. In the case of vertical arrays with multiple sensors at the same latitude and longitude but different depths, multiple “sites” (with distinct SSNs) are provided in the *Site* table, each having a different sensor depth.

5.1.2 Sources of Station Data

Regional ground-motion data were generally obtained from websites of organizations that operate local accelerograph or seismograph networks. These websites often have some basic station information, typically including station locations, instrument information, and in some cases, geotechnical data and seismic velocity profiles. Details on data sources are given in Chapter 3.

Most sites in Japan are part of the KIK-NET, K-NET, Port and Airport Research Institute (PARI), Japan Meteorological Agency (JMA), or Tokyo Electric Power Company (TEPCO) networks. Taiwan station data is derived from the Taiwan Strong Motion Instrumentation Program, managed by the Central Weather Bureau (CWB), as well as the broadband seismic observation network, co-managed by CWB and the Institute of Earth Sciences, Academic Sinica in Taiwan [NCREE 2017]. Station information from Alaska was obtained from the Alaska Earthquake Center at the University of Alaska at Fairbanks [AEC 2018]. In Cascadia, data was accessed from sites belonging to numerous networks, including the IRIS Transportable Array (TA array) [IRIS 2003], the Pacific Northwest Seismic Network (PNSN) [UW 1963], and the Canadian National Seismograph Network [GSC 1989], among others across California and other western states (BDSN, NCEDC, CI, CGS, USGS, NSN, ABSN, UO, UU). In Mexico, station data were mainly obtained from the Guerrero Network operated by University of Nevada, Reno (UNR) [Anderson et al. 2006, and the Center for Engineering Strong-Motion Data (CESMD). In Central America, major networks exist for most countries, such as the Red Sismológica Nacional de Costa Rica (TC) [UNR 1989], the Medio Ambiente y Recursos Naturales (MARN) network in El Salvador [SNET 2018], and the Tomography Under Costa Rica and Nicaragua (TUCAN) network [Abers and Fischer 2003]. In South America, station data comes from 36 different networks; particularly important networks within this region include the Chilean Seismological Network and RENADIC, operated by the University of Chile, the Red Nacional Accelerógrafos de Colombia (CM), the Peru Lithosphere and Slab Experiment (PULSE) [Wagner et al. 2010], and the Ecuador Seismic Network (EC). The data from New Zealand was taken from Kaiser et al. [2016; 2017], which contains site information for stations included in a flatfile in Van Houtte et al. [2017].

Each network has varying levels of existing site-characterization information, details of which are discussed below. Table 5.1 lists all networks in the NGA-Sub database and the number of sites from each. Network acronyms are as given Chapter 3, here, or in the footnote of Table 5.1. There are 92 networks represented in the database. Of the 6433 stations, 417 (6%) lack network assignments, with nearly all (412) coming from New Zealand.

Table 5.1 Number of sites in contributing strong motion station networks for NGA-Sub.

Network	Count	Network	Count	Network	Count	Network	Count
K-NET	1032	GFZ ¹	113	YC ¹	22	MX ¹	5
CWB	802	TUCAN	49	INETER ¹	20	IGP ¹	4
KIK-NET	702	UNR	45	ESCI GSMN ¹	18	ONA ¹	4
TA	414	COSMOS	39	XH ¹	17	CERESIS ¹	3
JMA	345	PULSE	39	CGS	24	G ¹	3
UW	191	XS ¹	38	NU ¹	13	II ¹	3
CSN	149	AV ¹	37	TEPCO	17	NR ¹	3
AEC	146	NSMP	100	XV ¹	13	RUT ¹	5
GSC	136	Historic	35	XJ ¹	11	IE ¹	2
RENADIC	132	IU ¹	35	GI ¹	10	NV ¹	2
LIS	122	OV	34	CM	9	TC	2
RNAC	121	BDSN	34	Idel ¹	9	UU	2
MARN	114	RENAC	33	CC ¹	8	AX ¹	1
PARI	102	C	32	ICE ¹	8	MG ¹	1
NCEDC	77	DGG ¹	29	SV ¹	8	PA ¹	1
BO ¹	69	CX	27	ABSN	7	PUCP ¹	1
PB ¹	64	NN	27	CU ¹	6	WC ¹	1
XY	64	C1	25	EC ¹	6	YJ ¹	1
CI	63	TW	24	GT ¹	6		
USGS	71	CISMID	23	UO	6		

¹ BO=Bosai-Ken Network, NIED, Japan; PB=Plate Boundary Observatory; GFZ=GFZ Potsdam, Germany (ZA, 2B, Y9, ZW arrays); AV=Alaska Volcano Observatory; IU=Global Seismograph Network; DGG = Deutsche Geophysikalische Gesellschaft; 2B=PUDEL Network, Argentina, GFZ Potsdam; Y9=Tocopilla, GEOFON Program, GFZ Potsdam; YC=Slab Geometry in the Southern Andes; INETER=Nicaraguan Geosciences Institute; ESCI GSMN=El Salvador Geotechnical Investigation Centre Strong Motion Network; XH=Altiplano-Puna Volcanic Complex Seismic Experiment; NU=Nicaraguan Seismic Network; XV=Fault Locations and Alaska Tectonics from Seismicity, Univ. Alaska, Fairbanks; XJ=Seismic Experiment in the Aisen Region of Chile, Univ. Cambridge; GI=Red Sismologica Nacional-Guatemala; Idel=Instituto de Ingenieria, Universidad Nacional Autonoma de Mexico (UNAM); CC=Cascade Chain Volcano Monitoring; ICE=Instituto Costarricense de Electricidad; SV=Servicio Nacional de Estudios Territoriales, El Salvador; CU=Caribbean USGS Network; EC=Ecuador Seismic Network; GT=Global Telemetered Seismograph Network; MX=Mexican National Seismic Network, Universidad Nacional Autónoma de México; IGP=Geophysical Institute of Peru; ONA=Onagawa Nuclear Plant, Japan; CERES=Regional Centre for Seismology for South America; G=GEOSCOPE Observatory, Institut de Physique du Globe de Paris; II=IRIS/IDA Seismic Network, Scripps Institution of Oceanography; NR=Network of Autonomously Recording Seismographs (NARS), Utrecht University, Netherlands; RUT=Rutgers Univ. (OO, ZX arrays); IE=Idaho National Laboratory Seismic Monitoring Program; NV=NEPTUNE Canada, Ocean Networks Canada; AX=Departamento Meteorologico Aruba; MG=Seismic Network of North Eastern Mexico, Universidad Nacional Autónoma de México; PA=Red Sismica Volcan Baru, Panama; PUCP=Pontificia Universidad Catolica del Peru; WC=Curacao Seismic Network; YJ=Studies of crust and upper mantle structure, mantle flow and geodynamics of the Chile Ridge subduction zone, IRIS/PASSCAL.

The remainder of this chapter describes site data and metadata used for NGA modeling purposes. Emphasis is placed on proxy-based models used to estimate V_{S30} and its aleatory variability and uncertainty for regions for which related studies were not already published. This includes Central America and Mexico (events from the Cocos subduction zone), and South America (Nazca subduction zone), excepting Chile. Regions for which V_{S30} prediction models have been published are briefly reviewed (Taiwan, Cascadia, Alaska, Chile, and New Zealand). For Japan, data and proxy-based models were published as part of NGA-West2 and other projects, and are updated here.

5.2 MEASURED V_S DATA FOR V_{S30} EVALUATION

5.2.1 Data Sources

Wherever possible, V_S profiles developed from *in situ* geophysical testing are identified for use in the characterization of site conditions at a ground-motion instrument site. The profile is used to compute and assign V_{S30} and, where applicable, to assign depths to 1.0 and 2.5 km/sec shear-wave velocity iso-surfaces. In general, V_S profile data is considered if it reflects direct measurements (from *in situ* geophysical testing), the profile extends to a profile depth z_p of at least 5 m, the profile begins within 5 m of the ground surface, and the profile location (geodetic coordinates) is known. Data derived using a wide array of geophysical measurement techniques were included. One technique that is not considered credible (CXW) [Poran et al. 1994] was nonetheless used for estimates of V_{S30} for sites in Alaska, as explained in Ahdi et al. [2017(b)]. In general, profiles from the ReMiTM method [Louie 2001] were not compiled for use in the profile databases from which V_S data was extracted this study, with the exception of a small number of sites in Chile.

Of the 6433 sites in the *Site* table, 2530 have a V_{S30} value computed using a V_S profile. As part of the NGA-Sub project, considerable effort was put into identifying suitable profiles. Correspondence with national and regional agencies was undertaken, as well as contact with individual researchers and geotechnical/geophysical consulting firms. Ultimately all of the data used in the project is in the public domain. The profiles and accompanying metadata had disparate formats in source documents. The V_S profiles were digitized (if not already in digital form) and assembled into “profile databases” (PDBs) for individual regions. Further information on these PDBs are described in Ahdi et al. [2017(a)] for Cascadia and Ahdi et al. [2017(b)] for Alaska (updated here). For Taiwan, profile data was obtained from a website maintained by the CWB; see NCREE [2017] and Kwok et al. [2018]. For Chile, the PDB was derived from a variety of university reports and profiles from the personal files of a consulting firm; see Contreras et al. [2018]. For Japan, V_S data for stations that are part of the KIK-NET and K-net networks was obtained from a web site maintained by National Research Institute for Earth Science and Disaster Resilience (NIED) (<http://www.kyoshin.bosai.go.jp/>). Site data for stations in the Port and Airport Research Institute (PARI) network were obtained from the PARI website (<https://www.eq.pari.go.jp/kyosin/>). We did not identify a source of V_S profile data for sites in the JMA network. In the case of New Zealand, we did not compile a PDB, but relied on site metadata compiled for strong-motion stations by Kaiser et al. [2016; 2017], some of which are measurement-based (their quality factor Q_1 , and in some cases, Q_2). This is described further in Section 5.3.3.

Figure 5.3 illustrates the distribution of both measurement- and proxy-based V_{S30} data in the NGA-Sub database, which shows a lognormal distribution skewed towards high- V_{S30} (stiffer) sites. Table 5.2 shows the regional breakdown of measured versus proxy-based V_{S30} data in the *Site* table. The number of sites with profiles (2530) is less than the number of sites with measured V_{S30} because in some cases source documents only provide a measured V_{S30} and lack a profile. The regions with the highest percentages of V_{S30} values based on measurements are Japan (76%) and Taiwan (56%); these regions also had the highest such percentages in NGA-West2, with Taiwan at 53% and Japan at 34% [Ancheta et al. 2013]. This shows that proxy-based models were needed in all regions, and that the need was greatest in regions other than Japan and Taiwan. The substantial need for V_{S30} assignments from proxy-based models motivated a series of studies to develop such models on a region-specific basis; see Sections 5.3.3 and 5.3.4. Figure 5.4 shows the distribution of profile depth z_p for measured V_S profiles where available [i.e., the total number of V_S profiles in Figure 5.4 (2205) is less than the number of sites with measured profiles (2530) because for some profiles no profile depth was assigned.

Table 5.2 Breakdown of measured- and proxy-based estimated V_{S30} data by NGA-Sub region.

Region	Total	Measured	Estimated
Alaska	311	16 (5%)	295 (95%)
Cascadia	1126	80 (7%)	1046 (93%)
Central America and Mexico	510	24 (5%)	486 (95%)
Japan	2283	1731 (76%)	552 (24%)
New Zealand	412	28 (7%)	384 (93%)
South America	942	178 (19%)	764 (81%)
Taiwan	849	473 (56%)	376 (44%)
Total	6433	2530 (39%)	3903 (61%)

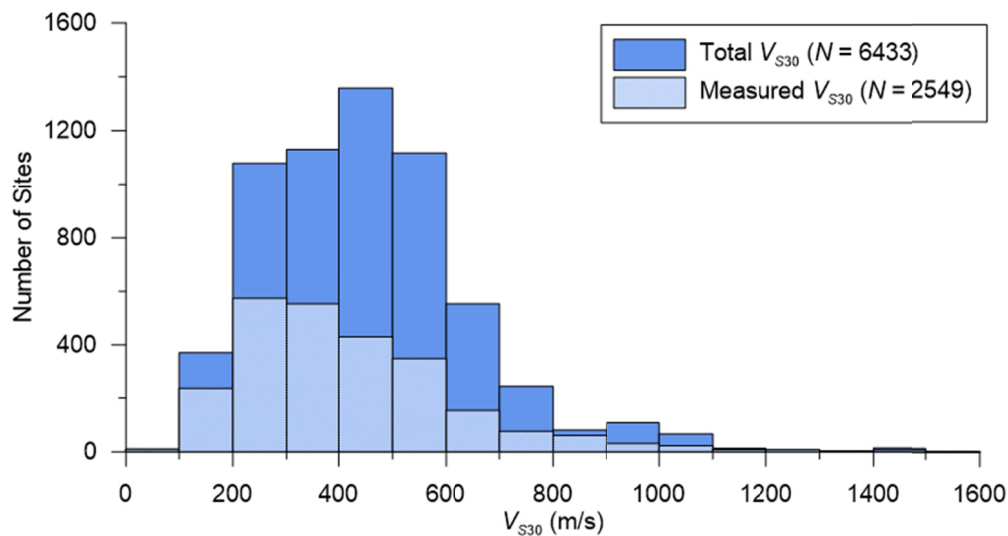


Figure 5.3 Distribution of all V_{S30} assigned to SMSs in the NGA-Sub database, with a histogram for the subset of sites with assignments from measured *in situ* V_S profiles.

Limited measured V_S profile/ V_{S30} data were acquired for the stations in regions that recorded events in the Cocos subduction zone (i.e., Central America and Mexico) and the Nazca subduction zone (i.e., South America, excepting Chile). Fifteen V_S profiles from geophysical testing using downhole and suspension log methods were collected in and around Mexico City at strong-motion stations and ground failure sites after the 1985 Mexico City Earthquake [Ohta et al. 1986; Seed et al. 1987]. These were applicable to 11 strong-motion stations in the *Site* table, with two profiles applicable to six different stations based on the criteria of proximity within 300 m; see Borchardt [2002] and Seyhan et al. [2014]. Arango et al. [2010] compiled V_{S30} values from measured V_S profile data (five profiles) acquired for past microzonation studies in El Salvador [Faccioli et al. 1988] and two profiles from Nicaragua [Faccioli et al. 1973]. V_{S30} from these profiles were assigned to seven and two strong-motion stations in each country, respectively. In South America, 27 V_S profiles were measured using SASW [Vera-Grunauer 2014] and combined MASW and SASW [Nikolau et al. 2016]. A subset of these were applied to 13 strong motion-stations in Ecuador, primarily concentrated in the Guayaquil region and measured during reconnaissance after the 2016 Musine earthquake. The digital V_S profile data were provided by X. Vera-Grunauer [2017]. Sixteen V_S profiles were collected in Peru [Cortez-Flores 2004], one of which could be matched to a strong-motion station for V_{S30} assignment. Finally, four measured V_{S30} values were obtained from the flatfile of the South America Risk Assessment (SARA) project of the Global Earthquake Model (GEM) and applied as V_{S30} assignments at five strong-motion station sites in Colombia [Castillo et al. 2016].

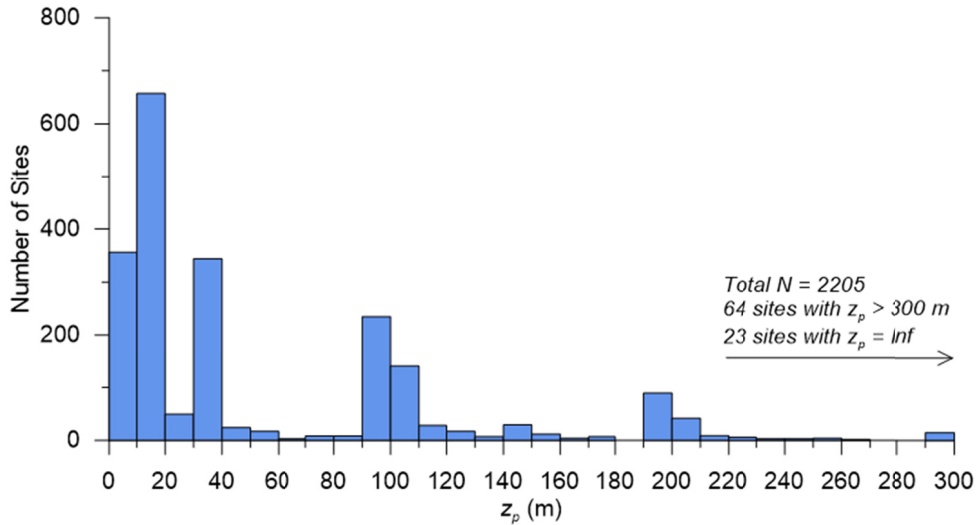


Figure 5.4 Distribution of z_p for measured V_S profiles assigned to SMSs in the NGA-Sub *Site* table. “Inf” indicates infinity and is associated with the bottom layer given a half-space velocity.

5.2.2 V_{S30} Computation

The time-averaged V_S to the maximum profile depth z_p is computed as

$$V_{SZ} = \frac{z_p}{tt_z} \tag{5.1}$$

in which

$$tt_z = \int_0^{z_p} \frac{dz}{V_S(z)} \quad (5.2)$$

where tt_z is the travel time for shear waves to travel from depth z_p to the ground surface. In practice, the integral is taken as a summation across depth intervals with constant velocities. When $z_p \geq 30$ m, which occurs for 1490 of 2530 sites with assignment of V_{S30} from measured V_S profiles, V_{S30} is computed by replacing z_p with 30 m.

For the 1024 sites having $z_p < 30$ m, V_{S30} is estimated by extrapolation. There exist numerous extrapolation schemes in the literature, which are described and compared in the Appendix of Ahdi et al. [2017(a)]. Statistical analyses of five different V_{SZ} -to- V_{S30} extrapolation schemes (Boore [2004]; Boore et al. [2011]; Dai et al. [2013]; Midorikawa and Nogi [2015]; and Wang and Wang [2015]), presented in the Appendix of Ahdi et al. [2017(a)] and expanded upon in Kwak et al. [2017], demonstrate that, in general, the model framework developed by Dai et al. [2013], which relies on regressions using V_S profiles for individual regions or datasets to predict the time-averaged V_S from z_p to 30 m, provides the lowest uncertainty in V_{S30} estimates for regions with available models. Dai et al. [2013] was used for shallow profiles in Japan, with regression coefficients provided in Table 2 of Kwak et al. [2017], and in the PNW [Ahdi et al. [2017(a)]. Similar but Taiwan-specific extrapolation V_{SZ} -to- V_{S30} procedures discussed in Kuo et al. [2012] were used in Taiwan by Kwok et al. [2018].

5.3 PROXY-BASED ESTIMATION OF V_{S30}

A substantial effort was made to develop region-specific, proxy-based V_{S30} prediction models for application to key NGA-Sub regions for which V_S profile data was accessible. This differs from the NGA-West2 project for which proxy-based V_{S30} prediction models from prior literature were generally used, with some exceptions; see Seyhan et al. [2014]. The region-specific prediction models used in NGA-Sub are:

- Pacific Northwest: Ahdi et al. [2017(a)];
- Alaska: Ahdi et al. [2017(b)];
- Taiwan: Kwok et al. [2018];
- Chile: Contreras et al. [2018];
- New Zealand: Kaiser et al. [2016; 2017]; and
- Japan: Not previously published and presented below.

Following a review of methods used for V_{S30} prediction in Section 5.3.1, Section 5.3.2 describes a general framework for development and application of models that reflects regional data availability and associated uncertainties. Region-specific models are then briefly summarized for NGA-Sub applications that are published elsewhere and described (in more detail) for regions where proxy-based models were not previously developed (i.e., Central America and Mexico, and South America, excepting Chile).

5.3.1 Methods used for Proxy-Based V_{S30} Prediction

Proxy-based models can be categorized in different manners. One is on the basis of region of applicability, with global models distinguished from local models. Global models require two attributes: (1) the proxy itself must be globally available and (2) the predictive model of V_{S30} given the proxy should be based on a geographically diverse dataset. Based on this definition, the principle global model is that of Wald and Allen [2007] and Allen and Wald [2009], which uses the proxy of topographic slope gradient at 30 arc-sec resolution and collections of V_{S30} measurements from California, Italy, and Taiwan (the model for active tectonic regions) and Australia and Tennessee (the model for stable continental regions). The same digital elevation model (DEM) used for topographic slope can also be used to define geomorphic terrain classes on the basis of slope gradient and metrics of convexity and texture (e.g., Iwahashi and Pike [2007] and Iwahashi et al. [2018]). Hence, while a global model is possible using these approaches, to date the applications have been local, specifically California [Yong et al. 2012; Yong [2016], Greece [Stewart et al. 2014], Taiwan [Kwok et al. 2018], and Cascadia [Ahdi et al. 2017a]. Different resolutions of DEMs can also be used [Allen and Wald [2009] and Stewart et al. [2014], but these different resolutions may result in biased slope estimates for a given location based on canopy effects due to vegetation or presence of buildings at higher DEM resolutions [Stewart et al. 2014].

Local models are applicable to a particular domain, typically defined on the basis of political boundaries or changes in the predominant crustal structure. For a given domain, a second level of categorization concerns the type of proxies considered. These include surface geology, geotechnical descriptors, slope gradient, geomorphic terrain class, elevation, and hybrids of more than one proxy. Table 5.3 summarizes some existing V_{S30} -prediction relationships, including the region of applicability and the proxies used. Several recent models use a combination of surface geology and ground slope, an approach introduced by Wills and Gutierrez [2008] and advanced by Thompson and Wald [2012], Thompson et al. [2014], and Parker et al. [2017], among others. The Thompson et al. [2014] study, later updated by Thompson [2018], begins with a geology-slope approach and then computes residuals between V_{S30} data at profile locations and the model, which are then mapped using a Kriging approach. For application to the USGS ShakeMap product, V_{S30} estimates are provided by combining the model prediction with location-specific residuals. The Japan Engineering Geomorphologic Classification Map (JEGM) provides an effective category-based proxy that reflects geological and morphological conditions; means and standard deviations of V_{S30} are provided by category, which is similar to the terrain-based methods. The other method listed in Table 5.3 is based on geotechnical descriptors [Chiou and Youngs 2008] and applied in California. This approach was not used in the present work.

5.3.2 Proposed V_{S30} Prediction Framework

For large, global projects like NGA-Sub, there is a need to estimate the site parameter V_{S30} for regions with highly variable levels of data availability and quality. Some regions, like California, Taiwan, and Japan, have relatively extensive V_S data and map resources (geology, etc.) that provide relevant proxies at high resolution. Other regions largely lack V_S profile data and may or may not have reliable maps for proxies other than global 30 arc-sec DEM maps (e.g., SRTM30,

and Farr and Kobrick [2000]). Project requirements dictate that values of V_{S30} are needed for all sites, so a framework is needed to provide this, along with appurtenant uncertainties.

The framework described here distinguishes between variability and uncertainty. *Variability* here refers to the standard deviation representing the dispersion of V_{S30} data relative to a mean estimate for a given set of predictor variables and is denoted as $(\sigma_{\ln V})$. *Uncertainty* here refers to lack of knowledge of the appropriate value of statistical moments (mean and standard deviation), also known as epistemic uncertainty, and is denoted as (σ_{ep}) . Emphasis is placed on epistemic uncertainty in mean estimates.

(a) Approach I: Good quality V_S data and proxy maps

Regions for which Approach I applies have ample V_S profile data and geological map resources that allow relevant proxies to be mapped at high spatial resolution. The development of appropriate V_{S30} -prediction models for such regions begins by assembling a V_S PDB. Preferably, this V_S data is of high quality, dense spatial resolution, and spans a wide array of geological and geomorphological environments. In most recent models, the primary proxy that is considered is surface geology, which should be presented at high resolution (ideally 1:50,000 or larger scale). Larger map scales provide more confidence of mapping accuracy with respect to the geological units present at a site of interest. Morphological information such as topographic gradient and/or elevation is often combined with mapped geologic category.

Judgment is used to group categories from various geological maps of different scales and potentially from different authors or institutions. Next, V_{S30} moments are computed for each category, usually under the assumption of a log-normal distribution. The aleatory uncertainty is taken as category standard deviation $(\sigma_{\ln V})$, the mean is the category mean in natural log units. By convention, the exponent of that mean is denoted $(\mu_{\ln V})$ in units of m/sec. Where justified by the data, the mean within a category may be dependent on slope and possibly elevation. V_{S30} moments are developed in a like manner for multiple groups, which taken together constitute a proxy-based V_{S30} prediction model. In some cases, additional factors, such as influence of basins or prior glaciation on V_{S30} (e.g., Parker et al. [2017] and Ahdi et al. [2017(a)]), can be investigated using residuals analyses to find particular groupings that improve the model's predictive power.

Epistemic uncertainties in mean estimates developed for Approach I can be represented by the standard errors, which decreases as standard deviation decreases and the number of data points used to compute moments increases. This uncertainty is generally small and is not reported.

For NGA-Sub, region-specific proxies developed in this manner were prepared for the Pacific Northwest [Ahdi et al. 2017(a)] and Taiwan [Kwok et al. 2018]. A prior model meeting this general description was updated for Japan. A proxy-based model conditioned on terrain categories instead of geology was developed for Chile [Contreras et al. 2018].

Table 5.3 Literature summary for proxy-based methods for V_{S30} estimation.

Proxies considered	Region	Parameterization (category/equation)	No. of groups	References	Description/notes
Surface geology	California Beijing	Categories, Equations	19 4	Wills and Clahan [2006] Xie et al. [2016]	Xie et al. [2016]: Bilinear model with two equations covering 4 surface geological units.
Topographic gradient	Global	Categories	8	Wald and Allen [2007] Allen and Wald [2009]	Slope gradient computed from 30 arc-sec (~1 km) resolution grid spacing from SRTM.
Terrain categories	California Greece, Taiwan, PNW	Categories	16	Iwahashi and Pike [2007] Yong et al. [2012] Yong [2016] Stewart et al. [2014] Kwok et al. [2018] Ahdi et al. [2017(a, b)]	Surface morphology categorized by slope gradient, local convexity, and surface texture. SRTM DEM at 30 arc-sec grid spacing.
Geotechnical Descriptors	California Japan	Categories	5	Chiou and Youngs [2008] Seyhan et al. [2014]	Geotechnical site categories, from Geomatrix 3 rd letter scheme.
Geomorphic/geologic maps	Japan	Categories	22	Matsuoka et al. [2006] Matsuoka and Wakamatsu [2008] Wakamatsu and Matsuoka [2013]	National geomorphic/geologic maps digitized at 7.5 arc-sec. V_{S30} predicted from JEGM category, slope gradient, elevation, and distance from mountain/hill.
Hybrid: geology and topographic gradient	California CENA Greece, PNW, Alaska	Categories, Equations	15 14 5	Wills et al. [2015] Parker et al. [2017] Stewart et al. [2014] Ahdi et al. [2017(a,b)]	Geologic units from various maps grouped into categories based on descriptions of lithology/ depositional environment. For certain groups, slope-dependent regression equations presented.
Hybrid: geotechnical and elevation	Taiwan	Categories, Equations	5	Chiou and Youngs [2008] Ancheta et al. [2013]	Grouped by GMX 3 rd letter geotechnical descriptors combined with station elevation within each GMX category.
Hybrid: surface geology, slope, elevation	Taiwan	Categories, Equations	3	Ahdi et al. [2017(b)] Kwok et al. [2018]	Surface geology classified using 1:50,000-scale maps (otherwise 1:250,000). SRTM DEM at 30 arc-sec grid spacing for gradient.

(b) Approach II: Limited V_S data, good quality maps

Approach II is applicable to regions where some V_S profile data is available, but the amount of information is not adequate to develop models for geologic categories in the manner described for Approach I. These regions generally have good-quality geologic maps, as with Approach I regions.

The concept behind this approach is to apply a proxy-based V_{S30} prediction model for a source (Approach I) region to a target (Approach II) region, and then to assess the applicability using residuals analysis. This allows variations between geologic categories, established from the data-rich source region, to be applied to the target region. If residuals analyses reveal bias, this bias should be removed by adjusting the source model for application to the target region.

The geologic categories used for the target region should be appropriate for the regional geologic conditions (e.g., accounting for local features such as glacial or volcanic deposits). A source region with categories appropriate for comparison to the target must be selected carefully. Prior to NGA-Sub, the primary example of Approach II was the use of a California geology-based model [Wills and Clahan 2006] for alluvial sites in Italy [Scasserra et al. 2009]. Approach II was used in NGA-Sub for some geology groups in Alaska, with the PNW taken as the source region (described in Ahdi et al. [2017(b)]).

Aleatory uncertainties for Approach II are generally taken from the source region. Epistemic uncertainties can be estimated from the standard error of the bias computed during validation.

(c) Approach III: V_S data absent or of low quality, variable access to geologic maps

Approach III is applied when little to no measured V_S/V_{S30} data is available for a region or for a specific geologic group of interest within a region. Approach III can also apply when data is available, but it is judged to be unreliable. These regions may or may not have reliable geologic maps. If geologic maps are available, region-specific geological groups are identified as in Approaches I and II. V_{S30} moments for similar groups are then assigned from other (source) regions. This is similar to Approach II, but without the validation step. If geologic maps are not available, global slope or terrain class models may be applied. This approach is not preferred if geologic maps are available because several studies have found stronger predictive power from geology-based proxies or hybrid geology-slope proxies [Seyhan et al. 2014; Ahdi et al. 2017(a); and Parker et al. [2017]].

Approach III involves larger epistemic uncertainty than other approaches. To estimate this uncertainty, $\mu_{\ln V}$ values are assembled from Approach I studies for California [Wills et al. 2015], Taiwan [Kwok et al. 2018], Greece [Stewart et al. 2014], the Pacific Northwest [Ahdi et al. 2017(a)], and CENA [Parker et al. 2017]; see Table 5.4. The standard deviations of the natural logs of these means provide an estimate of epistemic uncertainty. These standard deviations are estimated separately for Holocene sediments (principally alluvium), Pleistocene sediments (principally older alluvium and terrace deposits), and Tertiary-aged sedimentary bedrock materials. As shown in Table 5.4, the epistemic uncertainty (σ_{ep}) in each case is approximately 0.2 in natural log units. Accordingly, $\sigma_{ep} = 0.2$ is assigned as the epistemic uncertainty.

Examples where Approach III was implemented in NGA-Sub include geology groups in Alaska that had little to no measured V_{S30} data [Ahdi et al. 2017(b)] and geomorphic terrain classifications per Iwahashi and Pike [2007] for Central America, Mexico, and South America, excepting Chile.

Table 5.4 Computation of average epistemic uncertainty for similar V_{S30} geological age groups across multiple study regions.

Age	Mean (ln) V_{S30} values across regions (m/sec)					Group moments	
	PNW	CENA	CA	Greece	Taiwan	μ_{lnV} (m/sec)	(σ_{ep})
H	277	210	278	327	320	279	0.158
PI	458	271	362	471	508	404	0.229
T	455	351	405	456	702	460	0.232

Note: H = Holocene, PI = Pleistocene, T = Tertiary

5.3.3 Application of Existing Regional Proxy-Based V_{S30} Prediction Models

Over the five-year duration of the NGA-Sub project, regional proxy-based V_{S30} prediction models were developed for the Pacific Northwest, Alaska, Taiwan, New Zealand, and Chile. Those models are published elsewhere. In this section, those models are briefly reviewed, and comments are provided regarding their application to NGA-Sub sites.

(a) Pacific Northwest

The Pacific Northwest (Cascadia) model is presented in Ahdi et al. [2017(a)], and formally encompasses northern California, Oregon, Washington, and southwestern British Columbia. The V_S profile dataset gathered in Cascadia allowed for development of 18 well-populated surficial geology categories based on geologic map units largely at 1:24,000 to 1:100,000 scale, providing a high level of resolution in geologic units, encompassing a range of alluvial and glaciation-related sedimentary depositional environments, and three types of rock (sedimentary, igneous, and metamorphic). As such, this is an Approach I model.

Six of the 18 groups were found to exhibit correlation between V_{S30} and topographic slope, which is captured using a power-law model. A geomorphic terrain proxy-based model, following the 16 classes prescribed by Iwahashi and Pike [2007] (later updated by Iwahashi et al. [2018]) was also developed with 13 of 16 classes having well-populated groups (greater than 3 data points).

An electronic supplement to Ahdi et al. [2017(a)] contains V_{S30} assignments and supporting metadata for Cascadia sites. In a few cases, sites missing from that supplement have assignments added in to the *Site* table using the procedures described in Ahdi et al. [2017(a)]. Sites that recorded Cascadia events but are located in California have V_{S30} assignments from the Wills et al. [2015] V_{S30} prediction model, which is based on surficial geology and three slope bins for alluvial categories (254 sites). For 314 sites located in the intermountain west of the U.S., an Approach III framework was utilized whereby the terrain classification-based V_{S30} prediction model from Yong [2016] was used to assign mean and standard deviation V_{S30} values,

with an epistemic uncertainty assigned ($\sigma_{ep} = 0.2$). Sites that recorded Cascadia events that are located in CENA have V_{S30} assignments from the Parker et al. [2017] prediction model.

(b) Alaska

The V_{S30} prediction model for Alaska was developed in coordination with model development for Cascadia. The model is described in Ahdi et al. [2017(b)]. The V_S profile dataset in Alaska is limited in number, and the measurements that are available are clustered in relatively few areas (Anchorage, Fairbanks, Seward, Valdez, and areas considered in post-earthquake reconnaissance following the 2002 Denali event). For much of Alaska, large-scale geologic maps are not available, which necessitated the use of very small-scale regional maps (e.g., the statewide map of 1:584,000, see Wilson et al. [2015]).

As a result, much of the Alaska-specific regional model was developed following Approach II, but with some geological groups utilizing Approaches I and III as well. Comparing the 18 geological groups from Cascadia to the site conditions in Alaska resulted in an implementation of five different categories of proxy attribution. Approach I was used for one group (alluvium), which had enough Alaska-specific V_{S30} measurements. A combination of Approaches I and II was used for three groups (lacustrine, alluvial fan, and loess deposits) that had similar data populations in Alaska and Cascadia without appreciable inter-region bias. Approach II was used for two groups (artificial fill and glacial sediments) where bias was checked against Cascadia group moments and was found to be negligible. Approach III was used for other groups that were underpopulated with respect to Alaskan data or had site conditions not present in the Cascadia proxy framework (e.g., tectonic mélangé). The source region used to assign moments to Alaska was generally Cascadia, although California [Wills et al. 2015] was used for the tidal-flat and mélangé groups.

Metadata and V_{S30} assignments for Alaska sites were not presented in Ahdi et al. [2017(b)], but they are provided in the *Site* table based on the protocols presented in that paper.

(c) Chile

Chile is among the most seismically active countries in the world and has contributed substantially to the worldwide subduction event inventory (Chapter 4 of this report). The density of recording stations was relatively low up through the time of the 2010 M8.8 Maule earthquake, with the available networks primarily being operated by two academic departments in the University of Chile. Since that time, the number of strong-motion stations has increased significantly [Leyton et al. 2018], as has the amount of seismic site characterization performed at stations and for engineering projects.

As part of NGA-Sub, a profile database was assembled for Chile, drawing heavily upon university and industry contacts. Contreras et al. [2018] describes the V_S dataset (492 V_{S30} measurements) developed for Chile. To date, geologic maps have not been accessed to provide surface geology metadata. As a result, geomorphic terrain classes (based on Iwahashi and Pike [2007]) were used as the proxy for V_{S30} prediction. All but two of the 16 categories were well populated with profile data. In three cases, terrain classes of similar description were grouped. Aside from terrain class, the model considers regional effects caused by differences in climate in the arid north and more fertile regions to the south. The model is presented in Contreras et al. [2018] and was applied here for metadata and site class assignments in the *Site* table. Future

work for Chile entails development of a hybrid geology/slope V_{S30} model, once suitable geology maps are accessed.

(d) New Zealand

As noted in Section 5.2.1, Kaiser et al. [2016; 2017] assembled site metadata for strong-motion stations in New Zealand. Each site has an assigned value of V_{S30} along with an indicator of $Q1$, $Q2$, or $Q3$. These indicators qualitatively describe the quality and uncertainty of the site parameters, as follows:

- $Q1$ (assigned to 29/412 [7%] of New Zealand sites in the *Site* table) indicates “well-constrained measurements of V_{S30} from non-invasive surface-wave methods or borehole Seismic Cone Penetrometer Testing (SCPT).”
- $Q2$ (33 sites) is defined as being one or more of the following: (1) “estimates based on partly constrained near-surface V_S structure (i.e., well-constrained to depths less than 30 m); (2) “estimates from known local strata and V_S approximated using established correlations”; or (3) “well-constrained measurements at nearby geologically similar sites.” This description makes it difficult to determine on a site-specific basis which $Q2$ sites are measurement- or proxy-based.
- $Q3$ (350 sites) is defined as one or both of the following: (1) “Estimates from broad-scale national V_{S30} maps” or (2) “estimates at sites with poor constraints.” Sites with $Q2$ and $Q3$ estimates of V_{S30} are considered to be based on Approach I, given the local attributes of the estimates.

V_{S30} values provided by Kaiser et al. [2016] are adopted for NGA-Sub without modification. For $Q1$ sites, an aleatory variability is assigned that is appropriate for V_{S30} as established from a V_S profile, which is ($\sigma_{\ln V} = 0.1$) [Seyhan et al. 2014]. For $Q2$ sites, $\sigma_{\ln V}$ is assigned as 0.25, which is a typical value for V_{S30} uncertainty as derived from profiles developed using geotechnical data [Kwak et al. 2015]. For $Q3$ sites, $\sigma_{\ln V}$ is assigned as 0.4, which is a typical value for V_{S30} uncertainty as derived from surface geology proxies (e.g., Figure 13 of Ahdi et al. [2017(a)]).

Researchers in New Zealand developed a V_{S30} map of the entire country based on geological and topographic constraints, similar to work done by Thompson et al. [2014] in California. They used Bayesian inferencing to condition statistical groups based on *a priori* group moments obtained from the Cascadia hybrid geology/slope proxy model, and updated posterior distributions based on added New Zealand V_{S30} data [Foster et al. 2019].

(e) Taiwan

Kwok et al. [2018] assembled a V_S profile database from site data on the CWB website and used this data to develop a Taiwan-specific V_{S30} prediction model conditioned on geological age categories in combination with slope and elevation. The geological categories were derived using large-scale maps (1:50,000). A terrain classification proxy (based on the classes identified by Iwahashi and Pike [2007]) was also developed, with 15 of 16 classes being well-populated with measured V_{S30} data. These models are best described as Approach I. An electronic supplement to Kwok et al. [2018] provides V_{S30} assignments and supporting metadata; this information was transferred to the *Site* table.

5.3.4 Previously Unpublished Proxy-Based V_{S30} Assignments

This section describes V_{S30} assignments for NGA-Sub sites in regions where previous prediction models are modified from their published form. In the case of Japan, two previous Approach I models are adapted for use in NGA-Sub. For the remaining regions [CAM; SAM (excepting Chile), western Canada, and the Alaska panhandle], Approach III methods were applied.

(a) Japan

In Japan, V_S profiles were compiled from strong-motion recording sites within the K-NET and KIK-NET networks (Aoi et al. [2004]; <http://www.kyoshin.bosai.go.jp>) and the PARI network (Ichii et al. [1999]; <http://www.eq.pari.go.jp/kyosin/>). There are 1667 profiles with profile depths $z_p \geq 10$ m. In the K-NET network, typical profile depths are 10–20 m. For KIK-NET and PARI, typical profile depths are 100–200 m and < 200 m, respectively. If geotechnical investigations (e.g., SPT or CPT) at a site are available but geophysical investigations are not, models correlating V_S with penetration resistance and effective stress were used to estimate V_S [Kwak et al. 2015]. This method is applied to 42 of the PARI sites.

Each of the 1667 sites in the profile database were assigned one of the 16 terrain categories from the Iwahashi and Pike [2007] classification scheme. As was done for California initially by Yong et al. [2012] and then updated by Yong [2016], category moments μ_{lnV} and σ_{lnV} were computed using the Japanese data. Figure 5.5 shows the Japan category means along with 95% confidence intervals and means from Yong [2016]. Data for categories 2, 10, and 14 are too few to compute reliable statistics (≤ 4 observations). For those categories, results from Yong [2016] were adopted as indicated in Figure 5.5. For all other categories, Japan moments were used. Based on this rationale, recommended moments for each category are given in Table 5.5.

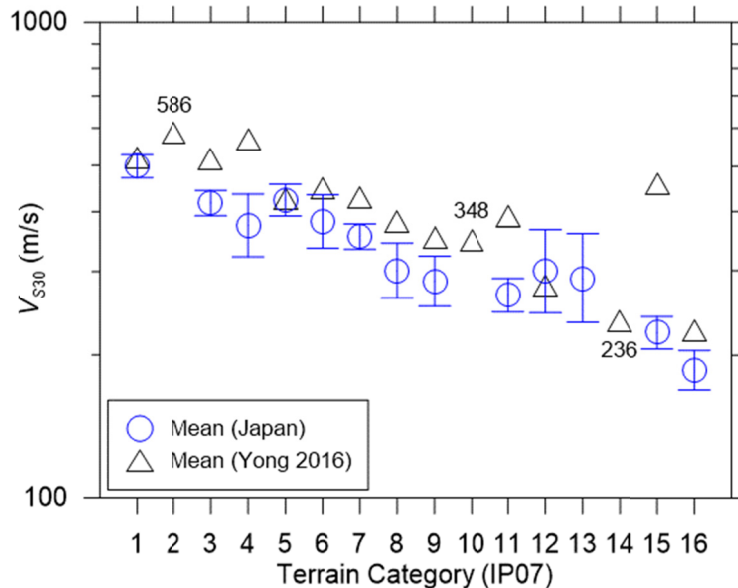


Figure 5.5 Comparison of V_{S30} means for Iwahashi and Pike [2007] terrain classes for Japan and California [Yong 2016]. Classes 2, 10, and 14 are poorly populated in the Japan dataset, and the values written in the figure from California are used for application in Japan.

Table 5.5 Moments for Iwahashi and Pike [2007] (IP07) terrain classes for application in Japan. Moments adopted from California are shown in parenthesis.

IP07 Terrain Class	N	μ_{Inv} (m/sec)	σ_{Inv}	μ_{Inv} of Y16 (m/sec)	σ_{Inv} of Y16
1	205	498	0.411	519	0.38
2 (CA)	4	(586)	(0.16)	586	0.16
3	212	416.8	0.456	517	0.38
4	29	374.6	0.415	568	0.46
5	120	422.8	0.43	425	0.37
6	6	381.6	0.16	448	0.14
7	245	354.9	0.479	429	0.38
8	16	301.4	0.27	382	0.32
9	46	286.4	0.421	353	0.16
10 (CA)	0	(348)	(0.09)	348	0.09
11	98	267.6	0.412	392	0.48
12	12	300.2	0.355	281	0.20
13	22	290.5	0.513	NA	NA
14 (CA)	2	(236)	(0.14)	236	0.14
15	83	223.3	0.365	460	0.52
16	40	186.1	0.309	225	0.20

The other proxy that was considered was introduced by Matsuoka et al. [2006] for categories within the “Japan Engineering Geomorphologic Classification Map” (JEGM). The JEGM utilizes geomorphology, surface geology, slope angle, and relative relief to classify locations into geomorphologic units. The empirical correlations are based on shear-wave velocity profiles from 1937 sites (this is a different dataset than that compiled for NGA-Sub). Subsequently, new categories were added, with the list as of 2013 provided in Table 5.6 (from Wakamatsu and Matsuoka [2013]; three categories that do not have stations in NGA-Sub have been omitted). Also shown in the table are: (1) category means and standard deviations as provided by Matsuoka et al. [2006]; and (2) the minimum, maximum, and median of the mapped V_{S30} values for the category, which differ from the Matsuoka et al. [2006] category mean due to varying morphological influences within the categories (from changes in slope angle and relative relief). Categories 1–4 correspond approximately to rock conditions, 5–7 are transitional categories, and categories of 8 and above represent various soil conditions. Matsuoka et al. [2006] provide intra-category regressions against elevation for categories 8–13, against slope for categories 3, 5, and 8–11, and against distance from hills for categories 8, 10, 13, 15, and 18–19. We used JEGM maps and associated values of V_{S30} at 7.5 arc-sec grid-size resolution by Wakamatsu and Matsuoka [2013]. No modifications to these V_{S30} values were applied.

Because two models (using different proxies) have been developed for prediction of the natural log mean and standard deviation of V_{S30} , a weighted combination of the two estimates is needed. An approach that has the objective of minimizing the standard deviation of the estimate of V_{S30} that results from the combination of the two proxies was applied; see Kwok et al. [2018] for the mathematical formulation. This approach was originally developed as part of NGA-Sub for V_{S30} assignments in Japan by the fifth author. The weights applied to the two proxies depend on the standard deviation of residuals for the respective categories used in each proxy ($\sigma_{\ln V}$) and the degree of correlation between proxies. Using the Japan PDB compiled for NGA-Sub, the standard deviations for the dataset as a whole are 0.44 for the prediction model based on terrain categories, and 0.30 for the JEGM-based model; however, different combinations of categories between proxies can lead to more similar dispersions. For example, JEGM category 3 (Hill) has ($\sigma_{\ln V} = 0.40$) and is shared for some sites with terrain class 15 ($\sigma_{\ln V} = 0.37$).

The correlation coefficient is calculated using normalized residuals:

$$\varepsilon_i = \frac{\ln(V_{S30}) - \mu_{\ln V_i}}{\sigma_{\ln V_i}} \quad (5.3)$$

where index i refers to model 1 (terrain) or 2 (JEGM), and $\ln(V_{S30})$ is a measured value from the profile database. Figure 5.6(a) shows that the two sets of residuals are relatively weakly correlated with ($\rho_{12} = 0.68$) for the dataset taken as a whole. This correlation coefficient is used for all category combinations. Based on this correlation coefficient and the respective $\sigma_{\ln V}$ values, the JEGM model typically receives higher weights. For example, the combination of category 15 for both JEGM and terrain provides $\sigma_{\ln V} = 0.25$ and 0.37, respectively, which gives a weight of essentially unity to JEGM with a combined standard deviation of 0.25. On the other hand, for sites with JEGM category 3 and terrain class 15, the weights are 0.35 (JEGM) and 0.65 (terrain). Each combination of categories in the application of the two models receives a unique set of weights.

Additional prediction models based on other proxies were considered for use in Japan, including a geotechnical classification scheme by Chiou and Youngs [2008] as updated in Seyhan et al. [2014], and topographic slope in Wald and Allen [2007] and Allen and Wald [2009]. The geotechnical scheme was not used because category assignments are subjective, and because the dispersion ($\sigma_{\ln V}$) is larger than that for the conceptually-similar JEGM approach. Topographic slope was not used because of strong correlation with the terrain-based approach ($\rho = 0.87$), which is shown in Figure 5.6(b).

Table 5.6 JEGM site categories, within-category moments from Matsuoka et al. [2006], (“Mea06”), and attributes of mapped V_{S30} within categories from Wakamatsu and Matsuoka [2013].

Cat.	Description	μ_{InV} (m/sec) (Mea06)	σ_{InV} (Mea06)	Max. V_{S30} (m/sec)	Med. V_{S30} (m/sec)	Min. V_{S30} (m/sec)
1	Mountain	707.5	0.295	775.5	708.4	641.3
2	Mountain footslope	400	0.212	400.3	400.3	400.3
3	Hill	428	0.403	526.1	408.3	294.7
4	Volcano	509	0.373	510.4	510.4	510.4
5	Volcano footslope	302	0.23	361.3	294.5	226.9
6	Volcanic hill	405	0.136	405.6	405.6	405.6
7	Rocky strath terrace	351	0.216	351.4	351.4	351.4
8	Gravelly terrace	418	0.281	589.2	466.6	252.9
9	Terrace covered with volcanic ash soils	269	0.265	418.5	270.5	197.4
10	Valley bottom lowland	345	0.364	544.2	394.5	191.5
11	Alluvial fan	323	0.267	436.2	337.5	253.1
12	Natural levee	198	0.286	267.1	201	185.2
13	Back marsh	160	0.267	192.9	166.55	140.6
14	Abandoned river channel	183	0.21	183.8	183.8	183.8
15	Delta and coastal lowland	171	0.246	207.5	168.15	141.6
16	Marine sand and gravel bars	258	0.262	260.2	260.2	260.2
17	Sand dune	194	0.283	194.5	194.5	194.5
18	Lowland between coastal dunes and/or bars	NA	NA	NA	NA	NA
19	Reclaimed land	182	0.283	236.3	173	149.9
20	Filled land	NA	0.276	253.3	188.3	152.6
21	Rocky shore, rock reef	NA	NA	429.1	429.1	429.1

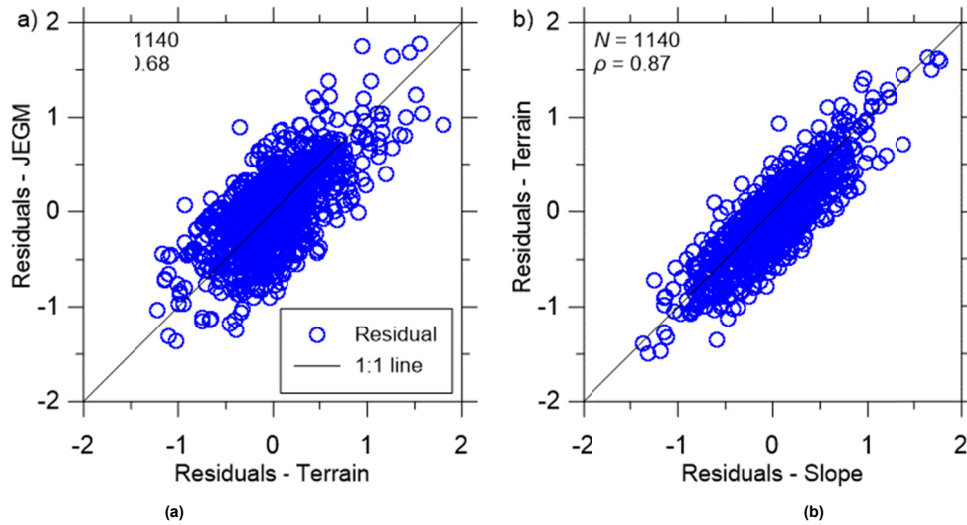


Figure 5.6 Correlations of residuals from proxy-based V_{S30} estimates using data from Japan: (a) modest correlation using JEGM and terrain proxies; and (b) strong correlation using terrain- and slope-based proxies.

(b) Central and South America, excepting Chile

As discussed in Section 5.2, V_S profile data is limited in Central and South American countries for which ground motions have been recorded from Cocos and Nazca subduction zone events [excluding Chile, see Section 5.3.3(c)]. This applies to Mexico, all of Central America, and all of South America, excepting Chile.

There was limited access to geologic maps for these regions. A series of small-scale (1:250,000) maps of Mexico from the Servicio Geológico Mexicano were identified [SGM 2017]. Geologic maps for other regions in Central and South America (excepting Chile) were not accessible. As a result, Approach III was applied to these regions using the Iwahashi and Pike [2007] terrain categories as the proxy. The selected source region for the model is California, using category moments from Yong [2016]. An epistemic uncertainty of $\sigma_{ep} = 0.2$ was assigned.

(c) Western Canada and Alaska Panhandle

Some stations, particularly in the majority of British Columbia, the Yukon Territory, and the Alaska Panhandle (seven sites, south of 60°N latitude), recorded events in both the Cascadia and Alaska subduction zones but were beyond the geographic extent of applicability of either the PNW- or Alaska-specific V_{S30} prediction models. The line of latitude at 55°N as depicted in Figure 5.7 (white line) is used to divide these stations by region (Alaska to the north, Cascadia to the south). Hence, a regional flag for western Canada and the Alaska panhandle is not present in the *Site* table. Procedures used to assign site parameters in these areas are given here.

The region encompassing western Canada and the Alaskan Panhandle was divided into different tectonic regimes based on the bedrock geological map shown in Figure 5.8. A thrust fault marks the eastern edge of deformation in the Canadian Cordillera that was associated with the Laraimde Orogeny of the Late Cretaceous period, east of which lies the relatively-undeformed Canadian Shield geographic province. V_{S30} is assigned to all stations southwest of this thrust fault with a geometric mean of the CAS and ALK models for groups where the V_{S30} moments differ; otherwise, the CAS V_{S30} moments are assigned. An epistemic uncertainty is also

applied ($\sigma_{ep} = 0.2$). Sites northeast of this fault lie in the Canadian Shield, and we assign V_{S30} moments from the model developed for CENA by Parker et al. [2017].

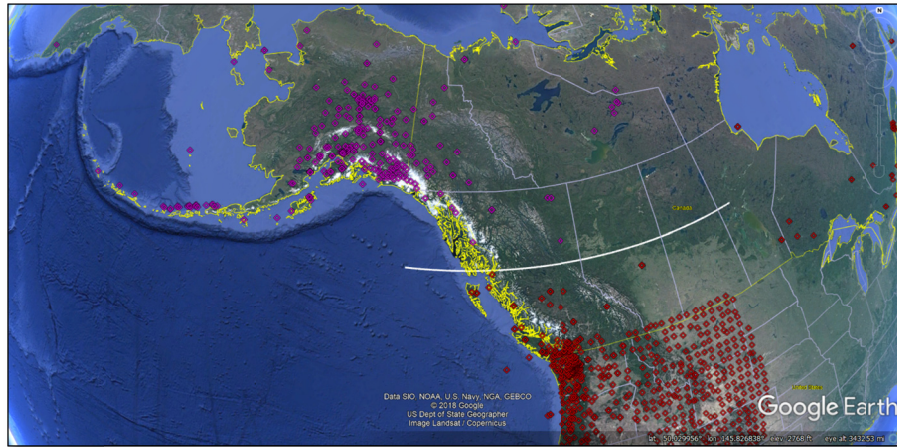


Figure 5.7 Map of stations in North America that have recorded Alaska events (purple icons) and Cascadia events (red icons), divided by the 55°N parallel (white line).

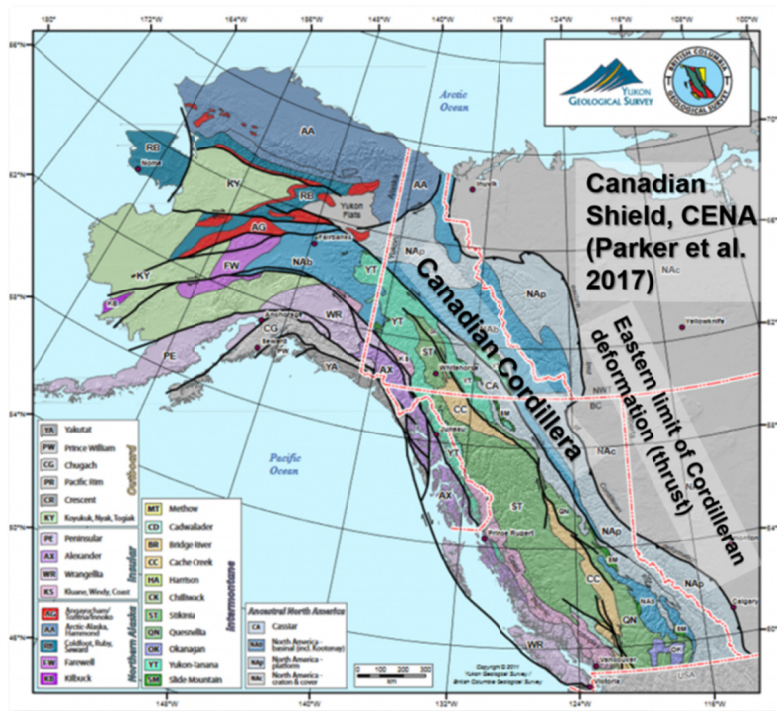


Figure 5.8 Bedrock geological map of terranes comprising the Canadian Cordillera in western Canada and Alaska. A thrust fault (thick black line) marks the “eastern limit of Cordilleran deformation”; the Canadian Shield lies east of this fault. Figure modified from Colpron and Nelson [2011].

5.4 V_{S30} ASSIGNMENTS

As described in preceding sections, assignments of V_{S30} can be made using a wide range of methods with variable levels of associated variability and uncertainty, depending on the availability of V_S measurements and locally-calibrated proxy-based V_{S30} prediction models. For each site in the NGA-Sub *Site* table, a preferred median V_{S30} ($\mu_{\ln V}$) and an associated variability ($\sigma_{\ln V}$) were assigned. In cases where mean estimates carry large epistemic uncertainty, a standard deviation on the mean (σ_{ep}) was also assigned. The process by which these assignments are made is shown in Table 5.7 (the codes are given in the site database file).

Table 5.7 Protocol used in NGA-Sub for assignment of preferred V_{S30} and related parameters.

Code	Description
0	V_{S30} computed using profile with $z_p \geq 30$ m. Standard deviation taken as $\sigma_{\ln V} = 0.1$. Epistemic uncertainty on mean not assigned.
1	Profile is available but maximum V_S profile depth $z_p < 30$ m. V_{S30} is estimated using an extrapolation relationship, preferably with region-specific regression coefficients, e.g. those in Kwak et al. [2017] for each region, for use with the method described in Dai et al. [2013]. $\sigma_{\ln V} = \sqrt{\sigma_e^2 + 0.1^2}$. Values of σ_e given in Kwak et al. [2017].
1.5	Estimate V_S profile from standard penetration test blow counts and local correlations between V_S and penetration resistance/effective stress (this correlation is only used in Japan; Kwak et al. [2015]). V_{S30} computed from estimated profile: $\sigma_{\ln V} = 0.25$.
2	No profile available. Mean V_{S30} estimated using region-specific models based on geology or hybrid geology-morphology proxies. This code applied in PNW, portions of Alaska and Canada, Japan, Taiwan, and New Zealand. $\sigma_{\ln V}$ assigned based on category statistics.
3	No profile available. V_{S30} and its variability are estimated using region-specific models based on geomorphic terrain categories [Iwahashi and Pike 2007]. This code used in Chile, Japan, and California (for Cascadia events). $\sigma_{\ln V}$ assigned based on category statistics.
4	No profile available. Mean V_{S30} estimated using models developed for source region other than the target region. Source region models can be based on geology, hybrid geology-terrain proxies, or geomorphic terrain categories. This code applied in portions of Alaska, Central and South America (excepting Chile), and western Canada and the Alaska Panhandle. $\sigma_{\ln V}$ assigned based on source region category statistics. Epistemic uncertainties (σ_{ep}) assigned.

5.5 BASIN-DEPTH TERMS

5.5.1 Overview

Basin depth terms as used in GMMs are defined as vertical distances from the ground surface to the first occurrence of a particular V_S horizon. These depths are used to provide a first-order representation of basin geometry in alluvial or sedimentary basin environments. Commonly used basin depths are $z_{1.0}$ and $z_{2.5}$, which are depths to the $V_S = 1.0$ km/sec and 2.5 km/sec velocity

horizons, respectively, and were used in four of the five NGA-West2 GMMs [Gregor et al. 2014].

Depth parameters are assigned to a site in the *Site* table from a measured *in situ* V_S profile that meets or exceeds the specified velocity horizon or, when such profiles are not available, from a 3D seismic velocity model for a particular region. An exception is New Zealand, where Kaiser et al. [2016; 2017] provide depth term $z_{1.0}$ from profiles where available, and otherwise estimate $z_{1.0}$ using various methods unrelated to a 3D seismic velocity models (resolution indicated by quality flags $Q1-Q3$). Table 5.8 summarizes the number of sites assigned basin depth terms in the NGA-Sub *Site* table from both of these assignment protocols. A significant portion of sites (2350/6433, i.e., 39%) do not have an assignment of a basin depth term. Such terms are not compiled in Alaska and Central America, and Mexico. Only three sites have this parameter assigned in South America.

Table 5.8 Summary of basin depth terms included in NGA-Sub *Site* table for various regions. “Estimated” depths are from 3D models, with exception of New Zealand.

Region	Total # sites	$z_{1.0}$			$z_{2.5}$		
		Assigned	Measured	Estimated	Assigned	Measured	Estimated
Cascadia	1126	15	15	NA	458	1	457
Japan	2283	2,228	609	1619	2,021	113	1908
New Zealand	412	412	29	383	0	0	NA
South America	942	3	3	NA	0	0	NA
Taiwan	849	802	0	802	NA	NA	NA

5.5.2 Cascadia 3D Velocity Models

The USGS has developed a 3D seismic velocity model for the PNW, which was first presented by Stephenson [2007] and recently updated by Stephenson et al. [2017]. The model was developed to support seismic hazard studies and ground-motion simulations. The model encompasses a region from approximately 40.2°N to 50°N latitude, and from about 122°W to 129°W longitude, and 0–60 km depth.

As described by Stephenson [2007], the backbone of the velocity model is a geologic model encompassing six units, as shown in Figure 5.9:

- continental sedimentary basins (a combination of Quaternary and Tertiary basin units);
- continental crust;
- continental mantle;
- oceanic sediments;
- oceanic crust; and
- oceanic mantle.

Some details of the geologic structure related to the Seattle fault are included in the 2017 update. The structure of sedimentary basins is described separately for Quaternary and Tertiary basins.

The lateral limits of Quaternary basins (all of which are in the Puget lowlands) are based on a smoothed representation of the Quaternary–Tertiary contact from the Schuster [2005] surface geologic maps for Washington state (1:500,000-scale). The lateral limits of Tertiary basins in the Puget lowlands are based on the $V_P = 4.5$ km/sec isocontour from the Seismic Hazards Investigations in the Puget Sound (SHIPS) [Brocher et al. 2001] and P -wave seismic tomography [Ramachandran et al. 2006]. The 4.5 km/sec 3D isosurface was projected to the ground surface to define the basin boundary. The Portland area has only Tertiary basins in the USGS model, and the boundaries of these basins are based on depth to bedrock constrained by well data intersecting the boundary of crystalline rocks under Tertiary sedimentary deposits [Yeats et al. 1996; Gannett and Caldwell 1998].

The thickness of Quaternary basins is constrained from borehole and seismic refraction data. Basins with Quaternary sedimentary cover less than 30 m in thickness are not included in the model, such as for the Portland and Tualatin basins or the Willamette Valley. Within Quaternary basins, a uniform V_P profile is used with values of 1500, 1905, and 1980 m/sec at depths of 0, 200, and 1000 m, respectively. V_S is derived from the V_P profile using a V_P / V_S ratio of 2.5, with some exceptions at depths beyond 150 m. Velocity limits within Quaternary units are 600 m/sec (minimum) and 900 m/sec (maximum).

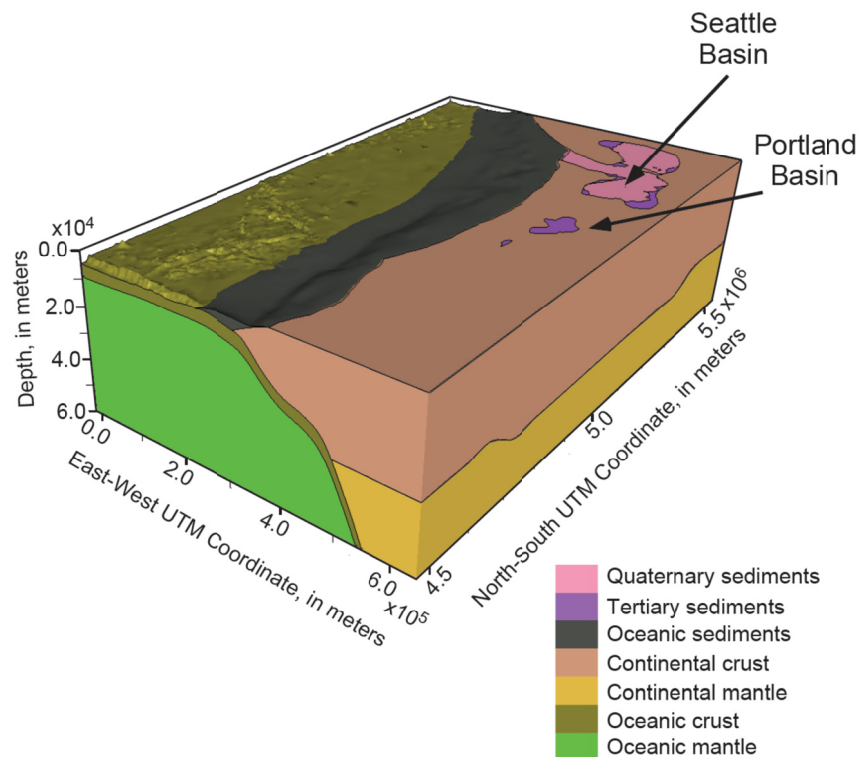


Figure 5.9 Three-dimensional representation of Cascadia geology as used in velocity model of Stephenson [2007] and Stephenson et al. [2017] (source: Stephenson et al. [2017]).

The thickness of Tertiary basins is taken as the 4.5 km/sec VP contour as derived from oil industry borehole data in the Puget Lowlands [Ramachandran et al. 2006] and from well data in the Portland area [Yeats et al. 1996; Gannett and Caldwell 1998]. V_P profiles within the Puget lowland basins was derived from tomographic studies [Ramachandran et al. 2006]. Variations on this process were used for other basins, including the Willamette Valley, where V_S is evaluated using a constant V_P / V_S ratio of 2.

Within these 3D velocity models, the 1.0 km/sec V_S horizon occurs within Quaternary or Tertiary basins structures, but it is not considered to be particularly meaningful or useful for ground-motion modeling. Rather, the 2.5 km/sec V_S horizon is preferred in this region, which does not occur within these basins but will typically occur at or near the base of basins of either age group.

As shown in Figure 5.9, surrounding and underlying basins in the 3D model is the continental crust unit. Seismic velocity structure in this unit in the Puget Lowland region is based on V_P as derived from SHIPS tomographic data [Ramachandran et al. 2006]. For the remainder of the model, seismic velocities are based on V_S derived from tomographic data from Moschetti et al. [2007]. V_P and V_S are related to each other in both tomographic datasets using empirical relationships from Brocher [2005].

Within the Cascadia region, only 15 sites had a measured $z_{1.0}$ from a V_S profile and only one site had a measured $z_{2.5}$ from a profile; see Table 5.8. Accordingly, almost all depths for Cascadia are based on the USGS model. Stephenson [2016] provided $z_{2.5}$ values at strong-motion sites located within Quaternary and Tertiary basins. Outside of these basin structures, basin depths are unassigned.

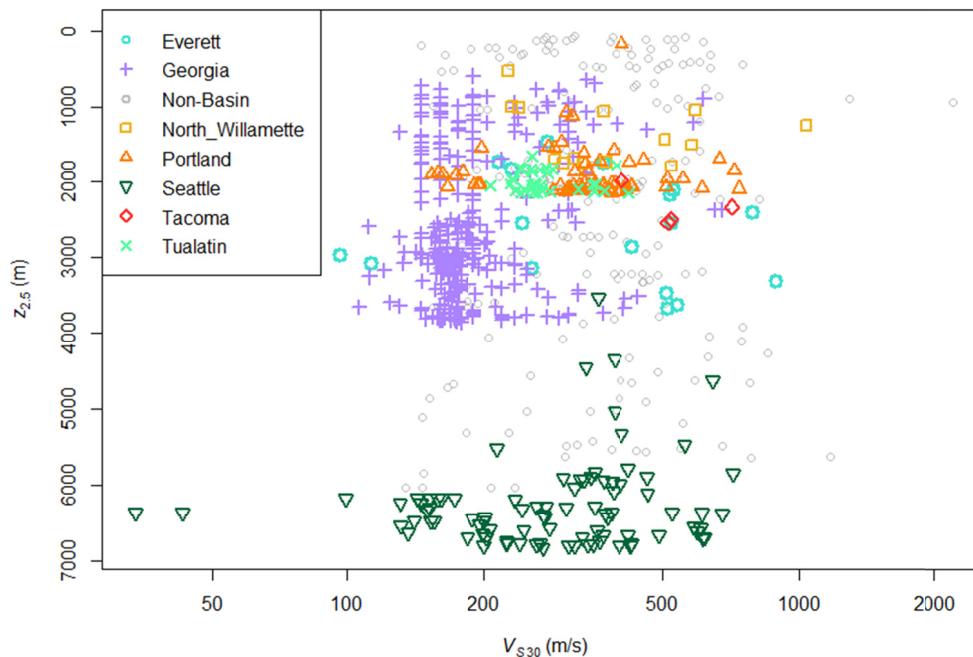


Figure 5.10 Basin depths ($z_{2.5}$) from Stephenson et al. [2017] as a function of V_{S30} for various basin structures in the Cascadia region.

Figure 5.10 shows $z_{2.5}$ values at strong-motion sites in the Cascadia region. Figure 5.11 shows outlines of the basins for which depths are available. Relationships between V_{S30} and $z_{2.5}$ for the Cascadia region as a whole are described elsewhere; see Chapter 5 of Parker et al. [2020]. There are strong differences in depths within specific basin structures. The Seattle basin has the largest depths. Portland has a very consistent distribution of depths between about 1.5–2.0 km. The Everett basin is much shallower than the Seattle basin, as is the Georgia basin near Vancouver. The City of Seattle and the USGS adopted an updated outline for the Seattle Basin after the present study had been completed; we show their outline in Figure 5.11 to compare with the one used in NGA-Sub.

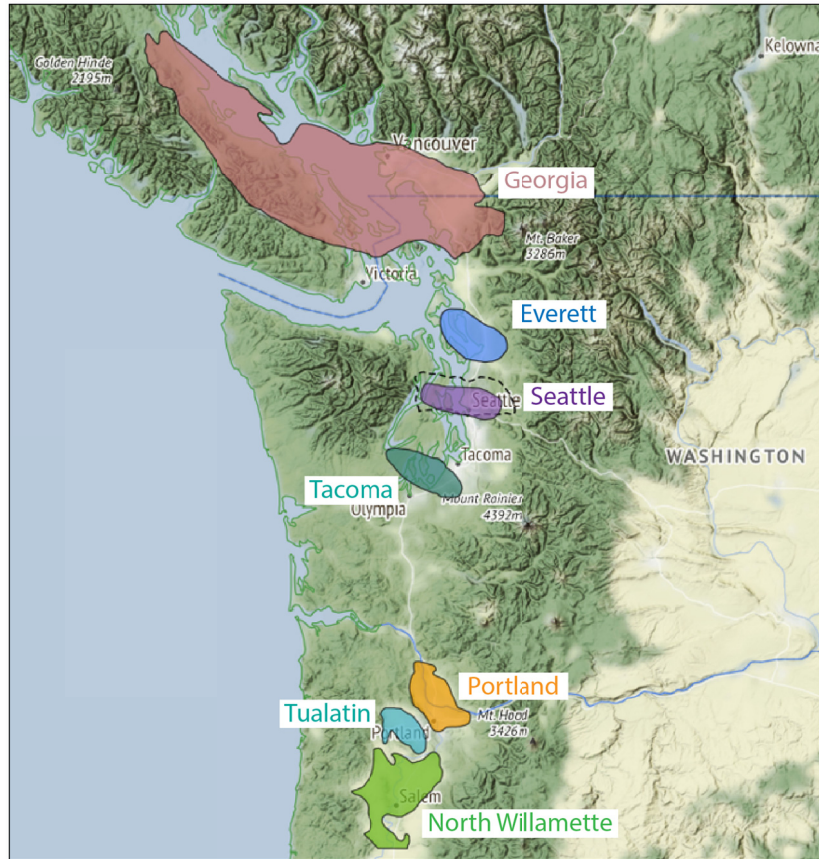


Figure 5.11 Basin edge outlines used in the definition of regional basin sediment-depth effects for the Pacific Northwest region of the U.S. Basin outlines modified from McPhee et al. [2014], Ramachandran et al. [2006], and Lowe et al. [2003]. Dashed line indicates Seattle basin outline subsequently adopted by the USGS and City of Seattle [Wirth et al. 2018].

5.5.3 Taiwan 3D Velocity Model

Seismic velocity models of the Western Plain and Taipei Basin of Taiwan have been developed by the Taiwan National Center for Research in Earthquake Engineering (NCREE). A Taipei basin model is presented by Lin et al. [2014] and a Western Plain basin model is presented by Kuo et al. [2016]. Most of the Taiwanese sites in the *Site* table (94%) have been assigned $z_{1.0}$ from models presented in these studies.

Figure 5.12 shows the location of the Taipei basin, which can be identified based on elevation. For Taipei, recordings of local events at ground-motion instruments were interpreted using the receiver function method (i.e., peaks in H/V spectral ratios used to infer depth to velocity contrasts). The observations were used in an inversion procedure to identify depths in an assumed six-layer profile. The P - and S -wave velocities of the layers were fixed to avoid trade-offs between the velocity and layer thickness. The result is a six-layer, spatially variable velocity model.

Figure 5.13 shows the limits of the Western Plain. In this region, passive circular arrays were used to record surface waves along with H/V spectra from microtremors. A frequency-wavenumber approach was used with the circular array data to provide frequency-phase velocity dispersion curves. These curves were jointly inverted with the H/V spectra to estimate shear-wave velocity structure at measurement locations. These results were combined to form the seismic velocity model.

The Taipei and Western Plains velocity models were queried by C.-K. Kuo [2017] for Taiwan strong-motion sites. These results were added to the *Site* table for use in NGA-Sub and are being used in a Taiwan seismic hazard study [NCREE 2017].

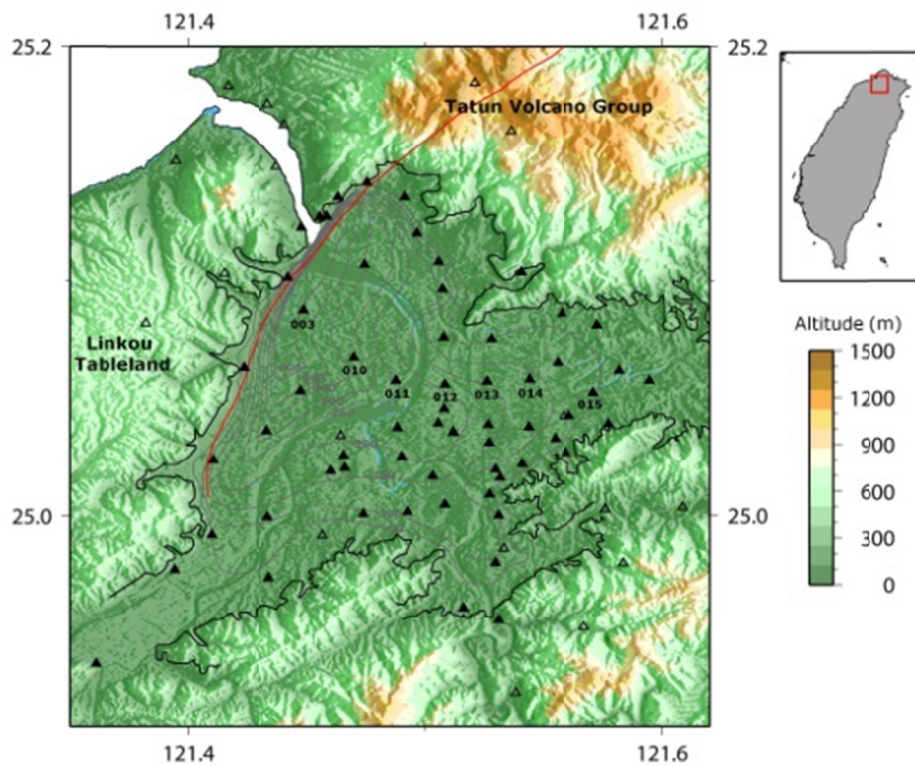


Figure 5.12 Map showing Taipei basin, as identified from topography (source: Lin et al. [2014]).

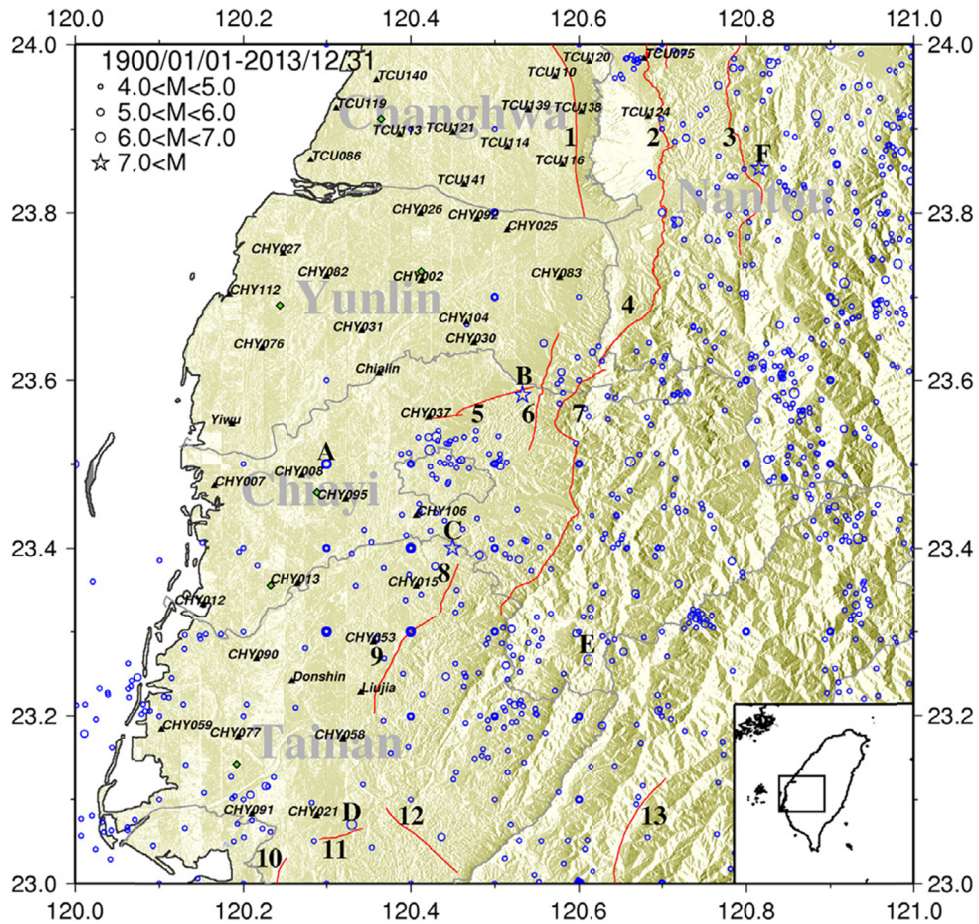


Figure 5.13 Map showing Western Plain in Taiwan (source: Kuo et al. [2016]).

5.5.4 Japan 3D Velocity Model

For Japan, the NIED seismic velocity model was utilized. The basin model was developed through a combination of deep boreholes, reflection and refraction surveys, micro-tremor surveys, and gravity surveys [Fujiwara et al. 2009; 2012]. Tomography was used to verify and refine the basin structure. The model covers depths for $x = 0.35$ to 3.0 km/sec. The basin depth lookups from the NIED model were performed by the fifth author using files accessible at <http://www.j-shis.bosai.go.jp/en/>. Figure 5.14 shows depth distributions in Japan based on these models. The same Japan basin model was used in NGA-West2 [Ancheta et al. 2013].

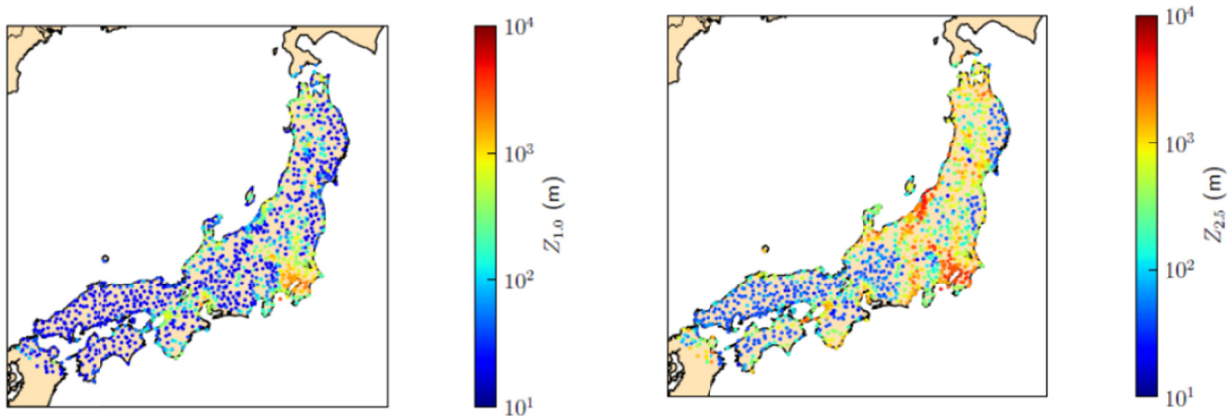


Figure 5.14 Spatial distributions of the $z_{1.0}$ and $z_{2.5}$ basin depth parameters in Japan based on NIED models (source: Ancheta et al. [2013]).

Suggested Citation:

Ahdi S.K., Ancheta T.D., Contreras V., Kishida T., Kwak D.Y., Kwok O.L., Parker G.A., Ruz F., Stewart J.P. (2020). Chapter 5: Site Condition Parameters, in *Data Resources for NGA-Subduction Project*, PEER Report No. 2020/02, J.P. Stewart (editor), Pacific Earthquake Engineering Research Center, University of California, Berkeley, CA (headquarters).

REFERENCES

- Abers G.A., Fischer K.M. (2003). Tomography under Costa Rica and Nicaragua. *International Federation of Digital Seismograph Networks*, https://doi.org/10.7914/SN/YO_2003.
- AEC (2018). Seismic Network webpage, *Alaska Earthquake Center*, University of Alaska Fairbanks, <https://earthquake.alaska.edu/network>.
- Ahdi S.K., Stewart J.P., Kwak D.Y., Ancheta T.D., Mitra D. (2017a). Development of V_S profile database and proxy-based models for V_{S30} prediction in the Pacific Northwest region of North America, *Bull. Seismol. Soc. Am.*, 107(4): 1781–1801.
- Ahdi S.K., Stewart J.P., Kwak D.Y., Ancheta T.D., Mitra D. (2017b). Proxy-Based V_{S30} prediction in the Pacific Northwest and Alaska, *Proceedings, 3rd International Conference on Performance-based Design in Earthquake Geotechnical Engineering*, Paper No. 482, Vancouver, Canada.
- Allen T.I., Wald D.J. (2009). On the use of high-resolution topographic data as a proxy for seismic site conditions (V_{S30}), *Bull. Seismol. Soc. Am.*, 99(2A): 935–943.
- Ancheta T.D., Darragh R.B., Stewart J.P., Seyhan E., Silva W.J., Chiou B. S.-J., Wooddell K.E., Graves R.W., Kottke A.R., Boore D.M., Kishida T., Donahue J.L. (2013). PEER NGA-West2 database, *PEER Report No. 2013/03*, Pacific Earthquake Engineering Research Center, University of California, Berkeley, CA.
- Anderson J. Alcántara L., Almora Mata, D., Weppen R., Brune J., Singh S.K., Parra G., Miranda E., Hernández M., Miranda J., Torres Noguez M., Yanez C. (2006). Guerrero accelerograph network: Highlights from 20 years of operation, *Proceedings, 8th U.S. National Conference on Earthquake Engineering*, San Francisco, CA.
- Aoi S., Takashi K., Fujiwara H. (2004). Strong-motion seismograph network operated by NIED: K-NET and KiK-net, *J. Japan Assoc. Earthq. Eng.*, 4(3): 65–74.
- Arango M.C., Strasser F.O., Bommer J.J., Hernandez D.A., Cepeda J.M. (2010). A strong-motion database from the Central American subduction zone, *J. Seismol.*, 15(2): 261–294.
- Boore D.M. (2004). Estimating V_{S30} (or NEHRP site classes) from shallow velocity models (depths < 30 m), *Bull. Seismol. Soc. Am.*, 94: 591–597.
- Boore D.M., Thompson E.M., Cadet H. (2011). Regional correlations of V_{S30} and velocities averaged over depths less than and greater than 30 m, *Bull. Seismol. Soc. Am.*, 101: 3046–3059.
- Borcherdt R.D. (2002). Empirical evidence for acceleration-dependent amplification factors, *Bull. Seismol. Soc. Am.*, 92(2): 761–782.
- Brocher T.M., Parsons T., Blakely R.J., Christensen N.I., Fisher M.A., Wells R.E., SHIPS Working Group (2001). Upper crustal structure in Puget Lowland, Washington—Results from the 1998 seismic hazards investigation in Puget Sound, *J. Geophys. Res.*, 106(B7): 13541–13564.
- Brocher T.M. (2005). Empirical relations between elastic wave speeds and density in the Earth’s crust, *Bull. Seismol. Soc. Am.*, 95(6): 2081–2092.
- Castillo L.F., Dimaté C., Drouet S., Fernandez G.A., Montalva G., Bastias N., Morales C., Pirchiner M., Singaicho J.C., Weatherill G. (2016). A South American strong motion database and selection of ground motion prediction equations (GMPEs) for seismic hazard analysis in South America, Research topic 6 (RT6). *Wiki of the South America Risk Assessment (SARA) project of the Global Earthquake Model (GEM)*, available at https://sara.openquake.org/hazard_rt6 (last accessed May 2017).
- Chiou B.S.-J., Youngs R.R. (2008). NGA model for average horizontal component of peak ground motion and response spectra, *PEER Report No. 2008/09*, Pacific Earthquake Engineering Research Center, University of California, Berkeley, California, USA.
- Colpron M., Nelson J.L. (2011). A digital atlas of terranes for the Northern Cordillera, Accessed online from Yukon Geological Survey (www.geology.gov.yk.ca), last visited 12 December 2018.

- Contreras V., Ruz F., Ahdi S.K., Stewart J.P. (2018). V_S profile database and proxy-based model for V_{S30} prediction in Chile for NGA-Subduction, *Proceedings, 11th National Conference on Earthquake Engineering (11NCEE)*, Paper No. 1473, Los Angeles, CA.
- Cortez-Flores A.M. (2004). *Site Response of the 2001 Southern Peru Earthquake*, M.S. Thesis, Department of Civil and Environmental Engineering, Washington State University, 291 pgs.
- Dai Z., Li X., Hou C. (2013). A shear-wave velocity model for V_{S30} estimation based on a conditional independence property, *Bull. Seismol. Soc. Am.*, 103(6): 3354–3361.
- Dobry R., Borcherdt R.D., Crouse C.B., Idriss I.M., Joyner W.B., Martin G.R., Power M.S., Rinne E.E., Seed R.B. (2000). New site coefficients and site classification system used in recent building seismic code provisions, *Earthq. Spectra*, 16: 41–67.
- Faccioli E.E., Santayo V., Leone J.L. (1973). Microzonation criteria and seismic response studies for the city of Managua, *Proceedings, Earthquake Engineering Research Institute Conference on the Managua, Nicaragua, Earthquake of December 23, 1972*, 1: 271–291.
- Faccioli E.E., Battistella C., Alemani P., Tibaldi A. (1988). Seismic microzoning investigations in the metropolitan area of San Salvador, El Salvador, following the destructive earthquake of 10 October 1986, *Proceedings, International Seminar on Earthquake Engineering*, Innsbruck, Austria, pp. 28–65.
- Farr T.G., Kobrick M. (2000). Shuttle radar topography mission produces a wealth of data, *EOS*, 81: 583–585.
- Foster K., Bradley B.A., McGann C.R., Wotherspoon L.M. (2019). A V_{S30} map for New Zealand based on geologic and terrain proxy variables and field measurements, *Earthq. Spectra*, 35(4): 1865–1897.
- Fujiwara H., Kawai S., Aoi S., Morikawa N., Senna S., Kudo N., Ooi M., Hao K.X.-S., Hayakawa Y., Toyama N., Matsuyama N., Iwamoto K., Suzuki H., Ei R. (2009). A study on subsurface structure model for deep sedimentary layers of Japan for strong-motion evaluation, National Research Institute for Earth Science and Disaster Prevention, *Technical Note No. 337* (in Japanese)
- Fujiwara H., Kawai S., Aoi S., Morikawa N., Senna S., Azuma H., Ooi M., Hao K.X.-S., Hasegawa N., Maeda T., Iwaki A., Wakamatsu K., Imoto M., Okumura T., Matsuyama H., Narita A. (2012). Some improvements of seismic hazard assessment based on the 2011 Tohoku earthquake, National Research Institute for Earth Science and Disaster Prevention, *Technical Note No. 379* (in Japanese).
- Gannett M.W., Caldwell R.R. (1998). Geologic framework of the Willamette Lowland aquifer system, Oregon and Washington, U.S. Geological Survey, *Professional Paper 1424-A*, 32 pgs., 8 plates.
- Global Volcanism Program (2013). *Volcanoes of the World*, v. 4.5.0 E. Venzke (ed.), Smithsonian Institution, downloaded 15 Jul 2016, <http://dx.doi.org/10.5479/si.GVP.VOTW4-2013>.
- Gregor N., Abrahamson N.A., Atkinson G.M., Boore D.M., Bozorgnia Y., Campbell K.W., Chiou B.S.-J., Idriss I.M., Kamai R., Seyhan E., Silva W.J., Stewart J.P., Youngs R.R. (2014). Comparison of NGA-West2 GMPEs, *Earthq. Spectra*, 30: 1179–1197.
- GSC (1989). Canadian National Seismograph Network. *International Federation of Digital Seismograph Networks, Geological Survey of Canada*, <https://doi.org/10.7914/SN/CN>.
- Ichii K., Sato Yu, Sato Yo, Hoshino Y, Iai S. (1999). Site characteristics of strong-motion earthquake stations in ports and harbours in Japan (Part VI), Port and Harbor Research Institute, Ministry of Transport, *Technical Note No 935*, Japan.
- IRIS (2003). US Array Transportable Array, *International Federation of Digital Seismograph Networks*, <https://doi.org/10.7914/SN/TA>.
- Iwahashi J., Pike R.J. (2007). Automated classifications of topography from DEMs by an unsupervised nested-means algorithm and a three-part geometric signature, *Geomorph.*, 86: 409–440.
- Iwahashi J., Kamiya I., Matsuoka M., Yamazaki D. (2018). Global terrain classification using 280 m DEMs: segmentation, clustering, and reclassification, *Prog. Earth Planet. Sci.*, 5(1), [https://doi: 10.1186/s40645-017-0157-2](https://doi.org/10.1186/s40645-017-0157-2).

- Kaiser A., Van Houtte C., Perrin N., Wotherspoon L., McVerry G., Cousins J., Dellow S., Wotherspoon L., Bradley B., Lee R. (2016). Characterizing GeoNet strong motion sites: Site metadata update for the 2015 Strong Motion Database, *2016 New Zealand Society of Earthquake Engineering Conference*, Christchurch, New Zealand.
- Kaiser A., Van Houtte C., Perrin N., Wotherspoon L., McVerry G. (2017). Site characterisation of GeoNet stations for the New Zealand strong motion database, *Bull. NZ Soc. Earthq. Eng.*, 50(1): 39–49.
- Kuo C.-H., Wen K.-L., Hsieh H.-H., Lin C.-M., Chang T.-M., Kuo K.-W. (2012). Site classification and V_{s30} estimation of free-field TSMIP stations using the logging data of EGDT, *Eng. Geol.*, 129–130: 68–75.
- Kuo C.-H., Chen C.-T., Lin C.-M., Wen K.-L., Huang J.-Y., Chang S.-C. (2016). S-wave velocity structure and site effect parameters derived from microtremor arrays in the Western Plain of Taiwan, *J. Asian Earth Sci.*, 128: 27–41.
- Kwak D.Y., Ancheta T.D., Mitra D., Ahdi S.K., Zimmaro P., Parker G.A., Brandenburg S.J., Stewart J.P. (2017). Performance evaluation of V_{SZ} -to- V_{S30} correlation methods using global V_S profile database, *Proceedings, 3rd International Conference on Performance-based Design in Earthquake Geotechnical Engineering (PBD-III)*, Paper No. 399, Vancouver, Canada.
- Kwak D.Y., Brandenburg S.J., Mikami A., Stewart J.P. (2015). Prediction equations for estimating shear-wave velocity from combined geotechnical and geomorphic indexes based on Japanese data set, *Bull. Seismol. Soc. Am.*, 105(4): 1919–1930.
- Kwok A.O., Stewart J.P., Kwak D.Y., Sun P.-L. (2018). Taiwan-specific model for V_{S30} prediction considering between-proxy correlations, *Earthq. Spectra*, 34: 1973–1993.
- Leyton F., Leopold A., Hurtado G., Pastén C., Ruiz S., Montalva G., Saéz E. (2018). Geophysical characterization of the Chilean seismological stations: First results, *Seismol. Res. Lett.*, 89(2A): 519–525.
- Lin C.-M., Wen K.-L., Kuo C.-H., Lin C.-Y. (2014). S-wave velocity model of Taipei Basin, *Proceedings, 5th Asia Conference on Earthquake Engineering (SACEE)*, Taipei, Taiwan.
- Louie J.N. (2001). Faster, better: Shear-wave velocity to 100 meters depth from refraction microtremor arrays, *Bull. Seismol. Soc. Am.*, 91(2): 347–364.
- Lowe C., Dehler S.A., Zelt B.C. (2003). Basin architecture and density structure beneath the Strait of Georgia, British Columbia, *Can. J. Earth Sci.*, 40: 965–981.
- Lundberg N., Reed D.L., Liu C.-S., Lieske Jr. J. (1997). Forearc-basin closure and arc accretion in the submarine suture zone south of Taiwan, *Tectonophys.*, 274: 5–23.
- Matsuoka M., Wakamatsu K., Fujimoto K., Midorikawa S. (2006). Average shear-wave velocity mapping using Japan Engineering Geomorphologic Classification Map. *Structural Eng. & Earthquake Eng.*, N(1): 57–68.
- Matsuoka M., Wakamatsu, K. (2008). Site amplification capability map based on the 7.5-arc-second Japan Engineering Geomorphologic Classification Map. No. H20PRO-93, National Institute of Advanced Industrial Science and Technology, Intellectual Property Management.
- McPhee D.K., Langenheim V.E., Wells R.E., Blakely R.J. (2014). Tectonic evolution of the Tualatin basin, northwest Oregon, as revealed by inversion of gravity data, *Geosphere*, 10, 264–275.
- Midorikawa S., Nogi Y. (2015). Estimation of V_{S30} from shallow velocity profile, *J. Japan Assoc. Earthquake Engineers*, 15(2), 91–96 (in Japanese).
- Moschetti M.P., Ritzwoller M.H., Shapiro N.M. (2007). Surface wave tomography of the western United States from ambient noise—Rayleigh wave group velocity maps, *Geochemistry, Geophysics, and Geosystems*, 8(Q08010), [http://doi: 10.1029/2007GC001655](http://doi:10.1029/2007GC001655).
- NCREC (2017). Site database for Taiwan strong motion stations, National Center for Research on Earthquake Engineering, Taiwan, Report No. NCREC-17-004, 86 pgs. (in Chinese).
- Nikolau S., Vera-Grunauer X., Gilsanz R. (2016). *GEER-ATC Earthquake Reconnaissance: April 16th 2016, Musine, Ecuador, Version 1b*, 24 October 2016, 604 pgs.

- Ohta T., Hiehata S., Takahashi K., Kitamura E., Motosaka M., Kamata M., Miyamura M. (1986). Research on the strong ground motion in Mexico City during the earthquake of September 19, 1985 Michoacan-Guerrero, Mexico, Kajima Institute of Construction Technology, Kajima Corporation, *KICT Report No. 68*, 42 pgs.
- Parker G.A., Harmon J.A., Stewart J.P., Hashash Y.M.A., Kottke A.R., Rathje E.M., Silva W.J., Campbell K.W. (2017). Proxy-based V_{S30} estimation in central and eastern North America, *Bull. Seismol. Soc. Am.*, 107(1): 117–131.
- Parker G.A., Stewart J.P., Boore D.M., Atkinson G.M., Hassani B. (2020). NGA-Subduction global ground motion models with regional adjustment factors, *PEER Report No. 2020-XX*, Pacific Earthquake Engineering Research Center, University of California, Berkeley, CA.
- Poran C.J., Rodriguez J.A., Satoh T., Borden R. (1994). A new interpretation method of surface wave measurements to obtain representative shear wave velocity profiles of soils, T.D. O'Rourke and M. Hamada (eds.), National Center for Earthquake Engineering Research, *Technical Report NCEER-94-0026*, pp. 425–443.
- Ramachandran K., Hyndman R.D., Brocher T.M. (2006). Regional P wave velocity structure of the Northern Cascadia Subduction Zone, *J. Geophys. Res.*, 111(B12301), <http://doi:10.1029/2005JB004108>.
- Scasserra G., Stewart J.P., Bazzurro P., Lanzo G., Mollaioli F. (2009). A comparison of NGA ground-motion prediction equations to Italian data, *Bull. Seismol. Soc. Am.*, 99(5): 2961–2978.
- Schuster J.E. (2005). Geologic map of Washington State, *Washington State Department of Natural Resources, Division of Geology and Earth Resources, Map GM-53*, scale 1:500,000, with pamphlet 44 pgs.
- Seed H.B., Romo M.P., Sun J., Jaime A., Lysmer J. (1987). Relationships between soil conditions and earthquake ground motions in Mexico City in the earthquake of Sept. 19, 1985, *Report No. UCB/EERC-87/15*, Earthquake Engineering Research Center, University of California, Berkeley, CA, 112 pgs.
- Seyhan E., Stewart J.P., Ancheta T.D., Darragh R.B., Graves R.W. (2014). NGA-West 2 site database, *Earthq. Spectra*, 30: 1007–1024.
- SGM (2017). Geological map series of Mexico, 1:250,000 scale, *Servicio Geológico Mexicano*, https://www.sgm.gob.mx/Gobmx/en/About_SGM/Geology.html, last accessed Dec. 2018.
- SNET (2018). Webpage of the Servicio Nacional de Estudios Territoriales (SNET) Seismic Network, Medio Ambiente y Recursos Naturales (MARN), El Salvador, available at <http://www.snet.gob.sv/ver/sismologia/>.
- Stephenson W.J. (2007). Velocity and density models incorporating the Cascadia subduction zone for 3D earthquake ground motion simulations, Version 1.3, U.S. Geological Survey, *Open-File Report 2007-1348*, 24 pgs.
- Stephenson W.J. (2016). *Personal Communication*.
- Stephenson W.J., Reitman N.G., Angster S.J. (2017). P- and S-wave velocity models incorporating the Cascadia Subduction Zone for 3D earthquake ground motion simulations—Update for Open-File Report 2007-1348, *U.S. Geological Survey Open-File Report 2017-1152*, Earthquake Hazards Ground Motion Investigations, 28 p.
- Stewart J.P., Klimis N., Savvaidis A., Theodoulidis N., Zargli E., Athanasopoulos G., Pelekis P., Mylonakis G., Margaris B. (2014). Compilation of a local V_S profile database and its application for inference of V_{S30} from geologic- and terrain-based proxies, *Bull. Seismol. Soc. Am.*, 104(6): 2827–2841.
- Thompson E.M., Wald D.J. (2012). Developing V_{S30} site-condition maps by combining observations with geologic and topographic constraints, *Proceedings, 15th World Conference on Earthquake Engineering*, Lisbon, Portugal.
- Thompson E.M., Wald D.J., Worden C.B. (2014). A V_{S30} map for California with geologic and topographic constraints, *Bull. Seismol. Soc. Am.*, 104: 2313–2321.
- Thompson E.M. (2018). An updated V_{S30} map for California with geologic and topographic constraints: U.S. Geological Survey data release, <https://doi.org/10.5066/F7JQ108S>.
- Universidad de Costa Rica (1989). Laboratorio de Ingeniería Sísmica. *International Federation of Digital Seismograph Networks*, <https://doi.org/10.7914/SN/MF>.
- University of Washington (1963). Pacific Northwest Seismic Network, *International Federation of Digital Seismograph Networks*, <https://doi.org/10.7914/SN/UW>.

- Van Houtte C., Bannister S., Holden C., Bourguignon S., McVerry G. (2017). The New Zealand strong motion database, *Bull. NZ Soc. Earthq. Eng.*, 50(1): 1–20.
- Vera-Grunauer X. (2014). *Seismic Response of a Soft, High Plasticity, Diatomaceous Naturally Cemented Clay Deposit*, Ph.D. Dissertation, Department of Civil and Environmental Engineering, University of California, Berkeley, CA.
- Vera-Grunauer (2017). *Personal Communication*.
- Wagner L., Beck S., Long M. (2010). PerU lithosphere and slab experiment. *International Federation of Digital Seismograph Networks*, https://doi.org/10.7914/SN/ZD_2010.
- Wakamatsu K., Matsuoka M. (2013). Nationwide 7.5-arc-second Japan engineering geomorphologic classification map and V_{S30} zoning, *J. Disaster Res.*, 8(5): 904–911.
- Wald D.J., Allen T.I. (2007). Topographic slope as a proxy for seismic site conditions and amplification, *Bull. Seismol. Soc. Am.*, 97: 1379–1395.
- Wang H.-Y., Wang S.-Y. (2015). A new method for estimating V_{S30} (30) from a shallow shear-wave velocity profile (Depth < 30 m), *Bull. Seismol. Soc. Am.*, 105(3): 1359–1370.
- Wills C.J., Clahan K.B. (2006). Developing a map of geologically defined site-condition categories for California, *Bull. Seismol. Soc. Am.*, 96: 1483–1501.
- Wills C.J., Gutierrez C.I. (2008). Investigation of geographic rules for improving site-conditions mapping, California Geological Survey, *Final Technical Report, USGS/NEHRP Award Number 07HQGR0061*, Sacramento, CA.
- Wills C.J., Gutierrez C.I., Perez F.G., Branum D.M. (2015). A next generation V_{S30} map for California based on geology and topography, *Bull. Seismol. Soc. Am.*, 105(6): 3083–3091.
- Wilson F.H., Hulst C.P., Mull C.G., Karl S.M. (2015). Geologic map of Alaska, U.S. Geological Survey, *Scientific Investigations Map 3340*, pamphlet 196 pgs., 2 sheets, scale 1:1,584,000, <http://dx.doi.org/10.3133/sim3340>.
- Wirth E.A., Chang S.W., Frankel A.D. (2018). 2018 Report on incorporating sedimentary basin response into the design of tall buildings in Seattle, Washington, U.S. Geological Survey, *Open-File Rept. 2018–1149*, 23 pgs.
- Xie J., Zimmaro P., Li X., Wen Z., Song Y. (2016). V_{S30} Empirical prediction relationships based on a new soil-profile database for the Beijing Plain area, China, *Bull. Seismol. Soc. Am.*, 106(6): 2843–2854.
- Yeats R.S., Graven E.P., Werner K.S., Goldfinger C., Popowski T.A. (1996). Tectonics of the Willamette Valley, Oregon, in A.M. Rogers, T.J. Walsh, W.J. Kockelman, and G.R. Priest, (eds.), *Assessing earthquake hazards and reducing risk in the Pacific Northwest*, U.S. Geological Survey, *Professional Paper 1560*, 1:183–222.
- Yong A. (2016). Comparison of measured and proxy-based V_{S30} values in California, *Earthq. Spectra*, 32(1), 171–192.
- Yong A., Hough S.E., Iwahashi J., Braverman A. (2012). A terrain based site conditions map of California with implications for the contiguous United States, *Bull. Seismol. Soc. Am.*, 102: 114–128.

PEER REPORTS

PEER reports are available as a free PDF download from <https://peer.berkeley.edu/peer-reports>. In addition, printed hard copies of PEER reports can be ordered directly from our printer by following the instructions at <https://peer.berkeley.edu/peer-reports>. For other related questions about the PEER Report Series, contact the Pacific Earthquake Engineering Research Center, 325 Davis Hall, Mail Code 1792, Berkeley, CA 94720. Tel.: (510) 642-3437; and Email: peer_center@berkeley.edu.

- PEER 2019/09** *Seismic Behavior of Special Concentric Braced Frames under Short- and Long-Duration Ground Motions.* Ali Hammad and Mohamed A. Moustafa. December 2019.
- PEER 2019/08** *Influence of Vertical Ground Motion on Bridges Isolated with Spherical Sliding Bearings.* Rushil Mojindra and Keri L. Ryan. December 2019.
- PEER 2019/07** *PEER Hub ImageNet (ϕ -Net): A Large-Scale Multi-Attribute Benchmark Dataset of Structural Images.* Yuqing Gao, and Khalid. M. Mosalam. November 2019.
- PEER 2019/06** *Fluid-Structure Interaction and Python-Scripting Capabilities in OpenSees.* Minjie Zhu and Michael H. Scott. August 2019.
- PEER 2019/05** *Expected Earthquake Performance of Buildings Designed to the California Building Code (California Alfred E. Alquist Seismic Safety Publication 19-01).* Grace S. Kang, Sifat Muin, Jorge Archbold, Bitanoosh Woods, and Khalid Mosalam. July 2019.
- PEER 2019/04** *Aftershock Seismic Vulnerability and Time-Dependent Risk Assessment of Bridges.* Sujith Mangalathu, Mehrdad Shokrabadi, and Henry V. Burton. May 2019.
- PEER 2019/03** *Ground-Motion Directivity Modeling for Seismic Hazard Applications.* Jennifer L. Donahue, Jonathan P. Stewart, Nicolas Gregor, and Yousef Bozorgnia. Review Panel: Jonathan D. Bray, Stephen A. Mahin, I. M. Idriss, Robert W. Graves, and Tom Shantz. May 2019.
- PEER 2019/02** *Direct-Finite-Element Method for Nonlinear Earthquake Analysis of Concrete Dams Including Dam–Water–Foundation Rock Interaction.* Arnkjell Løkke and Anil K. Chopra. March 2019.
- PEER 2019/01** *Flow-Failure Case History of the Las Palmas, Chile, Tailings Dam.* R. E. S. Moss, T. R. Gebhart, D. J. Frost, and C. Ledezma. January 2019.
- PEER 2018/08** *Central and Eastern North America Ground-Motion Characterization: NGA-East Final Report.* Christine Goulet, Yousef Bozorgnia, Norman Abrahamson, Nicolas Kuehn, Linda Al Atik, Robert Youngs, Robert Graves, and Gail Atkinson. December 2018.
- PEER 2018/07** *An Empirical Model for Fourier Amplitude Spectra using the NGA-West2 Database.* Jeff Bayless, and Norman A. Abrahamson. December 2018.
- PEER 2018/06** *Estimation of Shear Demands on Rock-Socketed Drilled Shafts subjected to Lateral Loading.* Pedro Arduino, Long Chen, and Christopher R. McGann. December 2018.
- PEER 2018/05** *Selection of Random Vibration Procedures for the NGA-East Project.* Albert Kottke, Norman A. Abrahamson, David M. Boore, Yousef Bozorgnia, Christine Goulet, Justin Hollenback, Tadahiro Kishida, Armen Der Kiureghian, Olga-Joan Ktenidou, Nicolas Kuehn, Ellen M. Rathje, Walter J. Silva, Eric Thompson, and Xiaoyue Wang. December 2018.
- PEER 2018/04** *Capturing Directivity Effects in the Mean and Aleatory Variability of the NGA-West 2 Ground Motion Prediction Equations.* Jennie A. Watson-Lamprey. November 2018.
- PEER 2018/03** *Probabilistic Seismic Hazard Analysis Code Verification.* Christie Hale, Norman Abrahamson, and Yousef Bozorgnia. July 2018.
- PEER 2018/02** *Update of the BCHydro Subduction Ground-Motion Model using the NGA-Subduction Dataset.* Norman Abrahamson, Nicolas Kuehn, Zeynep Gulerce, Nicholas Gregor, Yousef Bozorgnia, Grace Parker, Jonathan Stewart, Brian Chiou, I. M. Idriss, Kenneth Campbell, and Robert Youngs. June 2018.
- PEER 2018/01** *PEER Annual Report 2017–2018.* Khalid Mosalam, Amarnath Kasalanati, and Selim Günay. June 2018.
- PEER 2017/12** *Experimental Investigation of the Behavior of Vintage and Retrofit Concentrically Braced Steel Frames under Cyclic Loading.* Barbara G. Simpson, Stephen A. Mahin, and Jiun-Wei Lai, December 2017.
- PEER 2017/11** *Preliminary Studies on the Dynamic Response of a Seismically Isolated Prototype Gen-IV Sodium-Cooled Fast Reactor (PGSFR).* Benschun Shao, Andreas H. Schellenberg, Matthew J. Schoettler, and Stephen A. Mahin. December 2017.

- PEER 2017/10** *Development of Time Histories for IEEE693 Testing and Analysis (including Seismically Isolated Equipment)*. Shakhzod M. Takhirov, Eric Fujisaki, Leon Kempner, Michael Riley, and Brian Low. December 2017.
- PEER 2017/09** *“R” Package for Computation of Earthquake Ground-Motion Response Spectra*. Pengfei Wang, Jonathan P. Stewart, Yousef Bozorgnia, David M. Boore, and Tadahiro Kishida. December 2017.
- PEER 2017/08** *Influence of Kinematic SSI on Foundation Input Motions for Bridges on Deep Foundations*. Benjamin J. Turner, Scott J. Brandenburg, and Jonathan P. Stewart. November 2017.
- PEER 2017/07** *A Nonlinear Kinetic Model for Multi-Stage Friction Pendulum Systems*. Paul L. Drazin and Sanjay Govindjee. September 2017.
- PEER 2017/06** *Guidelines for Performance-Based Seismic Design of Tall Buildings, Version 2.02*. TBI Working Group led by co-chairs Ron Hamburger and Jack Moehle: Jack Baker, Jonathan Bray, C.B. Crouse, Greg Deierlein, John Hooper, Marshall Lew, Joe Maffei, Stephen Mahin, James Malley, Farzad Naeim, Jonathan Stewart, and John Wallace. May 2017.
- PEER 2017/05** *Recommendations for Ergodic Nonlinear Site Amplification in Central and Eastern North America*. Youssef M.A. Hashash, Joseph A. Harmon, Okan Ilhan, Grace A. Parker, and Jonathan P. Stewart. March 2017.
- PEER 2017/04** *Expert Panel Recommendations for Ergodic Site Amplification in Central and Eastern North America*. Jonathan P. Stewart, Grace A. Parker, Joseph P. Harmon, Gail M. Atkinson, David M. Boore, Robert B. Darragh, Walter J. Silva, and Youssef M.A. Hashash. March 2017.
- PEER 2017/03** *NGA-East Ground-Motion Models for the U.S. Geological Survey National Seismic Hazard Maps*. Christine A. Goulet, Yousef Bozorgnia, Nicolas Kuehn, Linda Al Atik, Robert R. Youngs, Robert W. Graves, and Gail M. Atkinson. March 2017.
- PEER 2017/02** *U.S.–New Zealand–Japan Workshop: Liquefaction-Induced Ground Movements Effects, University of California, Berkeley, California, 2–4 November 2016*. Jonathan D. Bray, Ross W. Boulanger, Misko Cubrinovski, Kohji Tokimatsu, Steven L. Kramer, Thomas O’Rourke, Ellen Rathje, Russell A. Green, Peter K. Robinson, and Christine Z. Beyzaei. March 2017.
- PEER 2017/01** *2016 PEER Annual Report*. Khalid M. Mosalam, Amarnath Kasalanati, and Grace Kang. March 2017.
- PEER 2016/10** *Performance-Based Robust Nonlinear Seismic Analysis with Application to Reinforced Concrete Bridge Systems*. Xiao Ling and Khalid M. Mosalam. December 2016.
- PEER 2017/09** *Detailing Requirements for Column Plastic Hinges subjected to Combined Flexural, Axial, and Torsional Seismic Loading*. Gabriel Hurtado and Jack P. Moehle. December 2016.
- PEER 2016/08** *Resilience of Critical Structures, Infrastructure, and Communities*. Gian Paolo Cimellaro, Ali Zamani-Noori, Omar Kamouh, Vesna Terzic, and Stephen A. Mahin. December 2016.
- PEER 2016/07** *Hybrid Simulation Theory for a Classical Nonlinear Dynamical System*. Paul L. Drazin and Sanjay Govindjee. September 2016.
- PEER 2016/06** *California Earthquake Early Warning System Benefit Study*. Laurie A. Johnson, Sharyl Rabinovici, Grace S. Kang, and Stephen A. Mahin. July 2006.
- PEER 2016/05** *Ground-Motion Prediction Equations for Arias Intensity Consistent with the NGA-West2 Ground-Motion Models*. Charlotte Abrahamson, Hao-Jun Michael Shi, and Brian Yang. July 2016.
- PEER 2016/04** *The M_w 6.0 South Napa Earthquake of August 24, 2014: A Wake-Up Call for Renewed Investment in Seismic Resilience Across California*. Prepared for the California Seismic Safety Commission, Laurie A. Johnson and Stephen A. Mahin. May 2016.
- PEER 2016/03** *Simulation Confidence in Tsunami-Driven Overland Flow*. Patrick Lynett. May 2016.
- PEER 2016/02** *Semi-Automated Procedure for Windowing time Series and Computing Fourier Amplitude Spectra for the NGA-West2 Database*. Tadahiro Kishida, Olga-Joan Ktenidou, Robert B. Darragh, and Walter J. Silva. May 2016.
- PEER 2016/01** *A Methodology for the Estimation of Kappa (κ) from Large Datasets: Example Application to Rock Sites in the NGA-East Database and Implications on Design Motions*. Olga-Joan Ktenidou, Norman A. Abrahamson, Robert B. Darragh, and Walter J. Silva. April 2016.
- PEER 2015/13** *Self-Centering Precast Concrete Dual-Steel-Shell Columns for Accelerated Bridge Construction: Seismic Performance, Analysis, and Design*. Gabriele Guerrini, José I. Restrepo, Athanassios Vervelidis, and Milena Massari. December 2015.
- PEER 2015/12** *Shear-Flexure Interaction Modeling for Reinforced Concrete Structural Walls and Columns under Reversed Cyclic Loading*. Kristijan Kolozvari, Kutay Orakcal, and John Wallace. December 2015.

- PEER 2015/11** *Selection and Scaling of Ground Motions for Nonlinear Response History Analysis of Buildings in Performance-Based Earthquake Engineering.* N. Simon Kwong and Anil K. Chopra. December 2015.
- PEER 2015/10** *Structural Behavior of Column-Bent Cap Beam-Box Girder Systems in Reinforced Concrete Bridges Subjected to Gravity and Seismic Loads. Part II: Hybrid Simulation and Post-Test Analysis.* Mohamed A. Moustafa and Khalid M. Mosalam. November 2015.
- PEER 2015/09** *Structural Behavior of Column-Bent Cap Beam-Box Girder Systems in Reinforced Concrete Bridges Subjected to Gravity and Seismic Loads. Part I: Pre-Test Analysis and Quasi-Static Experiments.* Mohamed A. Moustafa and Khalid M. Mosalam. September 2015.
- PEER 2015/08** *NGA-East: Adjustments to Median Ground-Motion Models for Center and Eastern North America.* August 2015.
- PEER 2015/07** *NGA-East: Ground-Motion Standard-Deviation Models for Central and Eastern North America.* Linda Al Atik. June 2015.
- PEER 2015/06** *Adjusting Ground-Motion Intensity Measures to a Reference Site for which $V_{S30} = 3000$ m/sec.* David M. Boore. May 2015.
- PEER 2015/05** *Hybrid Simulation of Seismic Isolation Systems Applied to an APR-1400 Nuclear Power Plant.* Andreas H. Schellenberg, Alireza Sarebanha, Matthew J. Schoettler, Gilberto Mosqueda, Gianmario Benzoni, and Stephen A. Mahin. April 2015.
- PEER 2015/04** *NGA-East: Median Ground-Motion Models for the Central and Eastern North America Region.* April 2015.
- PEER 2015/03** *Single Series Solution for the Rectangular Fiber-Reinforced Elastomeric Isolator Compression Modulus.* James M. Kelly and Niel C. Van Engelen. March 2015.
- PEER 2015/02** *A Full-Scale, Single-Column Bridge Bent Tested by Shake-Table Excitation.* Matthew J. Schoettler, José I. Restrepo, Gabriele Guerrini, David E. Duck, and Francesco Carrea. March 2015.
- PEER 2015/01** *Concrete Column Blind Prediction Contest 2010: Outcomes and Observations.* Vesna Terzic, Matthew J. Schoettler, José I. Restrepo, and Stephen A Mahin. March 2015.
- PEER 2014/20** *Stochastic Modeling and Simulation of Near-Fault Ground Motions for Performance-Based Earthquake Engineering.* Mayssa Dabaghi and Armen Der Kiureghian. December 2014.
- PEER 2014/19** *Seismic Response of a Hybrid Fiber-Reinforced Concrete Bridge Column Detailed for Accelerated Bridge Construction.* Wilson Nguyen, William Trono, Marios Panagiotou, and Claudia P. Ostertag. December 2014.
- PEER 2014/18** *Three-Dimensional Beam-Truss Model for Reinforced Concrete Walls and Slabs Subjected to Cyclic Static or Dynamic Loading.* Yuan Lu, Marios Panagiotou, and Ioannis Koutromanos. December 2014.
- PEER 2014/17** *PEER NGA-East Database.* Christine A. Goulet, Tadahiro Kishida, Timothy D. Ancheta, Chris H. Cramer, Robert B. Darragh, Walter J. Silva, Youssef M.A. Hashash, Joseph Harmon, Jonathan P. Stewart, Katie E. Wooddell, and Robert R. Youngs. October 2014.
- PEER 2014/16** *Guidelines for Performing Hazard-Consistent One-Dimensional Ground Response Analysis for Ground Motion Prediction.* Jonathan P. Stewart, Kioumars Afshari, and Youssef M.A. Hashash. October 2014.
- PEER 2014/15** *NGA-East Regionalization Report: Comparison of Four Crustal Regions within Central and Eastern North America using Waveform Modeling and 5%-Damped Pseudo-Spectral Acceleration Response.* Jennifer Dreiling, Marius P. Isken, Walter D. Mooney, Martin C. Chapman, and Richard W. Godbee. October 2014.
- PEER 2014/14** *Scaling Relations between Seismic Moment and Rupture Area of Earthquakes in Stable Continental Regions.* Paul Somerville. August 2014.
- PEER 2014/13** *PEER Preliminary Notes and Observations on the August 24, 2014, South Napa Earthquake.* Grace S. Kang and Stephen A. Mahin, Editors. September 2014.
- PEER 2014/12** *Reference-Rock Site Conditions for Central and Eastern North America: Part II – Attenuation (Kappa) Definition.* Kenneth W. Campbell, Youssef M.A. Hashash, Byungmin Kim, Albert R. Kottke, Ellen M. Rathje, Walter J. Silva, and Jonathan P. Stewart. August 2014.
- PEER 2014/11** *Reference-Rock Site Conditions for Central and Eastern North America: Part I - Velocity Definition.* Youssef M.A. Hashash, Albert R. Kottke, Jonathan P. Stewart, Kenneth W. Campbell, Byungmin Kim, Ellen M. Rathje, Walter J. Silva, Sissy Nikolaou, and Cheryl Moss. August 2014.
- PEER 2014/10** *Evaluation of Collapse and Non-Collapse of Parallel Bridges Affected by Liquefaction and Lateral Spreading.* Benjamin Turner, Scott J. Brandenburg, and Jonathan P. Stewart. August 2014.
- PEER 2014/09** *PEER Arizona Strong-Motion Database and GMPEs Evaluation.* Tadahiro Kishida, Robert E. Kayen, Olga-Joan Ktenidou, Walter J. Silva, Robert B. Darragh, and Jennie Watson-Lamprey. June 2014.

- PEER 2014/08** *Unbonded Pretensioned Bridge Columns with Rocking Detail.* Jeffrey A. Schaefer, Bryan Kennedy, Marc O. Eberhard, and John F. Stanton. June 2014.
- PEER 2014/07** *Northridge 20 Symposium Summary Report: Impacts, Outcomes, and Next Steps.* May 2014.
- PEER 2014/06** *Report of the Tenth Planning Meeting of NEES/E-Defense Collaborative Research on Earthquake Engineering.* December 2013.
- PEER 2014/05** *Seismic Velocity Site Characterization of Thirty-One Chilean Seismometer Stations by Spectral Analysis of Surface Wave Dispersion.* Robert Kayen, Brad D. Carkin, Skye Corbet, Camilo Pinilla, Allan Ng, Edward Gorbis, and Christine Truong. April 2014.
- PEER 2014/04** *Effect of Vertical Acceleration on Shear Strength of Reinforced Concrete Columns.* Hyerin Lee and Khalid M. Mosalam. April 2014.
- PEER 2014/03** *Retest of Thirty-Year-Old Neoprene Isolation Bearings.* James M. Kelly and Niel C. Van Engelen. March 2014.
- PEER 2014/02** *Theoretical Development of Hybrid Simulation Applied to Plate Structures.* Ahmed A. Bakhaty, Khalid M. Mosalam, and Sanjay Govindjee. January 2014.
- PEER 2014/01** *Performance-Based Seismic Assessment of Skewed Bridges.* Peyman Kaviani, Farzin Zareian, and Ertugrul Taciroglu. January 2014.
- PEER 2013/26** *Urban Earthquake Engineering.* Proceedings of the U.S.-Iran Seismic Workshop. December 2013.
- PEER 2013/25** *Earthquake Engineering for Resilient Communities: 2013 PEER Internship Program Research Report Collection.* Heidi Tremayne (Editor), Stephen A. Mahin (Editor), Jorge Archbold Monterossa, Matt Brosman, Shelly Dean, Katherine deLaveaga, Curtis Fong, Donovan Holder, Rakeeb Khan, Elizabeth Jachens, David Lam, Daniela Martinez Lopez, Mara Minner, Geffen Oren, Julia Pavicic, Melissa Quinonez, Lorena Rodriguez, Sean Salazar, Kelli Slaven, Vivian Steyert, Jenny Taing, and Salvador Tena. December 2013.
- PEER 2013/24** *NGA-West2 Ground Motion Prediction Equations for Vertical Ground Motions.* September 2013.
- PEER 2013/23** *Coordinated Planning and Preparedness for Fire Following Major Earthquakes.* Charles Scawthorn. November 2013.
- PEER 2013/22** *GEM-PEER Task 3 Project: Selection of a Global Set of Ground Motion Prediction Equations.* Jonathan P. Stewart, John Douglas, Mohammad B. Javanbarg, Carola Di Alessandro, Yousef Bozorgnia, Norman A. Abrahamson, David M. Boore, Kenneth W. Campbell, Elise Delavaud, Mustafa Erdik, and Peter J. Stafford. December 2013.
- PEER 2013/21** *Seismic Design and Performance of Bridges with Columns on Rocking Foundations.* Grigorios Antonellis and Marios Panagiotou. September 2013.
- PEER 2013/20** *Experimental and Analytical Studies on the Seismic Behavior of Conventional and Hybrid Braced Frames.* Jiun-Wei Lai and Stephen A. Mahin. September 2013.
- PEER 2013/19** *Toward Resilient Communities: A Performance-Based Engineering Framework for Design and Evaluation of the Built Environment.* Michael William Mieler, Bozidar Stojadinovic, Robert J. Budnitz, Stephen A. Mahin, and Mary C. Comerio. September 2013.
- PEER 2013/18** *Identification of Site Parameters that Improve Predictions of Site Amplification.* Ellen M. Rathje and Sara Navidi. July 2013.
- PEER 2013/17** *Response Spectrum Analysis of Concrete Gravity Dams Including Dam-Water-Foundation Interaction.* Arnkjell Løkke and Anil K. Chopra. July 2013.
- PEER 2013/16** *Effect of Hoop Reinforcement Spacing on the Cyclic Response of Large Reinforced Concrete Special Moment Frame Beams.* Marios Panagiotou, Tea Visnjic, Grigorios Antonellis, Panagiotis Galanis, and Jack P. Moehle. June 2013.
- PEER 2013/15** *A Probabilistic Framework to Include the Effects of Near-Fault Directivity in Seismic Hazard Assessment.* Shrey Kumar Shahi, Jack W. Baker. October 2013.
- PEER 2013/14** *Hanging-Wall Scaling using Finite-Fault Simulations.* Jennifer L. Donahue and Norman A. Abrahamson. September 2013.
- PEER 2013/13** *Semi-Empirical Nonlinear Site Amplification and its Application in NEHRP Site Factors.* Jonathan P. Stewart and Emel Seyhan. November 2013.
- PEER 2013/12** *Nonlinear Horizontal Site Response for the NGA-West2 Project.* Ronnie Kamai, Norman A. Abramson, Walter J. Silva. May 2013.
- PEER 2013/11** *Epistemic Uncertainty for NGA-West2 Models.* Linda Al Atik and Robert R. Youngs. May 2013.

- PEER 2013/10** *NGA-West 2 Models for Ground-Motion Directionality.* Shrey K. Shahi and Jack W. Baker. May 2013.
- PEER 2013/09** *Final Report of the NGA-West2 Directivity Working Group.* Paul Spudich, Jeffrey R. Bayless, Jack W. Baker, Brian S.J. Chiou, Badie Rowshandel, Shrey Shahi, and Paul Somerville. May 2013.
- PEER 2013/08** *NGA-West2 Model for Estimating Average Horizontal Values of Pseudo-Absolute Spectral Accelerations Generated by Crustal Earthquakes.* I. M. Idriss. May 2013.
- PEER 2013/07** *Update of the Chiou and Youngs NGA Ground Motion Model for Average Horizontal Component of Peak Ground Motion and Response Spectra.* Brian Chiou and Robert Youngs. May 2013.
- PEER 2013/06** *NGA-West2 Campbell-Bozorgnia Ground Motion Model for the Horizontal Components of PGA, PGV, and 5%-Damped Elastic Pseudo-Acceleration Response Spectra for Periods Ranging from 0.01 to 10 sec.* Kenneth W. Campbell and Yousef Bozorgnia. May 2013.
- PEER 2013/05** *NGA-West 2 Equations for Predicting Response Spectral Accelerations for Shallow Crustal Earthquakes.* David M. Boore, Jonathan P. Stewart, Emel Seyhan, and Gail M. Atkinson. May 2013.
- PEER 2013/04** *Update of the AS08 Ground-Motion Prediction Equations Based on the NGA-West2 Data Set.* Norman Abrahamson, Walter Silva, and Ronnie Kamai. May 2013.
- PEER 2013/03** *PEER NGA-West2 Database.* Timothy D. Ancheta, Robert B. Darragh, Jonathan P. Stewart, Emel Seyhan, Walter J. Silva, Brian S.J. Chiou, Katie E. Wooddell, Robert W. Graves, Albert R. Kottke, David M. Boore, Tadahiro Kishida, and Jennifer L. Donahue. May 2013.
- PEER 2013/02** *Hybrid Simulation of the Seismic Response of Squat Reinforced Concrete Shear Walls.* Catherine A. Whyte and Bozidar Stojadinovic. May 2013.
- PEER 2013/01** *Housing Recovery in Chile: A Qualitative Mid-program Review.* Mary C. Comerio. February 2013.
- PEER 2012/08** *Guidelines for Estimation of Shear Wave Velocity.* Bernard R. Wair, Jason T. DeJong, and Thomas Shantz. December 2012.
- PEER 2012/07** *Earthquake Engineering for Resilient Communities: 2012 PEER Internship Program Research Report Collection.* Heidi Tremayne (Editor), Stephen A. Mahin (Editor), Collin Anderson, Dustin Cook, Michael Erceg, Carlos Esparza, Jose Jimenez, Dorian Krausz, Andrew Lo, Stephanie Lopez, Nicole McCurdy, Paul Shipman, Alexander Strum, Eduardo Vega. December 2012.
- PEER 2012/06** *Fragilities for Precarious Rocks at Yucca Mountain.* Matthew D. Purvance, Rasool Anooshehpour, and James N. Brune. December 2012.
- PEER 2012/05** *Development of Simplified Analysis Procedure for Piles in Laterally Spreading Layered Soils.* Christopher R. McGann, Pedro Arduino, and Peter Mackenzie-Helnwein. December 2012.
- PEER 2012/04** *Unbonded Pre-Tensioned Columns for Bridges in Seismic Regions.* Phillip M. Davis, Todd M. Janes, Marc O. Eberhard, and John F. Stanton. December 2012.
- PEER 2012/03** *Experimental and Analytical Studies on Reinforced Concrete Buildings with Seismically Vulnerable Beam-Column Joints.* Sangjoon Park and Khalid M. Mosalam. October 2012.
- PEER 2012/02** *Seismic Performance of Reinforced Concrete Bridges Allowed to Uplift during Multi-Directional Excitation.* Andres Oscar Espinoza and Stephen A. Mahin. July 2012.
- PEER 2012/01** *Spectral Damping Scaling Factors for Shallow Crustal Earthquakes in Active Tectonic Regions.* Sanaz Rezaeian, Yousef Bozorgnia, I. M. Idriss, Kenneth Campbell, Norman Abrahamson, and Walter Silva. July 2012.
- PEER 2011/10** *Earthquake Engineering for Resilient Communities: 2011 PEER Internship Program Research Report Collection.* Heidi Faison and Stephen A. Mahin, Editors. December 2011.
- PEER 2011/09** *Calibration of Semi-Stochastic Procedure for Simulating High-Frequency Ground Motions.* Jonathan P. Stewart, Emel Seyhan, and Robert W. Graves. December 2011.
- PEER 2011/08** *Water Supply in regard to Fire Following Earthquake.* Charles Scawthorn. November 2011.
- PEER 2011/07** *Seismic Risk Management in Urban Areas.* Proceedings of a U.S.-Iran-Turkey Seismic Workshop. September 2011.
- PEER 2011/06** *The Use of Base Isolation Systems to Achieve Complex Seismic Performance Objectives.* Troy A. Morgan and Stephen A. Mahin. July 2011.
- PEER 2011/05** *Case Studies of the Seismic Performance of Tall Buildings Designed by Alternative Means.* Task 12 Report for the Tall Buildings Initiative. Jack Moehle, Yousef Bozorgnia, Nirmal Jayaram, Pierson Jones, Mohsen Rahnama, Nilesh Shome, Zeynep Tuna, John Wallace, Tony Yang, and Farzin Zareian. July 2011.

- PEER 2011/04** *Recommended Design Practice for Pile Foundations in Laterally Spreading Ground.* Scott A. Ashford, Ross W. Boulanger, and Scott J. Brandenberg. June 2011.
- PEER 2011/03** *New Ground Motion Selection Procedures and Selected Motions for the PEER Transportation Research Program.* Jack W. Baker, Ting Lin, Shrey K. Shahi, and Nirmal Jayaram. March 2011.
- PEER 2011/02** *A Bayesian Network Methodology for Infrastructure Seismic Risk Assessment and Decision Support.* Michelle T. Bensi, Armen Der Kiureghian, and Daniel Straub. March 2011.
- PEER 2011/01** *Demand Fragility Surfaces for Bridges in Liquefied and Laterally Spreading Ground.* Scott J. Brandenberg, Jian Zhang, Pirooz Kashighandi, Yili Huo, and Minxing Zhao. March 2011.
- PEER 2010/05** *Guidelines for Performance-Based Seismic Design of Tall Buildings.* Developed by the Tall Buildings Initiative. November 2010.
- PEER 2010/04** *Application Guide for the Design of Flexible and Rigid Bus Connections between Substation Equipment Subjected to Earthquakes.* Jean-Bernard Dastous and Armen Der Kiureghian. September 2010.
- PEER 2010/03** *Shear Wave Velocity as a Statistical Function of Standard Penetration Test Resistance and Vertical Effective Stress at Caltrans Bridge Sites.* Scott J. Brandenberg, Naresh Bellana, and Thomas Shantz. June 2010.
- PEER 2010/02** *Stochastic Modeling and Simulation of Ground Motions for Performance-Based Earthquake Engineering.* Sanaz Rezaeian and Armen Der Kiureghian. June 2010.
- PEER 2010/01** *Structural Response and Cost Characterization of Bridge Construction Using Seismic Performance Enhancement Strategies.* Ady Aviram, Božidar Stojadinović, Gustavo J. Parra-Montesinos, and Kevin R. Mackie. March 2010.
- PEER 2009/03** *The Integration of Experimental and Simulation Data in the Study of Reinforced Concrete Bridge Systems Including Soil-Foundation-Structure Interaction.* Matthew Dryden and Gregory L. Fenves. November 2009.
- PEER 2009/02** *Improving Earthquake Mitigation through Innovations and Applications in Seismic Science, Engineering, Communication, and Response.* Proceedings of a U.S.-Iran Seismic Workshop. October 2009.
- PEER 2009/01** *Evaluation of Ground Motion Selection and Modification Methods: Predicting Median Interstory Drift Response of Buildings.* Curt B. Haselton, Editor. June 2009.
- PEER 2008/10** *Technical Manual for Strata.* Albert R. Kottke and Ellen M. Rathje. February 2009.
- PEER 2008/09** *NGA Model for Average Horizontal Component of Peak Ground Motion and Response Spectra.* Brian S.-J. Chiou and Robert R. Youngs. November 2008.
- PEER 2008/08** *Toward Earthquake-Resistant Design of Concentrically Braced Steel Structures.* Patxi Uriz and Stephen A. Mahin. November 2008.
- PEER 2008/07** *Using OpenSees for Performance-Based Evaluation of Bridges on Liquefiable Soils.* Stephen L. Kramer, Pedro Arduino, and HyungSuk Shin. November 2008.
- PEER 2008/06** *Shaking Table Tests and Numerical Investigation of Self-Centering Reinforced Concrete Bridge Columns.* Hyung IL Jeong, Junichi Sakai, and Stephen A. Mahin. September 2008.
- PEER 2008/05** *Performance-Based Earthquake Engineering Design Evaluation Procedure for Bridge Foundations Undergoing Liquefaction-Induced Lateral Ground Displacement.* Christian A. Ledezma and Jonathan D. Bray. August 2008.
- PEER 2008/04** *Benchmarking of Nonlinear Geotechnical Ground Response Analysis Procedures.* Jonathan P. Stewart, Annie On-Lei Kwok, Youssef M. A. Hashash, Neven Matasovic, Robert Pyke, Zhiliang Wang, and Zhaohui Yang. August 2008.
- PEER 2008/03** *Guidelines for Nonlinear Analysis of Bridge Structures in California.* Ady Aviram, Kevin R. Mackie, and Božidar Stojadinović. August 2008.
- PEER 2008/02** *Treatment of Uncertainties in Seismic-Risk Analysis of Transportation Systems.* Evangelos Stergiou and Anne S. Kiremidjian. July 2008.
- PEER 2008/01** *Seismic Performance Objectives for Tall Buildings.* William T. Holmes, Charles Kircher, William Petak, and Nabih Youssef. August 2008.
- PEER 2007/12** *An Assessment to Benchmark the Seismic Performance of a Code-Conforming Reinforced Concrete Moment-Frame Building.* Curt Haselton, Christine A. Goulet, Judith Mitrani-Reiser, James L. Beck, Gregory G. Deierlein, Keith A. Porter, Jonathan P. Stewart, and Ertugrul Taciroglu. August 2008.
- PEER 2007/11** *Bar Buckling in Reinforced Concrete Bridge Columns.* Wayne A. Brown, Dawn E. Lehman, and John F. Stanton. February 2008.

- PEER 2007/10** *Computational Modeling of Progressive Collapse in Reinforced Concrete Frame Structures.* Mohamed M. Talaat and Khalid M. Mosalam. May 2008.
- PEER 2007/09** *Integrated Probabilistic Performance-Based Evaluation of Benchmark Reinforced Concrete Bridges.* Kevin R. Mackie, John-Michael Wong, and Božidar Stojadinović. January 2008.
- PEER 2007/08** *Assessing Seismic Collapse Safety of Modern Reinforced Concrete Moment-Frame Buildings.* Curt B. Haselton and Gregory G. Deierlein. February 2008.
- PEER 2007/07** *Performance Modeling Strategies for Modern Reinforced Concrete Bridge Columns.* Michael P. Berry and Marc O. Eberhard. April 2008.
- PEER 2007/06** *Development of Improved Procedures for Seismic Design of Buried and Partially Buried Structures.* Linda Al Atik and Nicholas Sitar. June 2007.
- PEER 2007/05** *Uncertainty and Correlation in Seismic Risk Assessment of Transportation Systems.* Renee G. Lee and Anne S. Kiremidjian. July 2007.
- PEER 2007/04** *Numerical Models for Analysis and Performance-Based Design of Shallow Foundations Subjected to Seismic Loading.* Sivapalan Gajan, Tara C. Hutchinson, Bruce L. Kutter, Prishati Raychowdhury, José A. Ugalde, and Jonathan P. Stewart. May 2008.
- PEER 2007/03** *Beam-Column Element Model Calibrated for Predicting Flexural Response Leading to Global Collapse of RC Frame Buildings.* Curt B. Haselton, Abbie B. Liel, Sarah Taylor Lange, and Gregory G. Deierlein. May 2008.
- PEER 2007/02** *Campbell-Bozorgnia NGA Ground Motion Relations for the Geometric Mean Horizontal Component of Peak and Spectral Ground Motion Parameters.* Kenneth W. Campbell and Yousef Bozorgnia. May 2007.
- PEER 2007/01** *Boore-Atkinson NGA Ground Motion Relations for the Geometric Mean Horizontal Component of Peak and Spectral Ground Motion Parameters.* David M. Boore and Gail M. Atkinson. May 2007.
- PEER 2006/12** *Societal Implications of Performance-Based Earthquake Engineering.* Peter J. May. May 2007.
- PEER 2006/11** *Probabilistic Seismic Demand Analysis Using Advanced Ground Motion Intensity Measures, Attenuation Relationships, and Near-Fault Effects.* Polsak Tothong and C. Allin Cornell. March 2007.
- PEER 2006/10** *Application of the PEER PBEE Methodology to the I-880 Viaduct.* Sashi Kunnath. February 2007.
- PEER 2006/09** *Quantifying Economic Losses from Travel Forgone Following a Large Metropolitan Earthquake.* James Moore, Sungbin Cho, Yue Yue Fan, and Stuart Werner. November 2006.
- PEER 2006/08** *Vector-Valued Ground Motion Intensity Measures for Probabilistic Seismic Demand Analysis.* Jack W. Baker and C. Allin Cornell. October 2006.
- PEER 2006/07** *Analytical Modeling of Reinforced Concrete Walls for Predicting Flexural and Coupled–Shear-Flexural Responses.* Kutay Orakcal, Leonardo M. Massone, and John W. Wallace. October 2006.
- PEER 2006/06** *Nonlinear Analysis of a Soil-Drilled Pier System under Static and Dynamic Axial Loading.* Gang Wang and Nicholas Sitar. November 2006.
- PEER 2006/05** *Advanced Seismic Assessment Guidelines.* Paolo Bazzurro, C. Allin Cornell, Charles Menun, Maziar Motahari, and Nicolas Luco. September 2006.
- PEER 2006/04** *Probabilistic Seismic Evaluation of Reinforced Concrete Structural Components and Systems.* Tae Hyung Lee and Khalid M. Mosalam. August 2006.
- PEER 2006/03** *Performance of Lifelines Subjected to Lateral Spreading.* Scott A. Ashford and Teerawut Juirnarongrit. July 2006.
- PEER 2006/02** *Pacific Earthquake Engineering Research Center Highway Demonstration Project.* Anne Kiremidjian, James Moore, Yue Yue Fan, Nesrin Basoz, Ozgur Yazali, and Meredith Williams. April 2006.
- PEER 2006/01** *Bracing Berkeley. A Guide to Seismic Safety on the UC Berkeley Campus.* Mary C. Comerio, Stephen Tobriner, and Ariane Fehrenkamp. January 2006.
- PEER 2005/17** *Earthquake Simulation Tests on Reducing Residual Displacements of Reinforced Concrete Bridges.* Junichi Sakai, Stephen A Mahin, and Andres Espinoza. December 2005.
- PEER 2005/16** *Seismic Response and Reliability of Electrical Substation Equipment and Systems.* Junho Song, Armen Der Kiureghian, and Jerome L. Sackman. April 2006.
- PEER 2005/15** *CPT-Based Probabilistic Assessment of Seismic Soil Liquefaction Initiation.* R. E. S. Moss, R. B. Seed, R. E. Kayen, J. P. Stewart, and A. Der Kiureghian. April 2006.

- PEER 2005/14** *Workshop on Modeling of Nonlinear Cyclic Load-Deformation Behavior of Shallow Foundations*. Bruce L. Kutter, Geoffrey Martin, Tara Hutchinson, Chad Harden, Sivapalan Gajan, and Justin Phalen. March 2006.
- PEER 2005/13** *Stochastic Characterization and Decision Bases under Time-Dependent Aftershock Risk in Performance-Based Earthquake Engineering*. Gee Liek Yeo and C. Allin Cornell. July 2005.
- PEER 2005/12** *PEER Testbed Study on a Laboratory Building: Exercising Seismic Performance Assessment*. Mary C. Comerio, Editor. November 2005.
- PEER 2005/11** *Van Nuys Hotel Building Testbed Report: Exercising Seismic Performance Assessment*. Helmut Krawinkler, Editor. October 2005.
- PEER 2005/10** *First NEES/E-Defense Workshop on Collapse Simulation of Reinforced Concrete Building Structures*. September 2005.
- PEER 2005/09** *Test Applications of Advanced Seismic Assessment Guidelines*. Joe Maffei, Karl Telleen, Danya Mohr, William Holmes, and Yuki Nakayama. August 2006.
- PEER 2005/08** *Damage Accumulation in Lightly Confined Reinforced Concrete Bridge Columns*. R. Tyler Ranf, Jared M. Nelson, Zach Price, Marc O. Eberhard, and John F. Stanton. April 2006.
- PEER 2005/07** *Experimental and Analytical Studies on the Seismic Response of Freestanding and Anchored Laboratory Equipment*. Dimitrios Konstantinidis and Nicos Makris. January 2005.
- PEER 2005/06** *Global Collapse of Frame Structures under Seismic Excitations*. Luis F. Ibarra and Helmut Krawinkler. September 2005.
- PEER 2005/05** *Performance Characterization of Bench- and Shelf-Mounted Equipment*. Samit Ray Chaudhuri and Tara C. Hutchinson. May 2006.
- PEER 2005/04** *Numerical Modeling of the Nonlinear Cyclic Response of Shallow Foundations*. Chad Harden, Tara Hutchinson, Geoffrey R. Martin, and Bruce L. Kutter. August 2005.
- PEER 2005/03** *A Taxonomy of Building Components for Performance-Based Earthquake Engineering*. Keith A. Porter. September 2005.
- PEER 2005/02** *Fragility Basis for California Highway Overpass Bridge Seismic Decision Making*. Kevin R. Mackie and Božidar Stojadinović. June 2005.
- PEER 2005/01** *Empirical Characterization of Site Conditions on Strong Ground Motion*. Jonathan P. Stewart, Yoojoong Choi, and Robert W. Graves. June 2005.
- PEER 2004/09** *Electrical Substation Equipment Interaction: Experimental Rigid Conductor Studies*. Christopher Stearns and André Filiatrault. February 2005.
- PEER 2004/08** *Seismic Qualification and Fragility Testing of Line Break 550-kV Disconnect Switches*. Shakhzod M. Takhirov, Gregory L. Fenves, and Eric Fujisaki. January 2005.
- PEER 2004/07** *Ground Motions for Earthquake Simulator Qualification of Electrical Substation Equipment*. Shakhzod M. Takhirov, Gregory L. Fenves, Eric Fujisaki, and Don Clyde. January 2005.
- PEER 2004/06** *Performance-Based Regulation and Regulatory Regimes*. Peter J. May and Chris Koski. September 2004.
- PEER 2004/05** *Performance-Based Seismic Design Concepts and Implementation: Proceedings of an International Workshop*. Peter Fajfar and Helmut Krawinkler, Editors. September 2004.
- PEER 2004/04** *Seismic Performance of an Instrumented Tilt-up Wall Building*. James C. Anderson and Vitelmo V. Bertero. July 2004.
- PEER 2004/03** *Evaluation and Application of Concrete Tilt-up Assessment Methodologies*. Timothy Graf and James O. Malley. October 2004.
- PEER 2004/02** *Analytical Investigations of New Methods for Reducing Residual Displacements of Reinforced Concrete Bridge Columns*. Junichi Sakai and Stephen A. Mahin. August 2004.
- PEER 2004/01** *Seismic Performance of Masonry Buildings and Design Implications*. Kerri Anne Taeko Tokoro, James C. Anderson, and Vitelmo V. Bertero. February 2004.
- PEER 2003/18** *Performance Models for Flexural Damage in Reinforced Concrete Columns*. Michael Berry and Marc Eberhard. August 2003.
- PEER 2003/17** *Predicting Earthquake Damage in Older Reinforced Concrete Beam-Column Joints*. Catherine Pagni and Laura Lowes. October 2004.

- PEER 2003/16** *Seismic Demands for Performance-Based Design of Bridges.* Kevin Mackie and Božidar Stojadinović. August 2003.
- PEER 2003/15** *Seismic Demands for Nondeteriorating Frame Structures and Their Dependence on Ground Motions.* Ricardo Antonio Medina and Helmut Krawinkler. May 2004.
- PEER 2003/14** *Finite Element Reliability and Sensitivity Methods for Performance-Based Earthquake Engineering.* Terje Haukaas and Armen Der Kiureghian. April 2004.
- PEER 2003/13** *Effects of Connection Hysteretic Degradation on the Seismic Behavior of Steel Moment-Resisting Frames.* Janise E. Rodgers and Stephen A. Mahin. March 2004.
- PEER 2003/12** *Implementation Manual for the Seismic Protection of Laboratory Contents: Format and Case Studies.* William T. Holmes and Mary C. Comerio. October 2003.
- PEER 2003/11** *Fifth U.S.-Japan Workshop on Performance-Based Earthquake Engineering Methodology for Reinforced Concrete Building Structures.* February 2004.
- PEER 2003/10** *A Beam-Column Joint Model for Simulating the Earthquake Response of Reinforced Concrete Frames.* Laura N. Lowes, Nilanjan Mitra, and Arash Altoontash. February 2004.
- PEER 2003/09** *Sequencing Repairs after an Earthquake: An Economic Approach.* Marco Casari and Simon J. Wilkie. April 2004.
- PEER 2003/08** *A Technical Framework for Probability-Based Demand and Capacity Factor Design (DCFD) Seismic Formats.* Fatemeh Jalayer and C. Allin Cornell. November 2003.
- PEER 2003/07** *Uncertainty Specification and Propagation for Loss Estimation Using FOSM Methods.* Jack W. Baker and C. Allin Cornell. September 2003.
- PEER 2003/06** *Performance of Circular Reinforced Concrete Bridge Columns under Bidirectional Earthquake Loading.* Mahmoud M. Hachem, Stephen A. Mahin, and Jack P. Moehle. February 2003.
- PEER 2003/05** *Response Assessment for Building-Specific Loss Estimation.* Eduardo Miranda and Shahram Taghavi. September 2003.
- PEER 2003/04** *Experimental Assessment of Columns with Short Lap Splices Subjected to Cyclic Loads.* Murat Melek, John W. Wallace, and Joel Conte. April 2003.
- PEER 2003/03** *Probabilistic Response Assessment for Building-Specific Loss Estimation.* Eduardo Miranda and Hesameddin Aslani. September 2003.
- PEER 2003/02** *Software Framework for Collaborative Development of Nonlinear Dynamic Analysis Program.* Jun Peng and Kincho H. Law. September 2003.
- PEER 2003/01** *Shake Table Tests and Analytical Studies on the Gravity Load Collapse of Reinforced Concrete Frames.* Kenneth John Elwood and Jack P. Moehle. November 2003.
- PEER 2002/24** *Performance of Beam to Column Bridge Joints Subjected to a Large Velocity Pulse.* Natalie Gibson, André Filiatrault, and Scott A. Ashford. April 2002.
- PEER 2002/23** *Effects of Large Velocity Pulses on Reinforced Concrete Bridge Columns.* Greg L. Orozco and Scott A. Ashford. April 2002.
- PEER 2002/22** *Characterization of Large Velocity Pulses for Laboratory Testing.* Kenneth E. Cox and Scott A. Ashford. April 2002.
- PEER 2002/21** *Fourth U.S.-Japan Workshop on Performance-Based Earthquake Engineering Methodology for Reinforced Concrete Building Structures.* December 2002.
- PEER 2002/20** *Barriers to Adoption and Implementation of PBEE Innovations.* Peter J. May. August 2002.
- PEER 2002/19** *Economic-Engineered Integrated Models for Earthquakes: Socioeconomic Impacts.* Peter Gordon, James E. Moore II, and Harry W. Richardson. July 2002.
- PEER 2002/18** *Assessment of Reinforced Concrete Building Exterior Joints with Substandard Details.* Chris P. Pantelides, Jon Hansen, Justin Nadauld, and Lawrence D. Reaveley. May 2002.
- PEER 2002/17** *Structural Characterization and Seismic Response Analysis of a Highway Overcrossing Equipped with Elastomeric Bearings and Fluid Dampers: A Case Study.* Nicos Makris and Jian Zhang. November 2002.
- PEER 2002/16** *Estimation of Uncertainty in Geotechnical Properties for Performance-Based Earthquake Engineering.* Allen L. Jones, Steven L. Kramer, and Pedro Arduino. December 2002.

- PEER 2002/15** *Seismic Behavior of Bridge Columns Subjected to Various Loading Patterns.* Asadollah Esmaeily-Gh. and Yan Xiao. December 2002.
- PEER 2002/14** *Inelastic Seismic Response of Extended Pile Shaft Supported Bridge Structures.* T.C. Hutchinson, R.W. Boulanger, Y.H. Chai, and I.M. Idriss. December 2002.
- PEER 2002/13** *Probabilistic Models and Fragility Estimates for Bridge Components and Systems.* Paolo Gardoni, Armen Der Kiureghian, and Khalid M. Mosalam. June 2002.
- PEER 2002/12** *Effects of Fault Dip and Slip Rake on Near-Source Ground Motions: Why Chi-Chi Was a Relatively Mild M7.6 Earthquake.* Brad T. Aagaard, John F. Hall, and Thomas H. Heaton. December 2002.
- PEER 2002/11** *Analytical and Experimental Study of Fiber-Reinforced Strip Isolators.* James M. Kelly and Shakhzod M. Takhirov. September 2002.
- PEER 2002/10** *Centrifuge Modeling of Settlement and Lateral Spreading with Comparisons to Numerical Analyses.* Sivapalan Gajan and Bruce L. Kutter. January 2003.
- PEER 2002/09** *Documentation and Analysis of Field Case Histories of Seismic Compression during the 1994 Northridge, California, Earthquake.* Jonathan P. Stewart, Patrick M. Smith, Daniel H. Whang, and Jonathan D. Bray. October 2002.
- PEER 2002/08** *Component Testing, Stability Analysis and Characterization of Buckling-Restrained Unbonded Braces™.* Cameron Black, Nicos Makris, and Ian Aiken. September 2002.
- PEER 2002/07** *Seismic Performance of Pile-Wharf Connections.* Charles W. Roeder, Robert Graff, Jennifer Soderstrom, and Jun Han Yoo. December 2001.
- PEER 2002/06** *The Use of Benefit-Cost Analysis for Evaluation of Performance-Based Earthquake Engineering Decisions.* Richard O. Zerbe and Anthony Falit-Baiamonte. September 2001.
- PEER 2002/05** *Guidelines, Specifications, and Seismic Performance Characterization of Nonstructural Building Components and Equipment.* André Filiatrault, Constantin Christopoulos, and Christopher Stearns. September 2001.
- PEER 2002/04** *Consortium of Organizations for Strong-Motion Observation Systems and the Pacific Earthquake Engineering Research Center Lifelines Program: Invited Workshop on Archiving and Web Dissemination of Geotechnical Data, 4–5 October 2001.* September 2002.
- PEER 2002/03** *Investigation of Sensitivity of Building Loss Estimates to Major Uncertain Variables for the Van Nuys Testbed.* Keith A. Porter, James L. Beck, and Rustem V. Shaikhutdinov. August 2002.
- PEER 2002/02** *The Third U.S.-Japan Workshop on Performance-Based Earthquake Engineering Methodology for Reinforced Concrete Building Structures.* July 2002.
- PEER 2002/01** *Nonstructural Loss Estimation: The UC Berkeley Case Study.* Mary C. Comerio and John C. Stallmeyer. December 2001.
- PEER 2001/16** *Statistics of SDF-System Estimate of Roof Displacement for Pushover Analysis of Buildings.* Anil K. Chopra, Rakesh K. Goel, and Chatpan Chintanapakdee. December 2001.
- PEER 2001/15** *Damage to Bridges during the 2001 Nisqually Earthquake.* R. Tyler Ranf, Marc O. Eberhard, and Michael P. Berry. November 2001.
- PEER 2001/14** *Rocking Response of Equipment Anchored to a Base Foundation.* Nicos Makris and Cameron J. Black. September 2001.
- PEER 2001/13** *Modeling Soil Liquefaction Hazards for Performance-Based Earthquake Engineering.* Steven L. Kramer and Ahmed-W. Elgamal. February 2001.
- PEER 2001/12** *Development of Geotechnical Capabilities in OpenSees.* Boris Jeremić. September 2001.
- PEER 2001/11** *Analytical and Experimental Study of Fiber-Reinforced Elastomeric Isolators.* James M. Kelly and Shakhzod M. Takhirov. September 2001.
- PEER 2001/10** *Amplification Factors for Spectral Acceleration in Active Regions.* Jonathan P. Stewart, Andrew H. Liu, Yoojoong Choi, and Mehmet B. Baturay. December 2001.
- PEER 2001/09** *Ground Motion Evaluation Procedures for Performance-Based Design.* Jonathan P. Stewart, Shyh-Jeng Chiou, Jonathan D. Bray, Robert W. Graves, Paul G. Somerville, and Norman A. Abrahamson. September 2001.
- PEER 2001/08** *Experimental and Computational Evaluation of Reinforced Concrete Bridge Beam-Column Connections for Seismic Performance.* Clay J. Naito, Jack P. Moehle, and Khalid M. Mosalam. November 2001.

- PEER 2001/07** *The Rocking Spectrum and the Shortcomings of Design Guidelines.* Nicos Makris and Dimitrios Konstantinidis. August 2001.
- PEER 2001/06** *Development of an Electrical Substation Equipment Performance Database for Evaluation of Equipment Fragilities.* Thalia Agnanos. April 1999.
- PEER 2001/05** *Stiffness Analysis of Fiber-Reinforced Elastomeric Isolators.* Hsiang-Chuan Tsai and James M. Kelly. May 2001.
- PEER 2001/04** *Organizational and Societal Considerations for Performance-Based Earthquake Engineering.* Peter J. May. April 2001.
- PEER 2001/03** *A Modal Pushover Analysis Procedure to Estimate Seismic Demands for Buildings: Theory and Preliminary Evaluation.* Anil K. Chopra and Rakesh K. Goel. January 2001.
- PEER 2001/02** *Seismic Response Analysis of Highway Overcrossings Including Soil-Structure Interaction.* Jian Zhang and Nicos Makris. March 2001.
- PEER 2001/01** *Experimental Study of Large Seismic Steel Beam-to-Column Connections.* Egor P. Popov and Shakhzod M. Takhirov. November 2000.
- PEER 2000/10** *The Second U.S.-Japan Workshop on Performance-Based Earthquake Engineering Methodology for Reinforced Concrete Building Structures.* March 2000.
- PEER 2000/09** *Structural Engineering Reconnaissance of the August 17, 1999 Earthquake: Kocaeli (Izmit), Turkey.* Halil Sezen, Kenneth J. Elwood, Andrew S. Whittaker, Khalid Mosalam, John J. Wallace, and John F. Stanton. December 2000.
- PEER 2000/08** *Behavior of Reinforced Concrete Bridge Columns Having Varying Aspect Ratios and Varying Lengths of Confinement.* Anthony J. Calderone, Dawn E. Lehman, and Jack P. Moehle. January 2001.
- PEER 2000/07** *Cover-Plate and Flange-Plate Reinforced Steel Moment-Resisting Connections.* Taejin Kim, Andrew S. Whittaker, Amir S. Gilani, Vitelmo V. Bertero, and Shakhzod M. Takhirov. September 2000.
- PEER 2000/06** *Seismic Evaluation and Analysis of 230-kV Disconnect Switches.* Amir S. J. Gilani, Andrew S. Whittaker, Gregory L. Fenves, Chun-Hao Chen, Henry Ho, and Eric Fujisaki. July 2000.
- PEER 2000/05** *Performance-Based Evaluation of Exterior Reinforced Concrete Building Joints for Seismic Excitation.* Chandra Clyde, Chris P. Pantelides, and Lawrence D. Reaveley. July 2000.
- PEER 2000/04** *An Evaluation of Seismic Energy Demand: An Attenuation Approach.* Chung-Che Chou and Chia-Ming Uang. July 1999.
- PEER 2000/03** *Framing Earthquake Retrofitting Decisions: The Case of Hillside Homes in Los Angeles.* Detlof von Winterfeldt, Nels Roselund, and Alicia Kitsuse. March 2000.
- PEER 2000/02** *U.S.-Japan Workshop on the Effects of Near-Field Earthquake Shaking.* Andrew Whittaker, Editor. July 2000.
- PEER 2000/01** *Further Studies on Seismic Interaction in Interconnected Electrical Substation Equipment.* Armen Der Kiureghian, Kee-Jeung Hong, and Jerome L. Sackman. November 1999.
- PEER 1999/14** *Seismic Evaluation and Retrofit of 230-kV Porcelain Transformer Bushings.* Amir S. Gilani, Andrew S. Whittaker, Gregory L. Fenves, and Eric Fujisaki. December 1999.
- PEER 1999/13** *Building Vulnerability Studies: Modeling and Evaluation of Tilt-up and Steel Reinforced Concrete Buildings.* John W. Wallace, Jonathan P. Stewart, and Andrew S. Whittaker, Editors. December 1999.
- PEER 1999/12** *Rehabilitation of Nonductile RC Frame Building Using Encasement Plates and Energy-Dissipating Devices.* Mehrdad Sasani, Vitelmo V. Bertero, James C. Anderson. December 1999.
- PEER 1999/11** *Performance Evaluation Database for Concrete Bridge Components and Systems under Simulated Seismic Loads.* Yael D. Hose and Frieder Seible. November 1999.
- PEER 1999/10** *U.S.-Japan Workshop on Performance-Based Earthquake Engineering Methodology for Reinforced Concrete Building Structures.* December 1999.
- PEER 1999/09** *Performance Improvement of Long Period Building Structures Subjected to Severe Pulse-Type Ground Motions.* James C. Anderson, Vitelmo V. Bertero, and Raul Bertero. October 1999.
- PEER 1999/08** *Envelopes for Seismic Response Vectors.* Charles Menun and Armen Der Kiureghian. July 1999.
- PEER 1999/07** *Documentation of Strengths and Weaknesses of Current Computer Analysis Methods for Seismic Performance of Reinforced Concrete Members.* William F. Cofer. November 1999.

- PEER 1999/06** *Rocking Response and Overturning of Anchored Equipment under Seismic Excitations.* Nicos Makris and Jian Zhang. November 1999.
- PEER 1999/05** *Seismic Evaluation of 550 kV Porcelain Transformer Bushings.* Amir S. Gilani, Andrew S. Whittaker, Gregory L. Fenves, and Eric Fujisaki. October 1999.
- PEER 1999/04** *Adoption and Enforcement of Earthquake Risk-Reduction Measures.* Peter J. May, Raymond J. Burby, T. Jens Feeley, and Robert Wood. August 1999.
- PEER 1999/03** *Task 3 Characterization of Site Response General Site Categories.* Adrian Rodriguez-Marek, Jonathan D. Bray and Norman Abrahamson. February 1999.
- PEER 1999/02** *Capacity-Demand-Diagram Methods for Estimating Seismic Deformation of Inelastic Structures: SDF Systems.* Anil K. Chopra and Rakesh Goel. April 1999.
- PEER 1999/01** *Interaction in Interconnected Electrical Substation Equipment Subjected to Earthquake Ground Motions.* Armen Der Kiureghian, Jerome L. Sackman, and Kee-Jeung Hong. February 1999.
- PEER 1998/08** *Behavior and Failure Analysis of a Multiple-Frame Highway Bridge in the 1994 Northridge Earthquake.* Gregory L. Fenves and Michael Ellery. December 1998.
- PEER 1998/07** *Empirical Evaluation of Inertial Soil-Structure Interaction Effects.* Jonathan P. Stewart, Raymond B. Seed, and Gregory L. Fenves. November 1998.
- PEER 1998/06** *Effect of Damping Mechanisms on the Response of Seismic Isolated Structures.* Nicos Makris and Shih-Po Chang. November 1998.
- PEER 1998/05** *Rocking Response and Overturning of Equipment under Horizontal Pulse-Type Motions.* Nicos Makris and Yiannis Roussos. October 1998.
- PEER 1998/04** *Pacific Earthquake Engineering Research Invitational Workshop Proceedings, May 14–15, 1998: Defining the Links between Planning, Policy Analysis, Economics and Earthquake Engineering.* Mary Comerio and Peter Gordon. September 1998.
- PEER 1998/03** *Repair/Upgrade Procedures for Welded Beam to Column Connections.* James C. Anderson and Xiaojing Duan. May 1998.
- PEER 1998/02** *Seismic Evaluation of 196 kV Porcelain Transformer Bushings.* Amir S. Gilani, Juan W. Chavez, Gregory L. Fenves, and Andrew S. Whittaker. May 1998.
- PEER 1998/01** *Seismic Performance of Well-Confined Concrete Bridge Columns.* Dawn E. Lehman and Jack P. Moehle. December 2000.

PEER REPORTS: ONE HUNDRED SERIES

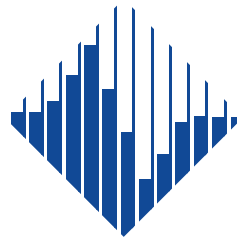
- PEER 2012/103** *Performance-Based Seismic Demand Assessment of Concentrically Braced Steel Frame Buildings.* Chui-Hsin Chen and Stephen A. Mahin. December 2012.
- PEER 2012/102** *Procedure to Restart an Interrupted Hybrid Simulation: Addendum to PEER Report 2010/103.* Vesna Terzic and Božidar Stojadinovic. October 2012.
- PEER 2012/101** *Mechanics of Fiber Reinforced Bearings.* James M. Kelly and Andrea Calabrese. February 2012.
- PEER 2011/107** *Nonlinear Site Response and Seismic Compression at Vertical Array Strongly Shaken by 2007 Niigata-ken Chuetsu-oki Earthquake.* Eric Yee, Jonathan P. Stewart, and Kohji Tokimatsu. December 2011.
- PEER 2011/106** *Self Compacting Hybrid Fiber Reinforced Concrete Composites for Bridge Columns.* Pardeep Kumar, Gabriel Jen, William Trono, Marios Panagiotou, and Claudia Ostertag. September 2011.
- PEER 2011/105** *Stochastic Dynamic Analysis of Bridges Subjected to Spatially Varying Ground Motions.* Katerina Konakli and Armen Der Kiureghian. August 2011.
- PEER 2011/104** *Design and Instrumentation of the 2010 E-Defense Four-Story Reinforced Concrete and Post-Tensioned Concrete Buildings.* Takuya Nagae, Kenichi Tahara, Taizo Matsumori, Hitoshi Shiohara, Toshimi Kabeyasawa, Susumu Kono, Minehiro Nishiyama (Japanese Research Team) and John Wallace, Wassim Ghannoum, Jack Moehle, Richard Sause, Wesley Keller, Zeynep Tuna (U.S. Research Team). June 2011.
- PEER 2011/103** *In-Situ Monitoring of the Force Output of Fluid Dampers: Experimental Investigation.* Dimitrios Konstantinidis, James M. Kelly, and Nicos Makris. April 2011.
- PEER 2011/102** *Ground-Motion Prediction Equations 1964–2010.* John Douglas. April 2011.
- PEER 2011/101** *Report of the Eighth Planning Meeting of NEES/E-Defense Collaborative Research on Earthquake Engineering.* Convened by the Hyogo Earthquake Engineering Research Center (NIED), NEES Consortium, Inc. February 2011.
- PEER 2010/111** *Modeling and Acceptance Criteria for Seismic Design and Analysis of Tall Buildings.* Task 7 Report for the Tall Buildings Initiative - Published jointly by the Applied Technology Council. October 2010.
- PEER 2010/110** *Seismic Performance Assessment and Probabilistic Repair Cost Analysis of Precast Concrete Cladding Systems for Multistory Buildings.* Jeffrey P. Hunt and Božidar Stojadinovic. November 2010.
- PEER 2010/109** *Report of the Seventh Joint Planning Meeting of NEES/E-Defense Collaboration on Earthquake Engineering. Held at the E-Defense, Miki, and Shin-Kobe, Japan, September 18–19, 2009.* August 2010.
- PEER 2010/108** *Probabilistic Tsunami Hazard in California.* Hong Kie Thio, Paul Somerville, and Jascha Polet, preparers. October 2010.
- PEER 2010/107** *Performance and Reliability of Exposed Column Base Plate Connections for Steel Moment-Resisting Frames.* Ady Aviram, Božidar Stojadinovic, and Armen Der Kiureghian. August 2010.
- PEER 2010/106** *Verification of Probabilistic Seismic Hazard Analysis Computer Programs.* Patricia Thomas, Ivan Wong, and Norman Abrahamson. May 2010.
- PEER 2010/105** *Structural Engineering Reconnaissance of the April 6, 2009, Abruzzo, Italy, Earthquake, and Lessons Learned.* M. Selim Günay and Khalid M. Mosalam. April 2010.
- PEER 2010/104** *Simulating the Inelastic Seismic Behavior of Steel Braced Frames, Including the Effects of Low-Cycle Fatigue.* Yuli Huang and Stephen A. Mahin. April 2010.
- PEER 2010/103** *Post-Earthquake Traffic Capacity of Modern Bridges in California.* Vesna Terzic and Božidar Stojadinović. March 2010.
- PEER 2010/102** *Analysis of Cumulative Absolute Velocity (CAV) and JMA Instrumental Seismic Intensity (I_{JMA}) Using the PEER–NGA Strong Motion Database.* Kenneth W. Campbell and Yousef Bozorgnia. February 2010.
- PEER 2010/101** *Rocking Response of Bridges on Shallow Foundations.* Jose A. Ugalde, Bruce L. Kutter, and Boris Jeremic. April 2010.
- PEER 2009/109** *Simulation and Performance-Based Earthquake Engineering Assessment of Self-Centering Post-Tensioned Concrete Bridge Systems.* Won K. Lee and Sarah L. Billington. December 2009.

- PEER 2009/108** *PEER Lifelines Geotechnical Virtual Data Center.* J. Carl Stepp, Daniel J. Ponti, Loren L. Turner, Jennifer N. Swift, Sean Devlin, Yang Zhu, Jean Benoit, and John Bobbitt. September 2009.
- PEER 2009/107** *Experimental and Computational Evaluation of Current and Innovative In-Span Hinge Details in Reinforced Concrete Box-Girder Bridges: Part 2: Post-Test Analysis and Design Recommendations.* Matias A. Hube and Khalid M. Mosalam. December 2009.
- PEER 2009/106** *Shear Strength Models of Exterior Beam-Column Joints without Transverse Reinforcement.* Sangjoon Park and Khalid M. Mosalam. November 2009.
- PEER 2009/105** *Reduced Uncertainty of Ground Motion Prediction Equations through Bayesian Variance Analysis.* Robb Eric S. Moss. November 2009.
- PEER 2009/104** *Advanced Implementation of Hybrid Simulation.* Andreas H. Schellenberg, Stephen A. Mahin, Gregory L. Fenves. November 2009.
- PEER 2009/103** *Performance Evaluation of Innovative Steel Braced Frames.* T. Y. Yang, Jack P. Moehle, and Božidar Stojadinovic. August 2009.
- PEER 2009/102** *Reinvestigation of Liquefaction and Nonliquefaction Case Histories from the 1976 Tangshan Earthquake.* Robb Eric Moss, Robert E. Kayen, Liyuan Tong, Songyu Liu, Guojun Cai, and Jiaer Wu. August 2009.
- PEER 2009/101** *Report of the First Joint Planning Meeting for the Second Phase of NEES/E-Defense Collaborative Research on Earthquake Engineering.* Stephen A. Mahin et al. July 2009.
- PEER 2008/104** *Experimental and Analytical Study of the Seismic Performance of Retaining Structures.* Linda Al Atik and Nicholas Sitar. January 2009.
- PEER 2008/103** *Experimental and Computational Evaluation of Current and Innovative In-Span Hinge Details in Reinforced Concrete Box-Girder Bridges. Part 1: Experimental Findings and Pre-Test Analysis.* Matias A. Hube and Khalid M. Mosalam. January 2009.
- PEER 2008/102** *Modeling of Unreinforced Masonry Infill Walls Considering In-Plane and Out-of-Plane Interaction.* Stephen Kadysiewski and Khalid M. Mosalam. January 2009.
- PEER 2008/101** *Seismic Performance Objectives for Tall Buildings.* William T. Holmes, Charles Kircher, William Petak, and Nabih Youssef. August 2008.
- PEER 2007/101** *Generalized Hybrid Simulation Framework for Structural Systems Subjected to Seismic Loading.* Tarek Elkhoraibi and Khalid M. Mosalam. July 2007.
- PEER 2007/100** *Seismic Evaluation of Reinforced Concrete Buildings Including Effects of Masonry Infill Walls.* Alidad Hashemi and Khalid M. Mosalam. July 2007.

The Pacific Earthquake Engineering Research Center (PEER) is a multi-institutional research and education center with headquarters at the University of California, Berkeley. Investigators from over 20 universities, several consulting companies, and researchers at various state and federal government agencies contribute to research programs focused on performance-based earthquake engineering.

These research programs aim to identify and reduce the risks from major earthquakes to life safety and to the economy by including research in a wide variety of disciplines including structural and geotechnical engineering, geology/seismology, lifelines, transportation, architecture, economics, risk management, and public policy.

PEER is supported by federal, state, local, and regional agencies, together with industry partners.



PEER Core Institutions

University of California, Berkeley (Lead Institution)
California Institute of Technology
Oregon State University
Stanford University
University of California, Davis
University of California, Irvine
University of California, Los Angeles
University of California, San Diego
University of Nevada, Reno
University of Southern California
University of Washington

PEER reports can be ordered at <https://peer.berkeley.edu/peer-reports> or by contacting

Pacific Earthquake Engineering Research Center
University of California, Berkeley
325 Davis Hall, Mail Code 1792
Berkeley, CA 94720-1792
Tel: 510-642-3437
Email: peer_center@berkeley.edu

ISSN 2770-8314
<https://doi.org/10.55461/RDWC6463>